

INFORMATION TO USERS

This manuscript has been reproduced from the microfilm master. UMI films the text directly from the original or copy submitted. Thus, some thesis and dissertation copies are in typewriter face, while others may be from any type of computer printer.

The quality of this reproduction is dependent upon the quality of the copy submitted. Broken or indistinct print, colored or poor quality illustrations and photographs, print bleedthrough, substandard margins, and improper alignment can adversely affect reproduction.

In the unlikely event that the author did not send UMI a complete manuscript and there are missing pages, these will be noted. Also, if unauthorized copyright material had to be removed, a note will indicate the deletion.

Oversize materials (e.g., maps, drawings, charts) are reproduced by sectioning the original, beginning at the upper left-hand corner and continuing from left to right in equal sections with small overlaps. Each original is also photographed in one exposure and is included in reduced form at the back of the book.

Photographs included in the original manuscript have been reproduced xerographically in this copy. Higher quality 6" x 9" black and white photographic prints are available for any photographs or illustrations appearing in this copy for an additional charge. Contact UMI directly to order.

UMI

A Bell & Howell Information Company
300 North Zeeb Road, Ann Arbor, MI 48106-1346 USA
313/761-4700 800/521-0600



CHARACTERIZATION OF CHEMICALLY SYNTHESIZED BARIUM TITANATE
IN THE FORMS OF POWDER, BULK AND THIN FILM CERAMICS

DISSERTATION

Presented in Partial Fulfillment of the Requirements for
the Degree Doctor of Philosophy in the Graduate
School of The Ohio State University

By

Weidong Zhu, B.S., M.S.

The Ohio State University

1995

Dissertation Committee:


Sheikh A. Akbar

David A. Rigney

Eric R. Kreidler

Prabir K. Dutta

Approved by



Adviser

Materials Science and Engineering

UMI Number: 9612308

UMI Microform 9612308

Copyright 1996, by UMI Company. All rights reserved.

**This microform edition is protected against unauthorized
copying under Title 17, United States Code.**

UMI

**300 North Zeeb Road
Ann Arbor, MI 48103**

To My Parents

ACKNOWLEDGMENTS

I would like to express my sincere appreciation to my advisor Dr. Sheikh A. Akbar for his persistent guidance and encouragement throughout this thesis work. His hard-working philosophy, deep and broad knowledge of materials science, and cheerful attitude have a profound influence on me. I gratefully acknowledge Dr. Ching-Chyr Wang for his invaluable support and discussion during this work. Special thanks go to Dr. M. A. Alim of Ohio Brass Company (Wadsworth, OH) for his valuable discussions on the immittance spectroscopy work. I also want to thank my dissertation committee members, Dr. David Rigney, Dr. Eric Kreidler and Dr. Prabir Dutta for their helpful advice and suggestions for this dissertation.

I would also like to thank each of the members of my research group, Abdul-Majeed Azad, Lora Younkman, Liming Wang, Virginia Patton and Matiur Rahman for their pleasant conversation, helpful discussions, friendship and invaluable memories. Thanks also go to Cheng-Hua Kou, Jai Subramanian, Thawi Iwagoshi, Shyue-woei Ko, Sen-Shan Yang, Weize Chen, Minggang (Bill) Zhu, Xiangjun Wang, Jian Ye, Xuejin Zheng, Wei Wang, Yunshu Zhang, Yirong

He, Minghui Zheng, Xiaodi Xu and Mulong Yu. Their friendship and understanding made my time here so enjoyable.

My sincere thanks go to Dr. Prabir Dutta and Reza Asiaie for their helpful collaboration which benefited this research tremendously. Special thanks also go to the other members of this research project, Dr. Patrick Gallagher, Dr. John Lannutti, Dr. Zhimin Zhong and Benedict Gaskins for their insightful suggestions and discussions.

Finally, I would like to express my gratitude to my parents who persistently encouraged me to achieve my best. Their generosity and support made my wish of pursuing an education in this beautiful country come true. My deepest appreciation goes to my girlfriend, Shunhua Xing. Without her love and support, this work could not be done.

The financial support of this research by the National Science Foundation (NSF DMR 9202565) is gratefully acknowledged.

VITA

December 21, 1967	Born - Nanjing, P. R. China
1990	B.S., Ceramic Engineering Nanjing Institute of Technology Nanjing, P. R. China
1990 – 1992	Graduate Research Associate The Ohio State University, Columbus, Ohio
1992	M. S., The Ohio State University, Columbus, Ohio
1992 – Present	Graduate Research Associate The Ohio State University, Columbus, Ohio

FIELDS OF STUDY

Major Field: Materials Science and Engineering

TABLE OF CONTENTS

DEDICATION	ii
ACKNOWLEDGMENTS	iii
VITA	iv
LIST OF TABLES	xiii
LIST OF FIGURES	xv
CHAPTER	
I. INTRODUCTION	1
II. LITERATURE REVIEW	8
2.1. Review of Ferroelectricity, Ferroelectric Domain and Hysteresis, Structure and Phase Transition	8
2.1.1. Introduction	8
2.1.2. Ferroelectricity	9
I. History of ferroelectricity	9
II. Definition of ferroelectricity	12
III. Dielectrics and ferroelectrics terminology	14
2.1.3. Ferroelectric Domain and Hysteresis	21
I. Ferroelectric Domains	21
II. Ferroelectric hysteresis	29
2.1.4. Crystal Structure and the Origin of Ferroelectricity of BaTiO ₃	32

2.1.5.	Ferroelectric Phase Transition	43
I.	Introduction	43
II.	Classification of phase transitions	43
III.	Phenomenological theory	46
IV.	Lattice dynamics theory (soft-mode)	60
V.	Size effect on ferroelectric phase transition	67
2.2.	Review of Low Temperature Powder Synthesis	69
2.2.1.	Chemical Coprecipitation Process	70
I.	Oxalate process	71
II.	Citrate process	72
2.2.2.	Double alkoxides process	73
2.2.3.	Sol-gel process	74
2.2.4.	Aerosol drying, freeze drying and spray drying	76
2.2.5.	Combustion synthesis	78
2.2.6.	Hydrothermal process	79
2.3.	Effects of Sintering and Microstructure on Dielectric Properties	84
2.3.1.	Ba to Ti Ratio	85
2.3.2.	Sintering Mechanism and Schedule	86
2.3.3.	Hot-Pressing and Fast-Sintering	88
2.3.4.	Additives for Sintering	92
2.4.	Impedance Spectroscopy (IS)	94
2.4.1.	Lumped Parameter/Complex Plane Analysis (LP/CPA)	95
2.4.2.	Equivalent Circuit Modeling	100

2.5.	Review of Thin Film Synthesis of BaTiO ₃	104
2.5.1.	Methods for Thin Film Fabrication	105
2.5.2.	Preparation of BaTiO ₃ Thin Films Using Hydrothermal Synthesis	110
III.	EXPERIMENTAL	112
3.1.	Hydrothermal Synthesis of BaTiO ₃ Powders and Thin Films	112
3.1.1.	Hydrothermal synthesis of BaTiO ₃ powders	112
I.	Synthesis with varying temperatures and reaction time	113
II.	Synthesis with different barium sources	114
III.	Hydrothermal synthesis with different NaOH concentrations	115
3.1.2.	Hydrothermal synthesis of BaTiO ₃ thin films	115
I.	Substrate preparation	115
II.	Thin film synthesis	116
3.2.	Characterization of BaTiO ₃ Powders	116
3.2.1.	Powder X-ray Diffraction (XRD)	116
3.2.2.	Elemental Analysis	118
I.	X-ray fluorescence spectroscopy	118
II.	Inductively coupled plasma-atomic emission spectroscopy (ICP-AES)	119
3.2.3.	Thermal Analysis	121
I.	Differential scanning calorimetry (DSC)	121
II.	Thermogravimetry and differential thermal analysis (TG/DTA)	122

3.2.4.	Electron Microscopy	122
I.	Scanning electron microscopy (SEM)	122
II.	Transmission electron microscopy (TEM) and convergent electron beam diffraction (CBD)	123
3.2.5.	Vibrational Spectroscopy	123
I.	Infrared (IR) spectroscopy	123
II.	Raman spectroscopy	124
3.3.	Sintering of BaTiO ₃ Powders	124
3.3.1.	Powder Compaction	124
3.3.2.	Dilatometry measurement	125
3.3.3.	Sintering of Powders under Different Conditions	125
I.	Conventional sintering	125
II.	Fast-sintering with very high sintering rate	126
3.4.	Characterization for Sintered Ceramic BaTiO ₃	127
3.4.1.	Bulk Density Measurement by Archimedes Method	127
3.4.2.	Scanning Electron Microscopy of Sintered BaTiO ₃ ...	128
3.4.3.	Dielectric Property Measurement	128
I.	Dielectric constant and loss measurement as a function of temperature	128
II.	Immittance spectroscopy analysis	129
3.5.	BaTiO ₃ Thin Film Characterization	130
3.5.1.	Room-temperature and hot-stage X-ray diffraction ..	130
3.5.2.	Scanning electron microscopy and energy dispersive analysis (SEM/EDS)	131
3.5.3.	Electrical properties measurement	131

IV. RESULTS	133
4.1. Characterization of BaTiO ₃ Powders	133
4.1.1. Method of Quantitative Determination of Tetragonal BaTiO ₃	133
4.1.2. BaTiO ₃ Powders Synthesized by Varying Reaction Temperatures and Times.....	137
I. BaTiO ₃ powder synthesized at 95°C	139
II. BaTiO ₃ powders synthesized at 240°C for various times	139
4.1.3. BaTiO ₃ Powders Synthesized with Different Barium Sources	146
4.1.4. BaTiO ₃ Powders Synthesized with Different NaOH Concentrations	155
I. Microstructure and phase determination	155
II. Lattice parameter and strain measurement	163
III. Thermal Analysis	167
IV. Vibrational spectroscopy	169
4.2. Characterization of Sintered Ceramic BaTiO ₃	178
4.2.1. BaTiO ₃ Ceramics from Hydrothermally Synthesized Powders with Different Barium Sources	179
I. Sintering and Microstructure	179
II. Dielectric properties measurement	187
4.2.2. BaTiO ₃ Ceramics from Hydrothermal Synthesized Powders with Various OH ⁻ concentrations	193
I. Microstructure and dielectric properties of hydrothermal powders by conventional sintering	196
II. Fast-Sintering	207
4.2.3. Impedance Spectroscopy Analysis	215

4.3.	Characterization of Hydrothermally Synthesized BaTiO ₃ Thin Films	222
4.3.1.	Microstructure	222
4.3.2.	Electrical Properties	227
I.	Temperature dependence of dielectric constant (K) and loss tangent ($\tan\delta$)	227
II.	Impittance spectroscopy analysis	230
V.	DISCUSSION	239
5.1.	Hydrothermal Synthesis of BaTiO ₃ Powders	239
5.1.1	Effect of Synthesis Conditions on Hydrothermal Synthesis of BaTiO ₃ Powders	239
5.1.2.	Particle Size Effect on the Structure and Properties of BaTiO ₃ Powders	245
I.	Particle size and tetragonality	245
II.	Defects and microstrains	246
III.	Crystal and molecular structure	248
IV.	Size effect on ΔH of transition	249
5.2.	Sintering, Microstructure and Dielectric Properties of BaTiO ₃	254
5.2.1	The Effect of Powder Characteristics and Sintering Conditions on Microstructure Development	254
5.2.2.	The Influence of Microstructure on Dielectric Properties	258
5.3.	Synthesis, Microstructure and Electrical Properties of BaTiO ₃ Thin Films	259
5.3.1	Synthesis and Microstructure of BaTiO ₃ Thin Film ...	259
5.3.2.	Electrical Properties of BaTiO ₃ Thin Films	262

5.4. Impedance Spectroscopy Analysis	264
5.4.1. Ceramic BaTiO ₃ by Sintering the Hydrothermally Synthesized Cubic Powder at 1250°C for 2 hours ...	264
5.4.2. Hydrothermally Synthesized BaTiO ₃ Thin Films	279
VI. SUMMARY AND CONCLUSION	281
VII. SUGGESTIONS FOR FUTURE WORK	285
LIST OF REFERENCE	287

LIST OF TABLES

TABLES	PAGE
2.1. The 32 Crystal Point Groups	13
2.2. Synthesis of BaTiO ₃ using oxalate process	72
2.3. Table 2.3. Conditions for satisfying equivalent circuit modeling	104
3.1. Operating conditions for ICP-AES measurement	121
4.1. Particle size, tetragonality and transition temperature as a function of synthesis time for hydrothermally synthesized BaTiO ₃	140
4.2. Particle size and percent tetragonality of the BaTiO ₃ powders synthesized with various barium sources	146
4.3. Lattice parameters, lattice strain and particle size calculations of the BaTiO ₃ powders A, B and C as determined by XRD	165
4.4. Dielectric properties, grain size and density of the BaTiO ₃ powders with various barium sources sintered at 1300°C for 5 hours	188
4.5. Dielectric properties, grain size and density of the BaTiO ₃ (Cl ⁻) powders sintered at various temperatures for 5 hours	190
4.6. Density and dielectric properties of the cubic, A, B and C powders sintered at various temperatures for 2 hours	208

4.7.	Density and dielectric properties of the cubic powders fast sintered at various temperatures for 5 minutes	209
------	---	-----

LIST OF FIGURES

FIGURES	PAGE
2.1. Schematic representation of different mechanisms of polarization	17
2.2. Frequency dependence of the polarization mechanisms in dielectrics: (a) contributions to the dielectric constant; (b) contributions to the loss tangent	18
2.3. (a) The elastic energy and domain wall energy as a function of grain size. The intersection of two curves determines the lower size limit, a_{crit} ; (b) Dependence of elastic energy on grain size with different domain configurations	25
2.4. Dielectric constant as a function of grain size of ceramic BaTiO ₃ ..	29
2.5. (a) A schematic representation of a typical ferroelectric hysteresis loop. (b) Domain growth in the direction of an applied field	31
2.6. The change in ferroelectric hysteresis with temperature for ceramic BaTiO ₃	33
2.7. Perovskite structure of BaTiO ₃	34
2.8. Schematics of unit-cell distortions of the single crystal BaTiO ₃ polymorphs	36
2.9. Properties of single-crystal BaTiO ₃ : (a) lattice dimensions vs. temperature; (b) spontaneous polarization vs. Temperature and (c) dielectric constants measured in the <i>a</i> and <i>c</i> directions vs. temperature	37
2.10. Displacements of the different ions in BaTiO ₃ in the cubic to tetragonal distortion: (a) oxygen ions and (b) unit cell lattice	39

2.11.	Variation of the potential energy of Ti^{4+} along the c axis	40
2.12.	(a) Surface charge associated with spontaneous polarization; (b) formation of 180° domains to minimize electrostatic energy	42
2.13.	Schematic illustrating the poling process	42
2.14.	(a) P_S vs. temperature and (b) K vs. temperature for a first- and second-order ferroelectric phase transition	45
2.15.	The free energy as a function of polarization at several different temperatures: (a) for a second-order phase transition; (b) for a first-order phase transition	52
2.16.	The temperature dependence of χ^{-1} for (a) second-order and (b) first-order phase transitions	55
2.17.	Calculated P - E curves for (a) second-order phase transition; (b) first-order phase transition	56
2.18.	A unit cell of cubic $BaTiO_3$ (i.e., ABO_3 perovskite) showing the atomic displacements of the four different normal modes	63
2.19.	A schematic diagram of E vs. k for the lowest TO branch in the paraelectric phase as the ferroelectric transition temperature T_c is approached from above	66
2.20.	A flow chart illustrating the hydrothermal steps used in commercial synthesis	82
2.21.	Stability diagram for the Ba-Ti hydrothermal system	83
2.22.	Phase diagram of BaO-TiO ₂ system: (a) the one given by Rase <i>et al.</i> and (b) the one modified by Kirby <i>et al.</i>	87
2.23.	Schematic diagram of the rates of two different mass transport mechanisms during sintering corresponding respectively to densification and grain growth as a function of temperature	91
2.24.	Phase diagram of BaTiO ₃ -SiO ₂ system	93

2.25.	Single relaxation semicircle is observed in multiple complex planes, suggesting the sample-electrode system can be represented by more than one equivalent circuit	97
2.26.	Determination of depression angle and peak frequency for impedance or capacitance plot	99
2.27.	Equivalent circuit modeling in polycrystalline materials	101
4.1.	X-ray diffraction pattern of the BaTiO ₃ powders with (a) tetragonal and (b) cubic structure, respectively	135
4.2.	DSC patterns of the (a) tetragonal and (b) cubic BaTiO ₃ samples which were also used in XRD measurement	136
4.3.	The calibration curve of ΔH as a function of tetragonal content obtained by physically mixing various amounts of 100% tetragonal sample with the cubic sample	138
4.4.	The SEM micrograph of BaTiO ₃ powders synthesized at 95°C	141
4.5.	SEM micrographs of the BaTiO ₃ powders synthesized for various times: (a) 3 and (b) 7 days	142
4.6.	SEM micrographs of the BaTiO ₃ powders synthesized for various times: (a) 3 and (b) 8 weeks	143
4.7.	Powder XRD patterns of hydrothermally synthesized BaTiO ₃ powders as a function of reaction time at 240°C for (a) 1 day; (b) 3 days; (c) 5 days; (d) 7 days; (e) 2 weeks and (f) 8 weeks	144
4.8.	Particle size and percent tetragonality of BaTiO ₃ powders as a function of synthesis time	145
4.9.	XRD patterns for BaTiO ₃ powders synthesized hydrothermally at 240°C from various barium sources in one week period. (a) BaI ₂ ; (b) BaBr ₂ ; (c) BaCl ₂ ; (d) Ba(C ₂ H ₃ O ₂) ₂ ; (e) Ba(NO ₃) ₂ and (f) Ba(OH) ₂	147
4.10	SEM micrographs of the BaTiO ₃ powders with different barium sources: (a) Ba(OH) ₂ ; (b) Ba(NO ₃) ₂ ; (c) Ba(C ₂ H ₃ O ₂) ₂ ; (d) BaCl ₂ ; (e) BaI ₂ , and (f) commercial (TAM HPB)	149

4.11. SEM micrographs of the BaTiO ₃ powders synthesized with various OH ⁻ concentrations: (a) powder A (b) powder B and (c) powder C	156
4.12. XRD patterns of powders: (a) A; (b) B and (c) C. The insets highlight the characteristic reflections of (200)-type planes of BaTiO ₃ crystals with 2θ ranging from 44 to 46°	159
4.13. XRD pattern with Si internal standard: (a) powder A; (b) powder B and (c) powder C	160
4.14. TEM micrographs of the hydrothermal powders: (a) A and (b) B ...	161
4.15. HREM micrograph of a representative particle from powder B	164
4.16. Hall-Williamson plot with Gaussian-Gaussian profile for the BaTiO ₃ powders: (a) A (b) B and (c) C	166
4.17. DSC curves around the Curie transition for BaTiO ₃ powders: (a) A (b) B and (c) C	168
4.18. TGA measurement of weight loss in the BaTiO ₃ powders: (a) A (b) B and (c) C, as a function of temperature	170
4.19. Raman spectra of the BaTiO ₃ powders: (a) A (b) B and (c) C	172
4.20. Raman spectra of the tetragonal BaTiO ₃ powder: (a) at room temperature; (b) upon heating above T _c and (c) upon cooling back to room temperature	173
4.21. Raman spectrum of the BaTiO ₃ powders synthesized at 95°C	174
4.22. Infrared spectra of the OH stretching vibration region for the BaTiO ₃ powders: (a) A (b) B and (c) C	176
4.23. Infrared spectra of the framework region of BaTiO ₃ powders: (a) A (b) B (c) C and (d) cubic synthesized at 95°C	177
4.24. Dilatometric curves of the BaTiO ₃ powders synthesized with various barium sources	180

4.25. SEM micrographs of the BaTiO ₃ powders sintered at 1300°C for 5 hours: (a) BaTiO ₃ (NO ₃ ⁻); (b) BaTiO ₃ (C ₂ H ₃ O ₂ ⁻); (c) BaTiO ₃ (Cl ⁻) and (d) commercial (TAM HPB)	183
4.26. SEM micrographs of the BaTiO ₃ (Cl ⁻) powder sintered at various temperatures: (a) 1200°C; (b) 1250°C and (c) 1350°C	185
4.27. Dielectric properties: (a) dielectric constant and (b) loss tangent as a function of temperature for the BaTiO ₃ samples synthesized from various barium sources	189
4.28. Dielectric properties: (a) dielectric constant and (b) loss tangent as a function of temperature for the BaTiO ₃ (Cl ⁻) sample sintered at various temperatures	191
4.29. Dielectric properties: (a) dielectric constant and (b) loss tangent as a function of temperature for the BaTiO ₃ (TAM) sample sintered at various temperatures	192
4.30. Dilatometric curves showing the linear percent shrinkage as a function of temperature for BaTiO ₃ powders: cubic, B and C	194
4.31. SEM micrographs of the cubic powder sintered at different temperatures: (a) 1250; (b) 1300 and (c) 1350°C	197
4.32. SEM micrographs of powder B sintered at different temperatures: (a) 1200; (b) 1250 and (c) 1300°C	199
4.33. SEM micrographs of powder C sintered at different temperatures: (a) 1200; (b) 1250 and (c) 1300°C	201
4.34. Dielectric constant and loss measurement as a function of temperature of the sample from the cubic powder sintered at 1250°C for 2 hours	203
4.35. Dielectric constant and loss measurement as a function of temperature of selected sintered samples from powder A	204
4.36. Dielectric constant and loss measurement as a function of temperature of selected sintered samples from powder B	205

4.37.	Dielectric constant and loss measurement as a function of temperature of selected sintered samples from powder C	206
4.38.	SEM micrographs of the hydrothermally synthesized BaTiO ₃ cubic powder sintered at various temperatures for 5 minutes (~ 200°C/min): (a) 1250, (b) 1300 and (c) 1350°C	210
4.39.	Dielectric properties: (a) dielectric constant and (b) loss tangent as a function of temperature for the hydrothermally synthesized cubic BaTiO ₃ sample sintered at various temperatures for 5 minutes with a rate of about 200°C/min	213
4.40.	Dielectric properties: (a) dielectric constant and (b) loss tangent as a function of temperature for the hydrothermally synthesized cubic BaTiO ₃ sample sintered at various temperatures for 15 minutes (≈ 200°C/min)	214
4.41.	The capacitance versus frequency for the cubic sample sintered at 1250°C for 2 hours	216
4.42.	Impedance plots of the sintered ceramic sample measured at various temperatures. For the purpose of clarity, two separate plots are shown to illustrate the entire measuring temperature range	217
4.43.	Modulus plots of the same sample as in Figure 4.42 at various temperatures	218
4.44.	Capacitance plots of the same sample as in Figure 4.42 at various temperatures	219
4.45.	Admittance plots of the same sample as in Figure 4.42 at various temperatures	220
4.46.	The SEM micrographs showing the morphology of the thin-film samples synthesized for various times: (a) 1; (b) 2; (c) 3 and (d) 4 weeks	223
4.47.	Low magnification SEM micrograph showing the smooth, dense film surface without observable cracks	225
4.48.	SEM micrograph of the cross-sectional view of the thin-film sample synthesized for 2 weeks	226

4.49.	XRD patterns of the BaTiO ₃ thin films synthesized for 1, 2, 3 and 4 weeks, respectively	228
4.50.	The XRD scans of 2θ between 44 and 46° at different temperatures for the BaTiO ₃ film synthesized for 2 weeks	229
4.51.	Dielectric properties of the film synthesized for 2 weeks at a frequency of 100 kHz from the room temperature to 200°C and subsequently cooled back to room temperature	231
4.52.	Dielectric measurement results of the films synthesized for 2, 3 and 4 weeks at a frequency of 100 kHz, together with that of the film synthesized for 2 weeks at a frequency of 1 kHz	232
4.53.	Measured capacitance data of the BaTiO ₃ films synthesized for 2 weeks as a function of frequency at temperatures ranging from 150 to 300°C	233
4.54.	Impedance (Z^*) plots of the BaTiO ₃ film synthesized for 2 weeks measured at various temperatures	235
4.55.	Modulus (M^*) plot of the same sample as in Figure 2.54 at various temperatures	236
4.56.	Complex capacitance (C^*) plot of the same sample as in Figure 2.54 at various temperatures	237
4.57.	Admittance (Y^*) plot of the same sample as in Figure 2.54 at various temperatures	238
5.1.	Variation of local polarization as a function of length from the surface to the interior of a ferroelectric particle	252
5.2.	Schematic diagram to illustrate a particle from ordered to partially disordered and completely disordered as particle size decreases	252
5.3.	Size dependence of the polarization of a ferroelectric particle with first order transition	253
5.4.	Temperature dependence of the relaxation times (τ_1 and τ_2) associated with high- and low- frequency semicircles in the Z^* -plane	266

5.5.	Temperature dependence of the resistances (R_1 and R_2) associated with the high- and low- frequency semicircles in the Z^* -plane	267
5.6.	Temperature dependence of the capacitances (C_1 and C_2) associated with the high- and low- frequency relaxations in the Z^* -plane	269
5.7.	Temperature dependence of the depression angles (θ_1 and θ_2) associated with the grain and grain boundary relaxations in the Z^* -plane	270
5.8.	Temperature dependence of the capacitances (C_1 and C_2) associated with the grain and grain boundary relaxations in the M^* -plane	274
5.9.	Equivalent circuit model corresponding to the two semicircular relaxations in the impedance plane. R_1-C_1 and R_2-C_2 combinations constitute the high- (grain) and low- frequency (grain boundary) relaxations, respectively	275
5.10.	Simulated results of frequency dependence of the capacitance for ferroelectric materials above T_c by assigning the R and C values	278

CHAPTER I

INTRODUCTION

Half a century ago, barium titanate (BaTiO_3) was first discovered as being a ferroelectric material [1-2]. Its unique perovskite structure and near room temperature ferroelectricity have made it the most extensively studied ferroelectric material. It has also led to the discovery of other perovskite ferroelectric materials and the establishment of the theories of ferroelectricity [3].

Barium titanate has an exceptional high dielectric constant at room temperature (about 1000 ~ 2000), much greater than those of the common capacitor materials used in the 1940's (titania has a dielectric constant of 80). The high dielectric constant of BaTiO_3 has made it one of the most popular materials for capacitor applications. Barium titanate is currently the controlling composition for Y5V (Z5U) and X7R multilayer ceramic capacitors (MLCC) that are used worldwide in electronic industries. It is estimated that the consumption of BaTiO_3 in the United States alone is about 13 million pounds in 1994 [4-5].

Barium titanate is not only one of the most important materials for the ceramic capacitor industry, its commercial applications have also spread into

many other areas, including positive temperature coefficient thermistors (PTCR), piezoelectrics for ultrasonic and measuring devices, pressure transducers, infra-red detectors and a variety of electro-optic devices. Recently, due to the advance in thin film processing techniques, there is a renewed interest in thin film ferroelectrics in possible applications for nonvolatile memories in the semiconductor industry.

Conventional synthesis of barium titanate compounds typically involves high temperature ($\sim 1200^{\circ}\text{C}$) calcination of solid mixtures of barium carbonate and titanium dioxide. The powders thus produced are often low in purity and composed of large and non-uniform particles. Recent advances in hybrid circuit and surface mount technology (SMT) favor the miniaturization and improved performance of the electronic components, which in turn put more stringent requirements on the starting powders. Homogeneous and pure powders with uniform and fine particle size can be achieved by wet-chemical synthesis methods or so-called solution methods, which allow the maximum stoichiometric control over the starting materials to yield stoichiometric precursors such as mixed Ba-Ti oxalates, citrate and alkoxide salt. Also, because of the intimate atomic level contact between Ba and Ti by the participating ligands, the formation temperatures of BaTiO_3 are much lower through wet-chemical routes.

The above mentioned wet-chemical syntheses require thermal decomposition of Ba-Ti precursors to prepare BaTiO_3 powders. Hydrothermal

synthesis, which involves the direct preparation of crystalline BaTiO_3 without high temperature calcination, has gained popularity recently. It involves the chemical reactions of Ba(OH)_2 , TiO_2 or gels of Ba-Ti acetate mixtures in a highly basic aqueous solution at temperatures of $80 \sim 150^\circ\text{C}$. The lower processing temperature has its advantages in producing finer particles with more uniform size. In addition, the synthesis allows one to control particle size via adjusting the synthesis parameters, such as the reaction temperature, time and pH values. Although the hydrothermal synthesis has the above mentioned advantages, its formation and growth mechanisms in the BaTiO_3 synthesis have not been well understood. It is one of the objectives of this study to understand how the various parameters influence the BaTiO_3 formation and subsequent growth of particles.

It has been reported [6-9] that the low temperature synthesized submicron-sized BaTiO_3 powders are often in a cubic-like structure and do not exhibit ferroelectricity. In contrast, the stable phase of single crystal BaTiO_3 or sintered samples with large grain sizes has a tetragonal structure which displays a typical ferroelectric behavior. Thus the unusual behavior for the fine BaTiO_3 powders and thin films with submicron crystal size appears to be particle size dependent. Various mechanisms have been proposed to explain the appearance of this cubic-like structure, including surface layer, surface tension,

defects, strains, depolarization field, *etc.* However, the exact reason is still unknown and is a subject of extensive debate in the literature.

In order to gain more insight into this size dependent phenomenon, it is desirable to be able to synthesize pure and well-crystallized BaTiO₃ powders with different sizes, so as to correlate the observed properties with particle size and crystal structure. Hydrothermal synthesis is one of the most appropriate methods as it allows an easy control over the particle size through adjusting the synthesis parameters. A combination of various characterization and analytical methods such as x-ray diffraction (XRD), electron microscopy (SEM and TEM), thermal analysis techniques (DSC, TG/DTA) and vibrational spectroscopy (Raman and IR) are essential in the study since it can provide valuable information about the microstructure, defects and strains, and changes of structure and related behaviors of the powders toward the phase transition.

Although BaTiO₃ powders produced by hydrothermal synthesis have been proved to be pure and homogeneous, limited studies have been conducted on the sintering behavior of these powders and the dielectric properties of the sintered body. It is important to study their sintering behavior and the influences of the starting powders with various characteristics (e.g., particle size, defect concentration and structure) on the sintering behavior and microstructure development, including the relationship between the microstructure and dielectric properties of the sintered body. An effort to optimize the dielectric

properties through microstructure control by adjusting the sintering conditions is also desired.

Recently, the renewed interest in ferroelectric films for nonvolatile semiconductor memory applications has led to intensive research in barium titanate for ferroelectric thin film applications, due to its relatively large dielectric constant and electrooptic coefficient. The research has focused on how to improve processing and properties of ferroelectric thin films. Various processing techniques have been studied such as thermal or electron evaporation, radio frequency ion beam and magnetron sputtering, laser ablation, chemical vapor deposition (CVD) and sol-gel method. The hydrothermal method is a new and promising technique for the processing of ferroelectric thin films, because it is a unique way to directly prepare crystalline films without the need for post-deposition annealing, which is normally required for other techniques. However, more work needs to be done to understand the synthesis mechanism, microstructure and especially the electrical properties of the synthesized films.

Electrical properties of the dielectric materials, such as BaTiO_3 , are usually studied at a fixed frequency (typically at 1 kHz). This seems to be justified for a single crystal system where no grain boundaries are present. However, it has been reported [10-13] that the ferroelectric behavior depends on grain size, porosity and many other variables in the ceramic system. Impedance spectroscopy (IS) has been proven to be a powerful technique to separate

individual contributions of various physical regions to the overall electrical properties by analyzing the electrical data over a wide range of frequencies. IS combined with electron microscopy can provide a useful correlation between microstructure and electric properties.

The objectives of this research were:

- to synthesize BaTiO_3 powders with various sizes using the hydrothermal method and to investigate the influence of the synthesis parameters such as temperature, time, different anion sources and OH^- concentrations on the powder characteristics;
- to characterize the synthesized powders in terms of phase purity, crystal symmetry and lattice distortions, as well as phase transition behavior using various characterization techniques, including x-ray diffraction, electron microscopy, thermal and vibrational spectroscopy analyses;
- to investigate the underlying mechanism for the size effect on the structure and ferroelectricity of fine BaTiO_3 powders;
- to study the sintering behavior of the synthesized powders and the effects of sintering conditions on the microstructure development and dielectric properties;

- to examine the synthesis and microstructure of BaTiO₃ thin films using the hydrothermal method and study their electrical properties;
- to analyze the frequency dependent dielectric behavior using immittance spectroscopy (IS) analysis to reveal a microstructure-property correlation.

CHAPTER II

LITERATURE REVIEW

2.1. Review of Ferroelectricity, Ferroelectric Domain and Hysteresis, Barium Titanate Structure and Phase Transition

2.1.1. Introduction

Ferroelectrics are an very important class of ceramic materials because of their large dielectric constants, normally greater than 1000. Their structure and properties have been reviewed by several authors [3, 14-15]. Their high dielectric constants originate from the spontaneous polarization or spontaneous alignment of electric dipoles in certain crystallographic directions, a characteristic most important for the ferroelectric materials. These electric dipoles are aligned parallel to each other within certain regions of a crystal called ferroelectric domains. When an electric field (E) is applied, the aligned electric dipoles within the domains can be switched, giving rise to a very large change in polarization along the electric field direction and thus a large dielectric constant. The switching of the ferroelectric domains, leading to a hysteresis behavior, is another important characteristic of the ferroelectrics. Since the

relation between the magnitudes of the polarization (P) and the applied electric field (E) is not linear, ferroelectrics are also referred to as nonlinear dielectrics. This nonlinear behavior resembles the nonlinear magnetic behavior of ferromagnetic materials.

2.1.2. Ferroelectricity

I. History of ferroelectricity

The phenomenon of pyroelectricity observed in some crystals, in which the spontaneous electric dipole moment is temperature dependent, has been known for a very long time. Studies to characterize the pyroelectric effect in a quantitative manner in the eighteenth and nineteenth centuries eventually led to the discovery of piezoelectricity. In 1880, J. Curie and P. Curie [16] first observed piezoelectricity manifested by a crystal exhibiting electric polarity when subjected to a stress. In 1920, Valasek discovered the first ferroelectric crystal: sodium potassium tartrate tetrahydrate ($\text{NaKC}_4\text{H}_4\text{O}_6 \cdot 4\text{H}_2\text{O}$), better known as Rochelle salt [17-18]. The main reason for the much later discovery of the ferroelectrics is because of the formation of domain structure with differently oriented polarization in virgin ferroelectric single crystals leading to a zero net polarization and very small pyroelectric and piezoelectric responses. Valasek recognized ferroelectricity by experiments which demonstrated a hysteresis effect in the electric field-polarization curve, a Curie temperature, T_c , and an

extremely large dielectric and piezoelectric response in and near the ferroelectric temperature region of the Rochelle salt crystal, which are in many respects similar to corresponding effects in ferromagnetism.

Barium titanate (BaTiO_3) was discovered in 1945 and its ferroelectricity was reported shortly thereafter [1-2]. Barium titanate is the first ferroelectric material ever found with a perovskite structure, and is of significant importance both in terms of simple structure and practical utility. Compared with other ferroelectric crystals, such as Rochelle salt and KH_2PO_4 (KDP), BaTiO_3 has many unique properties: (1) it has a cubic centro-symmetric perovskite structure which is highly symmetric above the Curie temperature, (2) there are only five atoms per unit cell, (3) it is chemically and mechanically very stable, (4) it is ferroelectric at room temperature and (5) it can be easily prepared in both polycrystalline ceramic and single crystal forms. Because of these structural and processing advantages, BaTiO_3 has become the most extensively studied ferroelectric material since its discovery. It also led to searches and discoveries of many other perovskite ferroelectric materials, such as KNbO_3 and KTaO_3 [19], LiNbO_3 and LiTaO_3 [20], and PbTiO_3 [21].

Along with the discovery of BaTiO_3 , there was significant progress in ferroelectric theory. Lattice dynamics theory focusing on lattice modes ('soft' modes) is most successful in explaining ferroelectric behavior at a microscopic level [22-27]. At a macroscopic level ferroelectric theory has progressed more

rapidly, overlooking the microscopic details such as ionic or electronic displacement, long- or short-range interactions, *etc.*, but focusing only on thermodynamic concepts. The theory developed by Landau, Ginzburg [29-30] and further modified by Devonshire [31-33], also referred to as phenomenological theory, is particularly successful in explaining the macroscopic properties such as dielectric, piezoelectric and elastic behavior at any temperature from a free-energy consideration. This phenomenological theory is capable of describing both polar and non-polar phases with the same energy function. In 1966, Buessem, Cross and Goswami [10] successfully applied this theory to fine-grained BaTiO₃ ceramics with the consideration of 90° domain and internal stresses to delineate the observed high dielectric constant of the fine-grained ceramics.

Accompanying the rapid development of the ferroelectric theories, a tremendous amount of work was also done to investigate the potential applications of ferroelectrics in the areas of capacitors, transducers, infra-red detectors and various electro-optic devices. However, the problems associated with the difficulties involving process and microstructure control significantly hindered the commercial applications of these materials. Therefore, even more than fifty years after the discovery of ferroelectricity, there is still active research on the synthesis, microstructure and electrical properties of these materials, as well as further applications in modern microelectronic industries.

II. Definition of ferroelectricity

All crystals can be classified into 7 crystal systems according to their minimum symmetry requirements: triclinic, monoclinic, orthorhombic, tetragonal, cubic, trigonal and hexagonal. These systems can be further divided into 32 point groups according to their symmetry with reference to a point. Among them, 11 are centro-symmetric and possess a center of symmetry. Thus they cannot maintain any polar properties or spontaneous polarization. One of the remaining 21 noncentro-symmetric point groups, cubic 432, has symmetry elements which prevent polar characteristics. The other 20 point groups have one or more polar axes (Table 2.1) and therefore exhibit various polar effects such as piezoelectricity, pyroelectricity and ferroelectricity.

Piezoelectricity is the property of a crystal which exhibits electrical polarization when subjected to a stress. On the other hand, if an electrical field is applied, a strain will be produced in the crystal and whether it will stretch or compress depends on the orientation of the field with the polarization in the crystal.

Of the 20 piezoelectric crystal classes, 10 have a unique polar axis. Crystals belonging to these classes are called polar crystals because they

Table 2.1. The 32 Crystal Point Groups [35]

Optical axes	Crystal systems	Centrosymmetric point groups		Noncentrosymmetric point groups				
				Polar		Nonpolar		
Biaxial	Triclinic	$\bar{1}$		1		none		
	Monoclinic	$2/m$		2	m	none		
	Orthorhombic	mmm		$mm2$		222		
Uniaxial	Tetragonal	$4/m$	$4/mmm$	4	$4mmm$	$\bar{4}$	$\bar{4}2m$	422
	Trigonal	$\bar{3}$	$\bar{3}m$	3	$3m$	32		
	Hexagonal	$6/m$	$6/mmm$	6	$6mmm$	$\bar{6}$	$\bar{6}2m$	622
Isotropic	Cubic	$m\bar{3}$	$m\bar{3}m$	none		23	$\bar{3}m$	432
Total number		11 groups		10 groups		11 groups		

possess a spontaneous polarization (electric moment/unit volume), i.e. a spontaneous alignment of electric dipoles in certain directions. The magnitude of the spontaneous polarization is temperature dependent and thus electric charges can be induced on the crystal surfaces perpendicular to the polar axis upon changing the temperature. This is the so-called pyroelectric effect and all of the 10 polar crystal classes are pyroelectric.

Ferroelectricity is defined as the property of a crystal with a spontaneous polarization and its orientation can be reversed by an electric field. The spontaneous polarization usually cannot be detected by charges on the surface of the crystal because the depolarization field which results from the

spontaneous polarization (charge distribution) can be compensated by the flow of free charge within the crystal and in the surrounding medium or by twinning (domain formation). Ferroelectricity requires the crystal to have at least two identical orientational states for polarization in the absence of the electric field so that the reversal of polarization by the electric field becomes possible. Ferroelectricity can be revealed only below a certain temperature, which is called the Curie temperature (T_c), above which the randomizing effect of thermal energy (kT) is dominant and the spontaneous polarization no longer exists. The phase existing above T_c is said to be in the paraelectric state.

III. Dielectrics and ferroelectrics terminology

For an ideal dielectric material, when exposed to an electric field, there is no long-range transport of charge carriers [34-35]. Instead, there is only a limited rearrangement of these charges so that a dipole moment (μ) is produced and the material is said to be polarized. The rearrangement of the charges can be viewed as charges (Q) stored in the dielectric, corresponding to the capacitance (C) of the dielectric. Thus, capacitance is a measure of the charge storage ability of a particular material between two parallel conductors under an externally applied electric field (V).

By considering the area (A) of the plates and the distance (d) between the plates (or capacitor thickness), a relation between the capacitance and permittivity (ϵ) can be derived:

$$C = Q/V = \frac{\epsilon(V/d)A}{V} = \epsilon A/d \quad (2.1)$$

The dielectric constant, K , also referred to as the relative permittivity, is defined as the ratio of the capacitance (or permittivity) of a capacitor and that of vacuum:

$$K = C/C_0 = \frac{\epsilon A/d}{\epsilon_0 A/d} = \epsilon/\epsilon_0 \quad (2.2)$$

where C_0 and ϵ_0 are the capacitance and permittivity of vacuum.

The electric dipole moment, μ , resulting from the separation of charge is defined as

$$\mu = Q \cdot \delta x \quad (2.3)$$

where δx is the distance between the opposite point charges. Polarization is defined as the dipole moment (μ) per unit volume. The polarization here is induced by the applied electric field and is thus called induced polarization (P_i), which is different from the spontaneous polarization (P_s) that a ferroelectric materials acquires naturally.

There are four principal mechanisms contributing to the induced polarization in materials [34-36]. Each of them involves a short-range rearrangement of charges and contributes to the total polarization of the

material. These polarization mechanisms are (1) atomic polarization, (2) ionic polarization, (3) dipolar polarization and (4) space charge or interfacial polarization.

Atomic polarization, which occurs in all materials, is a small displacement of the electron cloud in an atom relative to the nucleus. Atomic polarization occurs in the ultraviolet optical frequency range with frequencies as high as 10^{15} Hz. Ionic polarization involves the relative displacement of cations and anions, as in the Si-O bond in SiO_2 . Ionic polarization occurs at frequencies ranging from 10^{12} to 10^{13} Hz, which are in the infra-red range. Dipolar polarization, which is also referred to as orientational polarization, involves the rotation of molecular or ionic dipoles in the direction of the applied field, giving a net polarization. This polarization takes effect in the subinfra-red range of frequencies ($\sim 10^{11}$ Hz). As one of the special cases here, spontaneously polarized dipoles in the ferroelectric materials give rise to dipolar polarization when an electric field is applied. Space charge or interfacial polarization involves a limited migration of charge carriers until they are inhibited at a potential barrier, possibly a surface, a grain boundary or a phase boundary. This process occurs at frequencies as low as 10^{-3} Hz and gives rise to a very large capacitance. The various polarization mechanisms and their frequency dependence are shown in Figure 2.1 and 2.2, respectively.

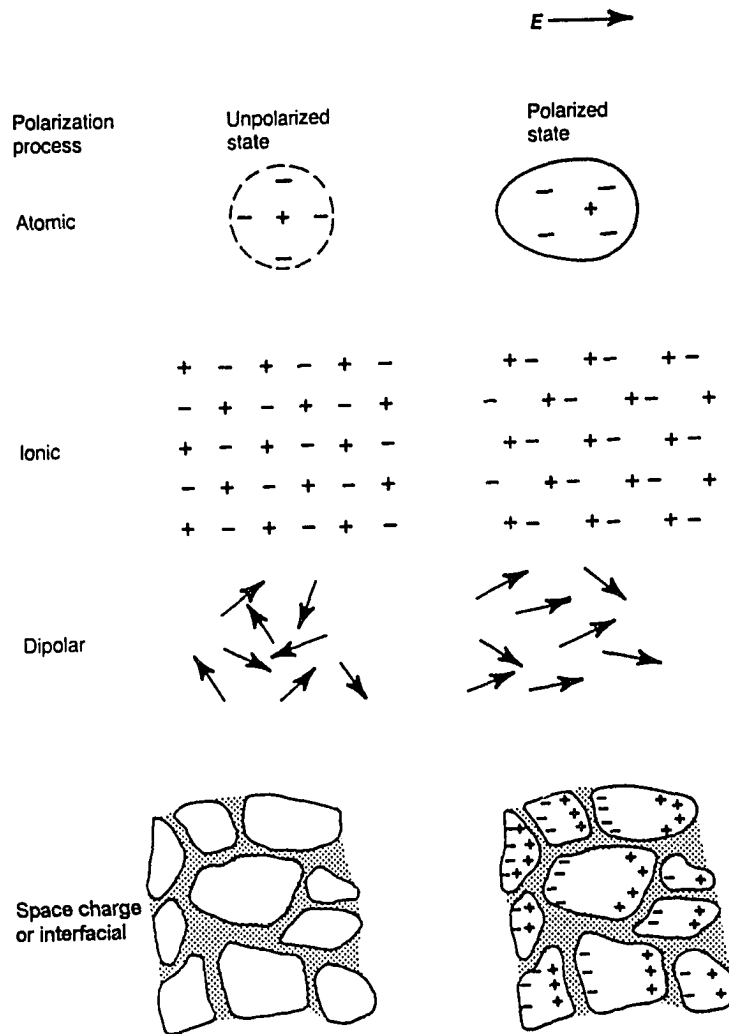


Figure 2.1. Schematic representation of different mechanisms of polarization [36].

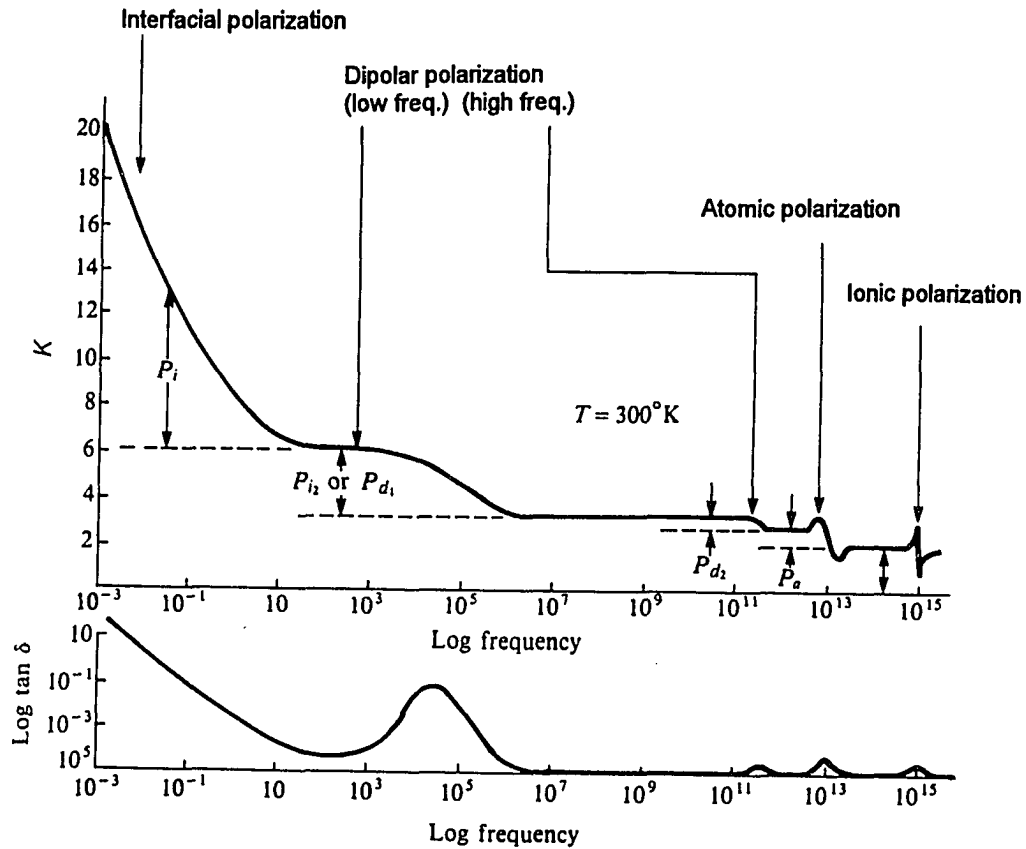


Figure 2.2. Frequency dependence of the polarization mechanisms in dielectrics: (a) contributions to the dielectric constant; (b) contributions to the loss tangent [35].

In dielectrics, the relationship between dielectric displacement (D), electric field (E) and total polarization (P) can be expressed as:

$$D = \epsilon_0 E + P \quad (2.4)$$

For normal dielectrics or the so-called 'linear' dielectrics, the total polarization arises entirely from the induced polarization, and is proportional to the applied electric field within the material:

$$P = \chi_e \epsilon_0 E \quad (2.5)$$

where χ_e is the electric susceptibility, a dimensionless constant. However, in non-linear dielectrics or ferroelectrics, the polarization includes both contributions from the dipole moment (μ) induced in the presence of a field-induced polarization, P_i , and from the spontaneous polarization, P_s :

$$P = P_i + P_s = \chi_e \epsilon_0 E + P_s(E) = \chi \epsilon_0 E \quad (2.6)$$

Since P_s exhibits a non-linear dependence on E , the electric susceptibility χ in ferroelectric materials is no longer a constant and depends on the applied field.

The dielectric constant, K , is defined as

$$K = \frac{\epsilon}{\epsilon_0} = 1 + \chi \quad (2.7)$$

Combining Equations (2.5) and (2.7) with the above equation, the following equation can be derived:

$$K = 1 + P / \epsilon_0 E \quad (2.8)$$

Equation (2.8) is very important since it describes a relationship between the dielectric constant and the total polarization in the material. The dielectric constant of a material will be large if the total polarization is significant, as in the case of ferroelectrics.

By considering the local field that individual atoms or ions are subjected to and its effect on the induced dipoles, the classical Clausius-Mosotti equation can be derived:

$$\frac{K-1}{K+2} = \frac{n\alpha}{3\epsilon_0} \quad (2.9)$$

where α is called the polarizability of the entity, i.e., the average dipole moment per unit of local field strength and n is the density of the dipoles. This equation can subsequently lead to the so-called Curie-Weiss law (by considering the temperature dependence of dipolar polarization):

$$\chi = \frac{C}{T - T_0} \quad (2.10)$$

where C is the Curie constant and T_0 is called the Curie-Weiss temperature. The Curie-Weiss law describes an important relationship between the dielectric constant ($= 1+\chi$) and temperature in the paraelectric region ($T > T_c$). However, it no longer holds when the temperature is near or below T_c , at which all the dipoles are aligned to some degree with each other. The aligned dipoles create a strong field within the boundary and thus the local field consideration is no longer valid. Two different approaches, phenomenological and "soft mode"

theories, have successfully elucidated the phenomena of ferroelectricity and the associated phase transition.

2.1.3. Ferroelectric Domain and Hysteresis

I. Ferroelectric Domains

When a ferroelectric crystal is cooled through the Curie temperature, T_C , from a paraelectric state in the absence of the applied field, spontaneous polarization may occur along several equivalent directions. In order to achieve a minimum energy state, neighboring regions of the crystal tend to polarize along each of these equivalent directions respectively. These various regions within which the dipoles are aligned in the same direction are referred to as ferroelectric domains. The boundaries separating adjacent domains are called domain boundaries or domain walls. Since there is an interruption or distortion of periodic lattice arrangement along the domain walls, there must be a certain amount of energy associated with them and this energy is termed the domain wall energy.

It has been observed that a complex domain configuration exists in BaTiO_3 and other ferroelectric single crystals [37-41] and ceramics [42-51]. The formation of the domains in ferroelectric materials is governed by free energy minimization. Without the applied electric field ($E = 0$), the total energy (w_{Tot}) to be minimized can be expressed in a general form [45-46, 48-49]:

$$W_{Tot} = W_X + W_P + W_D + W_W + W_S \quad (2.11)$$

Here w_X and w_P are respectively bulk elastic and electric energies. The elastic energy, w_X is proportional to the square of the strain ($\propto X^2$) and w_P is proportional to the square of the polarization ($\propto P^2$). The surface energy of the bulk crystal, w_S , can be ignored if crystals are relatively large in size, and w_W and w_D are the domain wall and depolarization energy, respectively. All energies are given in terms of energy density which has the unit of J/m^3 .

Depolarization energy is related to the depolarization field, E_D set up in the crystal by the spontaneous polarization. In a perfect infinite ferroelectric crystal, the spontaneous polarization is uniform. However, at the surface of the crystal where P_s decreases to zero, or in regions close to defects where P_s may differ from the ideal crystal, a spatial variation of P_s ($\text{div } P_s$) leads to the presence of a depolarization field. This field can be compensated or partially compensated by the flow of free charges within the crystal or from the surrounding medium. However, in an insulating crystal (or insulating environment), the compensating process is extremely slow and therefore w_D can reach a very high value. The depolarization energy, w_D can be written as [3]:

$$w_D = \frac{1}{2} \int \vec{D} \cdot \vec{E} dV / V = \frac{1}{2} \int \frac{\epsilon}{\epsilon_0} L^2 P^2 dV / V \quad (2.12)$$

where L is a depolarization factor which equals unity with uniform polarization for a thin crystal wafer. Assuming a simple 180° periodic domain structure in the crystal, the depolarization energy can be rewritten as:

$$w_D = \frac{\varepsilon^* P_0^2 d}{t} \quad (2.13)$$

where d is the domain width, ε^* is a constant related to the dielectric constant of the ferroelectric, t is the crystal thickness and P_0 is the polarization at the center of a domain.

Domain wall energy, w_W , arises from the additional energy created due to the interruption or distortion of periodic lattice arrangement along the domain wall. It can be expressed as:

$$w_W = \sigma / d \quad (2.14)$$

where σ is the surface tension of the wall.

In most ferroelectric materials, such as BaTiO_3 , lattice unit cells deform slightly during the structural phase transition, i.e., the Curie transition at 130°C for BaTiO_3 , leading to a slight deformation of the crystallite that is built up by the deformed lattice cells. In the case of ceramics, since the grains are clamped by their neighboring grains in all three dimensions, they can only deform to some degree by cooperative motion of the adjacent grains. To maintain at least the gross shape of the grain, it leads to either high internal stresses by deformation,

or mechanical twinning (domains) to release the stresses [46-49]. The depolarization energy of the grain is assumed to be negligible due to the compensation of the polarization charges at the grain (or domain) boundaries by free charge carriers. The surface energy is as well negligible as long as the grains are not very fine. The electric energy, w_P , does not change during the domain formation; thus it will not be considered in energy minimization. Therefore, the minimum energy configuration corresponding to the domain formation is now being dominated by minimizing the sum of the elastic field energy (w_x) and domain wall energy (w_w). The corresponding domain width can be thereby estimated as a result of the energy minimization. Assuming 90° simple alternating domains, which is most commonly observed in the ceramic BaTiO₃, the domain width (d) has been estimated as [46]:

$$d = \sqrt{\frac{128\pi\sigma a}{c_{11}s^2}} \propto \sqrt{a} \quad (2.15)$$

where a is the grain size, c_{11} the average longitudinal elastic constant and s is the strain induced by the structural deformation ($c/a - 1$). This equilibrium domain width dependence on grain size is similar to that described in magnetic materials [52-54]. Since the homogeneous elastic energy (not energy density) in the grain increases with a^3 (volume energy term), while the domain wall or interface energy increases with a^2 (surface energy term). Therefore, there is a critical grain size, a_{crit1} below which the domain wall energy is larger than the

elastic energy [48-49]. Figure 2.3a illustrates this lower limit of the grain size a_{crit1} which is at the intersection of the two curves. As a decreases below the critical size, no domains should exist since the energy of the system can no longer be lowered by domain formation.

It has been shown that above the critical grain size, the domain configuration is stable. However, it can occur in two different forms (shown in Figure 2.3b) depending on the grain size [48-49]. The first type of domain configuration exhibits lamellar twinning and the grain can only adjust its shape in two dimensions. The second one displays more complex interfaces with a banded twin or herringbone structure. It has higher interface energy and allows stress relief in the third dimension. Again a critical grain size, a_{crit2} sets in below which only the first type of domain configuration can exist. The elastic energy density of the two different domain configurations as a function of grain size is illustrated in Figure 2.3b.

On the other hand, in ferroelectric single crystals as well as free particles, the crystals can change their shape freely during the structural phase transition. Therefore, the elastic energy (w_x) will not be a dominating term in energy minimization. In contrast, the depolarization energy term (w_D) will be a major one in energy considerations, since there are few free charge carriers to compensate the polarization charges in single crystals. Therefore, in this case the sum of w_D and w_W will be considered in the energy minimization as long as

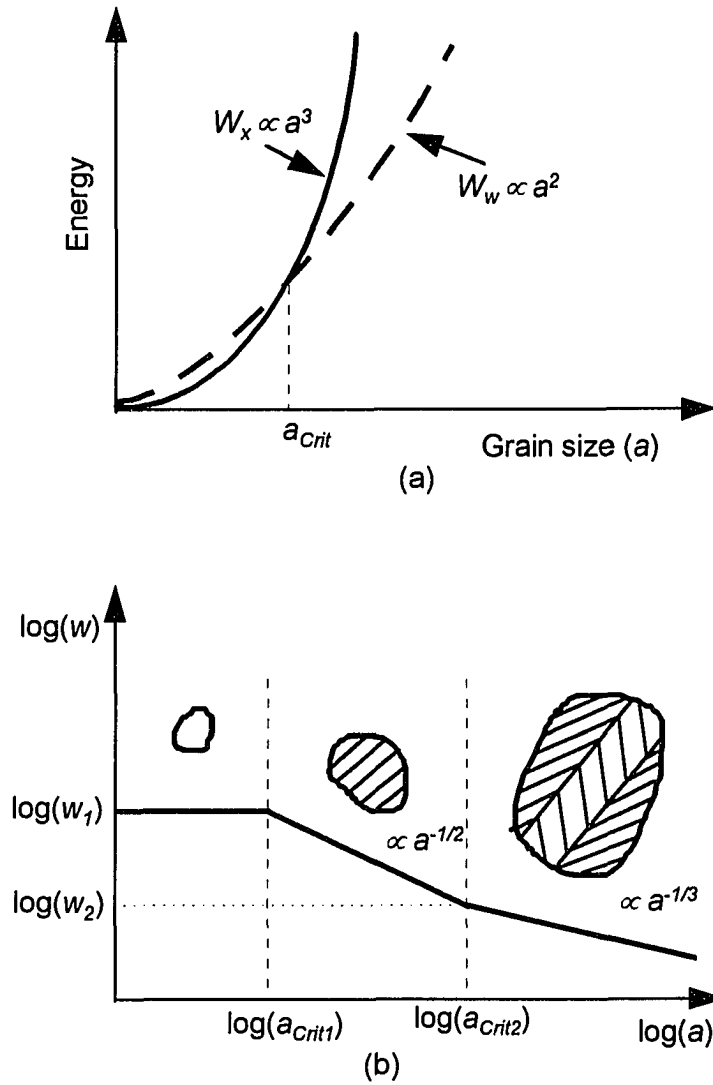


Figure 2.3. (a) The elastic energy and domain wall energy as a function of grain size. The intersection of two curves determines the lower size limit, a_{crit1} ; (b) Dependence of elastic energy on grain size with different domain configurations [48-49].

the crystal is large enough to ignore the surface energy. The equilibrium value of the domain width assuming a simple 180° periodic domain structure (the dominant type in single crystal BaTiO₃) can be written as [3]:

$$d = \sqrt{\frac{\sigma t}{\epsilon^* P_0^2}} \quad (2.16)$$

As the crystal or particle becomes smaller, the relative contributions of the various energy terms to the total energy change. Energies related to the surface become more important than volume energies [52]. Domain wall energy, w_w represents the energy of the boundary between domains, which is a surface energy term, while w_x and w_D are volume energy terms. Consequently, as the crystal becomes smaller, there will be a critical point at which it is favorable energetically to annihilate the domain walls so that the entire crystal becomes single domain. Similar behavior was predicted and observed in ferromagnetic materials [53-55]. As soon as the crystal becomes single domain, a strong depolarization field is present in the crystal and increases as the crystal size decreases, according to Equation (2.13). It has been estimated that without external charge compensation, a polarization with magnitude of $1\mu\text{C}/\text{cm}^2$ will lead to a depolarization field $\sim 10^7$ V/cm, under which ferroelectricity may be thermodynamically unstable [56].

The presence of the domain structure in BaTiO₃ ceramics has important effects on the dielectric properties [10, 45-50]. The room temperature dielectric

constant of a single crystal of BaTiO₃ is about 4770 along the *a* axis (ϵ_a) and 230 along the *c* axis (ϵ_c). In ceramic BaTiO₃, where grains are randomly oriented, the dielectric constant should have an intermediate value [36]:

$$\epsilon_a > \epsilon > \epsilon_c \quad (2.17)$$

However, very high dielectric constants ranging from 4500 ~ 6000 have been reported for ceramic BaTiO₃ with a dense body and a fine grain size [58-59]. The anomalous high dielectric constant in fine-grained ceramic BaTiO₃ was first explained by Buessem *et al.* by applying Devonshire's phenomenological theory [10]. The authors claimed that due to the partial or complete disappearance of domains in fine-grained ceramics, the internal stress inside the grains becomes very high, giving rise to a high dielectric constant as predicted by the phenomenological theory.

Arlt *et al.* [45-50] further investigated the domain behavior and found that 90°-domains exist even in very fine-grained ceramics. The width of the domains decreases as the grain size decreases ($d \propto a^{1/2}$), resulting in an increase in domain density. The internal stress was estimated to be of the same order of magnitude as predicted in Buessem's stress model for the fine-grained ceramics. The authors ascribed both the contributions of the internal stress and the high density of 90°-domain walls to the high dielectric constants of fine-grained ceramics. As shown in Figure 2.4, *K* shows a maximum at 1 μm grain size, below which *K* decreases again due to the presence of pseudocubic phases.

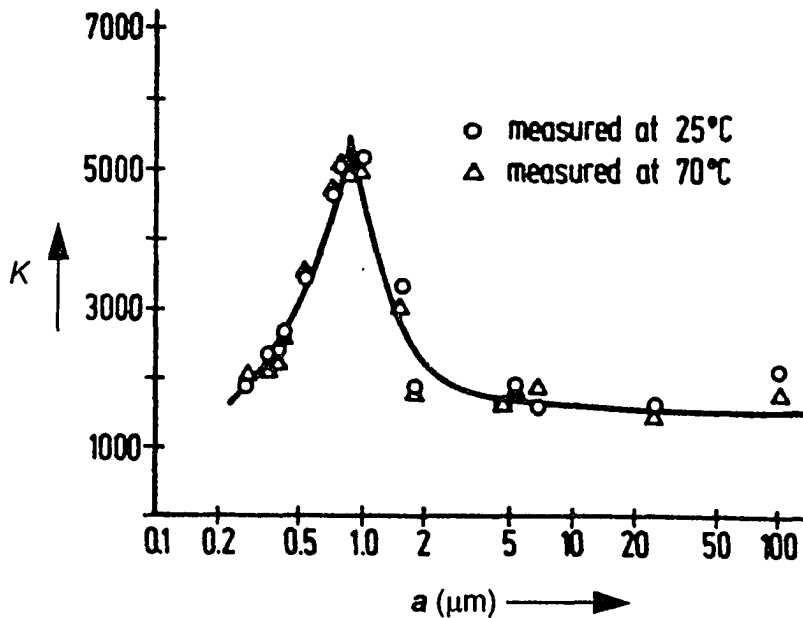


Figure 2.4. Dielectric constant as a function of grain size of ceramic BaTiO_3 [49].

II. Ferroelectric hysteresis

The appearance of the spontaneous polarization of a ferroelectric at T_c results in the presence of very high dielectric constant together with a hysteresis loop for polarization (Figure 2.5a). It is similar to the hysteresis loop observed for ferromagnetic materials and is due to the presence of ferroelectric domains aligned in different directions.

At low field strength, E , the polarization in unpolarized (or virgin) ferroelectric material is initially reversible and nearly linear with an applied field.

The slope of the curve gives the initial low field dielectric constant, K_i , as indicated in Figure 2.5a. This low field K_i is the one usually reported in the dielectric constant measurement. At higher E , the polarization increases more rapidly as a result of the switching of the ferroelectric domains, i.e., the polarization in different domains changes direction in order to be aligned with the applied field. This is achieved by domain boundaries moving through the crystal, as shown in Figure 2.5b. At even higher E , the change in polarization again decreases due to polarization saturation; that is, all the domains are aligned in the same direction as the applied field. Extrapolation of this curve back to $E = 0$ gives P_s , the saturation polarization, which corresponds to the spontaneous polarization with all the dipoles aligned in parallel. Any further increase in E will cause a linear increase in P , since the induced polarization still takes place with the TiO_6 sublattice distorted even further. This is different from ferromagnetic or ferrimagnetic materials where a further increase in magnetic field after saturation does not lead to an increase in the net magnetic moment of the material.

When the electrical field is cut off, P does not go to zero but remains at a finite value called the remanent polarization P_r . This results from the aligned domains being unable to return to their original random state without applying an oppositely directed electric field. The strength of the electric field required to return the polarization to zero is called the coercive field E_c (Figure 2.5a).

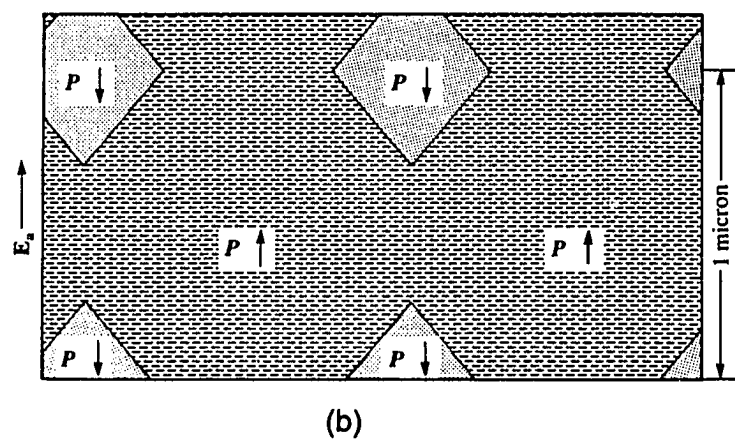
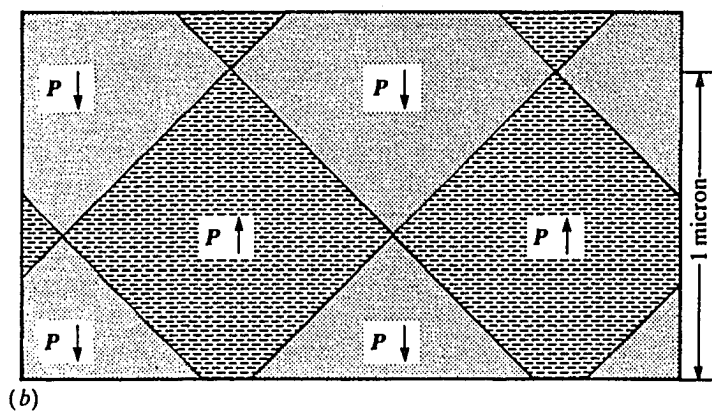
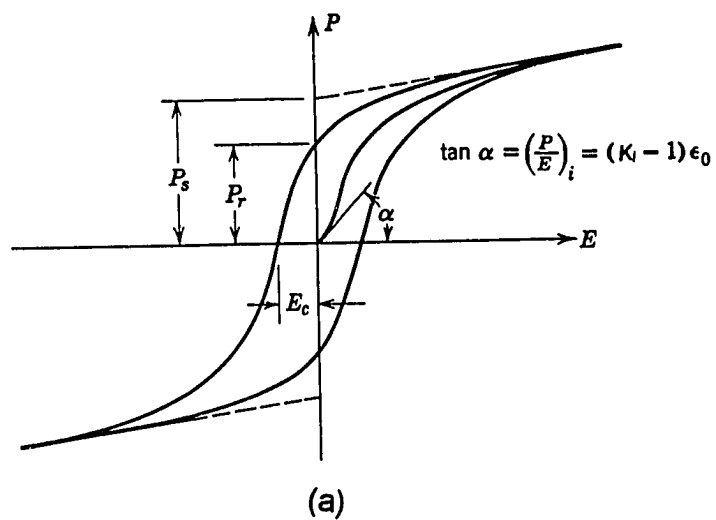


Figure 2.5. (a) A schematic representation of a typical ferroelectric hysteresis loop [34]; (b) Domain growth in the direction of an applied field [35].

Temperature has a significant effect on the shape of the hysteresis loop. At low temperatures, the hysteresis loop is fatter with higher coercive field corresponding to a larger energy required to reorient domain walls. The hysteresis loop keeps on shrinking (i.e., E_C becomes smaller) as the temperature increases until at T_C no hysteresis remains and a linear relationship between P and E results, which corresponds to a single valued dielectric constant characteristic of the paraelectric phase. This temperature dependent hysteresis behavior is shown in Figure 2.6.

2.1.4. Crystal Structure and the Origin of Ferroelectricity of BaTiO₃

BaTiO₃ has a prototype cubic perovskite-type structure above the Curie temperature (point group $m3m$) (Figure 2.7). Each large barium ion is surrounded by twelve nearest-neighbor oxygen ions, with each titanium ion sitting in an octahedral site with six-fold coordination. It could also be viewed as the barium and oxygen ions together forming a face-centered cubic lattice, with titanium ions fitting into octahedral interstices (Figure 2.7a).

At temperatures above the Curie point, T_C (~130°C), due to the large randomizing effect caused by thermal energy (kT), Ti ions "rattle" around the center position of the TiO₆ sublattices, resulting in a cubic symmetry of the BaTiO₃ crystal. The large size of Ba ions increases the volume of the FCC unit cells, causing a lower stability of Ti ions in the octahedral sites. In addition, the

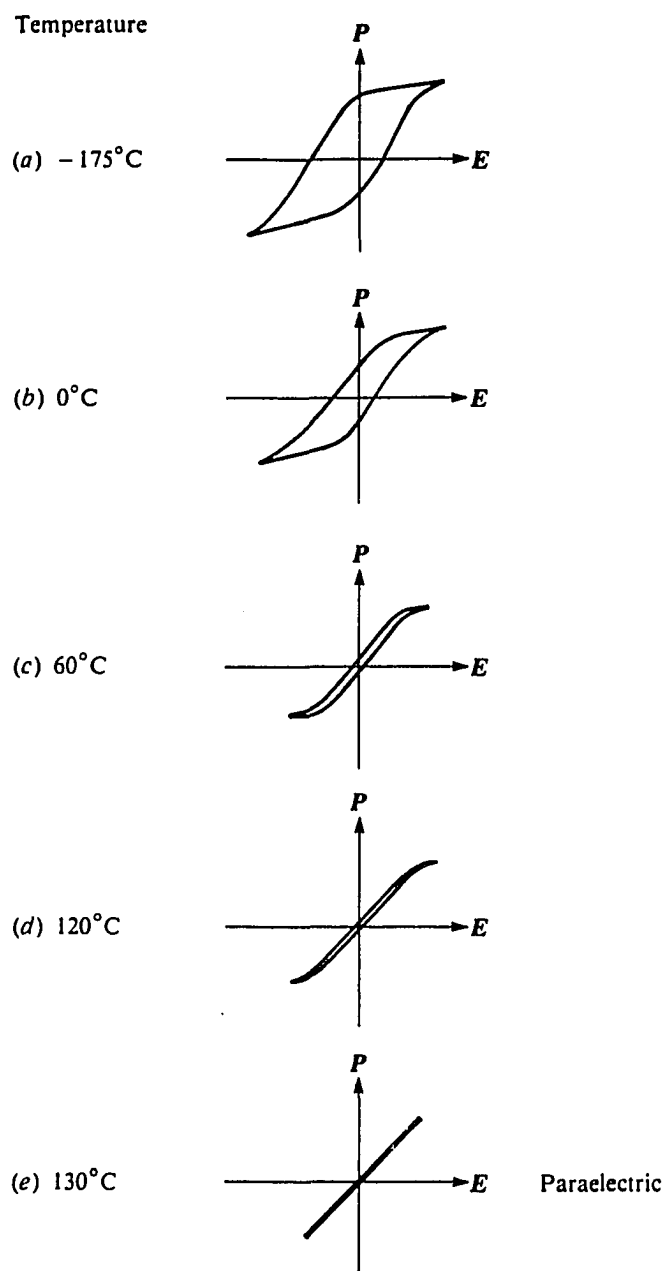
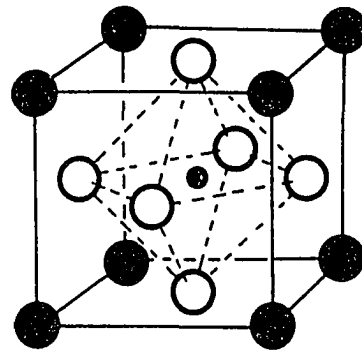


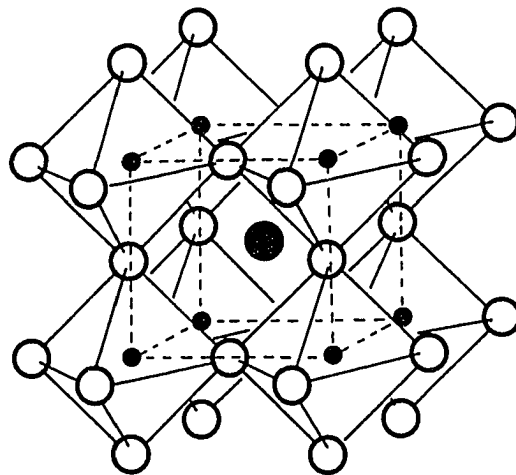
Figure 2.6. The change in ferroelectric hysteresis with temperature for ceramic BaTiO₃ [34].



● Ti (B)

○ O

(a) ● Ba (A)



(b)

Figure 2.7. Perovskite structure of BaTiO_3 [35].

open octahedral site allows the Ti ions to develop a large dipole moment when an electric field is applied, giving a relatively large dielectric constant, as compared with other simple oxides. However, due to the symmetry of the lattice, there is no spontaneous alignment of the dipoles in the crystal and thus the material is paraelectric (i.e., no net dipole moment when $E = 0$).

When the temperature decreases below T_c , the BaTiO_3 crystal transforms successively to three ferroelectric phases according to the different temperature ranges. It first distorts to the tetragonal symmetry ($4mm$) with the Ti ions moving to one of the six equivalent off-centered positions, resulting in distorted TiO_6 sublattices. This gives rise to spontaneous polarization with a dipole moment along the c direction. The BaTiO_3 crystals now possess ferroelectricity compared to the paraelectric phase above T_c . As the temperature decreases further to near 0°C and -90°C , two other transformations occur as the structure changes to orthorhombic and rhombohedral symmetries, leading to the distorted TiO_6 sublattice as well as the polar axis parallel to a face-diagonal, $[110]$ and a body-diagonal, $[111]$ directions, respectively (Figure 2.8). The crystallographic changes at each transformation can be related with the changes in both the spontaneous polarization and the dielectric constant, which are shown in Figure 2.9.

It is of great importance to understand the ferroelectric-paraelectric phase transition, or more often called the Curie transition, since it gives insight into how

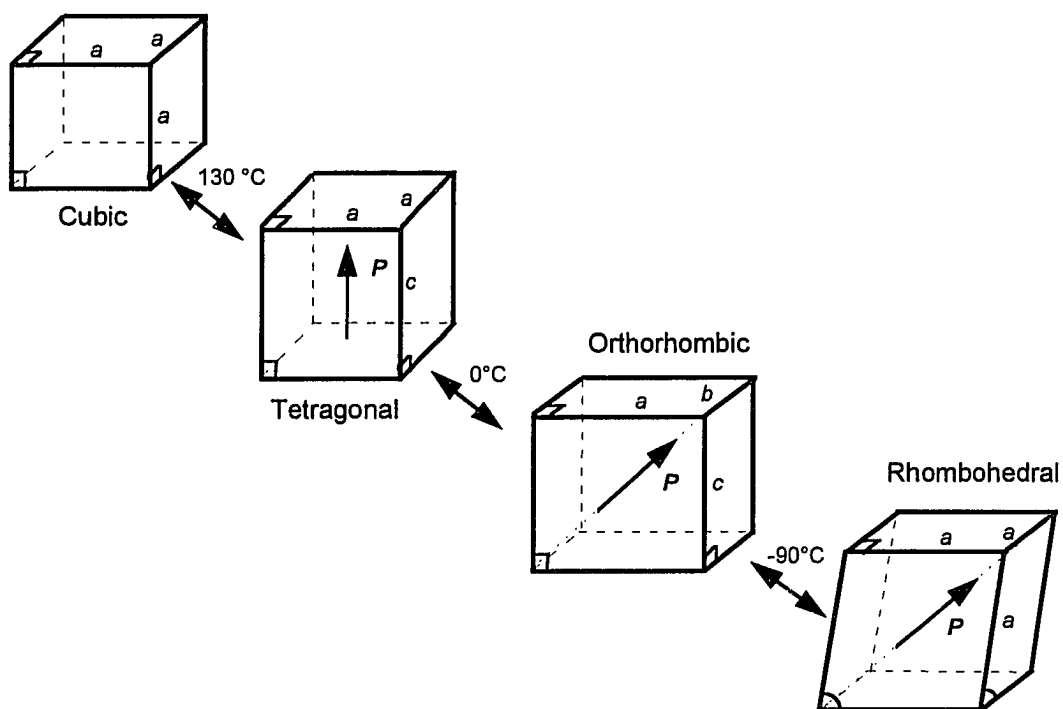


Figure 2.8. Schematics of unit-cell distortions of the single crystal BaTiO₃ polymorphs [36].

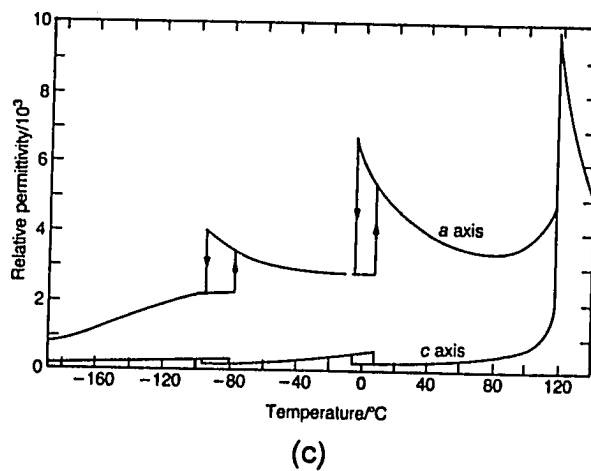
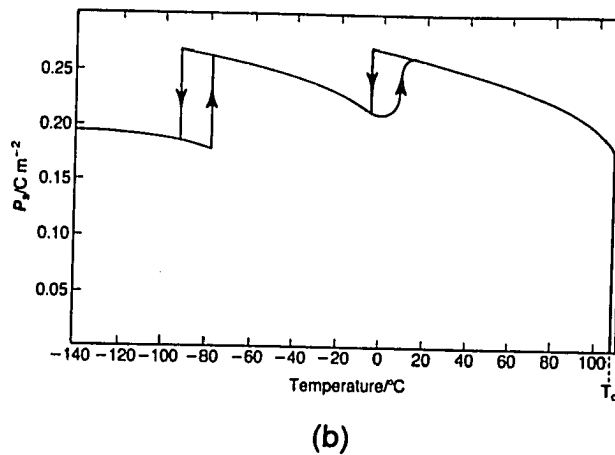
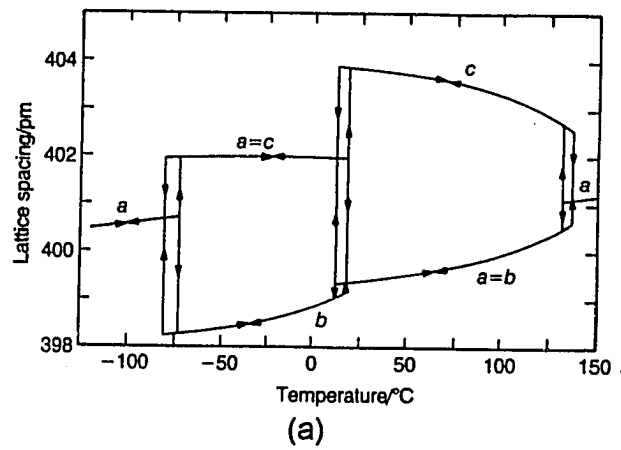


Figure 2.9. Properties of single-crystal BaTiO₃: (a) lattice dimensions vs. temperature; (b) spontaneous polarization vs. temperature and (c) dielectric constants measured in the *a* and *c* directions vs. temperature [36].

the spontaneous polarization is generated and coupled from unit cell to unit cell to form ferroelectric domains. X-ray [60-62] and elastic neutron diffraction studies [63-65] have demonstrated that, by taking the central plane of oxygen ions, i.e., O_I at $(0, 1/2, 1/2)$ in the cubic phase as origin, all the other ions are slightly shifted from their original positions as the $BaTiO_3$ crystal changes from the cubic to the tetragonal structure. It has been observed (Figure 2.10) that Ti and Ba ions move up about 0.11 \AA and 0.06 \AA respectively, while the O_{II} ions at $(1/2, 0, 1/2)$ and $(0, 1/2, 1/2)$ are displaced downward about 0.03 \AA . Thus, a net dipole moment can be produced in the TiO_6 octahedron by the displacement of the Ti ion against its surrounding oxygen (O_{II}) ions. It is also clear that, if the central Ti ion moves closer to one of the O_I ions, it will be energetically favorable for the Ti ion on the opposite side of that O_I ion to move away from it, thus giving rise to a similar displacement of all the Ti ions along the same direction in a particular column. Coupling between neighboring columns leads to all the Ti ions displaced in the same direction; in other words, all the permanent dipoles formed by the Ti distortion are aligned in one direction. Detailed studies of this structural transformation using thermodynamic, statistical mechanical and quantum-mechanical treatments have been reviewed by Burfoot [66].

In the tetragonal structure of $BaTiO_3$, the energy of the Ti ion along the c axis has two minima, as shown in Figure 2.11. As an electrical field is applied in the direction along the c axis opposite to the polarization of a dipole, the Ti ion in

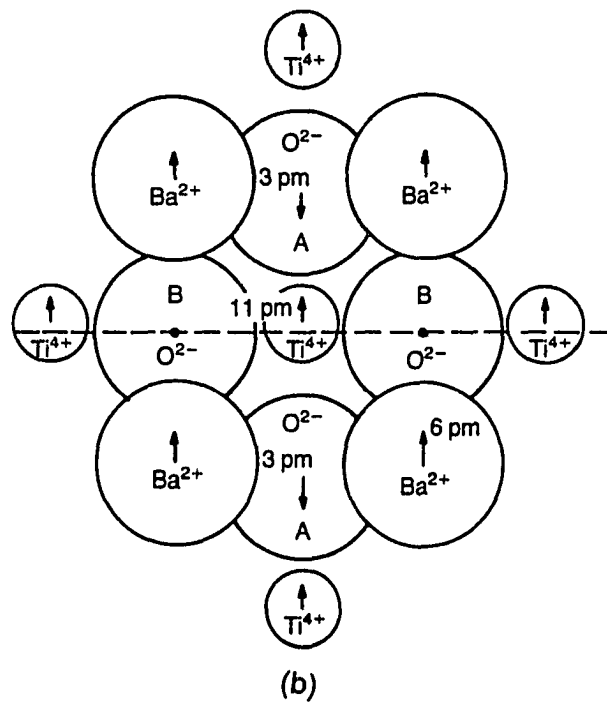
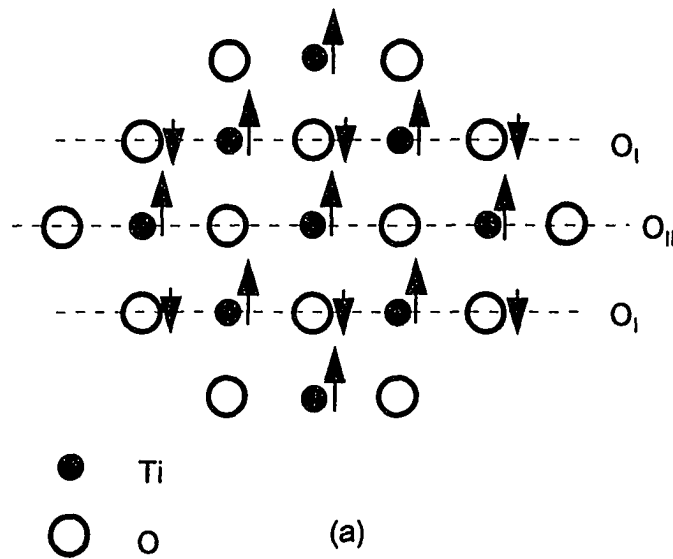


Figure 2.10. Displacements of the different ions in BaTiO_3 in the cubic to tetragonal distortion: (a) oxygen ions and (b) unit cell lattice [36].

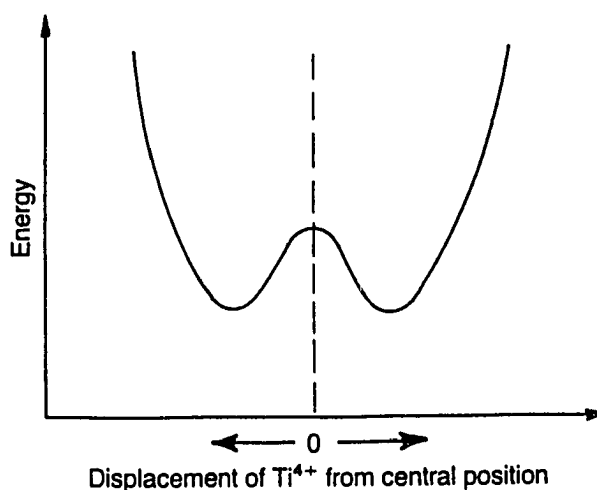


Figure 2.11. Variation of the potential energy of Ti^{4+} along the c axis [36].

the dipole may overcome the energy barrier between the two energy minima so that the direction of the polarization may be reversed. This will help to reduce the energy barriers for neighboring Ti ions such that the entire dipolar region may be affected by the field and eventually switch to the direction of the electrical field. A similar mechanism is available for changes of polarity through 90° by applying the electrical field perpendicular to the c axis; however, in this case there is an accompanying dimensional change because the polar c axis is longer than the non-polar a axis. Switching of polarization direction by 90° can also be induced through the ferroelastic effect by applying a compressive stress

along the polar axis without applying the electric field, while switching through 180° is unaffected by mechanical stress.

An immediate consequence of the onset of spontaneous polarization in a material is the appearance of an apparent surface charge density and an accompanying depolarizing field E_D (Figure 2.12). The energy associated with the polarization in the depolarizing field, or so-called depolarization energy, can be minimized by twinning, a process in which the crystal is divided into many oppositely polarized regions or domains. The surface consisting of a mosaic of areas carrying apparent charges of opposite sign results in a reduction in E_D and the associated energy. This multidomain state can usually be transformed into a single domain by applying a field parallel to one of the polar directions. The domains with their polar moment in the field directions grow at the expense of those directed oppositely until only a single domain remains. The presence of mechanical stress in a crystal results in the development of 90° domains so as to minimize the strain. A polycrystalline ceramic that has not been subjected to a static field behaves as a non-polar material even though the crystals comprising it are polar. One of the most valuable features of the ferroelectric behavior is that ferroelectric ceramics can be transformed into polar materials by applying a static field. This process is called 'poling'. The poling process is illustrated schematically in Figure 2.13.

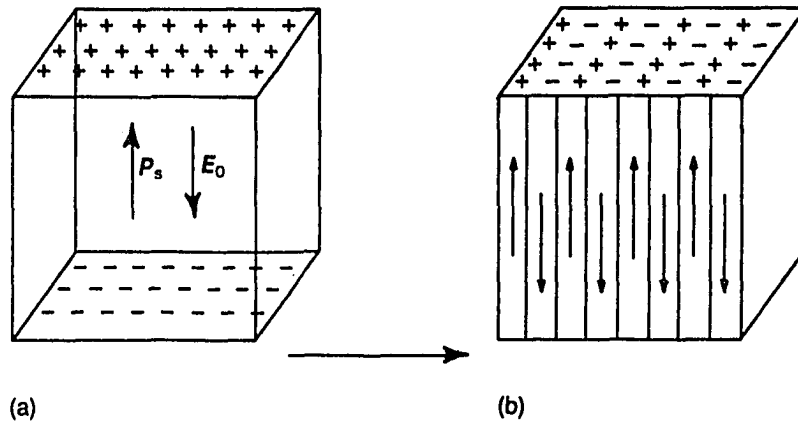


Figure 2.12. (a) Surface charge associated with spontaneous polarization; (b) formation of 180° domains to minimize electrostatic energy [36].

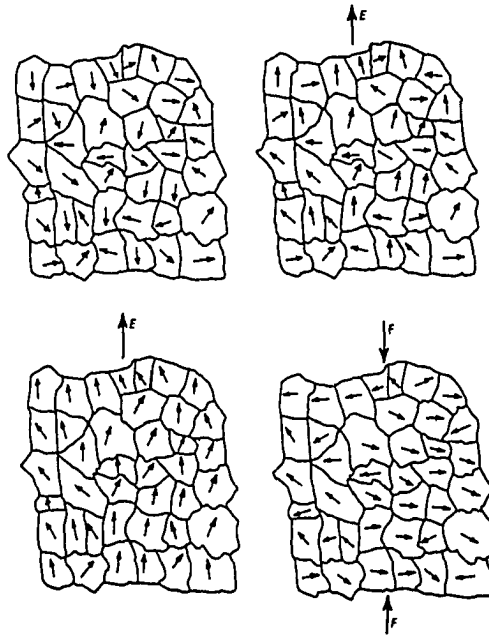


Figure 2.13. Schematic illustrating the poling process [36].

2.1.5. Ferroelectric Phase Transition

I. Introduction

A phase transition often occurs in ferroelectric materials when the temperature approaches a critical temperature, called the Curie temperature (T_C). During the transition, the phase changes from ferroelectric to paraelectric with a disappearance of the spontaneous polarization. This transition is termed the ferroelectric phase transition or the Curie transition. The ferroelectric phase transition is always accompanied by a structural change, such as from tetragonal to cubic in BaTiO_3 . Although several other phase transitions could occur at lower temperatures, only the phase transition from ferroelectric to paraelectric (the Curie transition) is of interest here.

II. Classification of phase transitions

For most pure materials, phase transitions can be classified as either first-order or second-order. A first-order phase transition is defined as the one in which there is a discontinuity in first-order derivative of the free energy (G) with respect to a given state variable (temperature, pressure, *etc.*) at the transition. To simplify terms, the quantities for the first- and second-order derivative of free energy are referred to as first and second order quantities hereafter. In a second-order transition, the change in first-order quantities such as volume or

entropy is continuous at the transition, but there is a discontinuity in second-order quantities such as specific heat and thermal expansion coefficient.

In a first-order ferroelectric phase transition, a discontinuity in spontaneous polarization, P_s , has been observed at the transition due to its first-order nature. As a result, a latent heat ΔH associated with the transition is expected at T_c . ΔH is related to P_s by the following equation [66]:

$$\Delta H = \frac{T_c(P_s)^2}{2C} \quad (2.18)$$

where C is the Curie constant which is approximately equal to 1.4×10^{14} degree in good crystals, and $(P_s)_{T_c}$ is the value of spontaneous polarization reached immediately below T_c .

However, in a second-order ferroelectric transition, P_s goes continuously toward zero although dP_s/dT is discontinuous at T_c (due to the discontinuity in the specific heat at T_c). The behavior is illustrated in Figure 2.14a. The same trend of continuous and discontinuous properties can be seen for the dielectric constant ϵ , which is shown in Figure 2.14b. Therefore, whether the transition is first- or second-order at the ferroelectric Curie transition, can be recognized by observing if there is a continuity or discontinuity of P_s at T_c .

A ferroelectric phase transition has also been described as a displacive or order-disorder type of transition. A displacive type of phase transition is one in which the displacements of the atoms in the low temperature phase from their

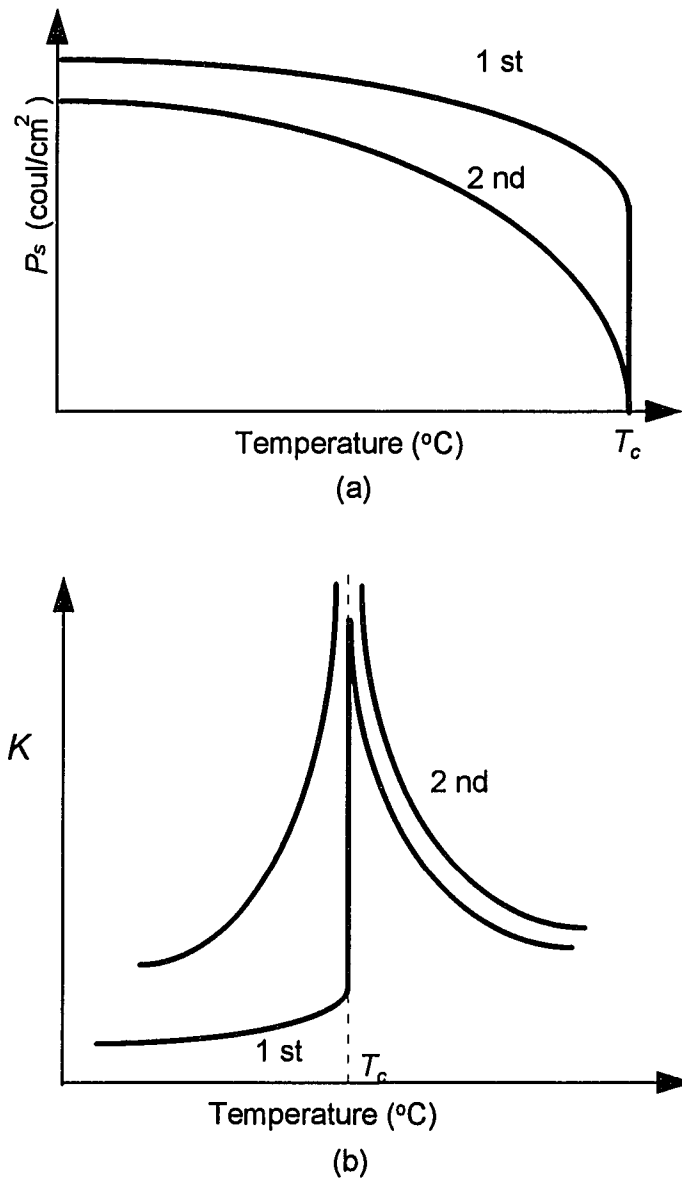


Figure 2.14. (a) P_s vs. temperature and (b) K vs. temperature for a first- and second-order ferroelectric phase transition [67].

positions in the high temperature phase are small compared to the nearest-neighbor internuclear distances. For an order-disorder transition, below T_C the displacements are comparable to the internuclear distance. The Curie transition in BaTiO_3 is said to be more similar to a displacive type phase transition [66].

III. Phenomenological theory

Most of the macroscopic properties of materials can be studied by applying thermodynamic principles. Phenomenological theory, or the Landau-Ginzburg free energy theory uses thermodynamic principles to describe the observed behavior upon phase transition in terms of change in the free-energy function with temperature. The phenomenological theory was first developed by Devonshire in a series of papers [31-33] around 1950 based on the Landau-Ginzburg phase transition theory [28-30]. Although such a theory does not give insight into mechanisms or the microscopic causes of the observed phenomenon, it provides a valuable framework for further development of microscopic theories.

In the phenomenological theory, an order parameter is used which measures the extent of the departure of the atomic (or electronic) configuration in the less symmetric (low temperature) phase from that in the more symmetric (high temperature) phase. In ferroelectrics, the appearance of the order parameter below T_C breaks the symmetry of the high temperature phase, while

the order parameter approaches zero as the temperature goes above T_c . In a displacive type of ferroelectric transition, the order parameter could be some measure of the displacement of certain ions from their high temperature equilibrium positions, while in an order-disorder type transition the order parameter would be some measure of the amount of long-range ordering of the permanent dipoles. For most ferroelectric materials with either order-disorder or displacive type transition, the polarization P can be taken as the order parameter. This is because P is a macroscopic quantity that can be easily measured.

Here, a simple ferroelectric case is considered, assuming a crystal with a perovskite structure where the transition is from a high temperature centrosymmetric (non-polar) cubic structure to a tetragonal ferroelectric structure with a polarization P . As P is parallel to the tetragonal c axis, the elastic Gibbs free energy of the system (G_1) can be expanded according to the Landau-Ginzburg theory [67]:

$$G_1(T, P) = G_{10}(T) + \frac{\alpha}{2} P^2 + \frac{\beta}{4} P^4 + \frac{\gamma}{6} P^6 + \dots \quad (2.19)$$

where G_{10} is the elastic Gibbs free energy term when $P = 0$, and the coefficients α , β and γ are all temperature dependent. It should be noticed that γ has to be positive and very small compared to α and β in order to have a stable state (or minimum G_1). Only even powers appear in this expansion because the non-

polar cubic phase above T_c has a center of symmetry, which gives the dependence of the free energy on even powers of the polarization.

A stable state of a thermodynamic system is achieved by the minimization of the free energy G . When an electric field $E = 0$, G_f can be replaced by the total Gibbs free energy G . So for a stable equilibrium configuration, the following two requirements have to be met [68]:

$$(\partial G / \partial P)_{P_s} = 0, \quad \text{and} \quad (2.20)$$

$$(\partial^2 G / \partial P^2)_{P_s} = (\partial E / \partial P)_{P_s} = (\epsilon_0 \chi)^{-1} > 0 \quad (2.21)$$

Combining Equation (2.19) with Equations (2.20) and (2.21), the following equations can be derived:

$$P_s (\alpha + \beta P_s^2 + \gamma P_s^4) = 0 \quad (2.22)$$

$$\chi^{-1} = \epsilon_0 (\alpha + 3\beta P_s^2 + 5\gamma P_s^4) > 0 \quad (2.23)$$

There are two solutions of Equation (2.22). The first one is $P_s = 0$, corresponding to a paraelectric, and the second one, with $P_s \neq 0$, is for a ferroelectric phase.

A. Paraelectric phase

In the case of $P_s = 0$, which corresponds to the paraelectric phase, the dielectric susceptibility can be expressed as

$$\chi^{-1} = \epsilon_0 \alpha > 0 \quad (2.24)$$

It is shown by the equation that α must be positive for a ferroelectric crystal to have a stable paraelectric phase. At the transition from a stable paraelectric toward a ferroelectric phase ($T \geq T_c$), the boundary condition can be expressed as

$$\alpha(T)|_{T_0} \geq 0 \quad (2.25)$$

Here T_0 is called the Curie-Weiss temperature. It will be shown later that $T_0 = T_c$ for the second-order phase transition, while $T_0 < T_c$ for the first-order one. Therefore, $\alpha(T)$ can be expanded into a Taylor series in terms of $T - T_0$ and by taking only the first-order term into account, we have:

$$\alpha(T) = \alpha_0(T - T_0) = \frac{4\pi(T - T_0)}{C} \quad (2.26)$$

where $\alpha_0 = 4\pi/C$ in the CGS unit system and C is called the Curie-Weiss constant. Thus by considering Equation (2.24), the following expression can be obtained:

$$\chi = \frac{C}{4\pi(T - T_0)} \quad (2.27)$$

This equation describes an important relationship between χ and temperature, and is often referred to as the Curie-Weiss law. The Curie-Weiss law applies to the dielectric susceptibility in a paraelectric phase. It has been experimentally proved that both β and γ only have a very weak dependence on temperature and it is reasonable to assume that they are temperature independent.

B. Ferroelectric phase

For the case where P_s is non-zero, which corresponds to the ferroelectric phase, the solution to the Equation (2.22) would be:

$$P_s^2 = \left[-\beta \pm (\beta^2 - 4\alpha\gamma)^{1/2} \right] / 2\gamma \quad (2.28)$$

There are two situations which need to be considered: $\beta > 0$ and $\beta < 0$. It can be shown that the solution $P_s^2 = \left[-\beta - (\beta^2 - 4\alpha\gamma)^{1/2} \right] / 2\gamma$ has to be discarded since it either results in $P_s^2 < 0$ or corresponds to an unstable state (free energy G_1 is maximum) according to Equation (2.21). Therefore the only solution needed to be considered is:

$$P_s^2 = \left[-\beta + (\beta^2 - 4\alpha\gamma)^{1/2} \right] / 2\gamma \quad (2.29)$$

In the following, two situations will be discussed : $\beta > 0$ and $\beta < 0$. It will be shown that by changing the sign of β , two quite different ferroelectric responses corresponding to second- and first-order phase transition can be produced.

(1) Second-order ferroelectric transition ($\beta > 0$)

As $\beta > 0$, a negative α is also required (γ is always positive as mentioned before) for the solution $P_s^2 = \left[-\beta + (\beta^2 - 4\alpha\gamma)^{1/2} \right] / 2\gamma$ to be valid. When substituting this into Equation (2.19), and considering $G_1 = G$ ($E = 0$) and $G_{10} = G_0$ as $P_s = 0$, the following equation is obtained:

$$G - G_0 = \left[\beta(\beta^2 - 6\alpha\gamma) - (\beta^2 - 4\alpha\gamma)^{3/2} \right] / 24\gamma^2 \quad (2.30)$$

From the above analysis, several conclusions can be drawn:

(i) *Ferroelectric phase is a stable phase*

For a typical ferroelectric crystal, $|\alpha\gamma| \ll \beta^2$ [69]. Thus, the value of the right side of Equation (2.30) would be negative, resulting in a negative value of $G - G_0$. G corresponds to a non-zero P_s , which is now smaller than G_0 corresponding to $P_s = 0$. Therefore the stable phase here is a ferroelectric phase with a non-zero spontaneous polarization. This is shown in Figure 2.15a where $G - G_0$ is plotted as a function of the polarization P at several temperatures. At $T < T_0$, there are two free energy ($G - G_0$) minima with non-zero P_s corresponding to stable ferroelectric states.

(ii) *Second-order phase transition*

As α tends to be infinitely small near the transition, Equation (2.30) can be simplified when substituted with Equation (2.26):

$$G - G_0 = -\alpha^2 / 4\beta = -\left(\frac{2\pi}{C}\right)^2 (T - T_0)^2 / \beta \quad (2.31)$$

The equation indicates that as the temperature approaches T_0 , a ferroelectric-paraelectric phase transition will occur ($G = G_0$). So the transition temperature

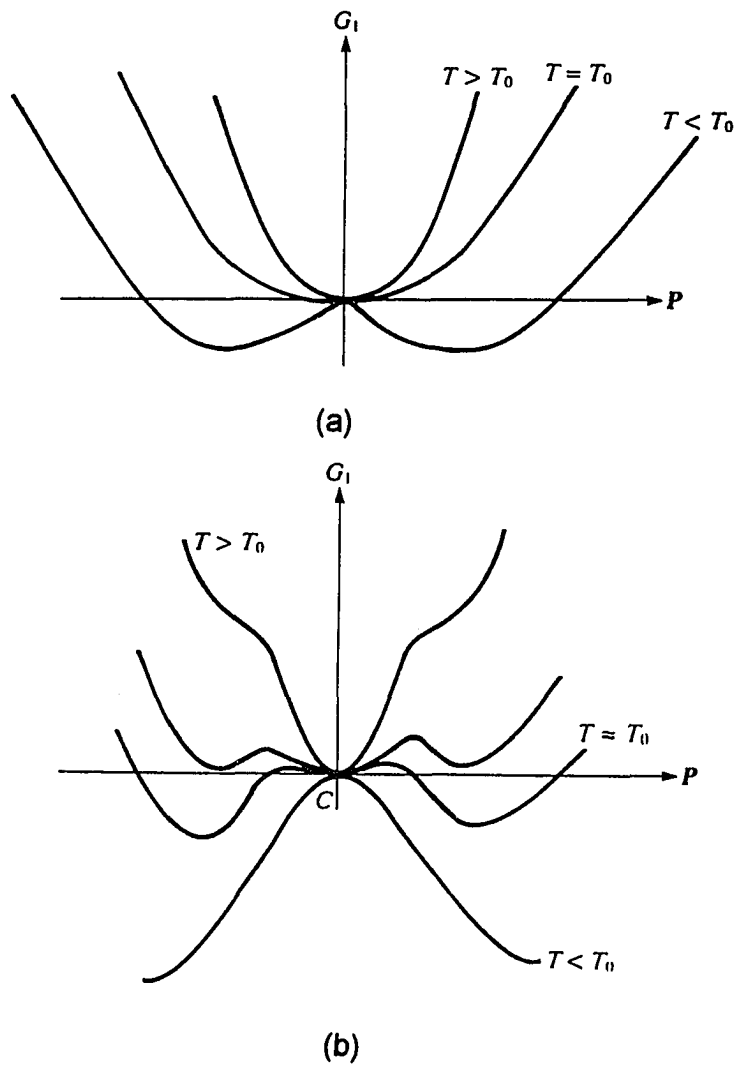


Figure 2.15. The free energy as a function of polarization at several different temperatures: (a) for a second-order phase transition; (b) for a first-order phase transition [67].

T_c is equal to T_0 in this situation. The entropy change (ΔS) upon the transition can be obtained by taking the first-order derivative of the free energy at $T = T_0$:

$$\Delta S = (\partial G / \partial T) - (\partial G_0 / \partial T) \Big|_{T_0} = 0 \quad (2.32)$$

However, the change in specific heat (ΔC_p) at $T = T_0$, which can be obtained by taking the second-order derivative of free energy, is discontinuous:

$$\Delta C_p = (\partial^2 G / \partial T^2) - (\partial^2 G_0 / \partial T^2) \Big|_{T_0} = -2\left(\frac{2\pi}{C}\right)^2 / \beta \neq 0 \quad (2.33)$$

Thus, in the case of $\beta > 0$, the first-order derivative of the free energy is continuous while the second-order derivative is discontinuous, which well defines the transition as second-order. Since in most ferroelectrics, $|\alpha\gamma| \ll \beta^2$, Equation (2.28) can be thus simplified as

$$P_s^2 = -\alpha / \beta \quad (\alpha < 0, \beta > 0) \quad (2.34)$$

Combining the Equations (2.31) and (2.34), the following expression can be obtained:

$$P_s^2 = -\frac{4\pi}{C}(T - T_0) / \beta \quad (T < T_0) \quad (2.35)$$

According to this equation, polarization should decrease continuously as the temperature approaches T_0 and becomes zero at T_0 , just as shown in Figure 2.14 for a second-order phase transition.

(iii) *Susceptibility and hysteresis loop*

In a stable ferroelectric phase region at the temperature below T_0 , according to Equation (2.23), the reciprocal of the susceptibility can be expressed as

$$\chi^{-1} = (\partial E / \partial P)_{P=P_s} = \alpha + 3\beta P_s^2 + 5\gamma P_s^4 \quad (2.36)$$

As the temperature nears T_0 , the term with P_s^4 can be neglected. Thus by substituting Equation (2.35) into the above equation, we have:

$$\chi^{-1} = -2\alpha = -\frac{8\pi}{C}(T - T_0) \quad (T < T_0) \quad (2.37)$$

Figure 2.16a shows the plot of χ^{-1} as a function of temperature for the second-order phase transition.

On the other hand, polarization P can be related to the electric field E by the relation $E = (\partial G_1 / \partial P)_T$, and by combining with Equation (2.19), we can obtain:

$$E = \alpha P + \beta P^3 + \gamma P^5 \quad (2.38)$$

Thus, according to Equation (2.38), P - E curves at various temperatures can be represented as in Figure 2.17a.

(2) First-order ferroelectric phase transition ($\beta < 0$)

In the case of $\alpha > 0$, the crystal is in the paraelectric phase since it corresponds to $T > T_0$ according to Equation (2.26). It is noteworthy that in the

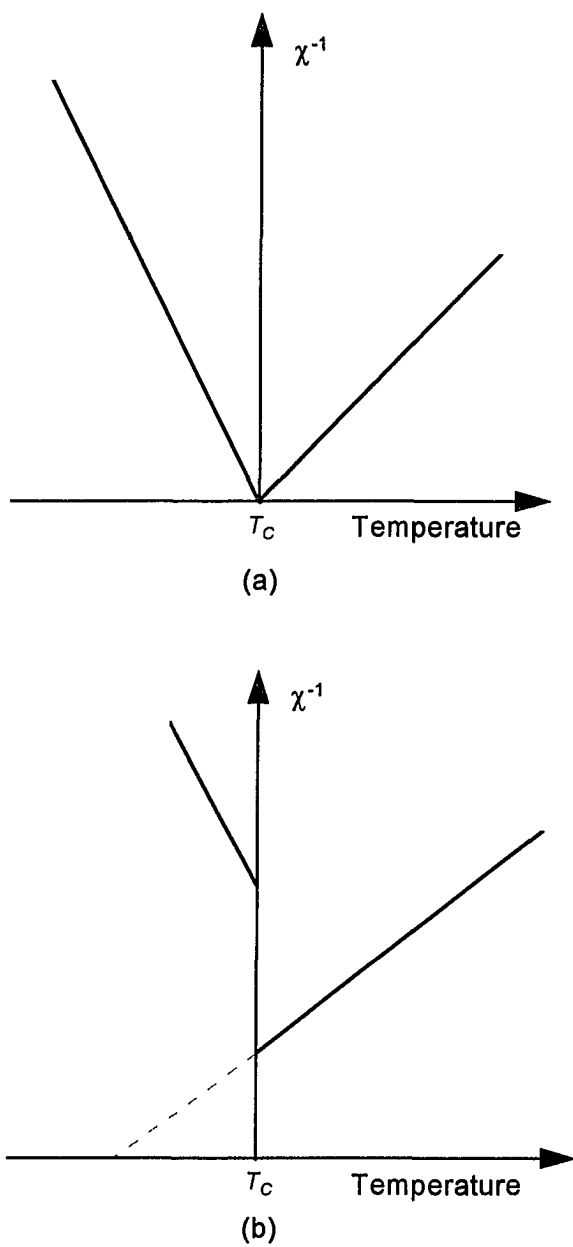


Figure 2.16. The temperature dependence of χ^{-1} for (a) second-order phase transition; (b) first-order phase transition [67].

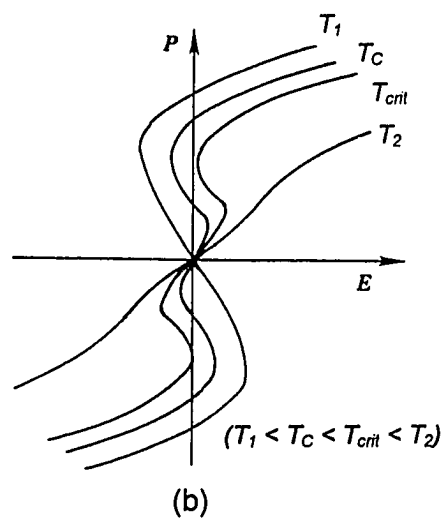
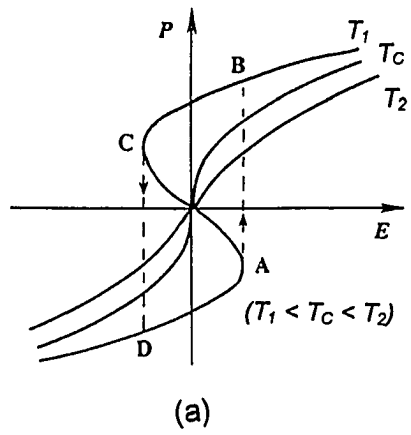


Figure 2.17. Calculated P - E curves for (a) second-order and (b) first-order phase transitions [68].

former case where $\beta > 0$, $P_s = 0$ is the only solution to Equation (2.22), since other solutions will give the imaginary value of P . However, in the present case of $\beta < 0$, besides the solution of $P_s = 0$, solution $P_s^2 = \left[-\beta + (\beta^2 - 4\alpha\gamma)^{1/2} \right] / 2\gamma$ is also valid. However, $P_s = 0$ corresponds to the lower energy state and thus the most stable configuration (Figure 2.15).

For $\alpha < 0$, which corresponds to the ferroelectric region ($T < T_0$), by substituting $P_s^2 = \left[-\beta + (\beta^2 - 4\alpha\gamma)^{1/2} \right] / 2\gamma$ into Equation (2.19), Equation (2.30) can again be obtained.

There is a non-zero solution of α at the transition ($T = T_c$) where $G = G_0$:

$$\alpha = 3\beta^2 / 16\gamma \quad (2.39)$$

This means that before the temperature decreases to the Curie-Weiss temperature, T_0 , the ferroelectric phase transition already takes place at T_c ($> T_0$), with a ferroelectric phase as the most stable phase which has a non-zero P_s .

The stable states can again be illustrated by plotting $G-G_0$ as a function of polarization, as shown in Figure 2.15b. At $T < T_c$, the lowest energies are at the two minima in Gibbs free energy (G) with non-zero P_s , which corresponds to a truly stable ferroelectric phase. At $T > T_c$, the lowest free energy is at $P_s = 0$, which corresponds to the stable paraelectric phase, although there are two

metastable positions where P_s has non-zero values. Once again, several conclusions can be drawn from the above discussion:

(i) *First-order phase transition*

Assuming that β and γ are temperature independent and no electric field is applied ($E = 0$), the entropy change (ΔS) at the transition temperature T_c can be expressed as follows:

$$\begin{aligned}\Delta S &= (\partial G / \partial T) - (\partial G_0 / \partial T) \Big|_{T_c} \\ &= \frac{1}{2} P_s^2 \Big|_{T_c} (\partial \alpha / \partial T) \\ &= 2\pi P_s^2 \Big|_{T_c} / C \neq 0\end{aligned}\tag{2.40}$$

and

$$\Delta H = T_c \Delta S = 2\pi P_s^2 T_c / C\tag{2.41}$$

Therefore, this case ($\beta > 0$) describes a first-order transition with an abrupt change in entropy that gives a latent heat at the Curie transition (T_c).

(ii) *Susceptibility and hysteresis*

In this case the ferroelectric transition is of the first order, so there is a discontinuous change in polarization at T_c as shown in Figure 2.14. Since the polarization is still large at temperatures just below T_c , the term P_s^4 cannot be ignored in Equation (2.36). The value of the spontaneous polarization P_s at T_c

can be obtained by substituting Equation (2.39) into (2.29) and subsequently simplified as:

$$P_s^2(T_c) = -3\beta/4\gamma \quad (2.42)$$

When substituting Equations (2.39) and (2.42) into Equation (2.36) and rearranging it, the expression for the susceptibility can be obtained as

$$\chi^{-1} = 4\alpha \quad (T < T_c) \quad (2.43)$$

The dependence of χ^{-1} on temperature is shown in Figure 2.16b and it is obvious that the slope of the curve at $T < T_c$ is four times that at T above T_c .

The hysteresis or P - E curves at several temperatures can also be obtained for the first-order phase transition according to Equation (2.38), as shown in Figure 2.17b.

It has been shown that by using a simple free energy expression with several adjustable expansion parameters (α , β and γ), various kinds of rather complex ferroelectric behaviors can be predicted and coincide very well with the experimental results. By changing the sign of β , the ferroelectric behaviors associated with the first-order and second-order phase transition are well delineated such as the hysteresis behavior, the dependence of χ^{-1} , polarization on temperatures, *etc.* Additional terms can be added to take into account effects due to stress and other macroscopic variables.

Although the phenomenological theory provides no microscopic information such as its structural change during the ferroelectric phase

transition, it can be used to explain a variety of macroscopic observation in terms of a few parameters. This is the strength of this theory. However, in order to really understand the ferroelectric behavior and the transition from a more microscopic point of view, the "soft" mode theory should be considered.

IV. Lattice dynamics theory (soft-mode)

One of the most striking features of the ferroelectric phase transition is the fact that the spontaneous appearance of an order parameter, P_S in the low temperature phase breaks an inherent symmetry of the high temperature phase. In other words, some symmetry elements of the high temperature phase are lost by very small displacements of atoms on cooling below T_c . The only way to accomplish the small displacements is by normal lattice vibration. Therefore, there may be a relationship between lattice dynamics and structural phase transitions, in particular the "gentle" displacive ferroelectric transitions such as in the case of BaTiO_3 and related materials.

In 1959 Cochran first made the connection between lattice dynamics and ferroelectricity [22], suggesting that the phase transition in some ferroelectrics might result from an instability of one of the normal vibrational modes of the lattice. The theory was further improved by him and many other investigators [23-27]. According to the Lyddane-Sachs-Teller (LST) relationship, the real part

of the static dielectric constant $\varepsilon(0)$ and the optical dielectric constant $\varepsilon(\infty)$ are related to the vibrational frequencies:

$$\frac{\varepsilon(0)}{\varepsilon(\infty)} = \frac{\omega_{LO}^2}{\omega_{TO}^2} \quad (2.44)$$

where ω_{LO} and ω_{TO} are the longitudinal and transverse optic modes (LO and TO), respectively. It can be shown that ω_{TO} can be considerably reduced if only short-range forces were considered (i.e., the electrostatic dipole forces act to reduce ω_{TO}), while ω_{LO} is not affected very much. Therefore, the increase in dielectric constant as T_C is approached from above may be caused by a decrease in ω_{TO} . In other words, normally the frequency of most lattice vibrational normal modes increase as the temperature decreases. However, the TO mode that is causing the phase transition must decrease in frequency with the temperature to be consistent with Equation (2.44). Such vibrational modes are called "soft modes".

The "soft mode" concept has been verified experimentally by infrared, neutron and Raman measurements. If assuming that all the temperature dependence of $\varepsilon(0)$ is associated with one TO mode (i.e., ω_{LO} is temperature independent), the temperature dependence of ω_{TO} can be derived according to Equation (2.54) together with the Curie-Weiss law for static dielectric constant as shown in Equation (2.39). The behavior in the high temperature phase is

$$\omega_{TO}^2 = A(T - T_0) \quad (2.45)$$

where A is a constant. Fortunately, this temperature dependence has been confirmed experimentally, which gives a strong support to the “soft mode” theory.

To examine the soft mode idea more carefully, the lattice vibrational normal modes of a ABO_3 unit cell with the perovskite structure is considered (Figure 2.18) [67]. It shows the displacements for all four of the allowed optic normal modes. All these modes are triply degenerate whereas only the motion along one $\langle 100 \rangle$ axis is shown in the figure. Similar displacements along the other two axes are allowed. Three of the four modes are infrared active, which means that there is a dipole moment oscillating at the particular TO frequency of the mode, and these modes contribute to $\varepsilon(0)$ in Equation (2.44). The last mode is ‘silent’, meaning it is not infrared or Raman active but can be seen with neutrons, and it is thus excluded in the consideration. The soft mode is referred to as the lowest frequency TO mode, which is shown in Figure 2.18a. As T_c is approached from above, the frequency of this soft mode decreases with temperature as given by Equation (2.45) and this determines the temperature dependence of $\varepsilon(0)$ via Equation (2.44). The decreasing frequency of ω_{TO} is another way to say that the restoring forces of this mode become weaker which causes the vibration of the mode to become slower. Finally, the restoring forces become so weak that the high temperature structure distorts into another structure (i.e., there is a phase transition).

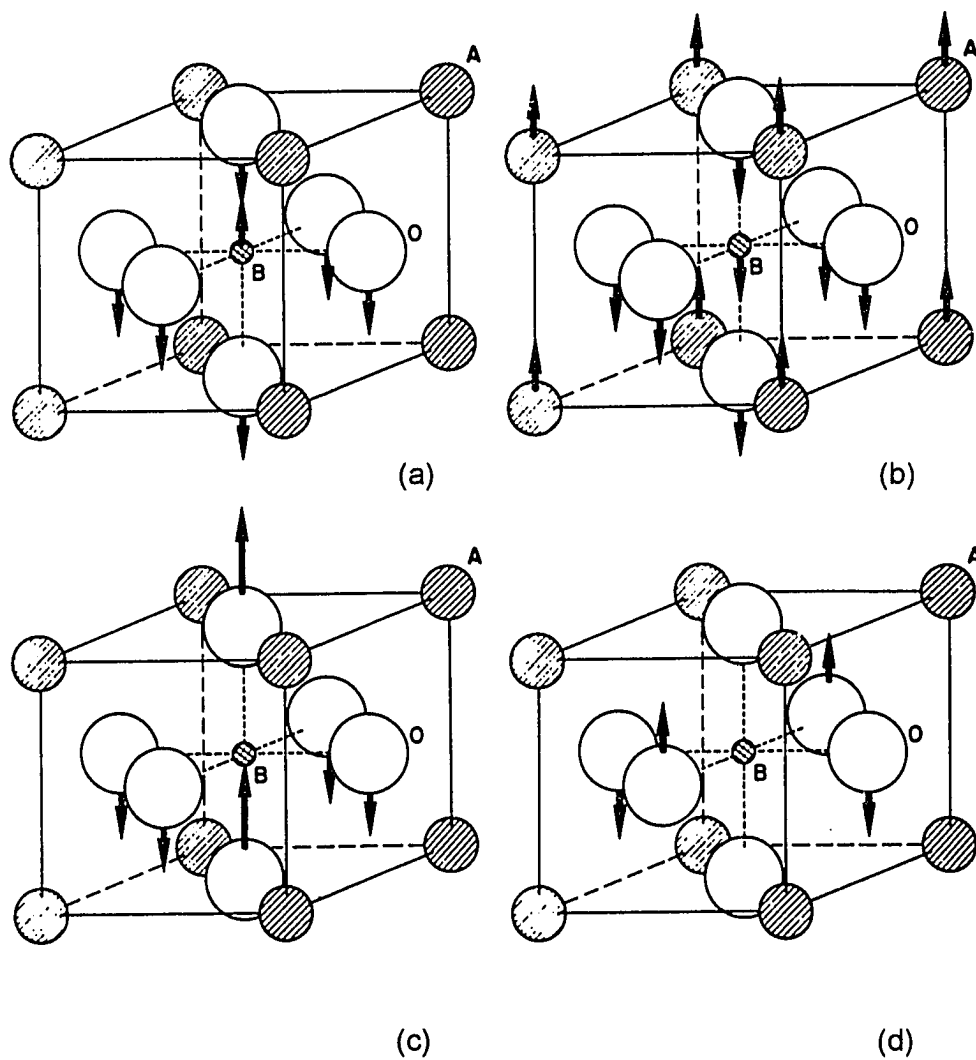


Figure 2.18. A unit cell of cubic BaTiO_3 (i.e., ABO_3 perovskite) showing the atomic displacements of the four different normal modes. Only displacements along one of the cubic axes is shown; it also occurs also along the other two cubic axes. Thus the modes are said to be triply degenerate [67].

One of the outcomes of the soft mode idea is that the displacements that occur in the low temperature phase are the result of the soft mode vibrational motion which is now 'frozen in'. Therefore, the distortion of the crystal structure found below T_C is just the frozen displacements shown in Figure 2.18a with an additional macroscopic strain, in which the crystal elongates along the direction of P_s and contracts perpendicular to P_s . Since the eigenvectors of the normal vibrational modes can be calculated from a knowledge of the interatomic forces between the ions (which can be determined experimentally), the soft mode idea can be and has been verified.

It is also important to know that the wavenumber, k of these soft modes is nearly zero ($k \approx 0$). This is because such modes used in the LST relationship (Equation 2.44) relates the macroscopic quantities (i.e., dielectric constants) to wave motion, and only wave motion with very large wave length (very small k) can directly affect macroscopic quantities. The fact that $k \approx 0$ allows the normal modes of all neighboring unit cells to oscillate in the same direction with the same displacements as shown in Figure 2.18a. If such motion has a very low frequency and 'freezes in', the tetragonal phase with the observed displacements results. This gives rise to a static dipole moment in each unit cell which adds together to give a macroscopic polarization. Since the displacements are generally small, in fact a weak electric field can reverse them, thereby changing the sign of P_s .

Figure 2.19 shows the temperature dependence of the lowest TO (soft mode) in a ferroelectric material. As T_C is approached from above, the frequency of TO at $k = 0$ decreases. Since the $k = 0$ part of the phonon branch is connected to the entire branch, the rest of the TO branch tends to move down as the figure shows.

It is also notable that while a P_S is observed along the z-axis of this normally cubic crystal, this distortion can have a very small effect on the vibrational motion in the x- and y-directions. However, the distortion is small so the effects on motions in the two perpendicular directions are relatively small. Thus, TO modes with very small k (≈ 0) in these two directions can still be soft and at temperatures lower than T_C these modes can cause other transitions. This is what is observed in BaTiO_3 . At about 0°C , there is another phase transition where the displacements are along the y-axis, and the sum of the displacements along both the z- and y- axes gives a polarization along one of the $\langle 011 \rangle$ -type directions. At still lower temperatures displacements along the x-axis occur with a resultant P_S along one of the $\langle 111 \rangle$ -type directions. Thus, a triply degenerate soft mode in the high temperature cubic phase of BaTiO_3 leads, in a very natural way via soft mode consideration, to the three different low temperature ferroelectric phases (tetragonal, orthorhombic and rhombohedral). Therefore, complicated phase transitions and crystal properties

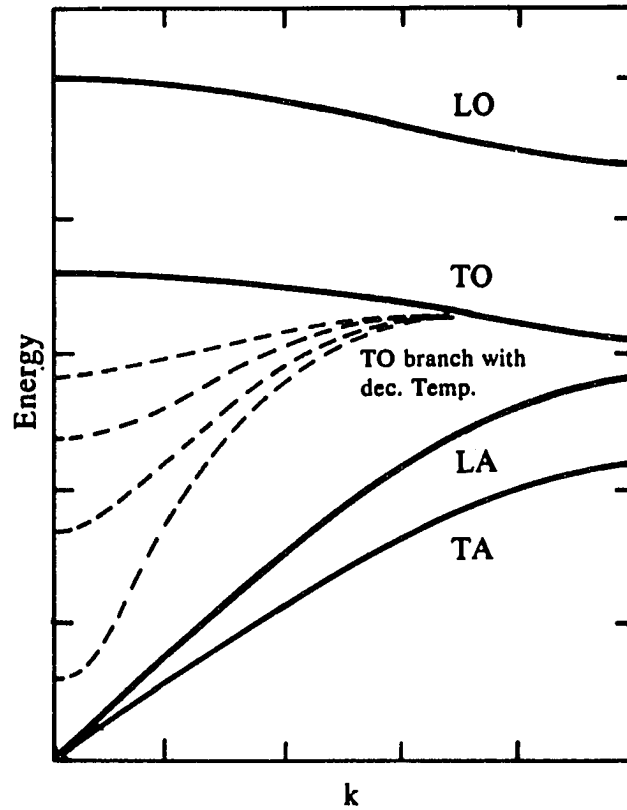


Figure 2.19. A schematic diagram of E vs. k for the lowest TO branch in the paraelectric phase as the ferroelectric transition temperature T_c is approached from above. The successively lower dashed curves refer to temperature closer to T_c . [67].

can be understood in terms of the lattice dynamics with the simple soft mode concept.

V. Particle size effect on ferroelectric phase transition

It is well known that ferromagnetic or ferroelectric thin films or powders with small particle sizes may behave differently as compared to bulk materials [70-79]. For example, BaTiO₃ powders produced by wet-chemical syntheses are usually in submicron sizes, and have a cubic-like structure at room temperature [6-9]. The particles appear to be paraelectric as suggested from the disappearance of the Curie transition at T_C (the stable structure of large single crystals of BaTiO₃ is tetragonal and possesses ferroelectricity at room temperature). Similar cubic-like structure has also been commonly observed in synthesized BaTiO₃ thin films [80], and the tetragonality starts to show only when the crystallites become large in size [81-82]. Apparently there is a critical particle size below which the tetragonal structure cannot be sustained. This critical size has been estimated to be around 100 nm [83-85].

Although the size dependence of ferroelectricity for powders and thin films has been recognized for a long time, the exact mechanism responsible for the appearance of the cubic-like structure and disappearance of ferroelectricity has been debated in the literature. Various explanations have been offered and are summarized in the following:

- a ferroelectric surface layer with higher Curie transition exists around particles and the misfit between the surface layer and the interior gives rise to lattice distortion and broadening of the Curie transition [6];
- a surface layer with cubic structure and low dielectric constant is present around the particles, smaller particles have a more severe surface layer effect, resulting in a “cubic-like” structure [7-8];
- surface tension acting as the hydrostatic pressure shifts the Curie temperature below the room temperature, causing the disappearance of the transition normally observed at $\sim 130^{\circ}\text{C}$ [83];
- large surface energy / volume associated with small particles requires the particles to adopt cubic structure for energy reduction [87].
- the presence of defects such as hydroxyl ions in the oxygen sublattice enforces a “loosely packed” cubic structure [88].
- the creation of lattice microstrains associated with hydroxyl defects maintains the particles in the metastable cubic form [9, 89].
- strong depolarization energy associated with the ferroelectric phase coerces the disappearance of ferroelectricity [56].
- a surface disordered state reduces the ferroelectricity, which becomes more dominant as the particle size decreases (mean field consideration) [77-78, 90].

Among them, defects and strain have been paid much attention recently. Hennings *et al.* [88] observed a large quantity of chemisorbed OH^- groups in BaTiO_3 lattices by using both thermogravimetry analysis (TGA) and infrared (IR) spectroscopy. These adsorbed OH^- groups and the compensating defects cause enlargement of the unit cell as well as stabilizing the cubic structure. Upon annealing of the BaTiO_3 powders, dehydration occurred with a successive reduction of OH^- concentration. A similar behavior was also observed by Vevekanandan *et al.* [89], and it was explained as the incorporation of these defects with the crystal lattice leading to the distortion of the lattice and the accompanying microstrains which stabilize the cubic structure. Recently, vibrational spectroscopy has been applied to investigate the structural behavior of the submicron particles [84, 91-93,]. Raman spectra have demonstrated that the local distortion of the TiO_6 sublattice still exists in the small particles, though the XRD shows that the particles are in the cubic form. The additional structural information obtained by the vibrational spectroscopy has been and will certainly benefit the research as well as the understanding of this interesting nano-size phenomenon in ferroelectric materials.

2.2. Review of Low Temperature Powder Synthesis

Technology advances in electronic industry have imposed increasing demand on high performance ceramic components, which can only be achieved

by improving the quality of the starting powders and the subsequent densification process. The traditional "mixing and calcination" approach has been commonly used to prepare ceramic powders [94-97]. Although the process is relatively simple, easy to scale-up and low cost, the powders produced have many problems, including large and non-uniform particle sizes, lack of chemical homogeneity and impurities.

To achieve higher quality powders, low-temperature wet chemical techniques for BaO-TiO₂ powder preparations are preferred and have been intensively studied. In wet chemical synthesis, intimate contact between Ba and Ti ions allows accelerated diffusion (short diffusion path) in the solution and complete mixing at the submicron level, leading to low reaction temperatures, fine particle sizes and a high degree of compositional homogeneity [98-100]. In the subsequent text, a brief review of various wet chemical synthesis techniques is presented.

2.2.1. Chemical Coprecipitation Process

The coprecipitation process involves simultaneous precipitation by mixing a number of different ions which are originally soluble in the aqueous solution. The formed precipitates should have a well-defined stoichiometry, so that the thermal decomposition of the precipitate results in the formation of the desired stoichiometric compound. Advantages of the coprecipitation process include a

better control of stoichiometry, low impurity level, controllable particle size and ease of introducing dopants. However, since calcination at relatively high temperatures is required in the process, high weight loss and agglomeration associated with the calcination are inevitable. In addition, a small amount of BaCO_3 formed during the combustion process is another drawback of this process.

I. Oxalate process

High quality BaTiO_3 powder of nearly perfect stoichiometry has been produced by precipitating barium titanyl oxalate (BTO) followed by calcination at an appropriate temperature [101-108]. This process is referred to as the 'oxalate process'. Since it is a relatively simple process, and powders with high purity and stoichiometry can be readily achieved, the process has been commercially used in preparing high purity powders in capacitor and thermistor industries.

The Ba:Ti ratio in BTO and in the resulting BaTiO_3 was found to depend greatly on reaction conditions, and the optimized synthesis condition was developed [101] by adding a mixture of aqueous solution of BaCl_2 and TiCl_4 to a hot aqueous solution ($\sim 80^\circ\text{C}$) of oxalic acid to form BTO precipitate. The BTO precipitate with a Ba:Ti ratio of 1 can be converted to high-purity stoichiometric BaTiO_3 at $700 \sim 900^\circ\text{C}$. The reactions are summarized in Table 2.2.

Similar syntheses to form BTO have also been carried out with different concentrations of reagents or temperatures [102-107]. Furthermore, titanyl nitrate, $\text{TiO}(\text{NO}_3)_2$, instead of TiCl_4 has been tried as the titanium source [105, 108], and BTO has also been successfully prepared from ethanolic solutions [105, 109-110].

II. Citrate process

The citrate process [111-114] is also known as the Pechini [111] or liquid mix (LM) process and it is similar to the oxalate process. Typically the titanium precursor is obtained by mixing tetrabutyl titanate with citric acid and ethylene to form an aqueous solution, and the barium precursor is obtained by dissolving

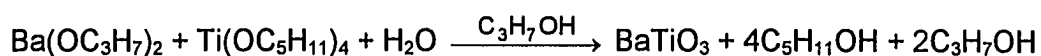
Table 2.2. Synthesis of BaTiO_3 using the oxalate process [99].

Synthesis of mixed Ba-Ti oxalate
$\text{TiCl}_4 + \text{H}_2\text{O} \rightarrow \text{TiOCl}_2 + 2 \text{HCl}$
$\text{BaCl}_2 + \text{TiOCl}_2 + 2 \text{H}_2\text{C}_2\text{O}_4 + 4 \text{H}_2\text{O} \rightarrow \text{BaTiO}(\text{C}_2\text{O}_4)_2 \cdot 4 \text{H}_2\text{O} + 4 \text{HCl}$
Thermal decomposition of oxalate to form BaTiO_3
100 ~ 140°C: $\text{BaTiO}(\text{C}_2\text{O}_4)_2 \cdot 4 \text{H}_2\text{O} \rightarrow \text{BaTiO}(\text{C}_2\text{O}_4)_2 + 4 \text{H}_2\text{O}$
300 ~ 350°C: $2 \text{BaTiO}(\text{C}_2\text{O}_4)_2 \rightarrow \text{BaTi}_2\text{O}_5 + \text{BaCO}_3 + 4 \text{CO} + 3 \text{CO}_2$
600 ~ 700°C: $\text{BaTi}_2\text{O}_5 + \text{BaCO}_3 \rightarrow 2 \text{BaTiO}_3 + \text{CO}_2$

BaCO₃ in formic acid and water. The barium precursor is then added to the titanium precursor (Ba:Ti ratio of 1), and by adjusting the pH, crystalline barium titanyl citrate (BaTi(C₆H₆O₇)₃·4H₂O) is precipitated. Calcination of the citrate precipitate above 600°C results in the formation of BaTiO₃.

2.2.2. Double Alkoxides Process

Stoichiometric BaTiO₃ powders and powders with various dopants have been prepared by using alkoxide process developed by Mazdiyasi *et al.* [115-120]. This route has also been applied to prepare many other ceramic powders [121]. The process for BaTiO₃ involves simultaneous hydrolysis of barium and titanium alkoxides mixed intensively in an alcohol solution (e.g., C₃H₇OH) by adding them to an excess of water. The hydrated BaTiO₃ (BaTiO₃·H₂O) precipitate is formed immediately for removal by filtering. After drying the precipitate in vacuum at temperatures as low as 50°C, a finely divided, stoichiometric BaTiO₃ powder with fine particles (50 ~ 150Å) and of very high purity (> 99.98%) is subsequently produced. The typical overall reaction for the formation of BaTiO₃ using barium isopropoxide and titanium ethoxide (derived from titanium isopropoxide) can be written as



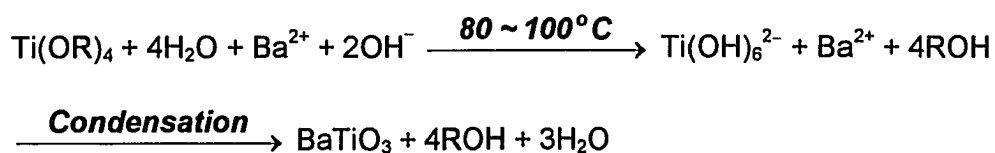
Since the organometallic reagents can be easily purified, levels of most impurities in BaTiO₃ are minimized and this is the major advantage of this process. Polytitanate phases with Ba:Ti ratio of 2:1, 1:2, 2:9 and 1:5 have also been successfully prepared by the alkoxide route [120, 122]. However, due to the sensitive nature of barium alkoxides to moisture and carbon dioxide, the experiment should be performed in a moisture and CO₂ free atmosphere (usually in Ar). Also, metal alkoxides require the use of large quantities of organic solvents [121]. Therefore, the preparation process suffers high costs of reagent materials and restricted operation conditions, which are the reasons that this process has not been developed on a large scale for industry.

2.2.3. Sol-Gel Process

The sol-gel process has been used to prepare a variety of glass and ceramic powders [123-128]. In the sol-gel process, colloidal sols of the mixture of different organic precursors are converted into monolithic gels (gelation) and the subsequent drying and calcination of the monolithic gels lead to the formation of crystalline powders.

The preparation of Ba-Ti gels is based on the hydrolysis of alcoholic solutions of titanium alkoxides (Ti(OR)₄) in concentrated solution of barium hydroxide (Ba(OH)₂) (pH ~ 14) at low temperatures (80 ~ 100°C) [129-134]. The

gels are calcined at above 600°C to form the crystalline BaTiO₃ powders. The hydrolysis and condensation reactions can be described as



In this process, the presence of a high concentration of OH⁻ is essential for gel formation. In neutral solutions, the reactions described above cannot occur and hydrated TiO₂ formation results. The hydrolysis and condensation steps are relatively fast, so titanium alkoxide precursors with a long C-chain (C₃ or C₄) are used to decrease the hydrolysis rate and molecular associations (Ti-O-Ti bonds). Since less expensive and moisture-insensitive barium acetate (Ba(CH₃COO)₂ or Ba(Ac)₂) is commercially available, the use of Ba(Ac)₂ instead of Ba(OH)₂ as the Ba source has been studied for BaTiO₃ formation [135-143]. Chemical additions such as acetic acid and acetylacetone are often used to control the hydrolysis kinetics so that fast hydrolysis and the precipitation of solid particles such as Ti(OH)₄ can be avoided [126, 135, 141]. Since better control of hydrolysis rate can be achieved by this process, it is also used for BaTiO₃ thin film synthesis.

In the sol-gel process, barium and titanium precursors can be mixed in various ratios to form homogeneous sols, thus the process can be easily applied to form some solid solutions [131, 140] and other compounds in the BaO-TiO₂

system, including $\text{Ba}_2\text{Ti}_9\text{O}_{20}$, $\text{BaTi}_5\text{O}_{11}$ and BaTi_4O_9 for microwave applications [137, 143]. The organic precursors used in the process are not very sensitive to moisture and CO_2 , so the synthesis is much simplified as compared to the double-alkoxide method. The technique can be easily applied to prepare BaTiO_3 thin films by dipping or spinning the substrate, which is a simple and inexpensive process and easier for scale-up as compared to other thin film deposition techniques. A detailed description of the techniques used in thin film deposition can be found in the latter part of the chapter. However, the sol-gel process also has similar disadvantages compared with the other process techniques in terms of high temperature calcination for crystallization and associated BaCO_3 formation.

2.2.4. Aerosol Drying, Freeze Drying and Spray Drying

Aerosol drying, freeze drying and spray drying are three major approaches to convert a solution to a homogeneous solid form. In these processes, rapid drying of the solutions can be achieved, a step essential to prevent liquid mixtures from segregation during the drying process.

Aerosol drying involves the formation of aerosol, which is a colloidal suspension of particles in a gaseous phase, and subsequent drying of the aerosol to ultrafine powders. This technique has been widely used to produce superconductor powders [144-145]. An aerosol consisting of ultrafine droplets of

the solution is produced by focusing an ultrasonic beam on the surface of the solution, and it is carried away by a purge gas [144]. As the size of the droplets in the aerosol is in the submicron range, the gravitational forces of the particles are not significant and particle movement resembles Brownian motion [127]. The aerosol is dried to ultrafine powders by passing it through a furnace. Since the droplets in the aerosol are very small and any segregation during drying is limited to the individual droplet, powders of high chemical homogeneity can be achieved by this technique. However, the process is very time consuming as only a small amount of powder can be prepared in one process cycle, resulting in the high cost of the synthesized powders.

Freeze drying has been used on a large scale in the food, biological and pharmaceutical industries [146]. It has also been used to prepare ceramic oxide powders [147-150] including BaTiO_3 . In the freeze drying process, the solution is initially frozen by exposing it to very cold air or an immiscible fluid. The solvent is removed as a vapor by sublimation from the frozen solution in a vacuum chamber below the triple point of the solvent.

Spray drying has long been used as a primary processing step in manufacturing ceramic products. Spray drying completes the required conversion from solution or slurry to powder in a single, continuous step [151-152]. In the spray drying process, the solution or slurry is first atomized into fine droplets, which are immediately contacted with a stream of hot drying air,

resulting in a rapid evaporation of the solvent. The dried powder is then separated from the drying air stream and gets collected. Powder properties in terms of particle size, flowability and moisture content can be controlled by adjusting temperature and feeding speed, *etc.* Since a small amount of residual solvent can hold the powder particles to form a hollow spherical shape agglomerate with sizes from several micron to hundreds of microns, sometimes intensive milling is required, which is a major disadvantage of this process. However, its ability to dry almost any kind of solutions or slurries and the relatively small compositional segregation (at the submicron level) associated with this process make it a very popular drying technique in the ceramic industries.

2.2.5. Combustion Synthesis

Combustion synthesis is also known as self-propagating high-temperature synthesis (SHS) or the anionic oxidation-reduction method [98, 153-166]. It has long been used to make non-oxide materials such as carbides, nitrides, borides, silicides, *etc.* [98, 153]. However, only recently has this technique been applied to process oxide ceramic powders such as α -Al₂O₃ [159], aluminates [160], ferrites [161, 164], high- T_c superconductor [155-158, 162], perovskite dielectric [163,165] as well as microwave materials [166].

In combustion synthesis, the precursor mixture is ignited at relatively low temperatures ($< 500^{\circ}\text{C}$) and chemical reactions (usually oxidation-reduction) occur very rapidly with large heat release (exothermic reactions) which further drives the reaction to complete. During the process the maximum or combustion temperature may reach a very high level (e.g., $> 2000^{\circ}\text{C}$), although the initial ignition temperature is low. Therefore, in this sense, the combustion synthesis is a high-temperature synthesis.

A commonly used combustion synthesis to form BaTiO_3 powder involves the reactions of metal nitrates, such as $\text{Ba}(\text{NO}_3)_2$ and $\text{TiO}(\text{NO}_3)_2$ and carbonaceous reductive fuel in a rapid, exothermic and self-sustained way. There are several advantages associated with this process technique. Since the rapid exothermic reactions provide the heat to complete the synthesis, there is no need for an external heat supply. The process is also very time efficient, which lowers the cost significantly. Very high combustion temperatures vaporize all volatile contaminants, thus the synthesized powders achieve high purity. Because the synthesis is rapid with a non-equilibrium characteristic, the powders produced are usually very defective.

2.2.6. Hydrothermal Process

The hydrothermal process was first given its name for the use of hot, pressurized water to precipitate various oxides. Numerous mineral systems

such as quartz, feldspar, wallastonite and analcite were prepared hydrothermally about a century ago. However, most of the early investigations were engaged merely in the preparation of minerals, while the systems were usually very complex and the experimental conditions were not well defined. The landmark study of Morey [167] opened a new area of hydrothermal synthesis which directed the investigations toward acquiring systematic equilibrium data and controlled and reproducible synthesis conditions. His study covered numerous mineral systems which were based on exploration of the underlying theories of hydrothermal synthesis, in particular crystal growth mechanisms, pressure and temperature effects on the synthesis, and experimental apparatus for the synthesis. After that, many other investigations looked further into single-crystal growth and ceramic powder synthesis.

Hydrothermal synthesis is a wet chemical process involving chemical reactions in a strong alkaline solution to form crystalline and anhydrous ceramic powders. It can be easily distinguished from the other processes, such as the sol-gel and coprecipitation, by the temperature and pressure applied in the synthesis. The typical temperatures used in hydrothermal synthesis ranges from 50 to 350°C with pressures up to 15 MPa. A flow chart below describes the hydrothermal steps used commercially (Figure 2.20) [168].

Hydrothermal formation of various ceramic oxides particles has been proposed based on a dissolution-reprecipitation mechanism [93, 168-169, 170].

A variety of compounds can be chosen as precursor materials, such as oxides, hydroxides, chlorides, nitrides as well as organic precursors like acetates and alkoxides. In BaTiO₃ synthesis, inexpensive materials, typically Ba(OH)₂ and TiO₂ or TiO₂ gels have been used as the precursor materials [167-186]. The reactions are carried out in a strongly alkaline solution (pH>13) at mild temperatures (<350°C). During the synthesis, the precursors are first dissolved in the solution due to the increased solubility of the precursors at elevated temperatures. As the concentrations of the component ions (e.g., Ba²⁺ and Ti⁴⁺) reach a sufficiently high value, the formation of the desired ceramic oxide particles may occur. However, the aqueous environment should be controlled by adjusting the chemical process variables such as temperature, pressure, reactant concentrations and the pH value [171-172] so that the desired phase is thermodynamically the most stable phase (lowest Gibbs free energy) in a given environment. Therefore, thermodynamic data and stability diagrams in terms of these variables are necessary to avoid tedious experimental trial and error. Recent work by Lencka *et al.* [172] successfully applied the thermodynamic method to generate phase stability diagrams for BaTiO₃ and PbTiO₃ systems. Figure 2.21 shows a stability diagram of the Ba-Ti hydrothermal system which illustrates the temperature, pressure and pH effects on BaTiO₃ formation.

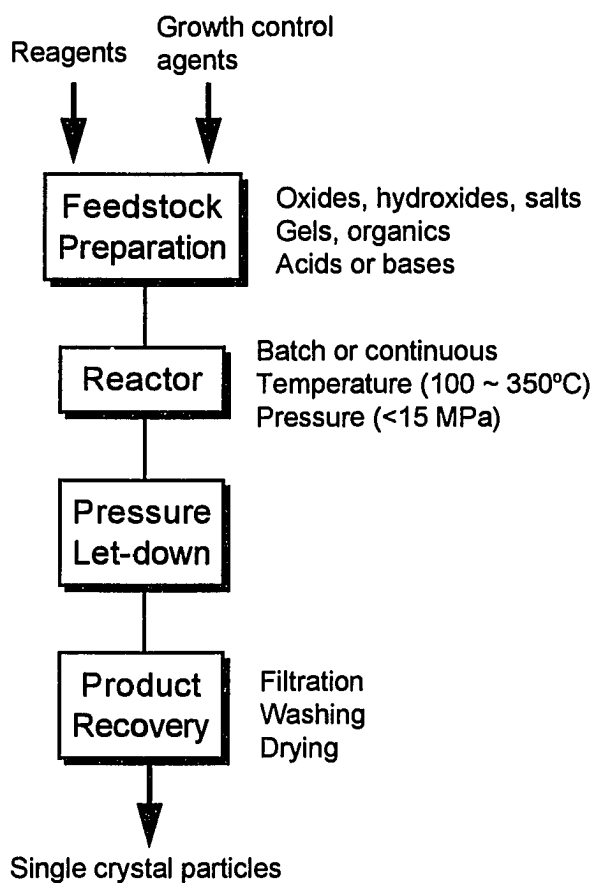


Figure 2.20. A flow chart illustrating the hydrothermal steps used in commercial synthesis [169].

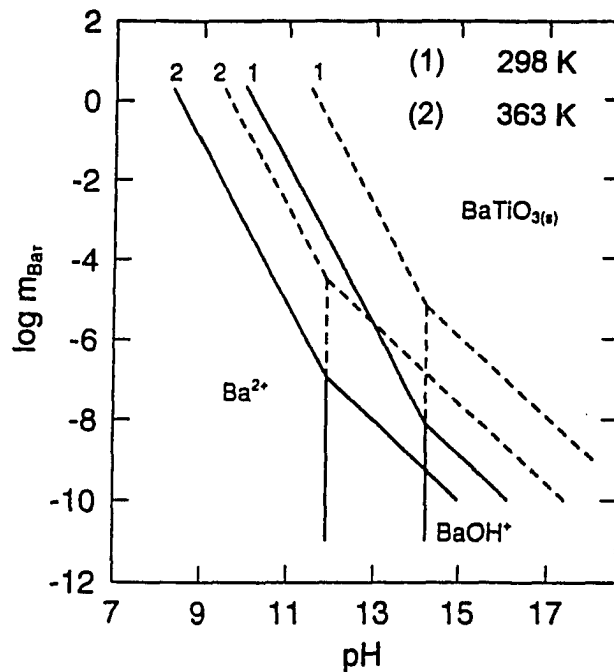


Figure 2.21. Stability diagram for the Ba-Ti hydrothermal system [172].

The major advantage that distinguishes hydrothermal synthesis from other process techniques such as sol-gel or coprecipitation techniques is that the powders thus produced usually have a high crystallinity, so that no high temperature calcination is needed for crystallization as required by other synthesis techniques, which in turn eliminates the milling step in hydrothermal synthesis. By controlling the process variables, powders with various particle sizes, stoichiometries, or even particle shapes can be achieved. The synthesis can employ relatively inexpensive raw materials. The synthesized powders have

high purity and good homogeneity, and have been demonstrated to be highly reactive toward sintering [168-170, 178, 180-182, 184-185]. Unfortunately, the process is limited to oxides which can be formed under hydrothermal conditions, and the quantitative control of dopants introduced into the main phase ceramic powders is relatively difficult.

In this study, hydrothermal synthesis was used for the BaTiO₃ formation. There are several reasons for this choice, including: (1) the formation and growth mechanisms in hydrothermal synthesis are not well understood; (2) the synthesis has the ability to control particle size by varying synthesis parameters, which facilitates the study of the particle size effect on the structure and ferroelectricity that is observed for submicron particles; (3) it is of interest to study the sinterability of the produced tetragonal powders (instead of the cubic powder that commonly are produced) and the microstructure and dielectric properties of the sintered samples, and (4) the synthesis allows the direct formation of ferroelectric thin films.

2.3. Effects of Sintering on Microstructure and Dielectric Properties

Single-crystal single-domain BaTiO₃ has a dielectric constant of 230 in the polar direction and 4770 in the perpendicular directions. The random orientation of axes in a ceramic would lead to a dielectric constant of 1740 [36]. In practice the low-field dielectric constant of the BaTiO₃ ceramics lies in the

range 2000–4500 and varies with the method of preparation. The higher than expected values of the dielectric constant of BaTiO₃ ceramic are believed to result from the presence of internal stresses and complex domains in the ceramic bodies [46–49]. A room temperature dielectric constant of approximately 5000 ~ 6000 can be reached if the sintered BaTiO₃ has a high density and an optimum grain size around 1 μm [58–59]. Porosity is very detrimental to the dielectric properties in the way that it leads to low dielectric constant, low breakdown strength and high loss due to water permeability.

Uniform microstructure with a high density and controlled grain size is critical for a BaTiO₃ ceramic to achieve a high dielectric constant. Therefore, it is very important to optimize the sintering process in terms of sintering temperature, time and sintering rate, which are the main factors in determining the final microstructure of the sintered sample. The properties of the starting powders (e.g., the Ba/Ti ratio) also significantly affect the sintering behavior. In the following sections, some factors affecting the sintering and microstructure development are reviewed.

2.3.1. Ba to Ti Ratio

The Ba to Ti ratio is the ratio of the total number of Ba ions to that of Ti ions. The Ba to Ti ratio of pure BaTiO₃ under exact stoichiometry should be 1. According to the phase diagram of BaO-TiO₂ system given by Rase *et al.* [187]

and later modified by Kirby *et al.* [188] (Figure 2.22), the solubility of either BaO or TiO₂ in BaTiO₃ is very limited. Excess TiO₂ (Ba:Ti < 1) leads to the formation of a second phase Ba₆Ti₁₇O₄₀ together with BaTiO₃, which results in liquid phase formation at about 1320°C by eutectic reaction. Therefore liquid phase sintering may take place at temperatures below 1350°C, giving rise to large grain size ranging from 5 to 50 μm. On the other hand, an excess of BaO (Ba:Ti > 1) results in the formation of Ba₂TiO₄ which forms another eutectic point with BaTiO₃ at about 1563°C. Since Ba₂TiO₄ is a separate insoluble phase in the BaTiO₃ matrix, it usually inhibits the grain growth of BaTiO₃ during sintering at temperatures up to 1450°C, which gives rise to a narrow grain size distribution of 1 ~ 5 μm.

2.3.2. Sintering Mechanism and Schedule

Sintering converts a compacted powder into a denser structure of crystallites (grains) joined to one another by grain boundaries. Sintering is the result of atomic motion facilitated by high temperature. The driving force for sintering is the reduction of high surface energy associated with unsintered powder, which can be achieved by mass flow from the interior of grains along the grain boundaries to adjacent pores through surface and bulk transport [34,189]. Many variables influence the sintering rate, including initial density, material, particle size, sintering atmosphere, temperature, time and heating rate. In order

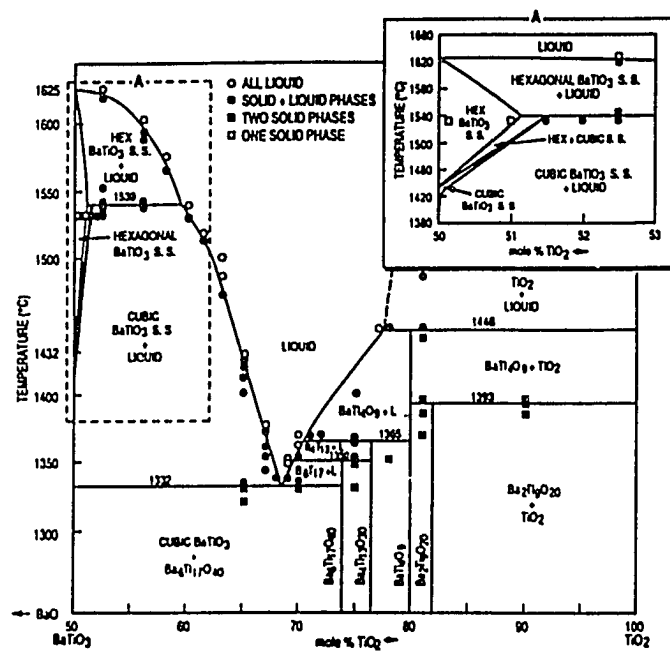
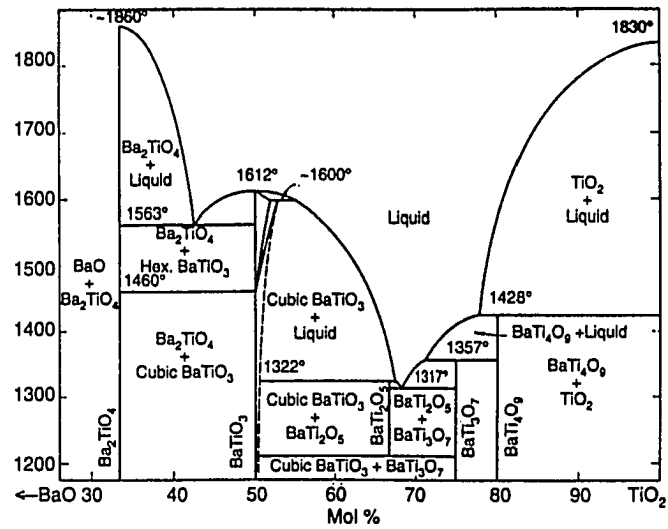


Figure 2.22. Phase diagram of BaO-TiO₂ system: (a) the one given by Rase *et al.* [187] and (b) the one modified by Kirby *et al.* [188].

to study sintering, it is important to monitor the density, surface area, shrinkage and some other measurable parameters that correlate favorably with the sintered properties in different sintering stages.

Ceramic powders of technical grade purity (97 ~ 99%) are usually sintered at temperatures approximately 10% below their thermodynamic melting temperatures for several hours. For commercial BaTiO₃ powders, the sintering temperature is around 1300 ~ 1400°C. In general, small and uniform grain sizes are preferred since they usually give better properties than large and non-uniform ones. Thus it is important to control the sintering variables, most importantly temperature and heating rate, to achieve the desired microstructure. For instance, the grain size of ferroelectric ceramics such as BaTiO₃ has a substantial effect on the dielectric constant, K , for the size range 1 ~ 50 μm [59]. A maximum dielectric constant values of 4500~6000 occurs at approximately 1 μm grain size [58-59]. It has been discussed in section 2.1.3 that the abnormal high dielectric constant was attributed to the high internal stress and domain density associated with fine-grained BaTiO₃ ceramics [10, 45-49].

2.3.3. Hot-Pressing and Fast-Sintering

It is often difficult to obtain a low-porosity ceramic body by normal 'pressureless sintering', i.e., by sintering at atmospheric pressure, or to achieve low porosity without significant grain growth. Hot-pressing, or pressure

sintering, is a commonly used fabrication method that utilizes both thermal and mechanical energy to affect the densification process [190]. The pressure now provides the major part of the driving force to eliminate porosity so that the temperature can be kept at a low level at which grain growth is minimized. The advantages of the hot pressing process relate directly to the additional energy source and the accompanying increased densification rate. Fully dense, fine-grained ceramics can be obtained at lower temperatures and at time cycles shorter than those required by conventional sintering techniques.

Two methods of hot pressing are typically used: uniaxial hot pressing and isostatic hot pressing (HIP). Uniaxial hot pressing uses a punch and a die made of certain materials to achieve desired pressures at high temperatures [191-192]. Molybdenum based alloys can be used up to 1000°C at pressures of about 80 MPa while alumina, silicon carbide and silicon nitride can be used up to about 1400°C at similar pressures. Graphite is widely used at very high temperatures up to 2200°C, although relatively low pressures, i.e., 10 to 30 MPa can be applied. In the HIP process, an inert gas such as nitrogen or argon is used to transmit pressure while the temperature is raised to the required level. Starting materials are typically in powder form or pieces containing interconnected pores, which are coated with a thin metallic layer or encapsulated in impervious envelopes of a ductile metal such as platinum to prevent the gas from penetrating into any voids in the processed body.

Disadvantages associated with these processes are that a corrosive reaction often takes place between the die (or metallic coating) and the ceramic material to be compacted, and only simple shapes can be manufactured. Moreover, the processes are expensive and not very cost-effective for mass production.

A modified HIP method was described by Hardtl [193-194] in which no metallic layer is necessary. It does not suffer from the disadvantages mentioned previously. The body is directly brought to a state with no surface-connected porosity by preliminary processing steps such as pressureless sintering, and the HIP process can be carried out without separate encapsulation using a process called cladless HIP or sinter-HIP.

To restrict grain growth at high temperatures, a fast-sintering procedure has first been proposed for the fabrication of dense, fine-grained polycrystalline β -alumina [195]. This procedure has recently been applied successfully to prepare translucent aluminas [196-198], ferrites [199] and BaTiO_3 [200-203] while it was found not successful for preparing MgO [204]. During the fast-sintering, powder compacts undergo a rapid high temperature non-isothermal treatment by being passed through a short hot zone. Under such conditions, the densification process is enhanced relative to the grain growth process since a higher lattice diffusion coefficient responsible for the densification can be achieved compared to the surface diffusion coefficient associated with grain growth.

Figure 2.23 shows a schematic diagram of the rates of two different mass transport mechanisms during sintering corresponding respectively to densification and grain growth as a function of temperature. The figure indicates that at high temperatures, kinetic processes with a high activation energy are favored; thus the densification rate is higher than the grain growth rate at high temperatures. This results in ceramics with high densities and fine grain sizes by using the fast-sintering procedure.

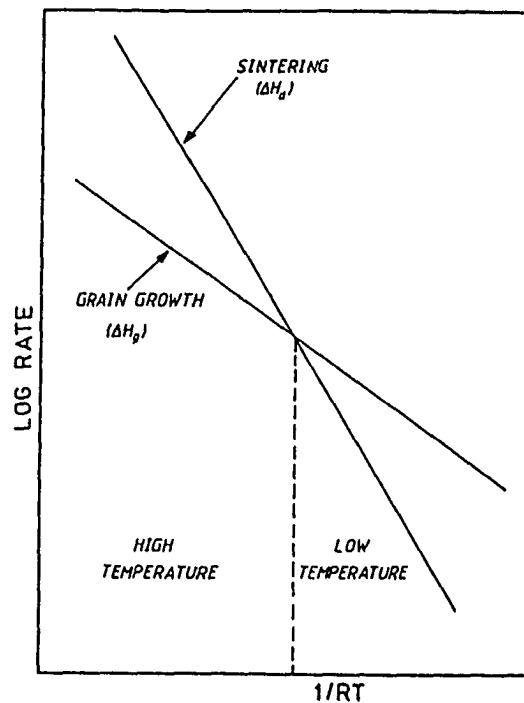


Figure 2.23. Schematic diagram of the rates of two different mass transport mechanisms during sintering corresponding respectively to densification and grain growth as a function of temperature [202].

2.3.4. Additives for Sintering

Dopants are usually added to improve densification. In general, the effects of dopants on densification include preserving the ideal characteristic of the starting powder, increasing the packing density of powder compacts, enhancing lattice diffusion and thus mass transport rate, and preventing abnormal grain growth. However, when the dopant concentration exceeds the solubility limit, a second phase forms in the sample and it may cause deterioration of the properties. Therefore, it is very important to obtain the composition as well as phase relations of different compounds in the powder before sintering. Sometimes liquid sintering is purposely desired to achieve uniform structure and chemical homogeneity (i.e., for PTCR materials preparation), so liquid sintering aids such as a mixture of Al_2O_3 , SiO_2 and TiO_2 (AST) is added to decrease the melting temperature by forming a lower eutectic point around 1260°C (Figure 2.24) [205].

Higher valency substituents (e.g., La^{3+} replacing for Ba^{2+} or Nb^{5+} for Ti^{4+}) at relatively high concentrations (>0.5 mol%) are sometimes introduced to inhibit crystal growth during the sintering process [36]. The resultant fine grain size has the effect of raising the dielectric constant below the Curie constant, which is very important in capacitor applications. On the other hand, low concentrations of higher valency substituents (<0.2 mol%) can cause a decrease in resistivity, leading to the important PTCR behavior [205-225]. Other additives are also

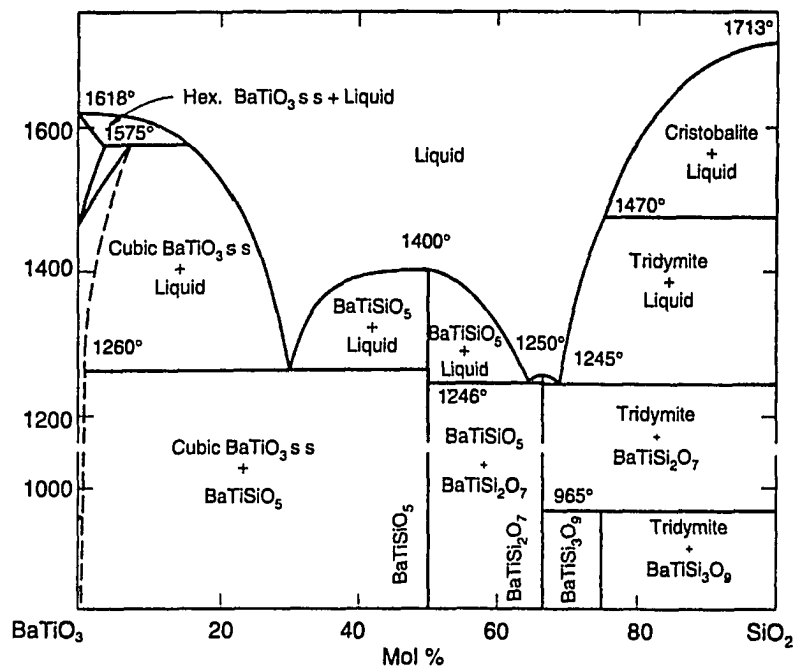


Figure 2.24. Phase diagram of BaTiO₃-SiO₂ system [187].

added in the sintering to modify the dielectric properties, such as to broaden the transition peak or to shift the Curie temperature. Details of this can be found elsewhere [36].

2.4. Impedance Spectroscopy (IS)

Impedance spectroscopy is an analytical method involving the study of the electrical behavior of materials over a wide range of frequencies. In most studies on the electrical properties of dielectric materials, such as BaTiO₃, the properties are usually reported at a fixed frequency, typically at 1 kHz. Although this is adequate for practical applications, a large amount of extra information could be obtained by analyzing electrical data as a function of frequency.

In polycrystalline materials, polarization and charge transport properties are strongly affected by microstructure. In order to correlate electric properties to the microstructure of the materials, it is necessary to separate the electrical contributions of the interfacial polarization at the electrode-bulk interface as well as the heterogeneity effects, such as grain boundaries, secondary phases and surface layers, from the bulk properties according to their frequency dependence. Impedance analysis can be used to distinguish the underlying competing phenomena through the use of lumped parameter/complex plane analysis (LP/CPA). When combined with other characterization techniques such

as electron microscopy, IS provides a powerful means of correlating the electrical properties of materials to their microstructure and composition [225].

The use of IS to characterize solid state ceramic materials was first introduced by Bauerle in the study of yttria stabilized zirconia [226]. Since then, IS and LP/CPA have been extensively applied to other solid electrolyte materials [227-228], and further extended to other systems such as mixed conducting oxides [229-232], semiconducting oxides [233-235] and thermistor materials [236-237]. Recently, IS measurements on BaTiO₃ and related materials, such as doped semiconducting BaTiO₃, have also been reported [214-216, 217-219], and their ferroelectric behavior as well as PTCR (positive temperature coefficient of resistance) effect have been analyzed.

2.4.1. Lumped Parameter/Complex Plane Analysis (LP/CPA)

IS measurement can be performed using an impedance analyzer and the results can be obtained in terms of equivalent circuit parameters such as capacitance, C , resistance, R (or conductance, G) in either series form (C_s and R_s) or parallel form (C_p and G_p) as a function of the frequency. These parameters are interrelated and can be transformed from one to another by the following expressions [238-240]:

$$R_s = \frac{G_p}{G_p^2 + \omega^2 C_p^2} \quad (2.46)$$

$$C_s = \frac{G_p^2 + \omega^2 C_p^2}{\omega^2 C_p} \quad (2.47)$$

$$G_p = \frac{R_s}{R_s^2 - (1/\omega C_s)^2} \quad (2.48)$$

$$C_p = \frac{1/\omega^2 C_s}{R_s^2 - (1/\omega C_s)^2} \quad (2.49)$$

and

$$\tan \delta = G_p / \omega C_p = \omega R_s \quad (2.50)$$

The impedance can be expressed in terms of these parameters:

$$Z^*(\omega) = Z' - jZ'' = R_s - j(1/\omega C_s) \quad (2.51)$$

and can be related to other immittance quantities, admittance, Y^* , modulus, M^* , and complex capacitance, C^* . These quantities can be expressed by the following equations:

$$Y^*(\omega) = 1/Z^* = Y' + jY'' = G_p + j\omega C_p \quad (2.52)$$

$$C^*(\omega) = Y^*/j\omega = C' - jC'' = C_p - j(G_p/\omega) \quad (2.53)$$

$$M^*(\omega) = j\omega Z^* = M' + jM'' = 1/C_s + j\omega R_s \quad (2.54)$$

In LP/CPA, the imaginary component of any of the complex quantities is usually plotted against the real component. This is the so-called Cole-Cole plot [241-242]. A single semicircular fit in any of the complex planes represents a relaxation phenomenon with a characteristic relaxation time, τ . Ambiguity exists when a semicircle is obtained simultaneously in more than one complex plane,

which suggests that the sample-electrode system can be represented by more than one equivalent circuit (Figure 2.25). Moreover, it has been reported that more than one form of an equivalent circuit can be constructed from a single semicircle in a complex plane [243]. In order to determine the appropriate equivalent circuit representation, the interpretation should be supported by other experimental evidences, such as electron microscopy, and basic knowledge related to the sample being measured.

Further complexity is often found in a system exhibiting multiple semicircles, indicating multiple relaxation phenomenon. In situations like these, it is always valuable to gather information in all four complex planes because each of these planes has a unique dependence on frequency, and therefore the significance within a given frequency range is different.

When a semicircular fit is obtained in a complex plane, several important parameters can be obtained by the simple geometrical analysis of the semicircle (Figure 2.26). These parameters include:

- right and left intercepts of the semicircle with the real axis;
- peak frequency (ω_c);
- relaxation time (time constant = $\tau = 1/\omega = RC$);
- diameter of the semicircle
- chord on the real axis for the depressed semicircle, and
- depression angle (θ)

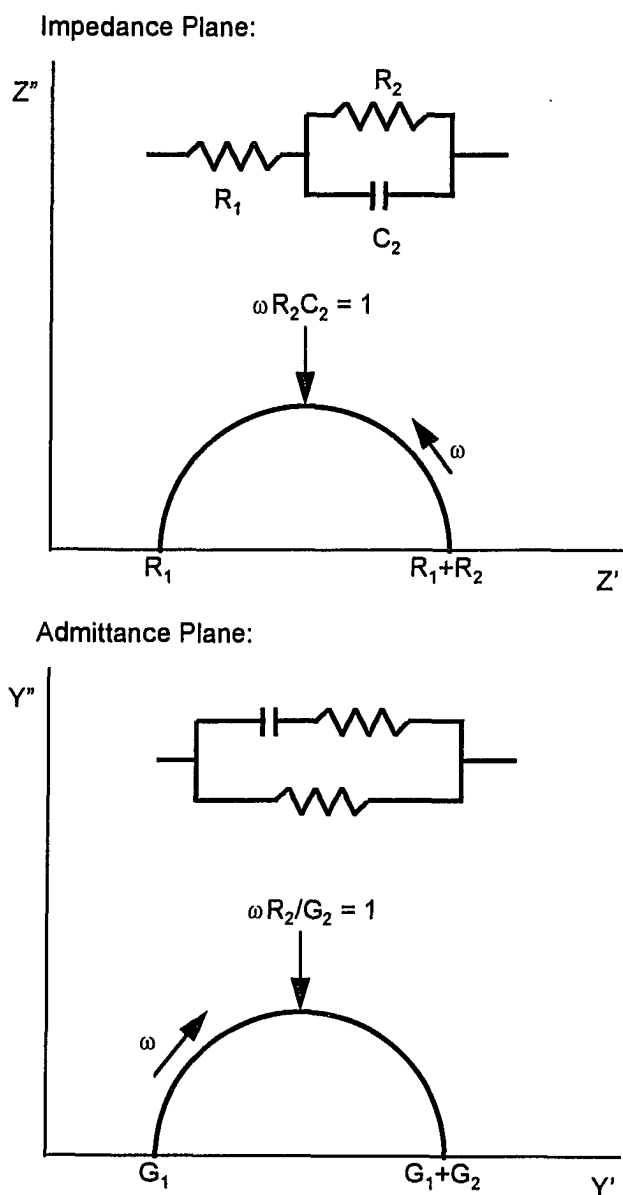


Figure 2.25. Single relaxation semicircle is observed in multiple complex planes (Z^* and Y^*), suggesting the sample-electrode system can be represented by more than one equivalent circuit [243].

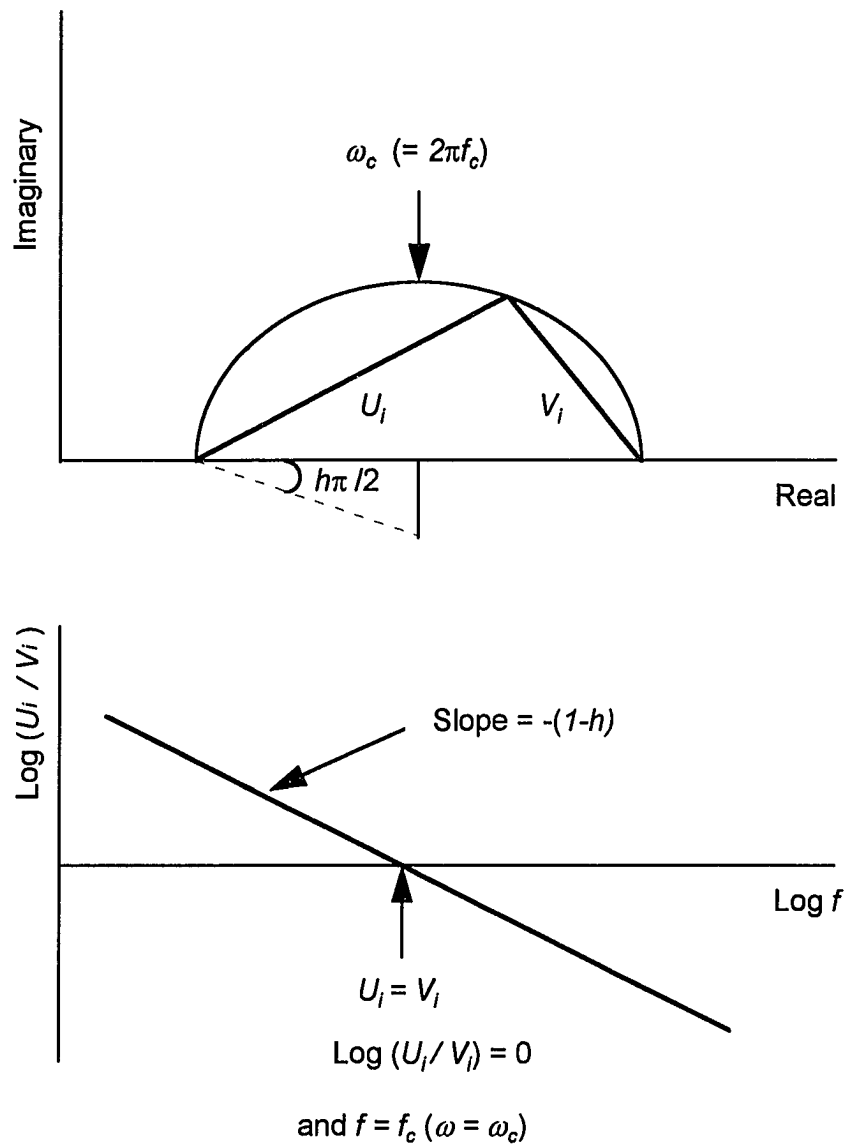


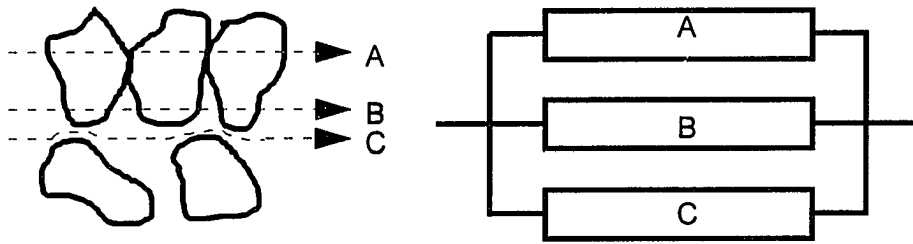
Figure 2.26. Determination of depression angle and peak frequency for impedance or capacitance plot [239, 243].

When a semicircle exhibits zero degree depression angle (center lying on the real axis), the relaxation it represents is referred to as a Debye-type relaxation. Debye-type behavior is an *ideal* relaxation process characterized with a single relaxation time. However, most real materials exhibit more complex behavior, i.e., non-Debye type relaxations. This is indicated in a complex plane showing a depressed semicircle with a nonzero depression angle. The non-Debye type relaxation is commonly explained in terms of the distribution of relaxation times possibly caused by disorder in materials (e.g., glasses and amorphous thin films) or the non-uniformity of the electrical path [244-246]. Therefore, the depression angle gives valuable information on the degree of homogeneity/heterogeneity of the electrical path through the material.

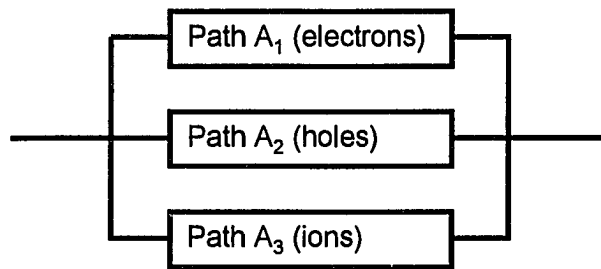
2.4.2. Equivalent Circuit Modeling

By examining a sample's electrical response through complex plane analysis, an equivalent circuit can be constructed to model the electrical behavior. The components within the equivalent circuit can be related to various types of polarization mechanisms as well as different conduction mechanisms, such as charge carrying species, physical regions for conduction and/or conduction paths. The following rules should be obeyed to characterize these phenomena [238]:

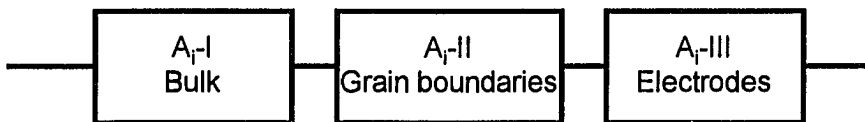
- each significant conduction path must be represented by a parallel equivalent circuit path (Figure 2.27a);
- each significant charge carrying species must be represented by a parallel equivalent path (Figure 28b);
- each region of significance within a path must be represented by a lumped parameter circuit with respect to the type of charge carrying species (Figure 2.27c);
- each mechanism of polarization and relevant phenomena must be represented by either a series or parallel combination of resistors, capacitors, and/or inductors;
- each of the components representing various conducting species and polarization processes each has its own composition, microstructure, temperature, voltage, pressure, environment and frequency dependence;
- the electrical paths of significance are those yielding the least impediment to current flow;
- the regions of significance within these electrical paths are those presenting the largest impediment to current flow; and



(a) Each significant conduction path is represented by a parallel equivalent circuit.



(b) Each significant charge carrying species is represented by a parallel equivalent circuit.



(c) Each region of significance within a path is represented by a lumped parameter circuit with $i = 1, 2, 3$ (Figure b) for the type of charge carriers.

Figure 2.27. Equivalent circuit modeling in polycrystalline materials [238].

- complex plane plotting techniques can be used to elucidate an appropriate equivalent circuit representation from measured electrical quantities when used in conjunction with information obtained from other methods of study.

As discussed in the previous section, more than one equivalent circuit may be visualized for the same type of relaxation, where the components can be combined either in series or parallel or a resultant equivalent lumped parameter. In order to further identify the genuine nature of an equivalent circuit model, a number of guidelines with real physical considerations should be followed [240, 243]:

- for each type of charge carrier, a parallel R - C leg must be designated;
- for each type of path that charge can traverse, a parallel R - C leg must be designated;
- for each type of physical region a specific type of charge carrier encounters within a conduction path, a separate R - C network in series must be used;
- admittance (Y^*) and complex capacitance (C^*) plots are best used to define a R - C series combination for each semicircle obtained; each of these legs will be in parallel in the equivalent circuit model; and

- impedance (Z^*) and complex modulus (M^*) plots are best used to define a R - C parallel combination for each semicircle obtained; each of these legs will be in series in the equivalent circuit model.

As also mentioned before, in order to obtain more information for appropriate equivalent circuit construction, all four complex planes should be carefully examined, since each plane has its own significant representation over a given frequency range. However, a general rule can be followed as shown in Table 2.3.

Table 2.3. Conditions for satisfying equivalent circuit modeling [238].

Conditions on magnitudes of resistance (R 's) and capacitance (C 's)	Series representation	Parallel representation
R 's equal: $R_1 = R_2$ or $R_1 \cong R_2$ C 's varied: $C_1 \gg C_2$ or $C_2 \gg C_1$	Z^* plane	Y^* plane
R 's varied: $R_1 \gg R_2$ or $R_2 \gg R_1$ C 's equal: $C_1 = C_2$ or $C_2 \cong C_1$	M^* plane	C^* plane

2.5. Review of Thin Film Synthesis of BaTiO₃

Because of renewed interest in ferroelectric films for nonvolatile semiconductor memories, extensive research is undergoing to improve processing and properties of ferroelectric thin films. Nonvolatile memories have

the potential advantages of high access speed, high density, radiation hardness, and low operating voltage. Applications include large-volume thin-film capacitors [247-249], microactuators [250], optical waveguide devices [251-252], spatial light modulators [253], DRAM's (dynamic random access memories) [254-258], pyroelectric detectors [252, 259], SAW (surface acoustic wave) [260-261] devices and chemical sensors [262-265]. Barium titanate, due to its relatively large dielectric constant and electro-optic coefficient, is a good candidate for the ferroelectric thin film applications.

2.5.1. Methods for Thin Film Fabrication

Thin film technologies for the fabrication of complex electronic oxides can be divided into two categories [266-267]: (i) physical and (ii) chemical techniques.

In physical techniques, precursor materials (source) to the desired films are vaporized and deposited on a substrate by various vaporization methods. It is also generally termed as physical vapor deposition (PVD). The physical techniques include thermal and electron beam evaporation; dc, radio frequency ion beam and magnetron sputtering; and laser ablation. PVD has been one of the most common deposition methods and has advantages in terms of quality of thin films and compatibility with semiconductor integrated circuit processing. However, a major disadvantage is that virgin films deposited by PVD are often

amorphous and high temperature post-deposition annealing is needed to achieve the desired crystallographic structure.

Thermal evaporation is achieved by heating the source material above its vaporization point in a vacuum or oxidized atmosphere either by resistive heating or by the impact of an electron beam. This technique has been widely applied to the deposition of metals (Cu or Al), simple oxides (SiO, SiO₂ and Y₂O₃, etc.) and compounds (ZnS, etc.), and ferroelectric films [268-271]. Radio frequency and dc sputtering techniques [272-281] employ high-energy ions to bombard a target source (normally oxides). The transfer of atoms from the target to a substrate is accomplished by momentum transfer. Radio-frequency (*rf*) sputtering is used for insulating the target so that electrons and positive ions impact on the target surface on alternate half cycles of the power cycle. This nullifies the surface charges that otherwise build up on the target as deposition proceeds. Magnetron sputtering is a recently developed technique which uses static magnetic fields to deposit thin films. It significantly increases deposition rate and has better quality control [272]. The laser ablation technique applies high-power lasers to evaporate ceramics at ambient pressures, or in controlled partial pressures of oxygen. The incident laser beam focuses on the target surface so that all elements within a small volume vaporize simultaneously and subsequently deposit onto a substrate. This technique is most extensively used

in high temperature (T_c) superconductor [282-283] and recently ferroelectric thin films [284-285].

Chemical techniques include spray pyrolysis, chemical vapor deposition (CVD), sol-gel and hydrothermal processes. The common feature in these methods is that they all involve chemical reactions between the sources (vapor or liquid) and the substrate. The principal advantages of the chemical methods are their relatively low cost and their suitability for large-area thin film production. However, except by the hydrothermal synthesis, the films thus produced are often amorphous and need annealing at higher temperatures to achieve crystallinity.

Spray pyrolysis is the simplest among these chemical techniques and it involves the reaction of chemical vapor streams with a heated substrate. It has been used to form simple oxides such as SnO_2 coating on glass plates. For more complex compounds, the difficulty of controlling the reactions limits its further application.

Chemical vapor deposition (CVD) has a potential ability to fabricate all types of oxide and nitride films. The process involves transporting several volatile reactants, such as metal/organic lead compounds, titanium tetrachloride and zirconyl chloride in PZT, through a reaction chamber by a carrier gas such that the desired complex compound grows in an equilibrium manner on a heated substrate. It is a well-established industrial process for epitaxial growth of

semiconductors such as GaAs. Recently, this technique has been applied to produce ferroelectric thin films [286-298]. Advantages of CVD include textured growth of the films, rapid deposition rates, good composition control and ability to produce complex compounds. However, relatively high processing temperatures limit the choice for substrate materials and introduce interdiffusion problems between the substrate and the film.

Sol-gel synthesis has been used to produce high quality powders for ferroelectric applications [129-143]. The sol-gel method involves the preparation of mixed solutions of organometallic precursors, often metal-alkoxides such as titanium isopropoxide ($\text{Ti}[(\text{CH}_3)_2\text{CHO}]_4$), in a suitable organic solvent [299-300]. This solution then undergoes hydrolysis and condensation to form a structured solution or gel containing long chain length metal/organic polymers. The viscosity and surface tension of the solution is adjusted by adding modifying agents before the solution is coated onto the substrate by spinning, dipping or spraying. The property of the polymer can be modified by adjusting the type of solvent and pH value of the solution. The resulting polymeric film is then dried and fired in a furnace to burn off the organic components, and it forms an inorganic ceramic film by subsequent oxidation. However, the film thus produced is amorphous or partially crystallized and post-deposition annealing is required to achieve complete crystallization as well as densification. The sol-gel method has the advantages of low cost and fast processing speed; however, the

requirement of post-deposition annealing is its major drawback. The sol-gel process has been applied to prepare various ferroelectric films such as BaTiO₃ [80, 82, 301-309], PbTiO₃ [310], PbZrO₃ [311], PZT [299, 312-316] and PLZT [317-318].

Hydrothermal synthesis is another chemical synthesis technique that has been used successfully in producing large quantities of perovskite and other structure electronic powders [168-186]. More recently, this method has also been adopted to prepare ferroelectric thin films such as BaTiO₃ and PZT. Since most of the ferroelectric films have a perovskite structure (ABO₃), in hydrothermal preparation, a substrate of the B metal (such as titanium in BaTiO₃) or B-coated glass, crystalline silicon or polymer is placed in a strongly alkaline solution (pH>10) containing the A component. Hydrothermal reaction takes place at temperatures of ~ 100-250°C to form a crystalline layer of ABO₃. Hydrothermal synthesis has a major advantage of eliminating the high temperature annealing procedure that is often required by other thin film synthesis techniques. In addition, it shares the advantages that most of the wet chemical syntheses (sol-gel, etc.) have: easy composition control, low processing temperature, easy fabrication of large-area thin films, and low cost.

2.5.2. Preparation of BaTiO₃ Thin Films Using Hydrothermal Synthesis

There are many perovskite ferroelectric thin films that have been synthesized using the hydrothermal technique. Among them, BaTiO₃ has been most intensively studied. For BaTiO₃ thin film preparation, a thin plate of high purity Ti metal is commonly used as a substrate [321, 326, 328, 330] mainly because of its convenience. Prior to use, the Ti substrate is cleaned ultrasonically in acetone and etched in 6 N hydrochloric acid (HCl). However, Ti-coated glass [325], crystalline Si [319, 322-323, 329] or a polymer [320] formed by a sputtering technique has also been employed as a substrate material. Ba(OH)₂ is most commonly used as a barium source and to maintain a high pH value (>11). Other barium sources include high purity Ba(NO₃)₂ and Ba(CH₃COO)₂ [323, 330]. The Ba(OH)₂ solution can be obtained by dissolving high purity (>98%) Ba(OH)₂·8H₂O powder in a certain amount of distilled and deionized water. The solution is boiled to remove dissolved CO₂ which might be responsible for the formation of insoluble BaCO₃, one major impurity present in BaTiO₃. The hydrothermal synthesis is carried out in a pressure chamber, usually a Teflon lined acid digestion bomb, in which the Ti or Ti-coated substrate is placed. The temperature and time of the synthesis can be varied around 80 to 250°C and 0.5 to 24 hours respectively to adjust the thickness and quality of the films. At lower temperatures, the formation of TiO₂ instead of BaTiO₃ was observed [319].

In order to increase the deposition rate and thickness of the thin films deposited on the substrate, a voltage is applied between the Ti substrate (anode) and Pt, which acts as a counter-electrode (cathode). This modified synthesis is called electrochemical-hydrothermal synthesis. In the synthesis, electrolysis along with the hydrothermal reaction takes place galvanostatically with a current density being controlled at 10 ~ 50mA/cm². Here a Ba(OH)₂ solution is also used as a liquid electrolyte for the electrolysis reaction. Electrochemical synthesis without the hydrothermal condition has also been studied to form BaTiO₃ films [328, 330].

The BaTiO₃ thin films prepared by hydrothermal, electrochemical or hydrothermal-electrochemical methods are generally of cubic structure. The films thus formed are pure, uniform and with high crystallinity. The thickness of the films are often around 0.5 μm or less. The films with tetragonal structure and greater thickness have been formed with higher temperature or longer reaction time [321, 328]. The dielectric constant of the film prepared has been reported to be around 100-300 [324, 328].

CHAPTER III

EXPERIMENTAL PROCEDURES

3.1. Hydrothermal Synthesis of BaTiO₃ Powders and Thin Films

BaTiO₃ powders and thin films were produced by using hydrothermal synthesis. The synthesis was mainly carried out by Dr. R. Asiaie in Professor P. K. Dutta's group in the Department of Chemistry. Only a brief description is given here. For more detailed information about the synthesis method, one can refer to Dr. R. Asiaie's Dissertation [331].

Although the fundamental requirements for the synthesis of BaTiO₃ powders and thin films are the same, there are some modifications of the synthesis going from the powder to the thin film. In the following, the syntheses for BaTiO₃ powders and thin films are described separately.

3.1.1. Hydrothermal synthesis of BaTiO₃ powders

As mentioned in the literature review, hydrothermal synthesis of BaTiO₃ involves chemical reactions of barium and titanium source materials in a very strong basic environment. In order to investigate the various possible effects on

the hydrothermal synthesis, various synthesis temperatures, reaction times, different barium sources and base concentrations were studied in each of the hydrothermal experiments.

I. Synthesis with varying temperature and reaction time

Hydrothermal synthesis was done in two different experimental set-ups, corresponding to two different temperatures. For the experiment performed at 95°C, a Teflon (PTFE) bottle with 125 mL capacity was used as a container for hydrothermal reactions. 0.05 mole of NaOH (J. T. Baker) was first dissolved in 50 mL of degassed and deionized (double-D) water in the Teflon bottle. After cooling the solution to room temperature, 0.0125 mole of BaCl₂ (99.999%, Johnson Matthey) and anatase TiO₂ (99.999%, Johnson Matthey) were added into the solution. N₂ (99.999%) was purged through the solution before the Teflon bottle was capped to prevent CO₂ dissolved in the solution, which would have been responsible for the formation of the BaCO₃ phase during synthesis. The solution was shaken vigorously before being placed in an oven at 95°C. The precipitate was taken out after 48 hours and washed with hot deionized water. After washing, the precipitate was dried at 95°C for 1 hour.

For the hydrothermal synthesis performed at 240°C, an acid digestion bomb (Parr Instrument Co.) with a 23 mL capacity was used as the hydrothermal reactor. 0.003 mole of hydrated TiO₂, which was prepared by hydrolyzing

titanium (IV) isopropoxide (99.999%, Johnson Matthey) with 1 M HCl (J. T. Baker) and washing the precipitate intensively with deionized water, was added with 0.005 mole of BaCl_2 into the digestion bomb. 10 mL double-D water was then added to dissolve the mixture. N_2 (99.999%) was again purged through the solution before and during the addition of 0.01 mole of NaOH. This gives a concentration of NaOH of 1M. Right after the NaOH addition, the bomb was sealed and placed in the oven preset at 240°C for a period of time. The time was controlled from 1 week up to 8 weeks. The precipitate was then removed and extensively washed with the double-D water to get rid of any absorbed anion species. X-ray fluorescent analysis was done once on the recovered BaTiO_3 from the BaCl_2 source to make sure no trace of Cl^- was left and this washing procedure was then followed by the following hydrothermal experiments.

II. Synthesis with different barium sources

In this set of experiments, various barium sources were used, including $\text{Ba}(\text{OH})_2$ (99%), $\text{Ba}(\text{C}_2\text{H}_3\text{O}_2)_2$ (99.999%) and BaF_2 (99.999%) from Aldrich Chemical Company, Inc.; $\text{Ba}(\text{NO}_3)_2$, BaCl_2 , BaBr_2 and BaI_2 from Johnson Matthey Company, Inc. Hydrated TiO_2 from hydrolyzing titanium (IV) isopropoxide was again used as the titanium source. The procedure followed was the same as the one described above at the synthesis temperature of 240°C . The time was fixed for 7 days.

III. Hydrothermal synthesis with different NaOH concentrations

The NaOH concentration was also adjusted in the hydrothermal experiments to study its effect on particle sizes and properties. By using the same barium (BaCl_2) and titanium (hydrated TiO_2) sources as mentioned above, three different sized powders were produced by varying the OH^- concentrations for the synthesis carried out at 240°C . The first two powders, which are labeled powder A and B, used 0.003 mole and 0.005 mole of NaOH respectively with 10 mL double-D water. These powders were heated for a period of one week. The last powder (labeled powder C) was prepared by modifying the powder A synthesis procedure by adding 0.003 mole of NaOH to the mixture after one week of synthesis and continued hydrothermal reactions for another week. The purpose of adding NaOH in the middle of the synthesis is to maintain the amount of OH^- in the solution. Normally the constant pH can be accomplished by providing a buffer solution, which is difficult to carry out at such high pH's (≥ 13). Here the term "buffered" 0.5 M NaOH is used to refer this procedure.

3.1.2. Hydrothermal synthesis of BaTiO_3 thin films

I. Substrate preparation

Titanium foil (99.99+%, Johnson Matthey) with a thickness of 0.25 mm was chosen as the substrate material for BaTiO_3 thin film synthesis. Square shaped plates with dimensions of $3 \times 3 \text{ cm}^2$ were cut from the Ti metal. The

plates were finely polished for 8 hours to achieve a mirror-like surface using a vibratory polishing machine with 0.05 μm alumina polishing agent. They were subsequently cleaned ultrasonically in acetone for 3 hours and etched in 6 M HCl (J. T. Baker) for 12 hours to activate the surface. The plates were then oxidized in a calcination chamber at 500°C under flowing oxygen for 12 hours in order to form a titanium oxide layer, which is essential for BaTiO_3 formation. The plates were finally washed with double-D water and placed in the Teflon bomb.

II. Thin film synthesis

The synthesis procedure for BaTiO_3 powders at 240°C was adopted and modified for thin film formation. The oxidized Ti plates described above were used as the titanium source and BaCl_2 (99.999%, Johnson Matthey) was used as the barium source. In the experiments, 0.005 mole of BaCl_2 was added in the Teflon bomb with 10 mL boiled water. Then nitrogen gas was purged through the solution before the addition of 10 moles NaOH. The bomb was immediately sealed and placed in the oven at 240°C for 1 to 4 weeks.

3.2. Characterization of BaTiO_3 Powders

3.2.1. Powder X-ray Diffraction (XRD)

Powder X-ray diffraction was done using an X-ray diffractometer (PAD-V, Scintag). The XRD patterns were collected using CuK_α radiation (1.5405Å) at a

voltage and current of 45 kV and 20 mA, respectively. A single crystal of Si (Scintag Inc.) with low background noise and no diffraction peaks in the applied diffraction range was used as the sample holder. The sample for XRD was prepared by placing a small amount of the powder on the sample holder and using ethanol to disperse it. After the evaporation of ethanol, a thin layer of powder was formed and adhered well to the sample holder.

For structure and phase purity determinations, the experiments were done in a continuous scan mode between $20 \sim 100^\circ$ (2θ) at a rate of $1^\circ/\text{min}$. Sometimes continuous scans were also done between $44 \sim 46^\circ$ at a lower rate of $0.1^\circ/\text{min}$ to study the peak splitting of BaTiO_3 crystals with a tetragonal structure.

For lattice parameter and line broadening experiments, continuous scans between $20 \sim 100^\circ$ (2θ) at a rate of $0.2^\circ/\text{min}$ were used. Si powder (99.999%, Johnson Matthey) was used as the internal standard to correct for line position, which is essential for accurate lattice parameter determination. In the line broadening measurement, LaB_6 (99.95%, Johnson Matthey) was used as the external standard to correct for instrumental broadening. Prior to use, the LaB_6 was annealed to 800°C in Ar for 5 hours to eliminate any residual strains.

The lattice refinement method (DMS-2000 software) was used to compute the lattice parameters. From the broadening, crystal sizes and lattice strains were calculated using the Hall-Williamson or Gaussian squared method

assuming a Gaussian-Gaussian profile. The peaks were first deconvoluted and the full widths at half maximum of the peaks (FWHM) were calculated by profile fitting. Assuming a Gaussian peak profile, the Hall-Williamson method uses a square relationship written as [332-333]:

$$(\beta_{1/2} \cos \theta / \lambda)^2 = (0.89 / d)^2 + \varepsilon^2 (4 \sin \theta / \lambda)^2 \quad (3.2)$$

where $\beta_{1/2}$ is the true breadth of diffraction line at half-maximum intensity using Warren's method for instrumental correction [334-336], d is the crystal size and ε is the elastic strain. When $(\beta_{1/2} \cos \theta / \lambda)^2$ was plotted vs. $(4 \sin \theta / \lambda)^2$ for different diffraction planes, a linear fit was obtained. From the slope and intercept of the line, lattice strains and crystal sizes were calculated.

3.2.2. Elemental Analysis

I. X-ray fluorescence spectroscopy [337]

Chloride (Cl^-) and strontium (Sr^{2+}) ion impurities were examined by X-ray fluorescence spectroscopy (XRF) for the synthesized BaTiO_3 powders. The experiment was performed using an energy dispersive XRF instrument (Kevex 0700/7000) with a Rh anode in the X-ray tube. The X-ray fluorescence was detected using a lithium-drifted silicon detector and was analyzed by a multichannel analyzer. Ge was used as the secondary target at 45 keV and 0.02 mA for Cl^- detection, while the target Ag was used at 37 keV and 0.5 mA for Sr^{2+} detection. The samples for the XRF analysis were prepared by mixing 70%

BaTiO₃ powder with 30% C₁₉H₃₈ON binder (Spectroblend, Chemplex Industrial Inc.).

II. Inductively coupled plasma-atomic emission spectroscopy (ICP-AES)

A. Decomposition of BaTiO₃ sample with HCl under pressure

0.5 gram of BaTiO₃ powder was weighted and added to 5 mL concentrated HCl solution (\approx 12M) in a Teflon-lined digestion bomb. After the bomb was sealed, the solution was heated at 160°C for 14 hours under high vapor pressure. The solution was then cooled down to room temperature and transferred to a volumetric flask, where it was diluted to 25 mL. High-purity HCl and distilled-deionized water ($>18\text{M}\Omega$) were used for sample preparation.

B. Standards preparation and calibration [338]

BaCl₂·2H₂O (99.999%, Johnson Matthey) and Ti metal (99.7%, Johnson Matthey) were used as the barium and titanium standards for ICP analysis. Dissolution of Ti metal in concentrated HCl was promoted by mild heating at 150°C for approximately 8 hours. Assuming that 0.05g BaTiO₃ sample is 100% pure and with a Ba/Ti ratio of 1, the amounts of Ba and Ti in the powder are both 2.14×10^{-4} mole. However, if the powder is not pure or the Ba/Ti ratio is different from 1, the amounts will deviate from 2.14×10^{-4} moles correspondingly. In order

to cover the entire range of concentrations, Ba and Ti standards each with three different concentrations ($1, 2, 3 \times 10^{-4}$ moles) were made.

The calibration curves for the amounts of Ba and Ti were constructed using a blank ($\approx 2.4\text{M HCl}$) and three standard solutions for Ba and Ti, respectively. The atomic emission spectra of Ba and Ti were taken three times for each BaTiO_3 sample, from which the concentrations of Ba and Ti can be calculated according to three emission lines (Ba: 230, 233 and 413 nm; Ti: 334, 336 and 368 nm). The final concentrations are the mean values calculated and the standard deviations are the root mean square values of two error sources coming from different measurements and using different emission lines.

C. Instrumentation

A sequential spectrometer with Ar plasma source (PE Optima 3000XL, Perkin-Elmer) was used. The instrument is equipped with a vertical torch for plasma generation and a cross flow nebulizer for sample introduction to the spray chamber. Detection was done using a modified CID (charge injection detector). A high order monochromator was used, by which ultraviolet (UV) and visible can be detected separately.

The operating conditions for the measurements are described in Table 3.1.

Table 3.1. Operating conditions for ICP-AES measurement

Power	1100 W
Primary flow rate	15 L/min
Auxiliary flow rate	1 L/min
Nebulizer flow rate	1 L/min
Fluid uptake rate	1 mL/min

3.2.3. Thermal Analysis

I. Differential scanning calorimetry (DSC)

Differential scanning calorimetry (DSC) was used to determine the enthalpy change associated with the Curie transition (ΔH) [331]. The experiments were performed with a differential scanning calorimeter (DSC 910S, TA Instruments). The data were acquired and processed with TA Instruments 9900 Computer/Thermal Analyzer. Sample weights of approximately 20 mg were used in crimped aluminum pans. DSC signals were measured against a crimped reference aluminum pan filled with 10 mg alumina. The alumina content of the reference pan was used to adjust the baseline. Thermal scans were measured from 50 to 200°C at a heating rate of 20°C/min. Enthalpy values at the transition peak were calculated by integrating the area under the curves. All

the samples were heated once to 200°C before DSC analysis to eliminate any water content and to ensure reversibility.

II. Thermogravimetry and differential thermal analysis (TG/DTA)

A thermal analysis system (SSC5200, Seiko) with TG/DTA module (320, Seiko) was used for the thermogravimetric experiments [331]. Approximately 20 mg of the powder was used in a platinum pan under 100 mL/min of air. Measurements were obtained from 20 to 1050°C at a heating rate of 10°C/min.

3.2.4. Electron Microscopy

I. Scanning electron microscopy (SEM)

The microstructure and morphology of the BaTiO₃ powders were examined using a scanning electron microscope (Hitachi S-4000) with a field emission gun. An accelerating voltage of 5 keV was used. Powder samples for SEM were prepared by diluting a small amount of the powders in ethanol and dispersing them ultrasonically. A drop of suspension was subsequently placed onto an aluminum stub and dried at 120°C for 30 minutes. Before the SEM analysis, a gold layer was sputter-coated onto the sample for electron conduction. The images of the particles were obtained and the average particle sizes were calculated as the mean values of measured diagonals of about 30 particles.

II. Transmission electron microscopy (TEM) and convergent electron beam diffraction (CBD)

Lattice images and convergent beam diffraction patterns of various sized hydrothermal BaTiO₃ particles were obtained using an Hitachi high resolution electron microscope (H-9000 NAR) with 1.8 Å resolution. The microscope was operated at a voltage of 300 kV. A small amount of the powder was first suspended with isopropyl alcohol in a 3.5 mL vial and allowed to settle for 24 hours. Then a drop of the supernatant solution was placed onto the carbon grid. The specimen was baked in an oven for several hours before study to minimize contamination.

3.2.5. Vibrational Spectroscopy

I. Infrared (IR) spectroscopy

The infrared spectra were obtained [331] on an FT-IR instrument (Mattson Cygnus) with a MCT detector. Samples of 2% synthesized powders were diluted in KBr and the mixtures were pressed into pellets and placed in an air-tight cell with NaCl windows. The IR pellets were heated at 110°C under vacuum (10^{-4} torr) for 3 hours to evaporate any surface absorbed water. Transfer of samples from the vacuum tube to the IR cell was done in a glove bag under nitrogen atmosphere.

II. Raman spectroscopy

Raman spectra were obtained [331] using a Spectra-Physics Model 171 argon ion laser as the excitation source. For all samples, the 514.5 nm line at an initial power of 800 mW and slit widths of 150-300 nm were used. A Spex 1403 double monochromator and a RCA C131034 GaAs photon counting photomultiplier tube were used to filter and detect the scattered light. The temperature controlled Raman experiments were performed with an in-house Raman cell made from a MACOR jacket, copper tube heating element, and quartz window. The cell is capable of temperatures ranging from 150 to 200°C.

3.3. Sintering of BaTiO₃ Powders

Hydrothermally synthesized BaTiO₃ powders were compacted and sintered at various conditions. For comparison, two kinds of commercial BaTiO₃ powders: TAM HPB (TAM Ceramics, Niagara Falls, NY) and Ferro (Transelco Ferro Corp., Penn Yan, NY), were sintered together with the hydrothermal powders.

3.3.1. Powder Compaction

Prior to sintering, the synthesized powders were pressed uniaxially into a disc 7.06 mm in diameter and approximately 2 mm in thickness. The pressure during pressing was calculated to be approximately 173 MPa. No binders and

additives were used for purity considerations. The pressed powder discs were dried at 120°C in the oven for 5 hours before sintering.

3.3.2. Dilatometry measurement

Dilatometry describes a continuous measurement of the length of a sample as it is subjected to a controlled linear heating rate. It gives information including the shrinkage of the sample and, more importantly, the onset and completion of the sintering cycle. The percent linear shrinkage is given as [190]:

$$s = (L_t - L_0) / L_0 \times 100\% \quad (3.1)$$

where L_0 is the initial sample length and L_t the length after a time t . The dilatometry measurements were performed on various synthesized powders using a high temperature dilatometer (1600D, Orton Ceramic Foundation). The measurements were performed at a rate of 5°C/min for both the heating and cooling runs. Shrinkage information was acquired and analyzed using a computer with commercial software provided by Orton.

3.3.3. Sintering of Powders under Different Conditions

I. Conventional sintering

Conventional sintering of the pressed powder discs was done using a high temperature box furnace (1700°C, Lindberg) with an integral temperature controller. The sintering was done in air in a temperature range of 1200 to

1350°C. The dwell time was controlled from 2 to 5 hours. The heating and cooling rates were maintained at 5°C/min for all the runs.

II. Fast sintering with very high sintering rate (~ 200°C/min)

Fast sintering of the hydrothermally synthesized cubic BaTiO₃ powders was performed under various sintering temperatures and sintering times. A high purity alumina rod (99.99%) was used as a sample holder. Its front end was cut flat and samples were placed on the flat surface of the rod. The samples were then covered by another piece of alumina and the assembly was gently tightened by platinum wires. Two pieces of platinum foil were placed between the samples and alumina surfaces to avoid possible high temperature reactions. A high temperature tube furnace (1800°C, CM Inc.) was used for the sintering. The thermal gradient in the tube of the furnace from the outer low temperature zone toward the central hot zone of the tube was measured for each sintering temperature, and calibration curves of temperature versus position in the tube were constructed accordingly. For fast sintering experiments, the sample assembly was pushed into the center hot zone from the outer low temperature zone within a controlled period of time, which resulted in an estimated heating rate of about 200°C/min. After a short dwell time, the furnace was shut down to cool the assembly before taking it out of the tube.

3.4. Characterization for Sintered Ceramic BaTiO₃

3.4.1. Bulk Density Measurement by Archimedes Method

The Archimedes method was used to measure the density of the sintered BaTiO₃ samples. The Archimedes principle describes the density of solids based on buoyancy of the solids in a certain fluid. According to the principle, the apparent density of the sample (considering only closed porosity) can be calculated as following:

$$\text{Apparent Density}(\rho) = \frac{W_d}{W_d - W_l} \times \rho_{liquid} \quad (3.2)$$

where W_d is the sample's dry weight measured in air, W_l is the sample weight measured in a liquid and ρ_{liquid} is the density of the liquid.

In the measurements, the sample was first cleaned in isopropyl alcohol and dried in an oven at 120°C for 30 minutes. The dry weight (W_d) was then measured in the ambient air using an electronic balance (AE 163, Mettler). The sample was subsequently submerged in isopropyl alcohol for 15 minutes with extensive stirring in order to fill the open pores completely with the liquid. The saturated sample was then suspended in isopropyl alcohol by a wire basket and the weight in the liquid (W_l) was measured. The apparent density for each sample was calculated according to equation 3.2.

3.4.2. Scanning Electron Microscopy (SEM) of Sintered BaTiO₃

For the SEM experiments on sintered ceramic samples, the samples were first ground and roughly polished using diamond paste to 1 μm finish. Then the samples were fine polished using a vibratory polishing machine with 0.05 μm alumina polishing agent for 12 hours. After polishing, the samples were thermally etched at 1200°C for 1 hour followed by ultrasonically cleaning in acetone. A gold layer was sputter coated on the samples for conducting purposes. SEM was done in the same Hitachi S-4000 machine using an accelerating voltage of 5 keV. The grain sizes of the sintered specimen were calculated according to the SEM images as an average of about 30 grains using a linear interception method.

3.4.3. Dielectric Property Measurement

I. Dielectric constant and loss measurement as a function of temperature

The dielectric properties of the sintered samples were studied as a function of temperatures using an LCR meter (HP 4263A) with 50 mV signal level at a frequency of 1 kHz. The samples were first surface polished using #1000 grinding papers. Electrodes were made by applying silver paste and fired at 700°C for 1 hour. Prior to applying the electrodes, the thickness and the diameter of the samples were measured. Two tiny silver foils (5 mm in diameter) were then spring clamped to the sample by an alligator clip (with thin sheets of

alumina placed in between the sample and the clip for insulating) to form ohmic contacts, with two lead wires attached to the LCR meter. The temperatures of the samples were controlled from room temperature to 500°C with 0.5°C accuracy by a temperature controller (Orton Model 29). The samples were first heated to 250°C and kept at that temperature for 30 minutes to remove any surface-adsorbed water. The measurements were done during the cooling cycle in the ambient environment with a rate of 1°C/min.

II. Impedance spectroscopy analysis

The impedance data were obtained using an impedance analyzer (HP4192A) in an experimental set-up as mentioned above. A signal level of 100 mV was used. The parallel capacitance (C_p) and conductance (G_p) were recorded over the frequency range from 5 Hz to 13 MHz. The analyzer was interfaced with a computer (PC/XT, IBM) through an HP-IB interface card. Both data acquisition and data analysis were done using computer programs developed in our laboratory. Unlike most commercial software, this program is capable of extracting all the necessary parameters without assuming or simulating any equivalent circuit configuration *a priori*.

Some scatter in the data was observed at low frequencies (< 100 Hz) or with AC power on for heating. Thus longer time intervals were allowed for equilibration at low frequencies and DC heating was used. In order to obtain the

maximum information, four complex plane (impedance, admittance, capacitance and modulus) analyses were done and the desired electrical parameters were thus extracted.

3.5. BaTiO₃ Thin Film Characterization

3.5.1. Room-Temperature and Hot-stage X-ray Diffraction

Room-temperature X-ray diffraction for hydrothermally synthesized BaTiO₃ thin films was performed using the Scintag powder X-ray diffractometer (PAD-V). The operation conditions and procedures were similar to those used for the powder XRD experiments (45 kV and 20 mA). The films with the Ti metal substrates were directly placed on the diffraction machine without any kind of sample holder. The thin film samples were cleaned with acetone and dried in air prior to the diffraction experiments.

X-ray diffraction at various temperatures was done using a hot-stage X-ray diffractometer (HT-PAD, Scintag). The samples rested on a platinum strip. By controlling the current through the platinum metal, the temperatures could be controlled from room temperature to 1300°C. To study the evolution of the cubic structure from the tetragonal, the experiments were done at 30, 50, 80, 120, 150 and 200°C from 44 to 46° (2θ) at a rate of 0.1°/min.

3.5.2. Scanning electron microscopy and energy dispersive analysis (SEM/EDS)

Strips of the synthesized films were cut from the samples and sputter-coated with gold. Scanning electron microscopy was done on the strips using an SEM instrument (SL-30, Phillips) with an EDS detector. An accelerating voltage of 20 keV was used. Elementary analysis was done using the energy dispersive spectroscopy system with the SEM instrument.

3.5.3. Electrical Properties of Thin Films

The electrical properties of the synthesized films were studied both as a function of temperature and frequency using an impedance analyzer (HP4192A) with an ac signal of 100 mV. Prior to the measurement, gold dots of 1 mm² in area were vacuum-evaporated onto the films to form top electrodes. The titanium substrate acted as the counter electrode. The films were then placed on the platinum coated surface of a hot chuck, which controlled the sample temperature from room temperature to 300°C with an accuracy of 0.1°C. The measurement was performed with the help of a probe station (MC System) using two probes to form ohmic contacts with the sample with a metal-insulator-metal (MIM) configuration. For the measurement as a function of temperature, two fixed frequencies of 1 kHz and 100 kHz were used. Only one time the sample was measured during the heating cycle to examine the humidity effect on the electrical properties. For all subsequent measurements, the samples were first

heated up to 220°C and kept at that temperature for 30 minutes to remove any surface-adsorbed water. The measurements were taken during the cooling cycle in the ambient environment with a rate of 1°C/min.

CHAPTER IV

RESULTS

4.1. Characterization of BaTiO₃ Powders

BaTiO₃ powders with different characteristics were synthesized using the hydrothermal synthesis under various synthesis conditions. The produced powders were extensively studied using various characterization techniques. In the following, the results of these experiments are presented.

4.1.1. Method for Quantitative Determination of Tetragonal BaTiO₃

Since one of the objectives of this research was to produce tetragonal BaTiO₃ powders, it was necessary to establish a method which can be used to quantitatively determine the tetragonality of the produced powders. The typical way of distinguishing tetragonal structure of BaTiO₃ from the cubic is by X-ray diffraction (XRD). Figure 4.1 shows the diffraction patterns of BaTiO₃ powders with tetragonal and cubic structure, respectively. The tetragonal powder was synthesized at 240°C for a week and annealed at 1300°C for 5 hours, while the cubic powder was synthesized at 95°C for 48 hours. The insets in Figure 4.1

highlight the characteristic reflections of (200) type planes of BaTiO₃ crystals with 2θ ranging from 44 to 46°. The splitting into two peaks around 44-46° for tetragonal BaTiO₃ is due to the separation of reflections of (200) + (020) and (002), whereas there is only a single peak for cubic BaTiO₃ due to the equal unit cell dimensions along 3 crystal axes.

Although the diffraction method can be used to differentiate the cubic from tetragonal structure, quantitative determination of the tetragonal content or tetragonality of the powders is not possible. This is because of the line-broadening effect associated with small particles, which makes the peak splitting ambiguous, and the insensitive nature of the diffraction method, particularly when the concentration of a phase is low (< 5 wt%). Dielectric measurement is another way to distinguish these two polymorphic forms; however, difficulty in achieving high density for the powders to minimize the contributions from trapped air in pores makes the measurement unrealistic.

In this study, differential scanning calorimetry (DSC) was found to be a practical method to quantitatively determine the tetragonal phase. It is known that the Curie transition occurring at about 130°C gives rise to an enthalpy change (ΔH) which can be measured by DSC. Figure 4.2 shows the DSC results of the tetragonal and the cubic BaTiO₃ samples used in the XRD measurement shown in Figure 4.1. There is a clear endothermic peak around 125°C corresponding to the tetragonal to cubic phase transition for the tetragonal

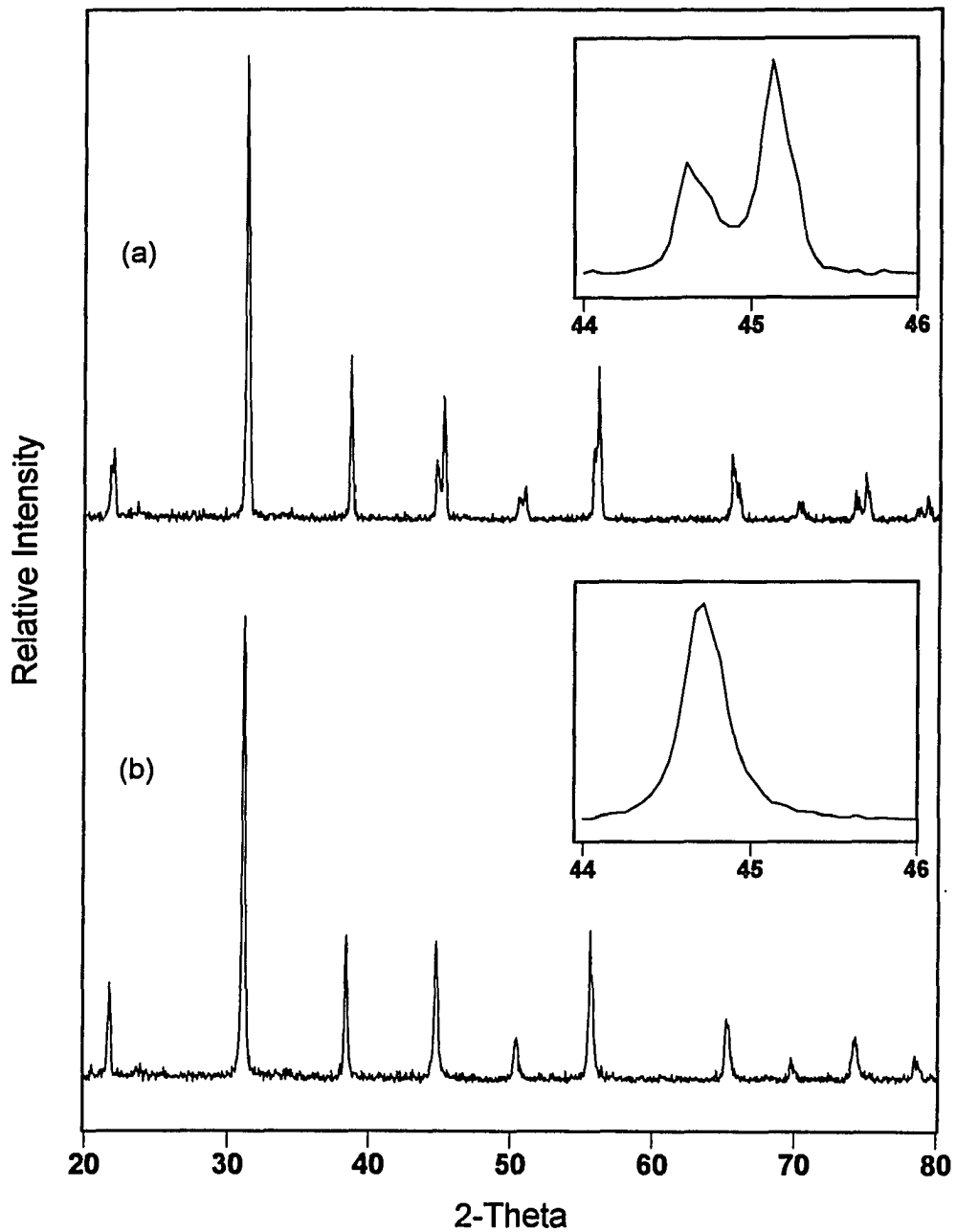


Figure 4.1. X-ray diffraction patterns of the BaTiO_3 powders with (a) tetragonal and (b) cubic structure, respectively. The insets highlight the characteristic reflections of $\{200\}$ planes of BaTiO_3 crystals with 2θ ranging from 44 to 46°.

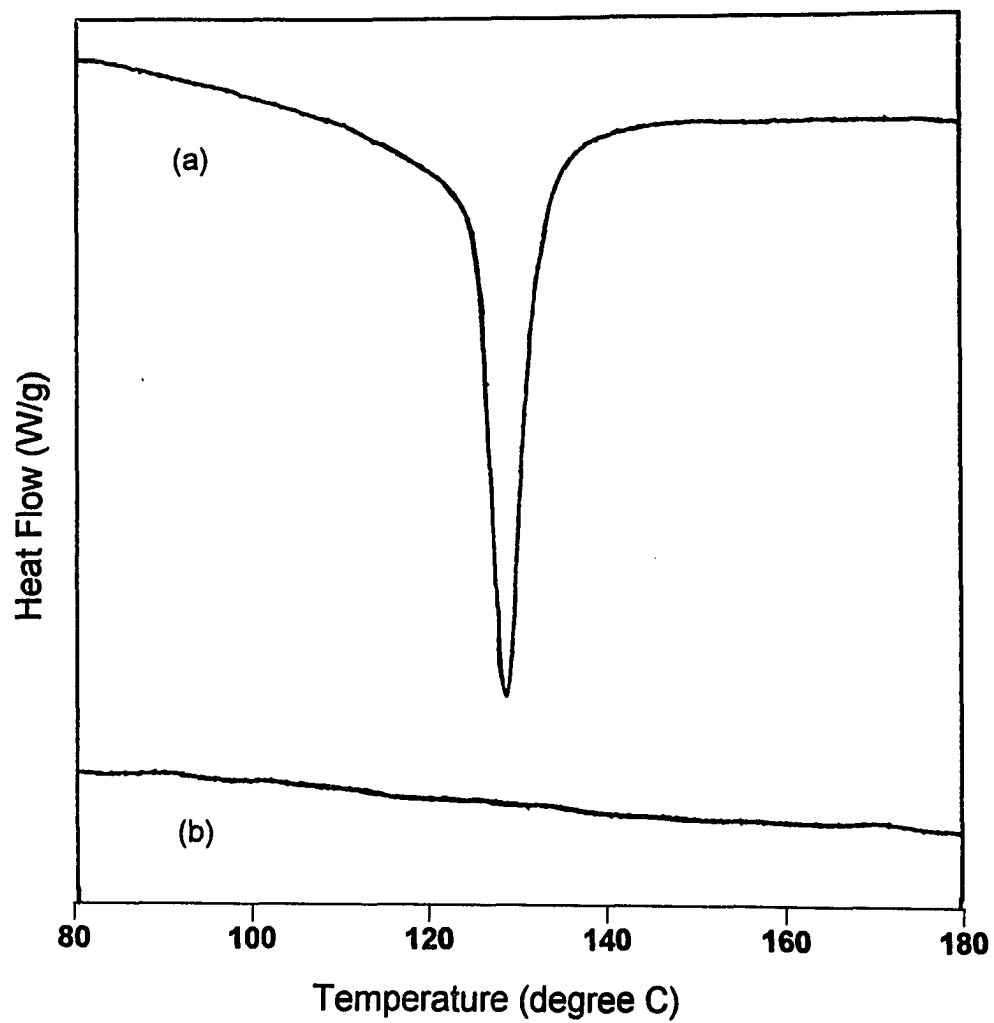


Figure 4.2. DSC patterns of the (a) tetragonal and (b) cubic BaTiO_3 samples which were also used in XRD measurement as in Figure 4.1.

sample, whereas the cubic sample shows no apparent transition. The ΔH value associated with the transition for the tetragonal sample is 0.9 J/g.

An effort was made to roughly correlate the tetragonal contribution or tetragonality of the BaTiO₃ powders to the measured ΔH associated with the transition. Assuming that the sample annealed at 1300°C for 5 hours is 100% tetragonal, while the cubic sample synthesized at 95°C has zero percent tetragonality, a calibration curve was constructed by physically mixing various amounts of 100% tetragonal sample with the cubic sample (Figure 4.3). It shows a good linear correlation between ΔH and percent tetragonality. According to the calibration curve, the tetragonality of each powder can be evaluated by measuring ΔH associated with the Curie transition.

4.1.2. BaTiO₃ Powders Synthesized by Varying Reaction Temperatures and Times

BaTiO₃ powders were synthesized at two temperatures, 95°C and 240°C. Well crystallized powder was obtained at 95°C for 48 hours which is of the cubic form determined by XRD and DSC mentioned earlier. Powders synthesized at 240°C for various synthesis time were tetragonal according to both XRD and DSC. Detailed characterization results are presented below.

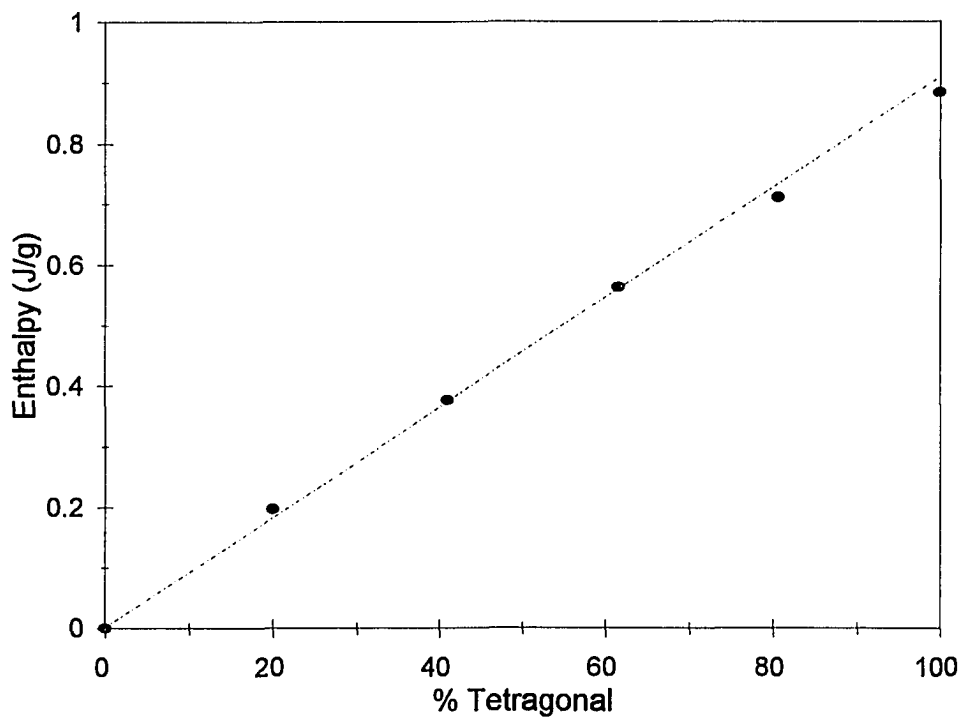


Figure 4.3. The calibration curve of ΔH as a function of tetragonal content obtained by physically mixing various amounts of 100% (annealed) tetragonal sample with the cubic sample.

I. BaTiO₃ powder synthesized at 95°C

As shown in the X-ray diffraction spectra (Figure 4.1), there is no apparent peak splitting at 2θ of 45° for the BaTiO₃ powder synthesized at 95°C. In addition, there is no evidence of the Curie transition around 130°C (Figure 4.2). So the powder is concluded to be in a cubic-like structure. The SEM micrograph of the powder is shown in Figure 4.4. The particles are agglomerated to some degree and the average size was calculated to be approximately 0.1 μm . Since the cubic-form BaTiO₃ powder synthesized hydrothermally has been well studied by other investigators [88-89, 92, 184-185] and it is not the principal interest in this research, further characterization of the cubic BaTiO₃ powder was not attempted.

II. BaTiO₃ powders synthesized at 240°C for various times

The microstructure and properties of BaTiO₃ powders were studied as a function of the reaction time. Figures 4.5 and 4.6 show the SEM micrographs of powders synthesized for 3 and 7 days, 3 and 8 weeks, respectively. The very long synthesis time (up to 8 weeks) is not practical for real industrial production, but it is important for study of underlying synthesis mechanism. Figure 4.7 shows the XRD patterns of the powders. The sharp diffraction peaks with relatively high intensity indicate that the powders produced hydrothermally have good crystallinity. It is noticed that a peak at $\sim 24^\circ$ is present in the diffraction

patterns in the early synthesis (< 7 days), which corresponds to the second phase BaCO₃. As the synthesis proceeds, the peak disappears. The intermediate carbonate may be caused by the residual CO₂ trapped in the reaction solution. Average particle sizes (with standard deviation) were obtained from the SEM micrographs for the powders and are shown in Table 4.1. ΔH was obtained from the DSC measurement which was then converted to percent tetragonality according to the calibration curve (Figure 4.3). The results are shown in Table 4.1 and Figure 4.8.

Table 4.1: Particle size and tetragonality as a function of synthesis time for hydrothermally synthesized BaTiO₃.

Synthesis time	Particle size (μm)	% Tetragonal
1 day		9
3 days		13
5 days		19
6 days		23
1 week	0.23 ± 0.07	37
2 wks	0.26 ± 0.11	68
3 wks	0.31 ± 0.13	69
5 wks	0.34 ± 0.10	76
8 wks	0.52 ± 0.11	99

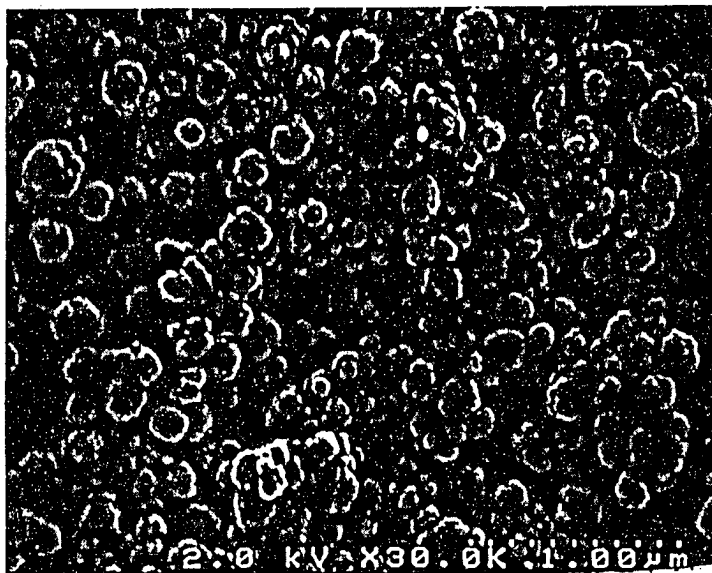
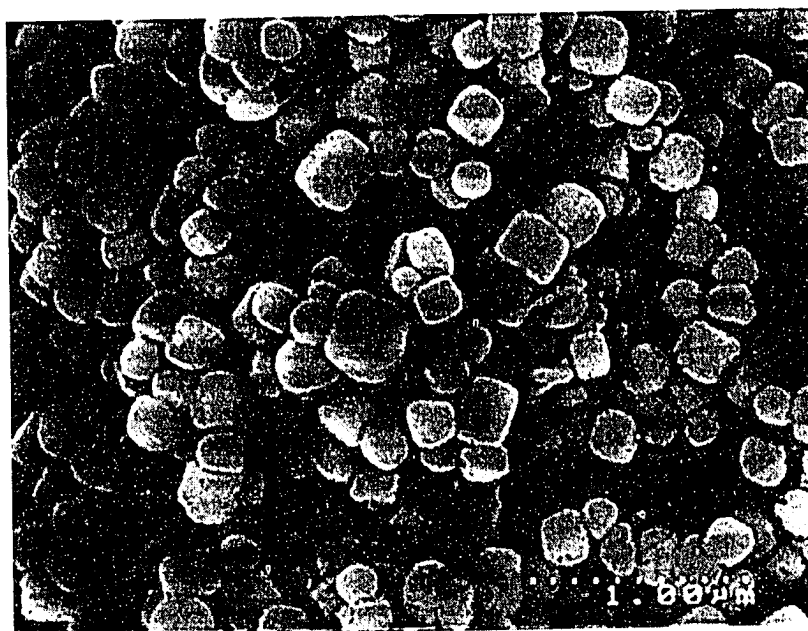
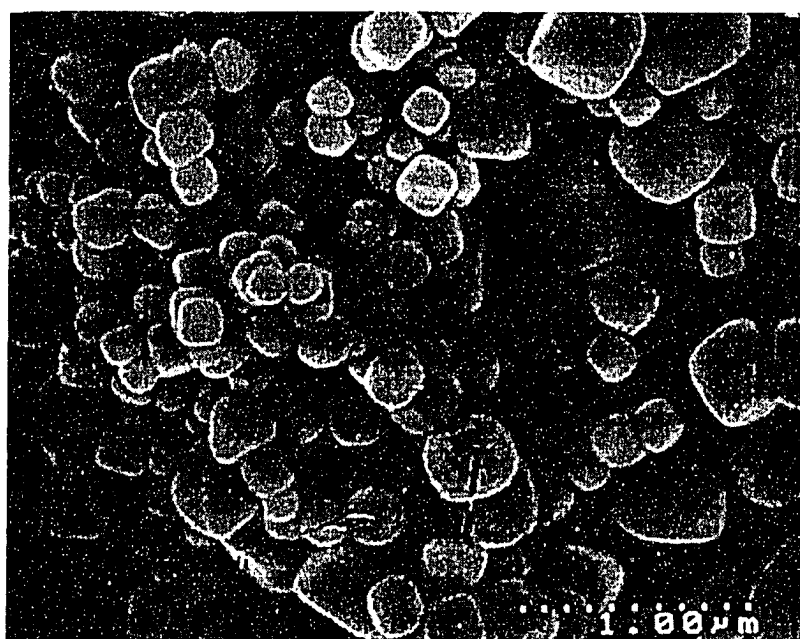


Figure 4.4. The SEM micrograph of BaTiO₃ powders synthesized at 95°C.

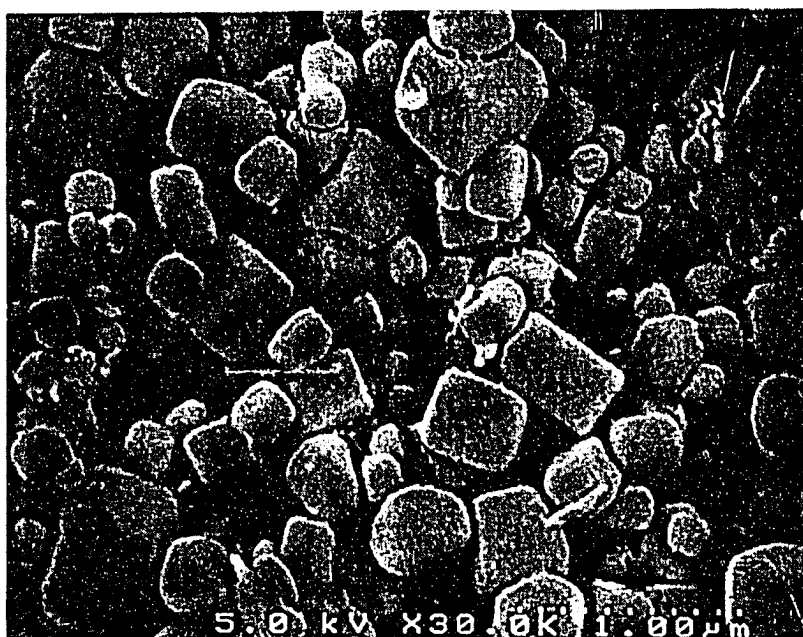


(a)

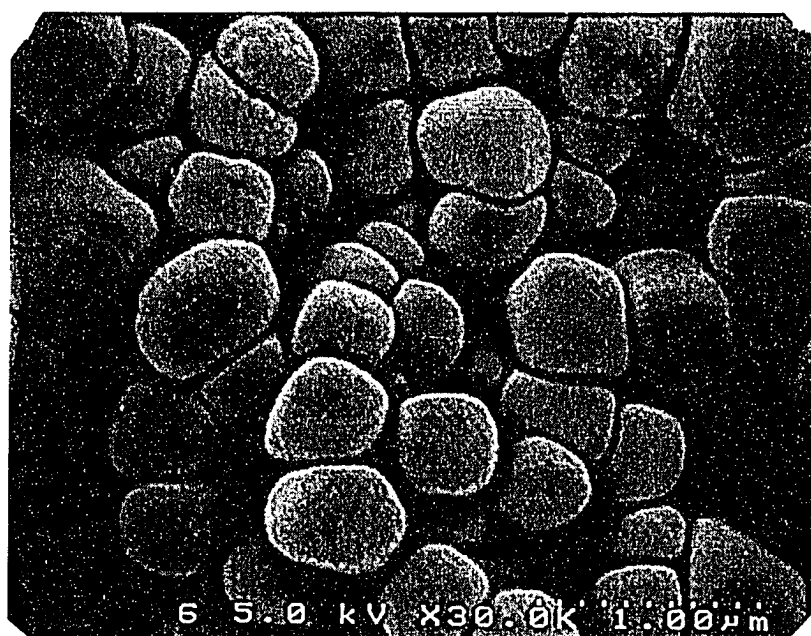


(b)

Figure 4.5. SEM micrographs of the BaTiO_3 powders synthesized for various times: (a) 3 and (b) 7 days.



(a)



(b)

Figure 4.6. SEM micrographs of the BaTiO₃ powders synthesized for various times: (a) 3 and (b) 8 weeks..

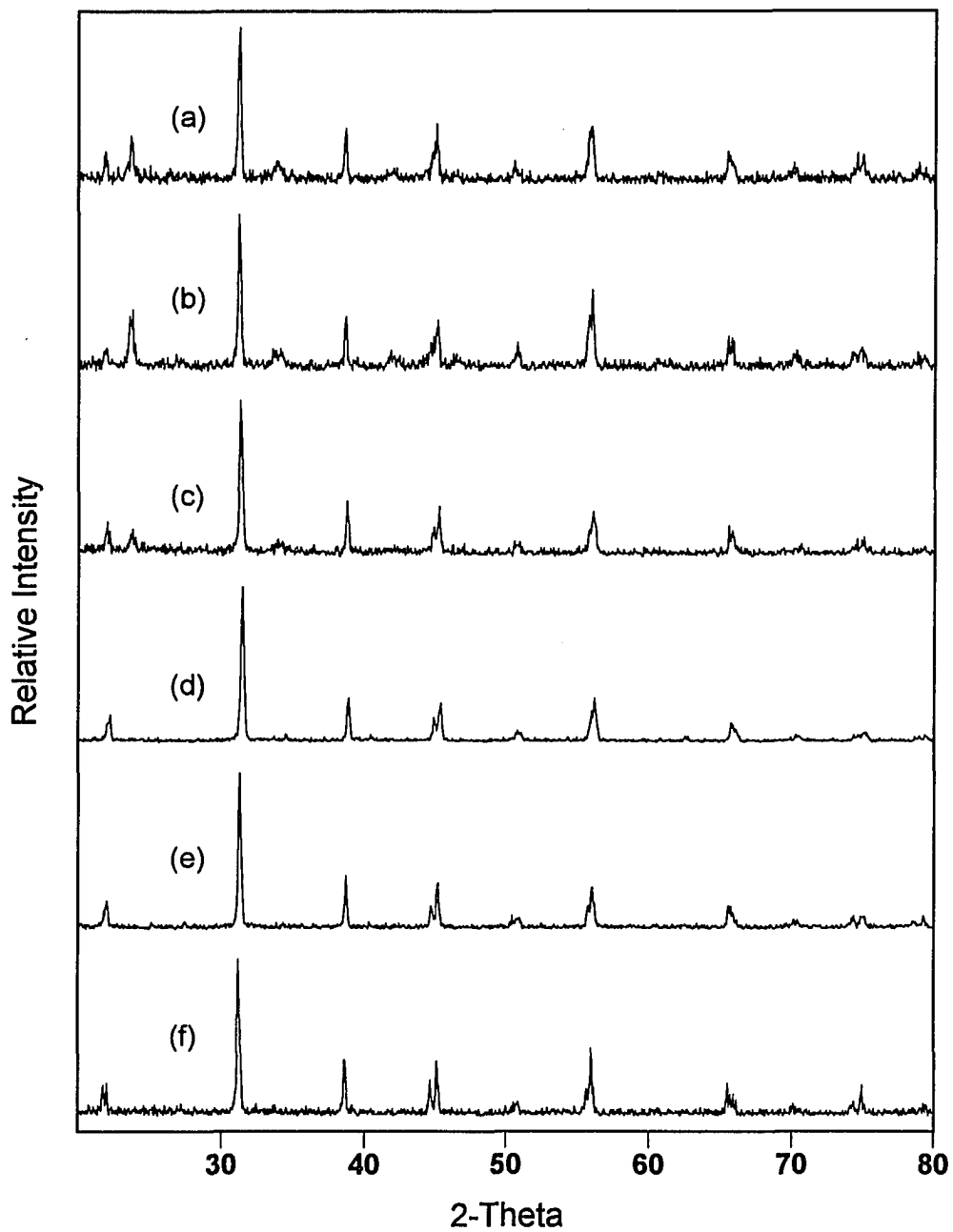


Figure 4.7. Powder XRD patterns of hydrothermally synthesized BaTiO₃ powders as a function of reaction time at 240°C for (a) 1 day; (b) 3 days; (c) 5 days; (d) 7 days; (e) 2 weeks and (f) 8 weeks.

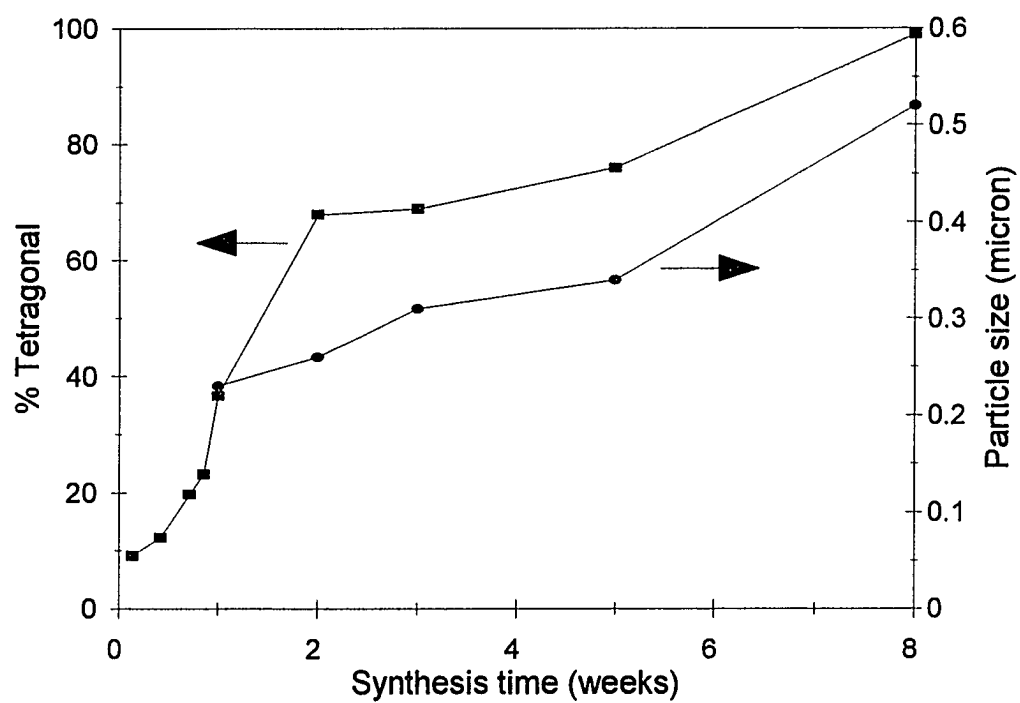


Figure 4.8. Particle size and percent tetragonality of BaTiO_3 powders as a function of synthesis time.

4.1.3. BaTiO₃ Powders Synthesized with Different Barium Sources

To study the effects of various anions on the hydrothermal synthesis and powder properties, barium salts with different anions (I⁻, Br⁻, Cl⁻, C₂H₃O₂⁻, NO₃⁻, and OH⁻) were used as the barium source in the synthesis.

Figure 4.9 shows the XRD patterns of the powders synthesized with different barium salts for one week. All the powders display good crystallinity with no indication of second phases. The powders synthesized with I⁻, Br⁻, Cl⁻, C₂H₃O₂⁻ ions are suggested to be in the tetragonal structure based on the splitting of the (200) peak. More precise determination of the tetragonality of the powders was done by DSC and the results are presented in Table 4.2. The particle sizes of the powders were obtained from SEM micrographs shown in

Table 4.2. Particle size and percent tetragonality of the BaTiO₃ powders synthesized with various barium sources.

Barium source	Particle size	% Tetragonality
BaI ₂	0.37 ± 0.19	39
BaBr ₂	0.31 ± 0.10	38
BaCl ₂	0.23 ± 0.07	37
Ba(C ₂ H ₃ O ₂) ₂	0.19 ± 0.07	23
Ba(NO ₃) ₂	0.17 ± 0.04	8
Ba(OH) ₂	0.15 ± 0.04	0
Commercial BaTiO ₃ (TAM)	0.46 ± 0.18	14

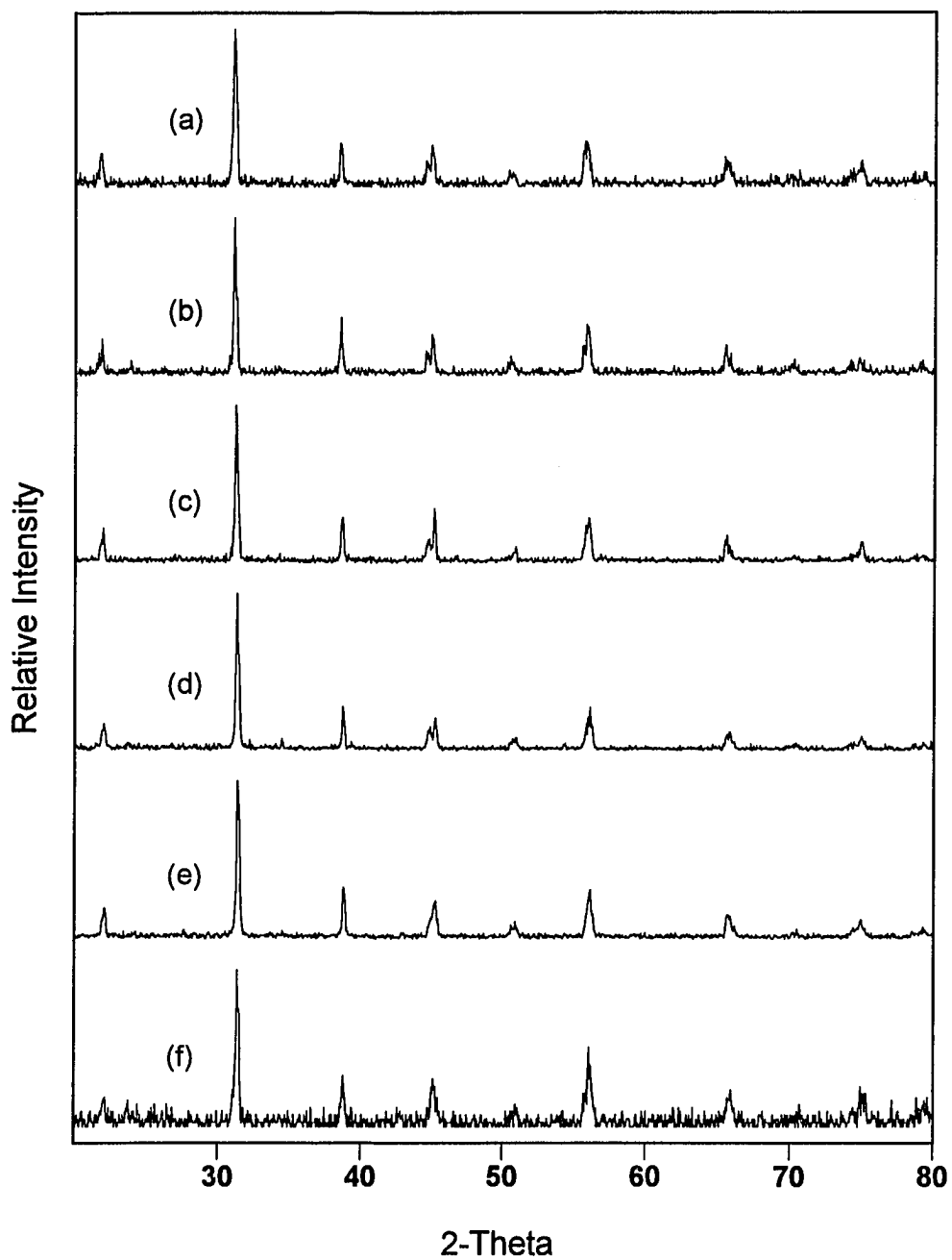
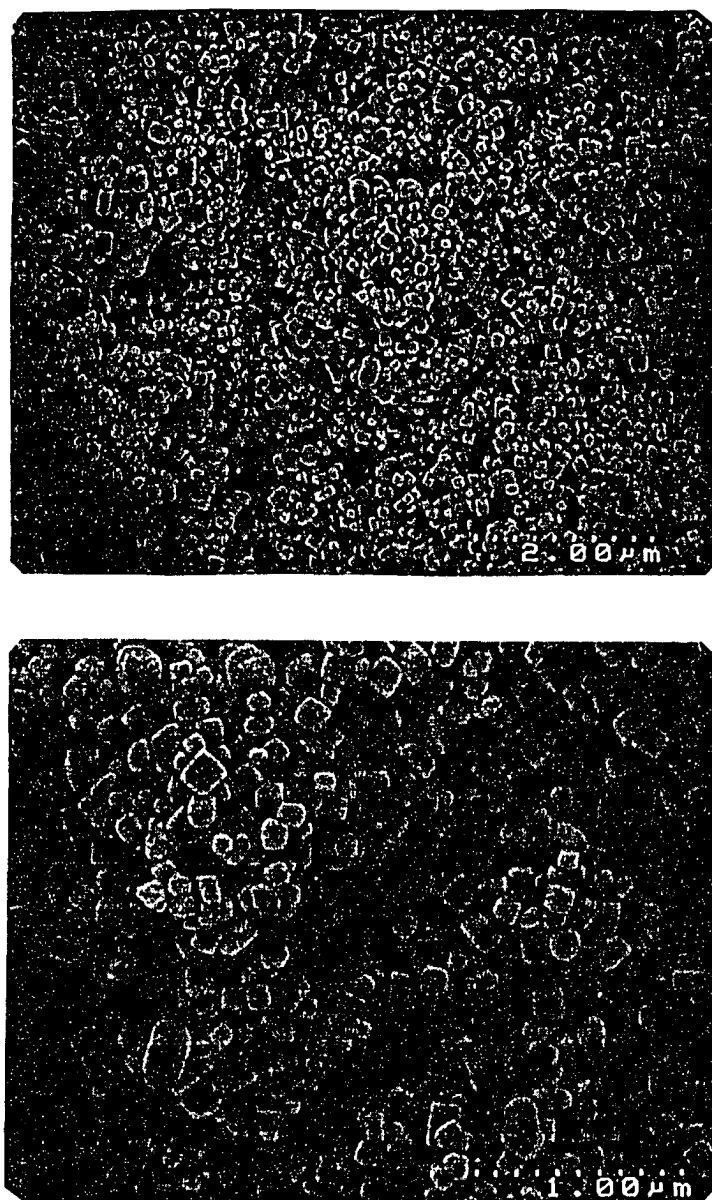


Figure 4.9. XRD patterns for BaTiO₃ powders synthesized hydrothermally at 240°C from various barium sources in one week period.

(a) BaI₂; (b) BaBr₂; (c) BaCl₂; (d) Ba(C₂H₃O₂)₂; (e) Ba(NO₃)₂ and (f) Ba(OH)₂.

Figure 4.10. The BaTiO_3 powder synthesized with BaI_2 shows the largest particle size ($\sim 0.37 \mu\text{m}$) as well as the highest tetragonality ($\sim 39\%$), while the powder synthesized with $\text{Ba}(\text{NO}_3)_2$ gives the smallest size ($\sim 0.15 \mu\text{m}$) and is nearly cubic. A commercial BaTiO_3 powder (TAM HPB) synthesized via coprecipitation is also included in Table 4.2. The average size of the TAM powder is about $0.5 \mu\text{m}$, and it shows a low level of tetragonality ($< 27\%$). The nature of the TAM powder is very different from the hydrothermal powders, since it was synthesized by a coprecipitation method where the powder was subjected to a high temperature calcination ($\sim 1100^\circ\text{C}$) for a complete conversion to BaTiO_3 .

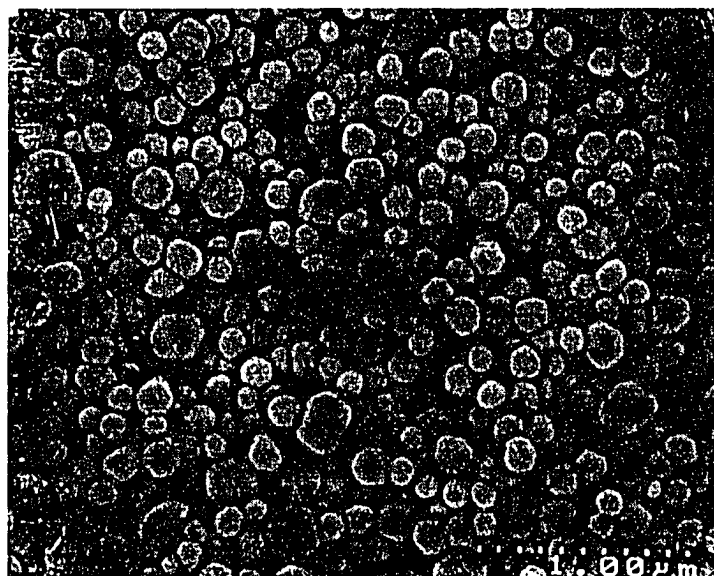
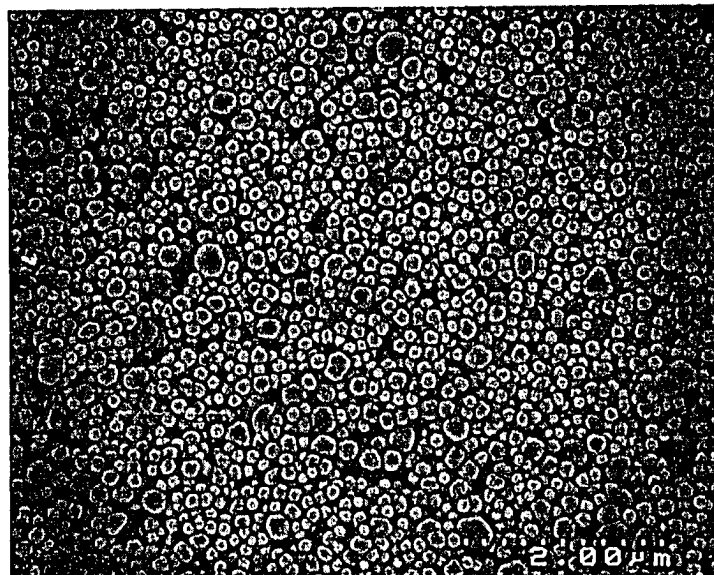
Figure 4.10 shows SEM micrographs of the BaTiO_3 powders synthesized from hydroxide (OH^-), nitrate (NO_3^-), acetate ($\text{C}_2\text{H}_3\text{O}_2^-$), chloride (Cl^-), bromide (Br^-) and iodide (I^-) anions, respectively, together with a commercial powder (TAM HPB). All powders synthesized hydrothermally exhibit well dispersed particles with relatively uniform size distributions. The SEM micrographs of samples (a) to (d) at higher magnification gives a more clear view of the particles' morphology. The TAM powder synthesized display irregular particles with a non-uniform size distribution, which is completely different from the powders synthesized hydrothermally.



(a)

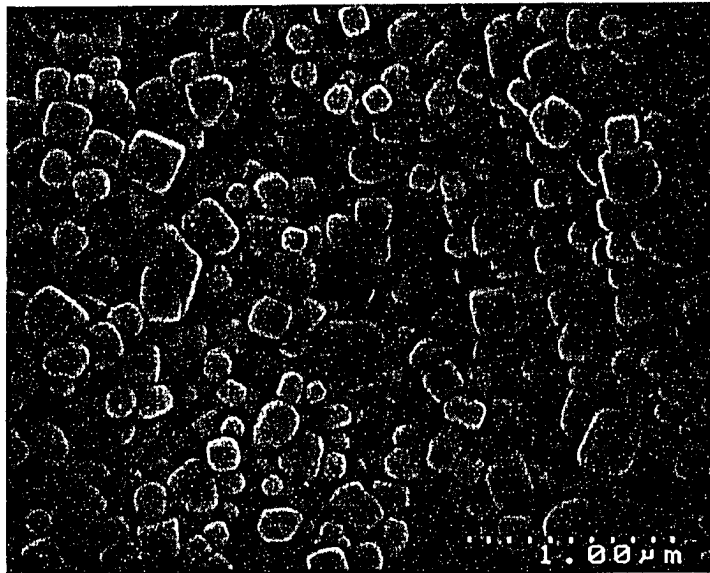
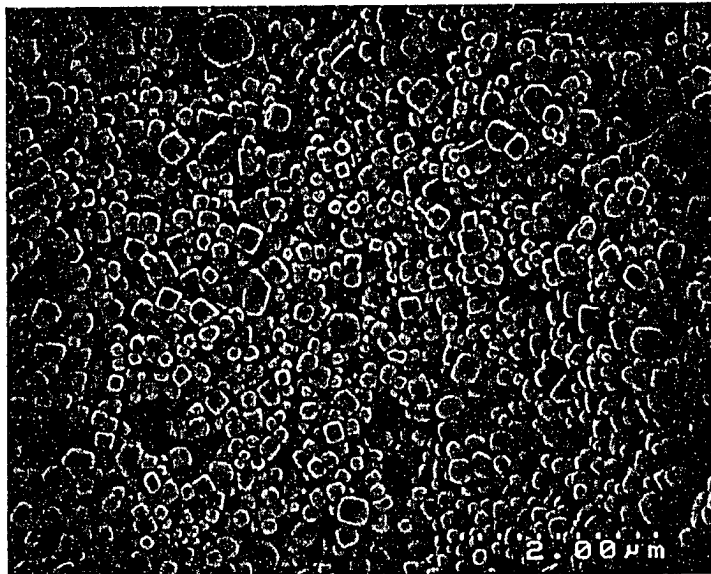
Figure 4.10. SEM micrographs of the BaTiO₃ powders with different barium sources: (a) Ba(OH)₂; (b) Ba(NO₃)₂; (c) Ba(C₂H₃O₂)₂; (d) BaCl₂; (e) BaI₂, and (f) commercial (TAM HPB). Note that two magnifications are shown for samples (a) to (d).

Figure 4.10. (continued),



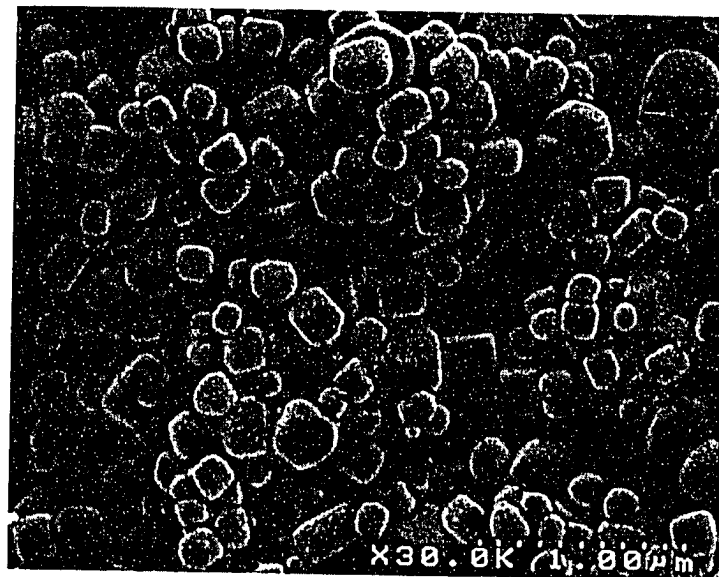
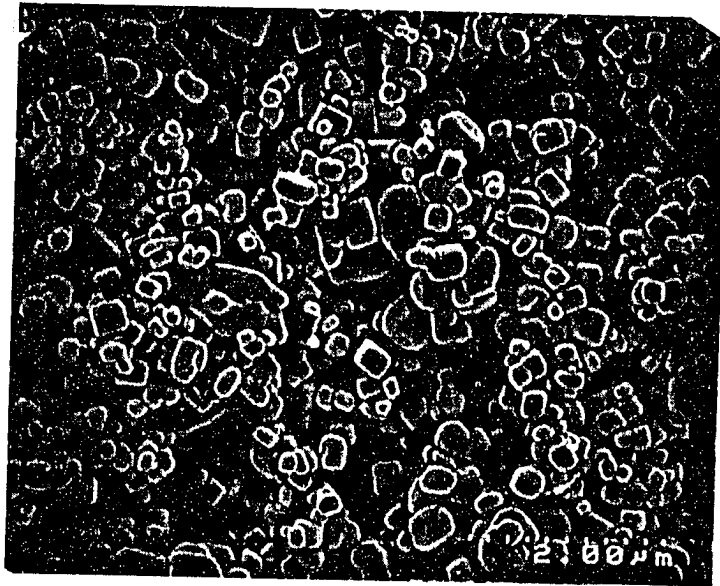
(b)

Figure 4.10. (continued),



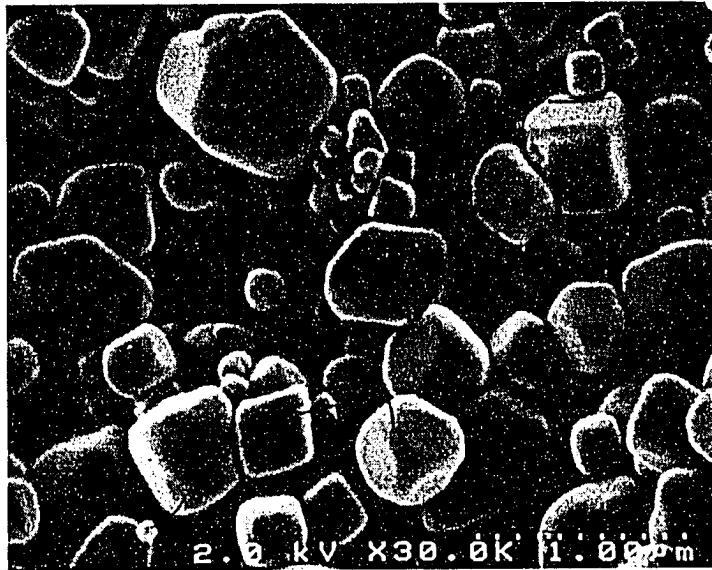
(c)

Figure 4.10. (continued),



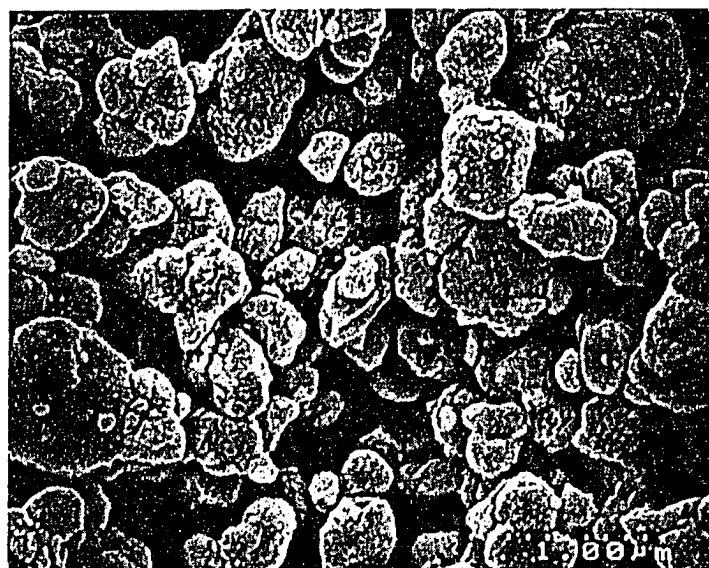
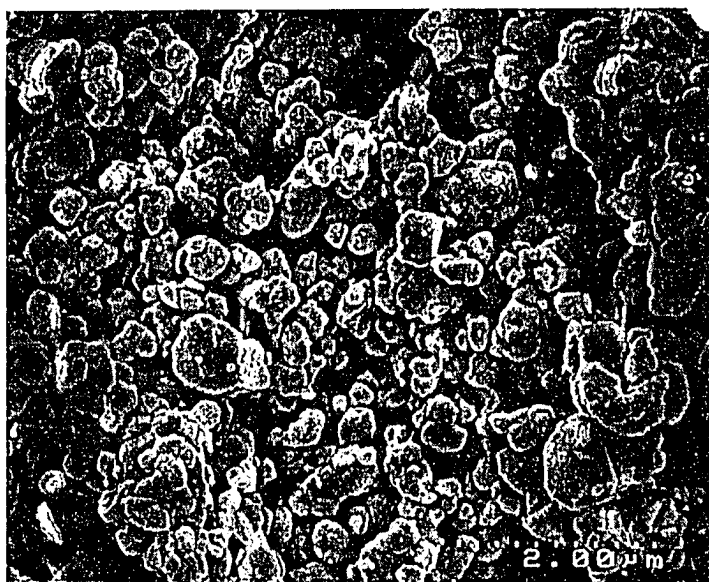
(d)

Figure 4.10. (continued),



(e)

Figure 4.10. (continued),



(f)

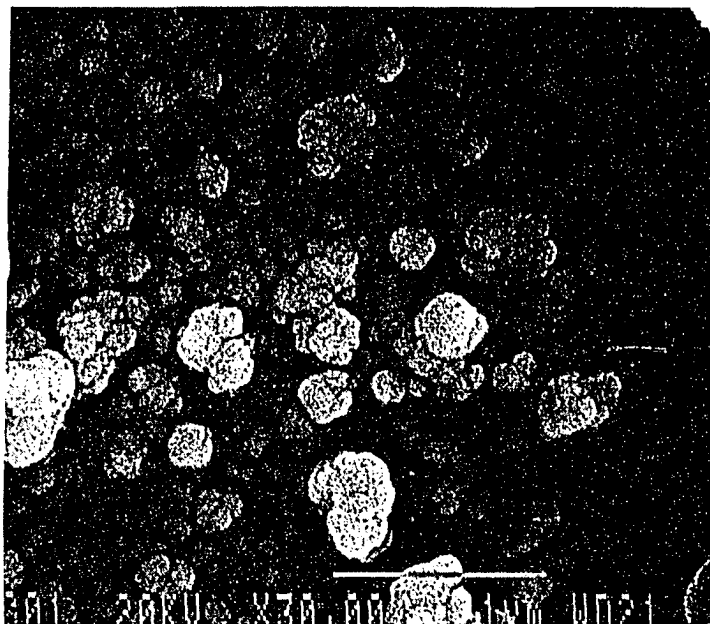
4.1.4. BaTiO₃ Powders Synthesized with Different NaOH Concentrations

As mentioned in previous sections, the tetragonal BaTiO₃ powders can be synthesized hydrothermally at 240°C with various barium sources. And it was found that by increasing the synthesis time, the powders show an increased particle size and a higher tetragonality. However, all these experiments were done under the same OH⁻ concentration (1.0M). It is known that the pH of the solution is a critical factor for the hydrothermal formation of BaTiO₃ powders and, therefore, it is certainly beneficial to investigate the influence of the OH⁻ concentration on the synthesis and properties of the produced powders.

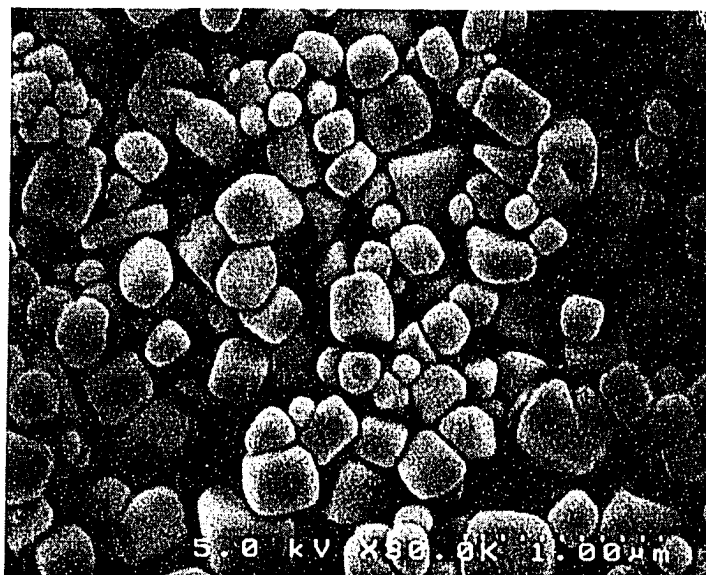
Three different BaTiO₃ powders, labeled A, B and C, were synthesized with various OH⁻ concentrations (0.3, 0.5 and 'buffered' 0.5 M). The detailed description can be found in section 3.1.1. The Ba to Ti ratio determined by ICP are 0.531, 0.988 and 1.004 for samples A, B and C, respectively. The results of the characterization of these powders are presented in the following.

I. Microstructure and phase determination

Figure 4.11 shows SEM micrographs of powders A, B and C. Particles in powder A appear to be agglomerated, whereas those in powders B and C are well-dispersed. Particle sizes calculated from the SEM micrographs are on the average of 0.1, 0.3 and 0.5 μm, respectively.



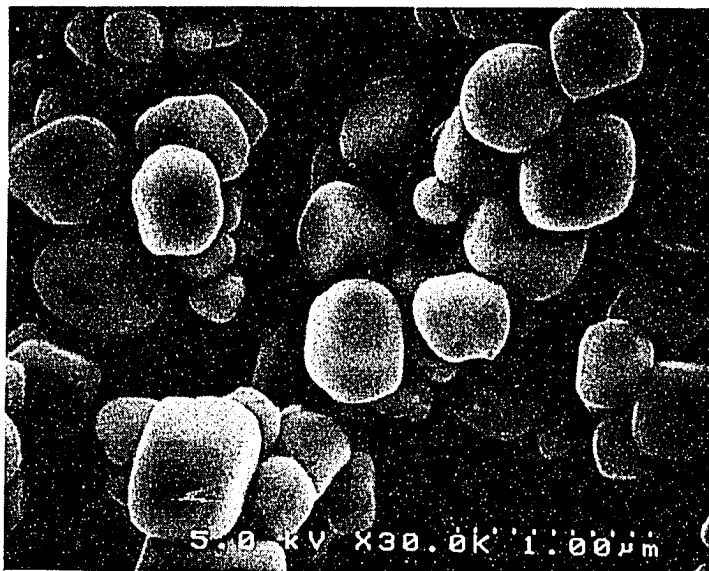
(a)



(b)

Figure 4.11. SEM micrographs of the BaTiO_3 powders synthesized with various OH^- concentrations: (a) powder A (b) powder B and (c) powder C.

Figure 4.11. (continued),



(c)

Figure 4.12 shows the XRD patterns of powders A, B and C. No apparent second phases are present in the spectra. The insets highlight the (200)-type reflections around a 2θ of 45° . The splitting of (200) reflections is apparent for powders B and C, suggesting a tetragonal structure. However, for powder A, the splitting is difficult to distinguish because of the broadening effect associated with small particles.

It is also noteworthy that in the XRD pattern of powder A, the signal to noise ratio seems to be lower, indicating the possible existence of an amorphous phase in powder A. To further confirm this, BaTiO₃ powders (20 mg) were mixed with 10 mg Si (99.999%) powder and their XRD patterns were obtained as shown in Figure 4.13. The intensity ratio of two neighboring peaks due to BaTiO₃ and Si ($I_{\text{BaTiO}_3} / I_{\text{Si}}$) are calculated to be 2.27, 2.33 and 0.82 for powders A, B and C, respectively. The significant decrease in the intensity ratio for powder A confirms the existence of the amorphous material in powder A. The amorphous material is assumed to be the unreacted TiO₂, which remains in the powder, and may be the cause of the low Ba/Ti ratio (0.531) detected by ICP.

The powders were also examined under transmission electron microscopy (TEM) and high resolution TEM (HREM). Representative TEM micrographs show the morphology of the particles from powders A and B (Figure 4.14). The particles can be easily dispersed in ethanol, suggesting that the powders are not

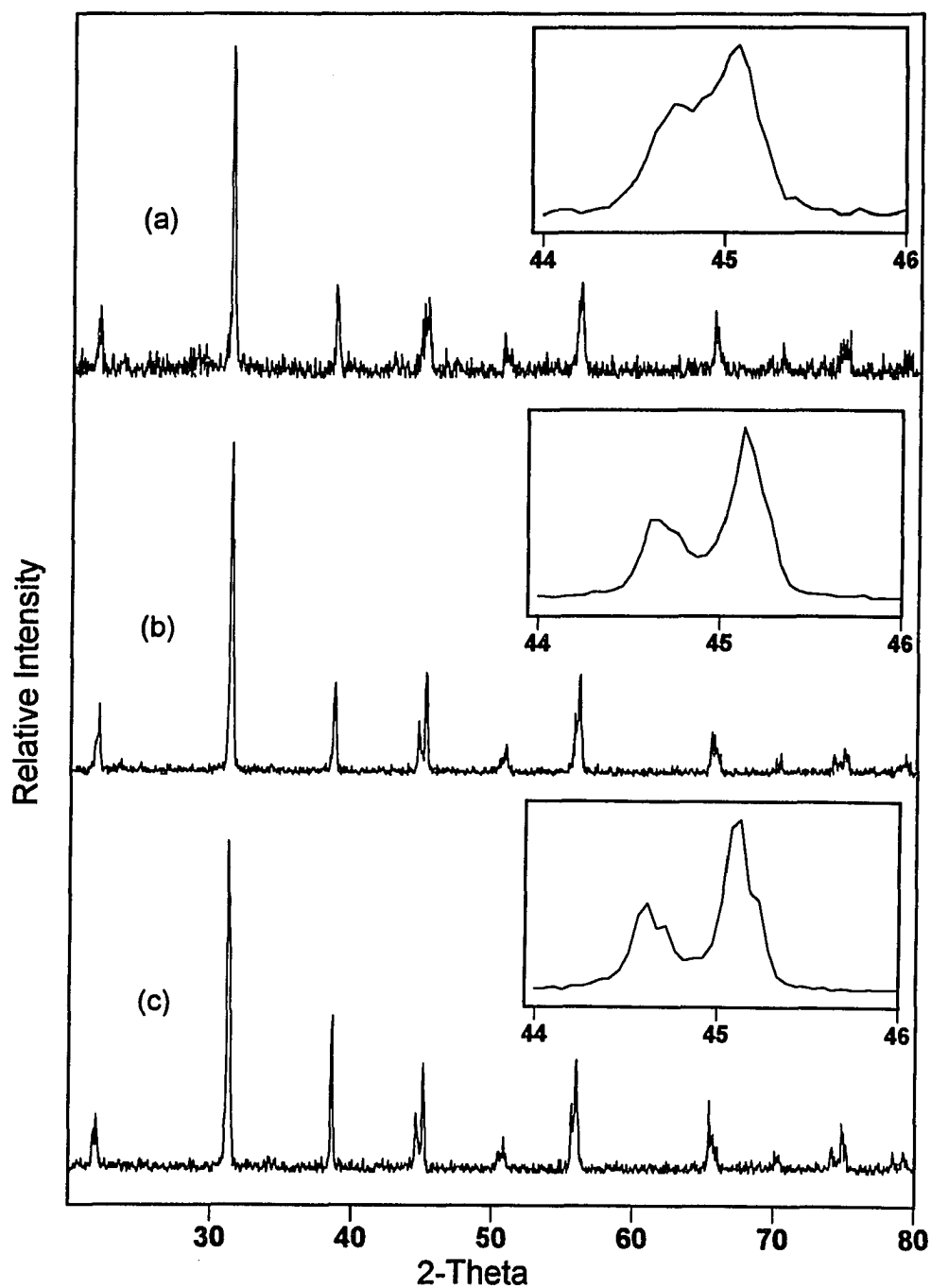


Figure 4.12. XRD patterns of powders: (a) A; (b) B and (c) C. The insets highlight the characteristic reflections of (200)-type planes of BaTiO_3 crystals with 2θ ranging from 44 to 46°.

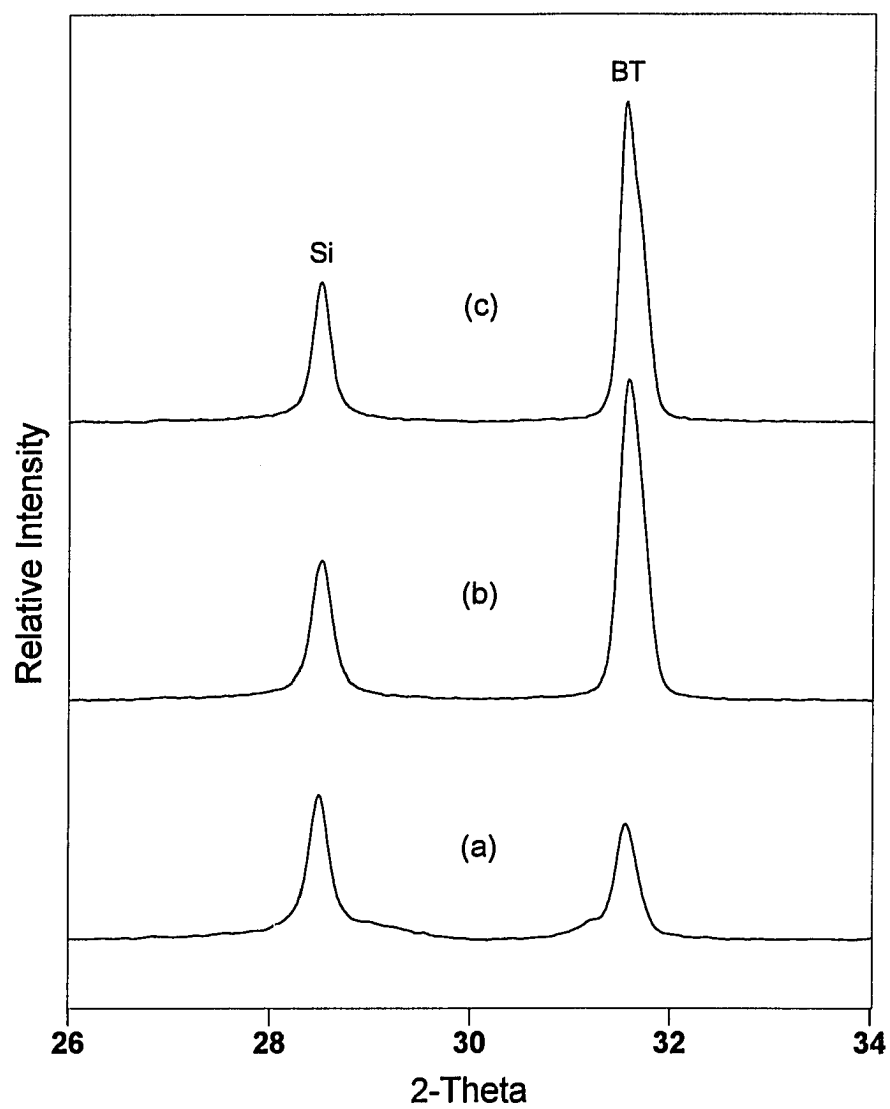
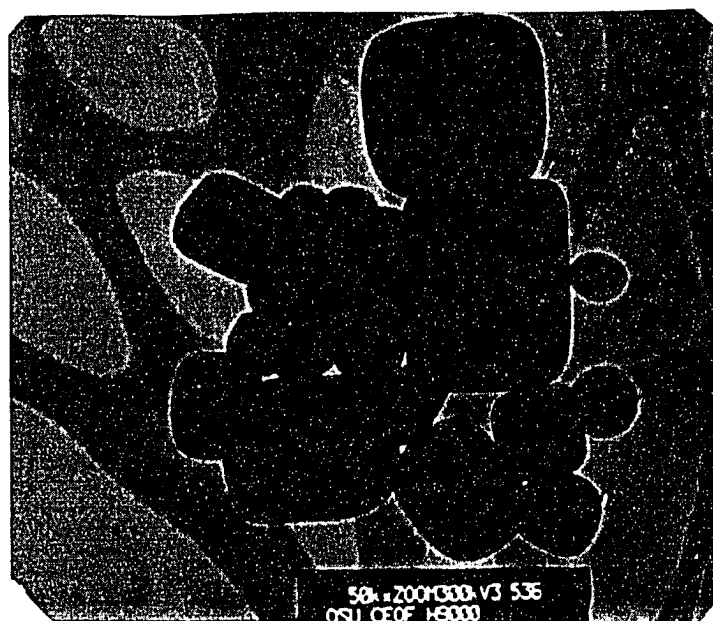


Figure 4.13. XRD pattern with Si internal standard: (a) powder A; (b) powder B and (c) powder C. It indicates the partial crystallinity of powder A.



(a)



(b)

Figure 4.14. TEM micrographs of the hydrothermal powders: (a) A and (b) B. Note the gray area in (a) corresponding to the unreacted amorphous TiO_2 .

hard agglomerates, which is often the case for the powders produced by some other wet-chemical syntheses (such as coprecipitation and combustion methods). It appears that there is some material with amorphous nature in powder A (middle gray area shown in Figure 4.14a). This gives additional evidence to support the assumption that there is some unreacted amorphous TiO_2 present in powder A.

The powders were also examined using high resolution transmission electron microscopy (HREM), and the micrographs are shown in Figure 4.15 for a representative particle from powder B. At such a high resolution, a periodic fringe image is produced as a result of phase interference between transmitted and diffracted beams. Under certain well-defined conditions the spacing of the fringe image corresponded to that of the reflecting planes. The presence of ferroelectric domains thus could be observed due to the phase contrast produced from boundary walls between domains with a right focusing condition.

However, as shown in Figure 4.15, there are no observable domain boundaries and lattice fringes run continuously toward the interior of the particle. The image of the bottom part of the particle is shown in the left inset of the figure for clarity. Since the lattice fringes at two different edges of the crystallite are similar and no domain boundary contrast was observed, it is reasonable to assume that the crystallites have a single domain configuration. For larger particles, as in powder C, the high resolution image of the whole particle could

not be obtained because the sample was too thick for the electron beam to transmit. Only areas very close to the edges of the particles were observed. Convergent beam diffraction was also performed to confirm that the particles are single crystals. The upper left inset in Figure 4.15 shows the diffraction spot pattern with [001] incident beam direction obtained from the particle. The diffraction patterns also suggest monodomain characteristics, since doubling of diffraction spots, which may be caused by multidomain structure, are not observed.

II. Lattice parameters and strain measurement

Lattice parameters and strains associated with the powders were calculated from the XRD data using Si and LaB₆ as internal and external standards, respectively, to correct for the peak position and instrumental broadening. The results shown in Table 4.3 indicate that the c/a ratio for powders A, B and C increases from 1.0078 to 1.0105. The lattice parameters reported for tetragonal BaTiO₃ single crystal are $a = b = 3.9920$ and $c = 4.0361$ Å (and $a = b = c = 3.996$ Å for the cubic unit cell) [339]. The c/a ratio is calculated to be 1.0110. Therefore, the lattice parameters and the c/a ratio of crystals in powders B and C are close to the values of the tetragonal single crystal, while the c/a ratio calculated for powder A is significantly lower.

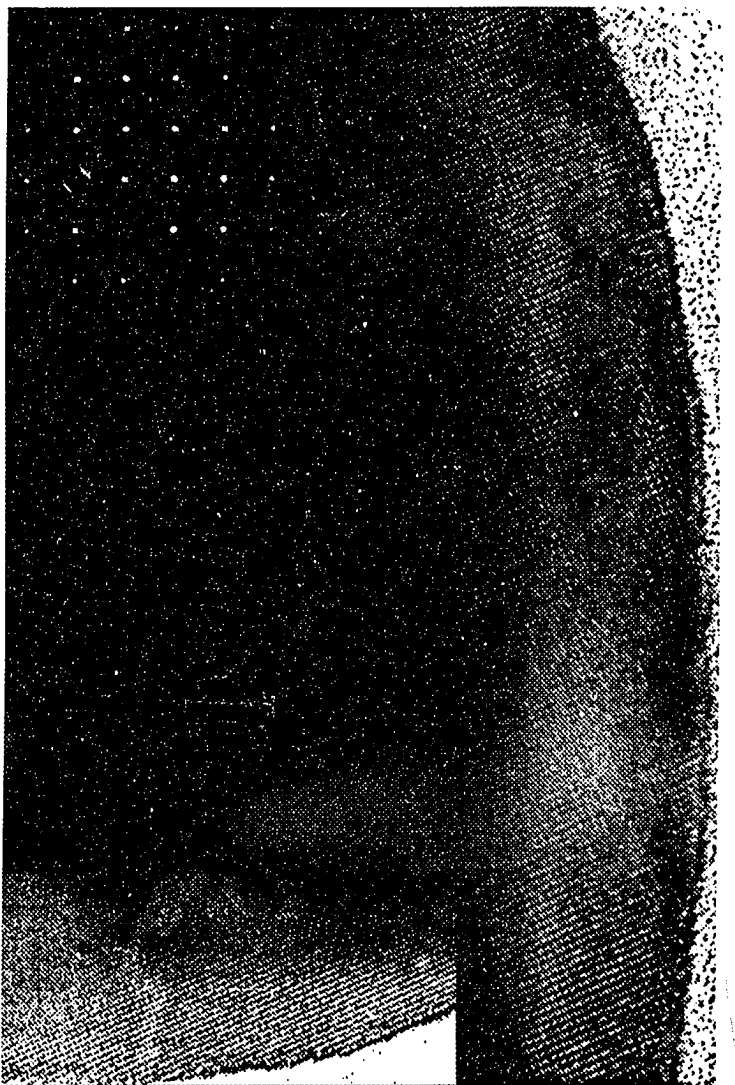


Figure 4.15. HREM micrograph of a representative particle from powder B. Insets showing an area in bottom edge and converged beam diffraction pattern along [001] direction, respectively.

Table 4.3. Lattice parameters, lattice strain and crystal size calculations of the BaTiO₃ powders A, B and C as determined by XRD.

Powders	A	B	C
Particle size by SEM (μm)	0.1	0.3	0.5
Lattice parameter (\AA)	$a = 3.9977 \pm 0.0021$	3.9941 ± 0.0006	3.9940 ± 0.0003
	$c = 4.0272 \pm 0.0022$	4.0362 ± 0.0008	4.0357 ± 0.0005
c/a ratio	1.0078	1.0105	1.0104
Lattice strain ($\times 10^3$)	0.763	0.408	0.216
Particle size by XRD (μm)	0.055	0.064	0.098

The plots of $(\beta_{1/2} \cos \theta / \lambda)^2$ versus $(4 \sin \theta / \lambda)^2$ for each powder are shown in Figure 4.16. A linear dependence was obtained, assuming that the strains in the three powders are distributed uniformly (along the different crystallographic directions). The values of lattice strain and crystal sizes were calculated from the slopes and the intercepts using the linear regression method (Table 4.3). It is noticed that there is some scatter in the obtained data, especially for samples A and B, and this may result from the structural heterogeneity of the powders and the error associated with the experiment. It appears that there is a decrease in strain values from powders A to C, though the overall magnitude is very small (< 0.001). The crystal sizes of the powders obtained are smaller than the mean values measured from the SEM micrographs (Table 4.3). This discrepancy may be attributed to the experimental limitations associated with the X-ray

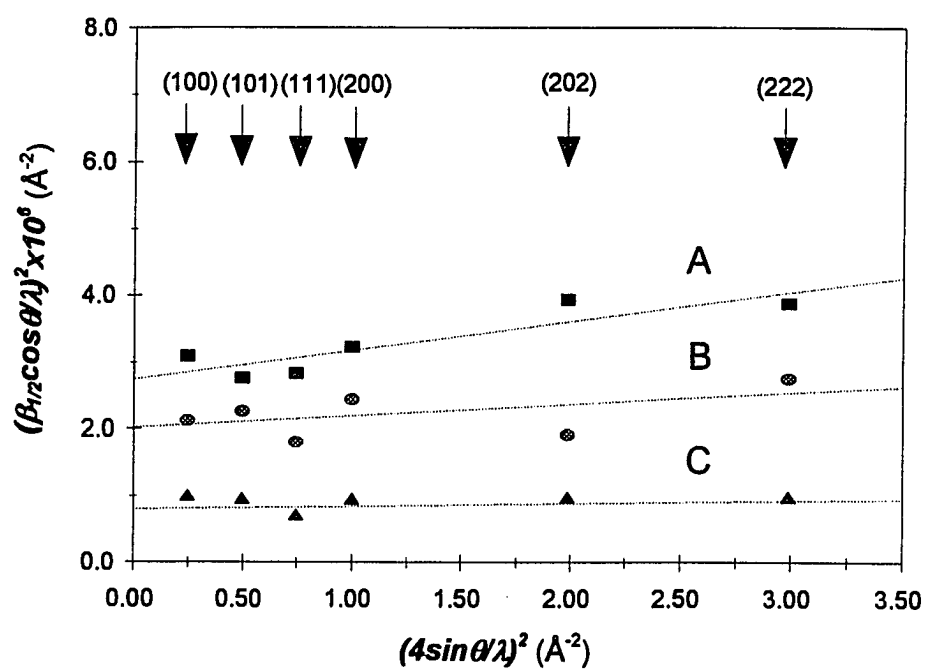


Figure 4.16. Hall-Williamson plot with Gaussian-Gaussian profile for the BaTiO₃ powders: (a) A; (b) B and (c) C.

broadening method. Crystal size measurement via X-ray line broadening method is applicable and accurate only for very fine particles ($< 2000 \text{ \AA}$). For particles with larger sizes, SEM gives a better size estimation. In this study, the particle sizes of 0.3 and 0.5 \mu m obtained by SEM for powders B and C are believed to be more accurate than those obtained by X-ray line broadening method.

III. Thermal Analysis

A. Differential scanning calorimetry (DSC) measurement

DSC curves around the Curie transition for powders A, B and C are presented in Figure 4.17. A phase transition around 125 to 130°C was observed in each case. The enthalpies of transition (ΔH) were calculated to be 0.07 , 0.50 , and 0.85 J/g for powders A, B and C, respectively. The amorphous content in powder A was roughly estimated and taken out from the total sample amount for the calculation. The enthalpy change associated with the Curie transition (ΔH) has been reported to be 0.73 and 0.84 J/g by DSC and specific heat measurements, respectively [174, 340]. A dependence of ΔH on the particle size is once again observed with ΔH increasing with the particle size.

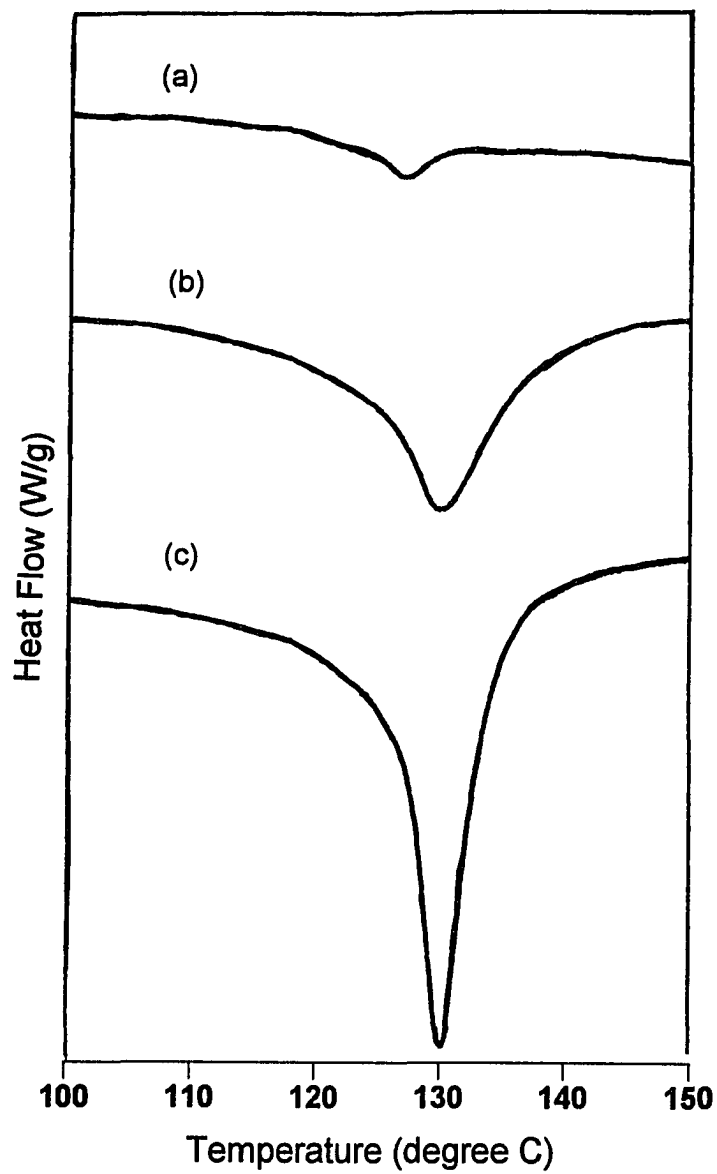


Figure 4.17. DSC curves around the Curie transition for BaTiO₃ powders: (a) A (b) B and (c) C.

B. Thermogravimetric analysis

Hydroxyl content of the particles of powders A, B and C were obtained from the TGA measurement (Figure 4.18), by estimating the weight loss between 200 ~ 600°C. The percentage weight losses calculated are 0.6, 0.1, and 0.06 wt.% for the powders A, B, and C respectively. The corresponding weight loss in terms of OH⁻ groups are 8.2, 1.4 and 0.8 mole % for the samples A, B and C, respectively. The weight loss above 800°C due to CO₂ released from the decomposition of carbonate species is constant for all samples (about 0.25 wt.%).

IV. Vibrational spectroscopy

A. Raman spectroscopy

Figure 4.19 shows Raman spectra of powders A, B and C, respectively. The spectra have been displaced from each other vertically to illustrate the similarities, both in peak frequencies and relative intensities. The amorphous material in sample A is not contributing to the spectrum. The spectra display a weak peak around 715 cm⁻¹, two strong and broad peaks around 515 and 260 cm⁻¹, and a sharp peak at 305 cm⁻¹.

The Raman spectra of samples A, B and C are consistent with that of the tetragonal BaTiO₃ reported in the literature [341-345]. The bands around

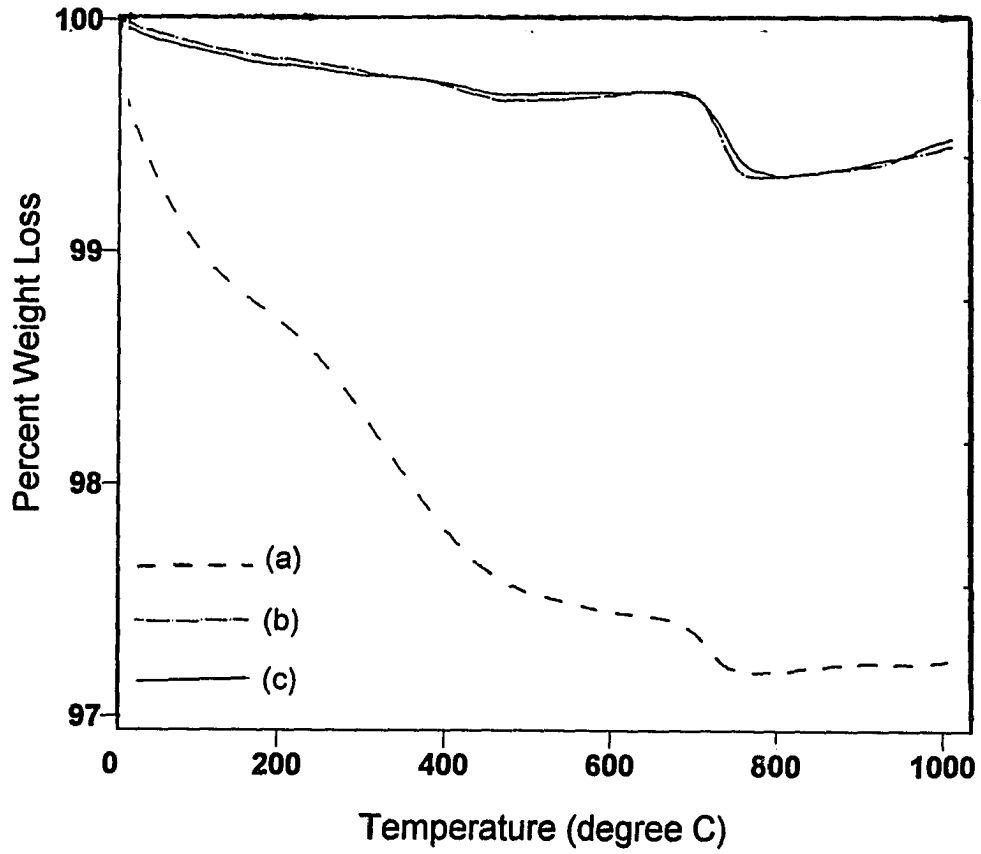


Figure 4.18. TGA measurement of weight loss in the BaTiO₃ powders: (a) A (b) B and (c) C, as a function of temperature.

515 and 260 cm^{-1} are assigned to the TO modes of A_1 symmetry, whereas the sharp peak at 305 cm^{-1} has been assigned to the B_1 mode. The weak band around 715 cm^{-1} has been associated with the highest frequency longitudinal optical mode (LO) of A_1 symmetry. The bands at 305 and 715 cm^{-1} disappeared upon heating above the Curie temperature (Figure 4.20). The presence of the two remaining bands above T_c , though the selection rules forbid Raman bands in the cubic form, has been noted before and assigned to second order transitions. The Raman spectrum of the sample synthesized at 95°C, which has been referred to as the metastable cubic form, is shown in Figure 4.21. Note that the sharpness of the 305 cm^{-1} is reduced, indicating partial tetragonality. The quantitative analysis of the Raman spectra of the three powders (A-C) was attempted, but the precision of the method was too poor to make any judgment. This arises from the difficulty in focusing the laser beam reproducibly. The use of an internal standard (NaNO_3) did not alleviate this problem, as it was difficult to mix the two solids uniformly.

B. Infrared spectroscopy

The two regions of the infrared spectrum of interest are the framework bands and the OH^- stretching region. Figure 4.22 shows infrared data of the OH^- stretching vibration around 3600 cm^{-1} . Since the samples for IR spectroscopy were prepared from powders heated to 110°C under vacuum for 3

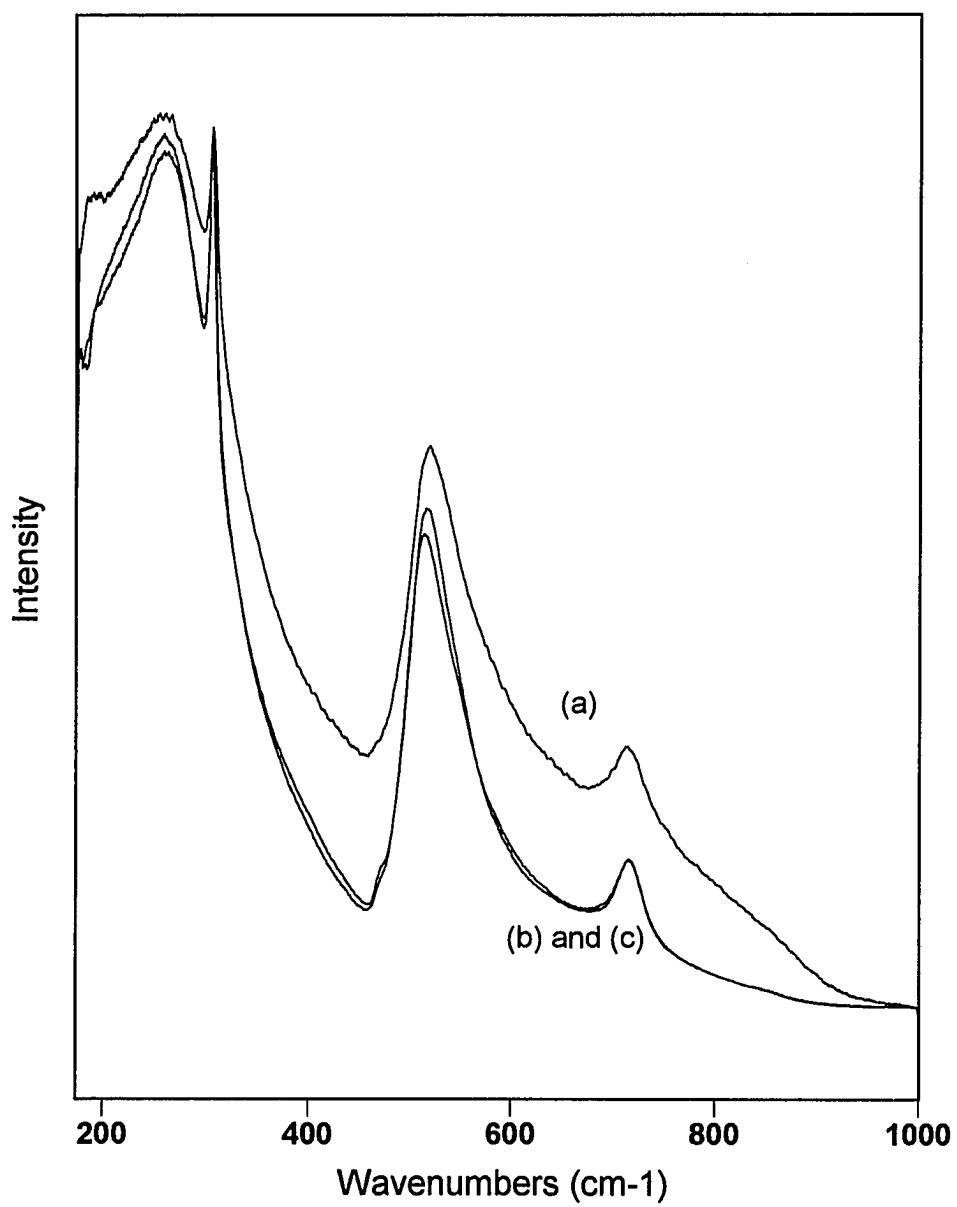


Figure 4.19. Raman spectra of the BaTiO₃ powders: (a) A (b) B and (c) C.

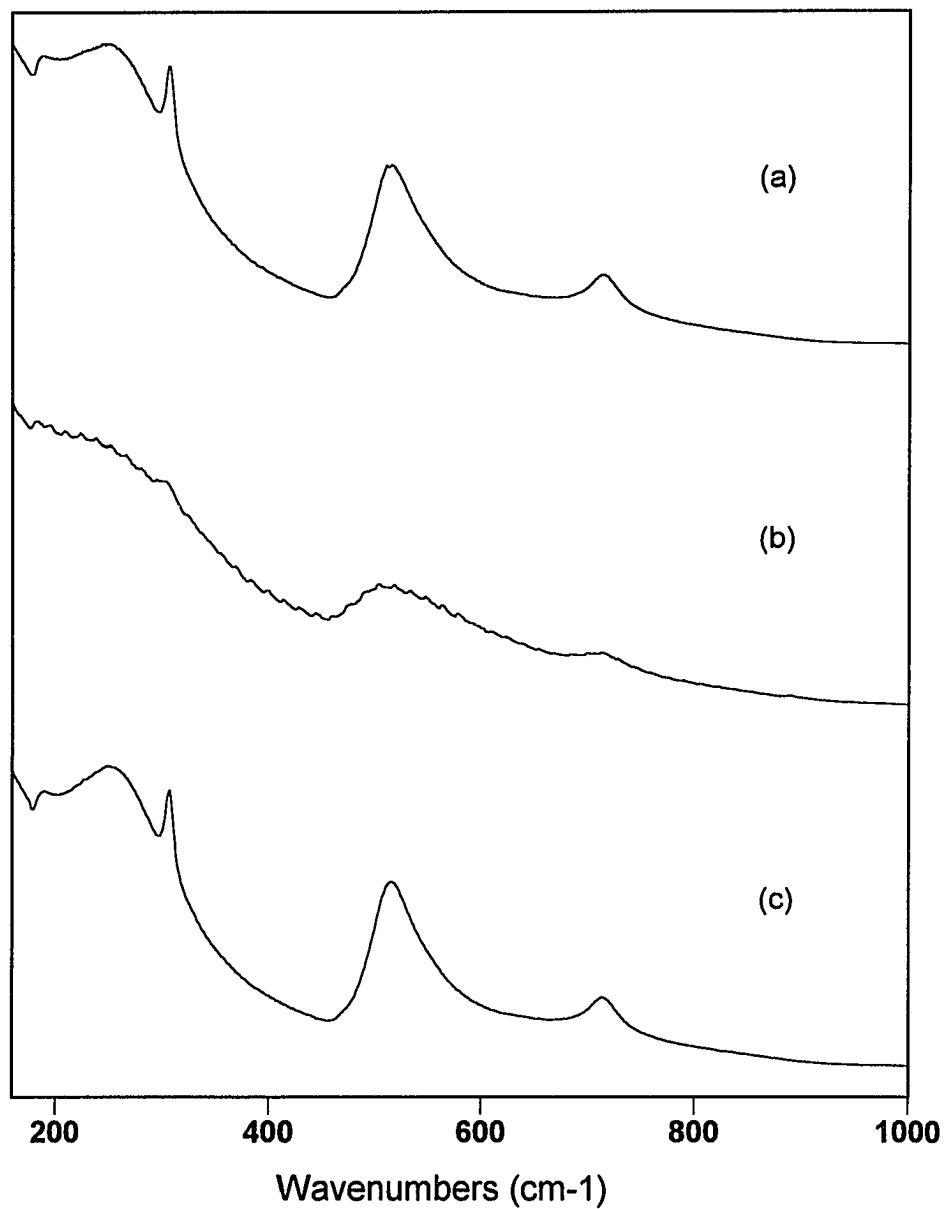


Figure 4.20. Raman spectra of the tetragonal BaTiO₃ powder: (a) at room temperature; (b) upon heating above T_c ($\sim 130^\circ\text{C}$) and (c) upon cooling back to room temperature. Note that the peaks at 305 and 715 cm⁻¹ disappear at temperature above T_c .

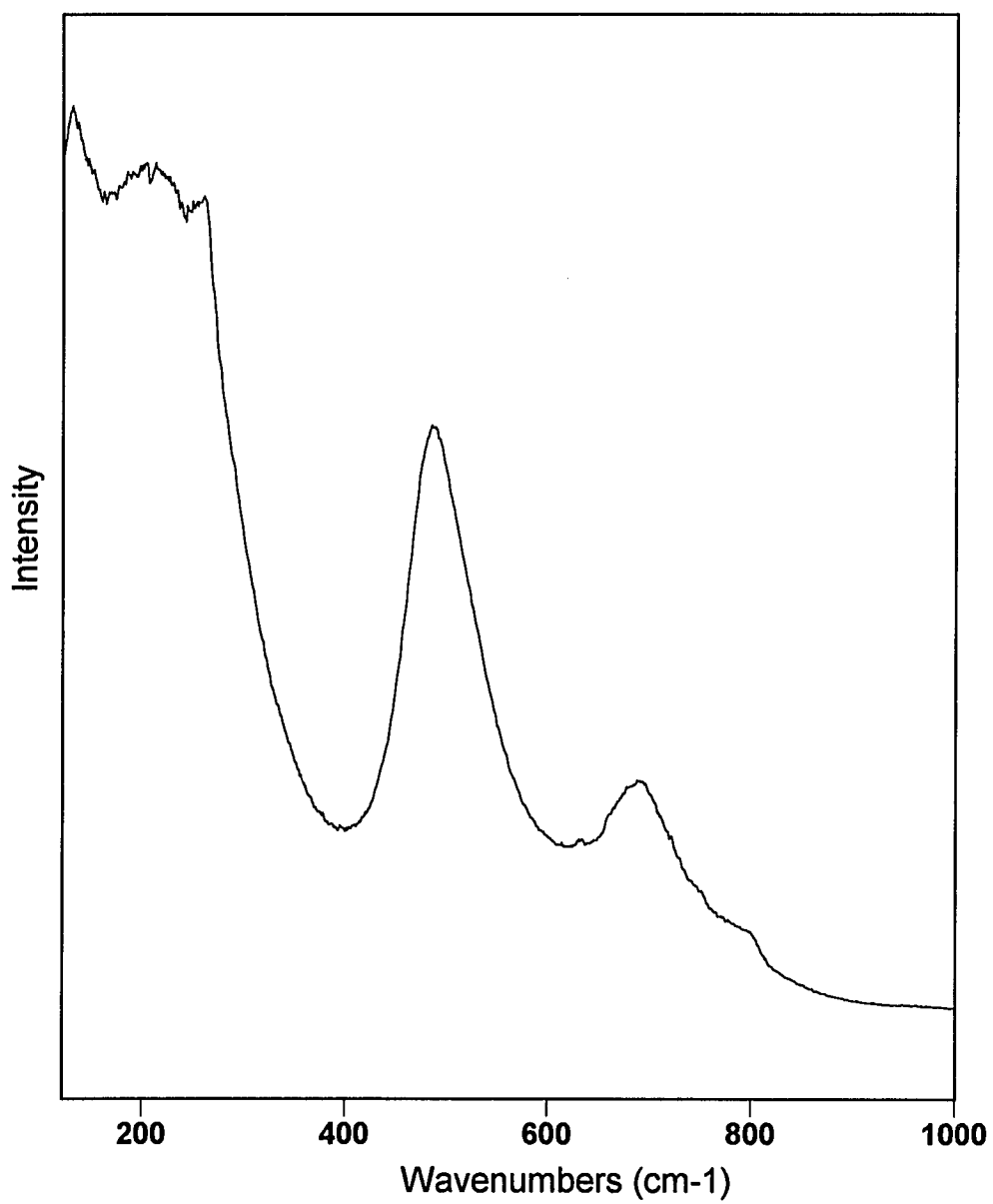


Figure 4.21. Raman spectrum of the BaTiO₃ powders synthesized at 95°C.

hours, no interference from surface water is expected. The much higher IR absorption peak for powder A indicates that it contains considerably more hydroxyl groups than the other two powders, which supports the results obtained from the TGA measurement. However, it is difficult to determine whether the hydroxyl groups arise from the BaTiO₃ crystallites or from the amorphous unreacted titanium dioxide.

Figure 4.23 shows infrared spectra of the samples A, B and C in the framework region. Two broad bands around 560 and 431 cm⁻¹ are observed. It has been pointed out [346-347] that there are three types of optical phonon modes, transverse, longitudinal and surface modes. The frequencies that were observed agree with the literature [346-350] and have been assigned to the surface modes. As the size of the particles becomes smaller compared to the wavelength of infrared radiation, there is uniform polarization of the particle, and this results in the surface or Fröhlich modes. The profiles of the observed bands for all three particles are similar, except that the half-widths of the bands in sample A are about 25% greater, with components mostly in the higher-frequency parts of the bands.

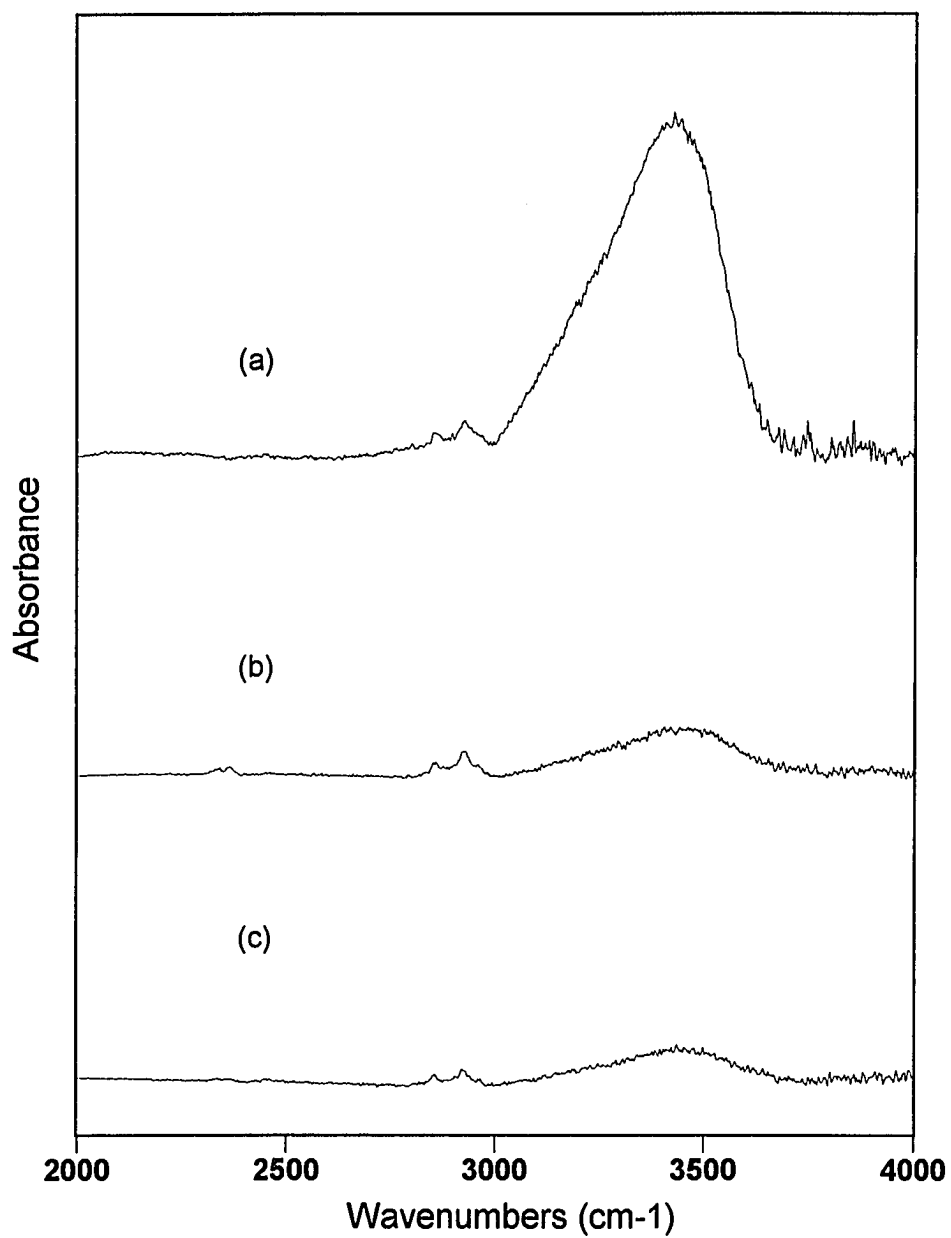


Figure 4.22. Infrared spectra of the OH stretching vibration region for the BaTiO₃ powders: (a) A (b) B and (c) C.

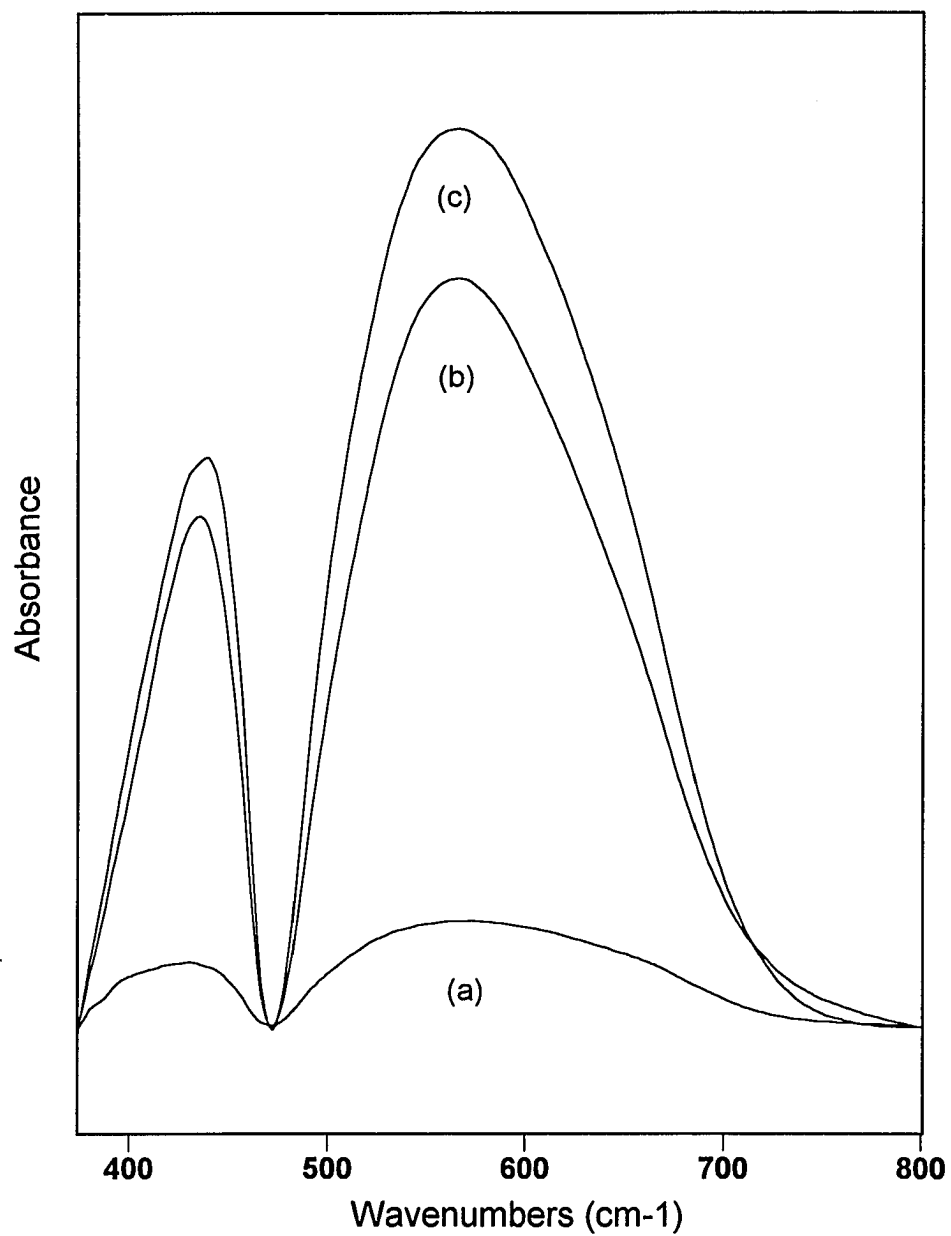


Figure 4.23. Infrared spectra of the framework region of BaTiO₃ powders: (a) A (b) B and (c) C.

The infrared spectra shown in Figure 4.23 for samples A, B, and C were obtained from the same amounts of powder under identical conditions, and these intensities were reproducible to within 10% for different sample preparations. There is an increase in band intensities with increasing particle size. Correcting for the presence of unreacted TiO_2 in sample A, the integrated band intensities for the 560 cm^{-1} increases in the order 1: 9: 13 for samples A, B and C, respectively.

4.2. Characterization of Sintered Ceramic BaTiO_3

BaTiO_3 powders synthesized hydrothermally with different barium sources and OH^- concentrations were sintered at various conditions and the microstructure, and dielectric properties of these sintered ceramics were studied. Attempts were made to understand the effects of powder properties and sintering conditions on microstructure development of the BaTiO_3 ceramics, as well as to correlate the microstructure (grain size and distribution, porosity, *etc.*) to the dielectric properties of the ceramic BaTiO_3 .

4.2.1. BaTiO₃ Ceramics from Hydrothermally Synthesized Powders with Different Barium Sources

The sintering and dielectric property studies were carried out using the BaTiO₃ powders synthesized hydrothermally with various barium sources: BaCl₂, Ba(C₂H₃O₂)₂ and Ba(NO₃)₂, together with the commercial powder (TAM HPB).

I. Sintering and Microstructure

The BaTiO₃ powders were pressed uniaxially into discs with a pressure calculated to be 173 MPa. No binders or additives were used in the sintering. The green density was calculated to be roughly 55% of the theoretical density, with a small variation associated with different particle sizes (samples with smaller particle size show slightly higher green densities).

The densification behavior of the hydrothermally synthesized powders was studied using the dilatometry method, where the linear shrinkage of a sample was continuously monitored with time during sintering. Figure 4.24 shows the dilatometric curves of the powders synthesized hydrothermally with BaCl₂, Ba(C₂H₃O₂)₂ and Ba(NO₃)₂ as barium sources, which are labeled as BaTiO₃ (Cl⁻), BaTiO₃ (C₂H₃O₂⁻) and BaTiO₃ (NO₃⁻), respectively. The sintering (shrinkage) began at 800-1000°C for all the powders, but it did not go to completion even above 1400°C. This may be due to the relatively large particle sizes of the powders. A careful examination reveals that the shrinkage takes

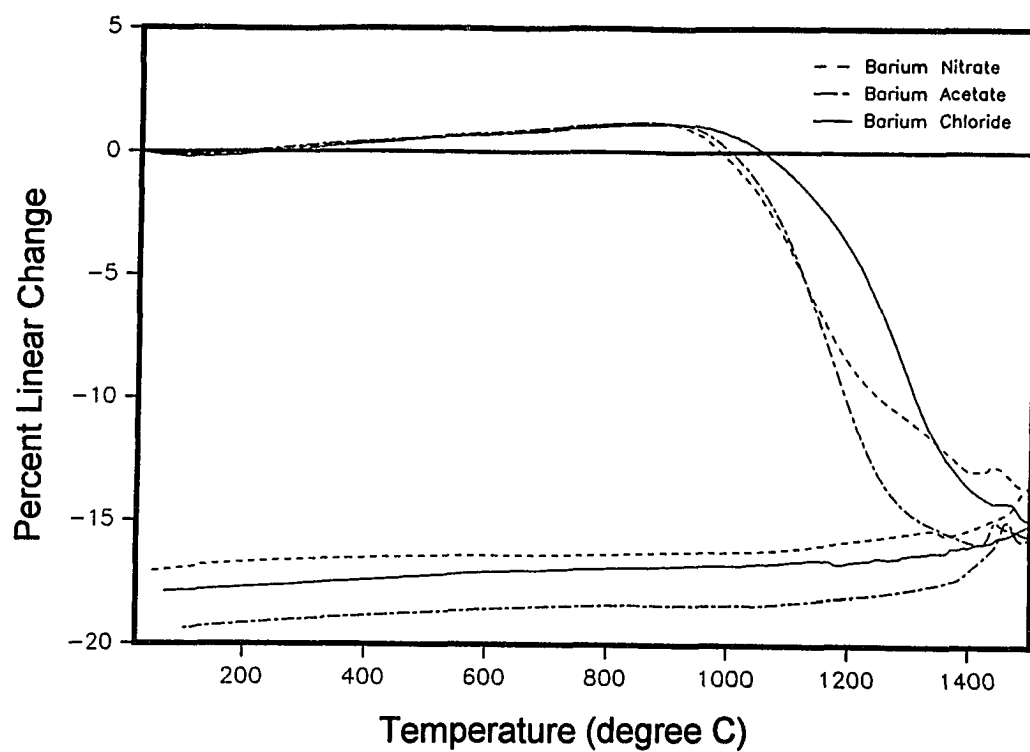


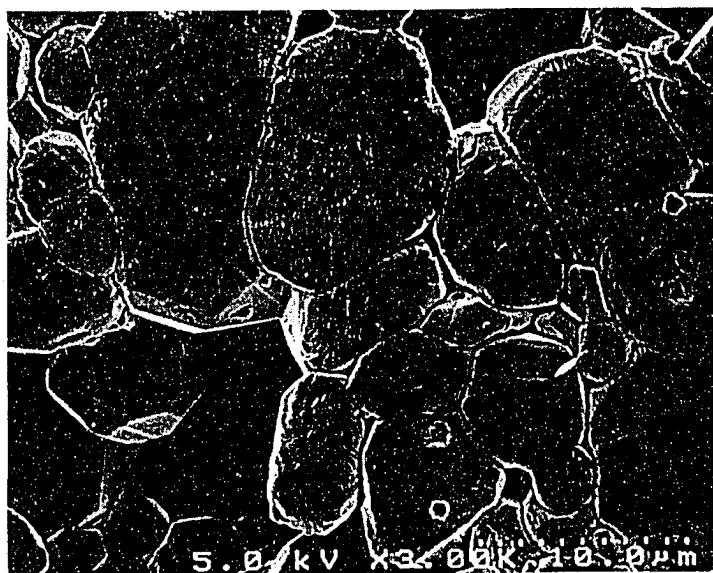
Figure 4.24. Dilatometric curves of the BaTiO₃ powders synthesized with various barium sources.

place earlier for $\text{BaTiO}_3 (\text{NO}_3^-)$, followed by $\text{BaTiO}_3 (\text{C}_2\text{H}_3\text{O}_2^-)$ and $\text{BaTiO}_3 (\text{Cl}^-)$, which corresponds well with the increasing particle sizes of the powders (0.15, 0.17 and 0.23 μm). This behavior may be due to the fact that small particles have higher surface energy per unit volume, thus they tend to be sintered at lower temperatures and with higher sintering rates. It is interesting to note that the shrinkage of $\text{BaTiO}_3 (\text{NO}_3^-)$ slowed down at 1200°C, suggesting that another mechanism might take over at higher temperatures. In addition, it achieved the lowest final density toward sintering (~16% linear shrinkage compared to ~19% for the other two powders), which is not consistent with the fact that powders with smaller particles usually result in higher density. Finally, it is noticed that there is a small peak in all the dilatometric curves at around 1450°C and this is most probably due to the cubic to hexagonal phase transition that occurs at 1460°C.

The powder compacts of the hydrothermally synthesized powders were sintered at 1300°C for 5 hours, together with the commercial powder (TAM HPB) for comparison. The densities of the sintered BaTiO_3 samples are 5.23 (87%), 5.75 (96%), 5.81 (97%) and 5.68 g/cm^3 (94%) for $\text{BaTiO}_3 (\text{NO}_3^-)$, $\text{BaTiO}_3 (\text{C}_2\text{H}_3\text{O}_2^-)$, $\text{BaTiO}_3 (\text{Cl}^-)$ and TAM HPB, respectively. The values in parentheses are the relative densities compared to the theoretical density of BaTiO_3 (6.02 g/cm^3). Figure 4.25 shows SEM micrographs of the sintered BaTiO_3 samples. The sintered $\text{BaTiO}_3 (\text{NO}_3^-)$ sample reveals a high porosity, as shown in the

microstructure and density measurement. This correlates well with the dilatometric curve where a shrinkage slow-down was observed. This may be due to some impurities in the powder which decomposes at about 1200°C, creating pores that inhibit further densification. Further characterization of this powder is necessary but was unintended in this study. The BaTiO₃ (C₂H₃O₂⁻) and BaTiO₃ (Cl⁻) samples show relatively high densities; however, the BaTiO₃ (C₂H₃O₂⁻) sample gives large grain sizes in the range of 10~20 μm, whereas the BaTiO₃ (Cl⁻) sample displays much smaller grain sizes which are in the range of 1~5 μm. The commercial powder shows a bimodal size distribution with small particles of about 1 μm, and large particles around 10 μm. This results from the abnormal grain growth that might occur during sintering.

Since the BaTiO₃ (Cl⁻) sample exhibits a high density and a limited grain growth during sintering, which is desired for the dielectric properties, its sintering behavior was further investigated by adjusting the sintering conditions. The powder was sintered at temperatures in the range of 1200 to 1350°C for a fixed time of 5 hours, together with the commercial BaTiO₃ (TAM HPB) for comparison. Figure 4.26 shows the SEM micrographs of the powder sintered at 1200, 1250 and 1350°C and the densities were calculated to be 5.52 (92%), 5.95 (99%) and 5.76 (96%), respectively. A decrease in density at higher temperatures may be caused by the rapid abnormal grain growth at high temperatures which traps the pores permanently in the grains during sintering.



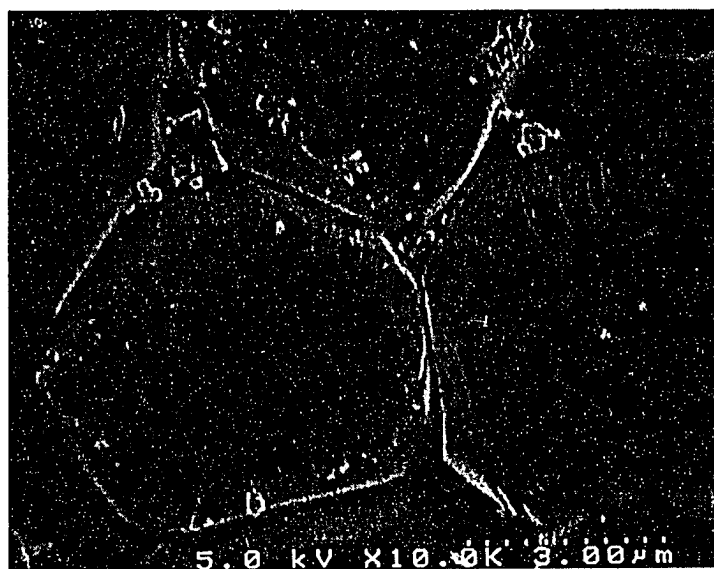
(a)



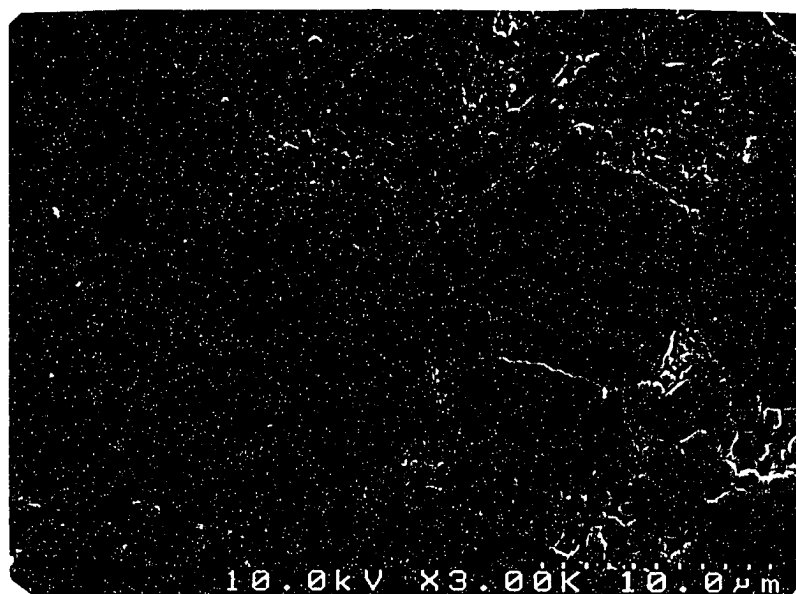
(b)

Figure 4.25. SEM micrographs of the BaTiO₃ powders sintered at 1300°C for 5 hours: (a) BaTiO₃ (NO₃⁻); (b) BaTiO₃ (C₂H₃O₂⁻); (c) BaTiO₃ (Cl⁻) and (d) commercial (TAM HPB).

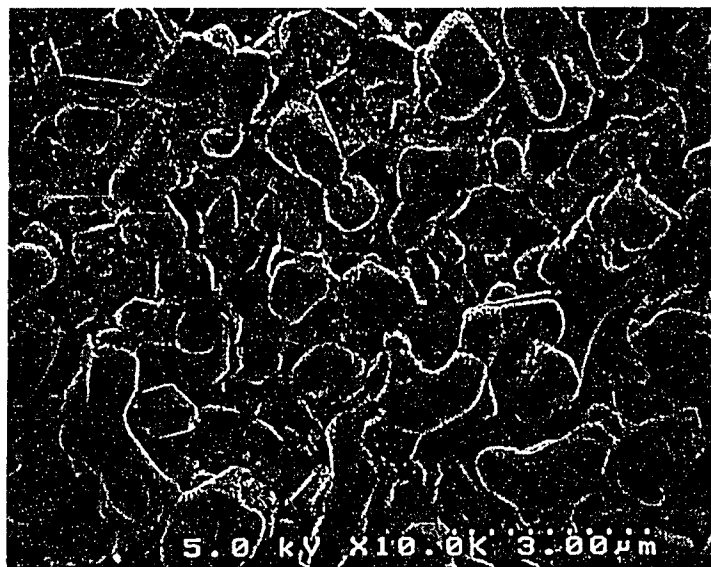
Figure 4.25. (continued),



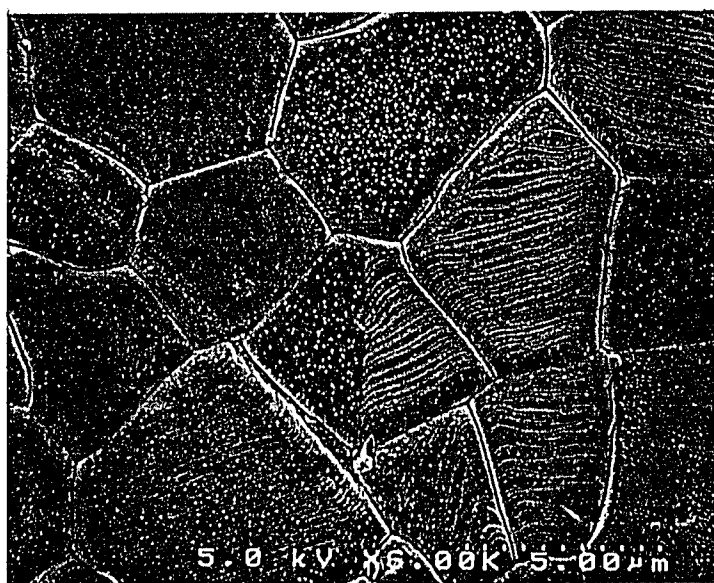
(c)



(d)



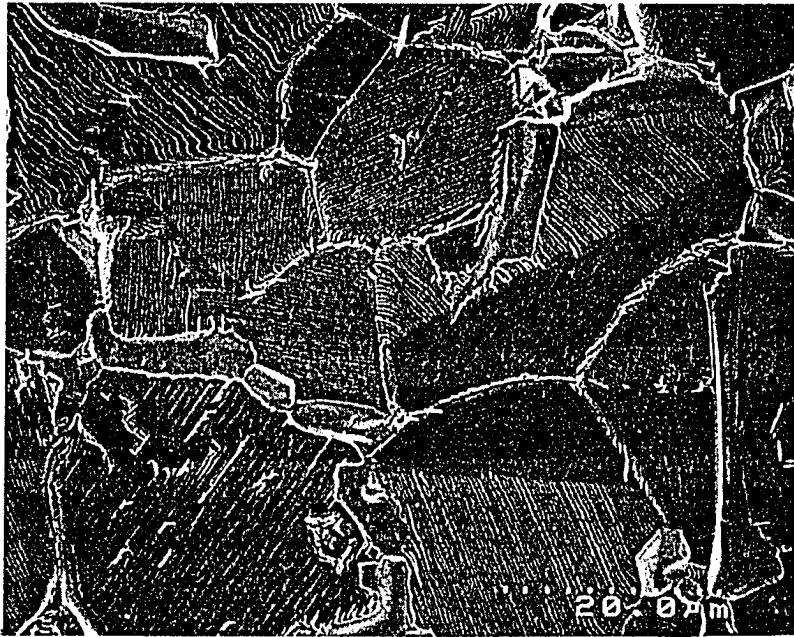
(a)



(b)

Figure 4.26. SEM micrographs of the $\text{BaTiO}_3 (\text{Cl}^-)$ powder sintered at various temperatures: (a) 1200°C ; (b) 1250°C and (c) 1350°C .

Figure 4.26. (continued),



(c)

Average grain sizes were calculated from the SEM micrographs of the powder sintered at 1200, 1250 and 1350°C and found to be roughly 0.6, 2.5 and 20 μm . The density of the commercial BaTiO_3 (TAM HPB) sintered at 1200, 1250 and 1350°C were measured to be 4.43 (74%), 5.27 (88%) and 5.79 (96%), respectively. The microstructure of the samples sintered at 1200 and 1250°C were examined and found to be very porous with grain sizes around 1 μm , indicating the final sintering stage was not reached. The sample sintered at 1350°C shows a relatively dense structure with grain size around 10 μm .

II. Dielectric properties measurement

The dielectric constant and loss tangent as a function of temperature were measured for samples obtained from the various powder sources and sintered at different temperatures. Figure 4.27 shows the results of samples from various barium sources sintered at 1300°C for 5 hours. There is a clear phase transition around 125°C, at which the samples transform from the ferroelectric to the paraelectric phase. The rise of dielectric constant in the paraelectric regime as temperature decreases obeys the Curie-Weiss law, and it goes to a maximum at the Curie temperature. Below the Curie temperature, spontaneous polarization occurs and domain structure starts to form. This leads to the decrease of the dielectric constant, since now dipoles are less polarizable by applying a small electric field. However, if a large enough field is applied, a

maximum dielectric constant can be obtained. The BaTiO_3 (Cl^-) sample shows a high dielectric constant around 1940 at room temperature, which may stem from the fact that it possesses the highest density and relatively small grain size (1~5 μm), as shown in Figure 4.25c. The BaTiO_3 (NO_3^-) sample exhibits the lowest dielectric constant which is about 677 at room temperature, corresponding to its lowest density (87% of the theoretical density). Thus, a high grain density and a fine grain size are essential for the high dielectric constant of the samples. The loss tangents ($\tan\delta$) (Figure 4.27) are comparable at lower temperatures for these samples, but at elevated temperatures, the BaTiO_3 (NO_3^-) sample displays the highest loss which may be caused by the high porosity. The results are summarized in Table 4.4.

Table 4.4. Dielectric properties, grain size and density of the BaTiO_3 powders with various barium sources sintered at 1300°C for 5 hours.

BaTiO_3 samples	K (30°C)	$\tan\delta$ (30°C)	Grain size (μm)	Density* (g/cm^3)
BaTiO_3 (NO_3^-)	677	0.019	3~15	5.23 (87%)
BaTiO_3 ($\text{C}_2\text{H}_3\text{O}_2^-$)	1162	0.028	10~20	5.75 (96%)
BaTiO_3 (Cl^-)	1938	0.029	1~5	5.81 (97%)
Commercial (TAM)	1525	0.011	1~10	5.74 (95%)

*: values in parentheses are the relative densities compared to the theoretical density.

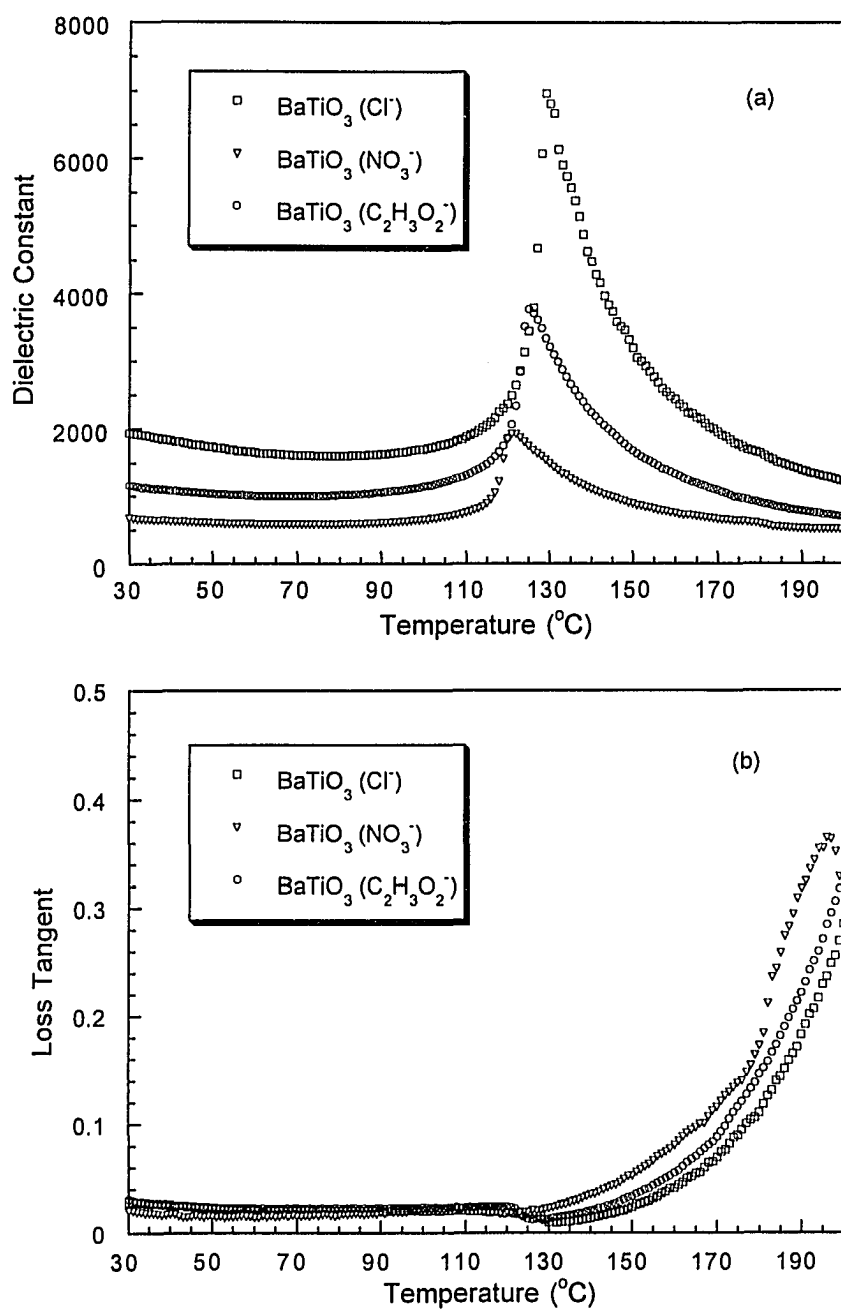


Figure 4.27. Dielectric properties: (a) dielectric constant and (b) loss tangent as a function of temperature for the BaTiO₃ samples synthesized from various barium sources.

Figure 4.28 shows the dielectric property measurement as a function of temperature for the BaTiO₃ (Cl⁻) sample sintered at 1200, 1250 and 1300°C. The result is compared with that obtained for the BaTiO₃ (TAM) sample (Figure 4.29). The BaTiO₃ (Cl⁻) sample sintered at 1250°C gives the highest dielectric constant of 2960. This corresponds to the highest density (almost 100% of theoretical density) and near optimum grain sizes (~ 2.5 μm). The dielectric constant decreases at either lower and higher sintering temperatures, resulting from the high porosity and large grain size of the sintered samples, respectively. The loss tangent of the sintered samples is roughly proportional to the porosity with a higher porosity yielding a higher loss tangent. The results are summarized in Table 4.5.

Table 4.5. Dielectric properties, grain size and density of the BaTiO₃ (Cl⁻) powders sintered at various temperatures for 5 hours.

Sintering temperature (°C)	K (30°C)	$\tan\delta$ (30°C)	Grain sizes (μm)	Density* (g/cm ³)
1200	1365	0.050	< 1	5.52 (92%)
1250	2960	0.027	2	5.95 (99%)
1300	1938	0.029	3	5.88 (98%)
1350	1745	0.034	20	5.76 (96%)

*: values in parentheses are the relative densities compared to the theoretical density.

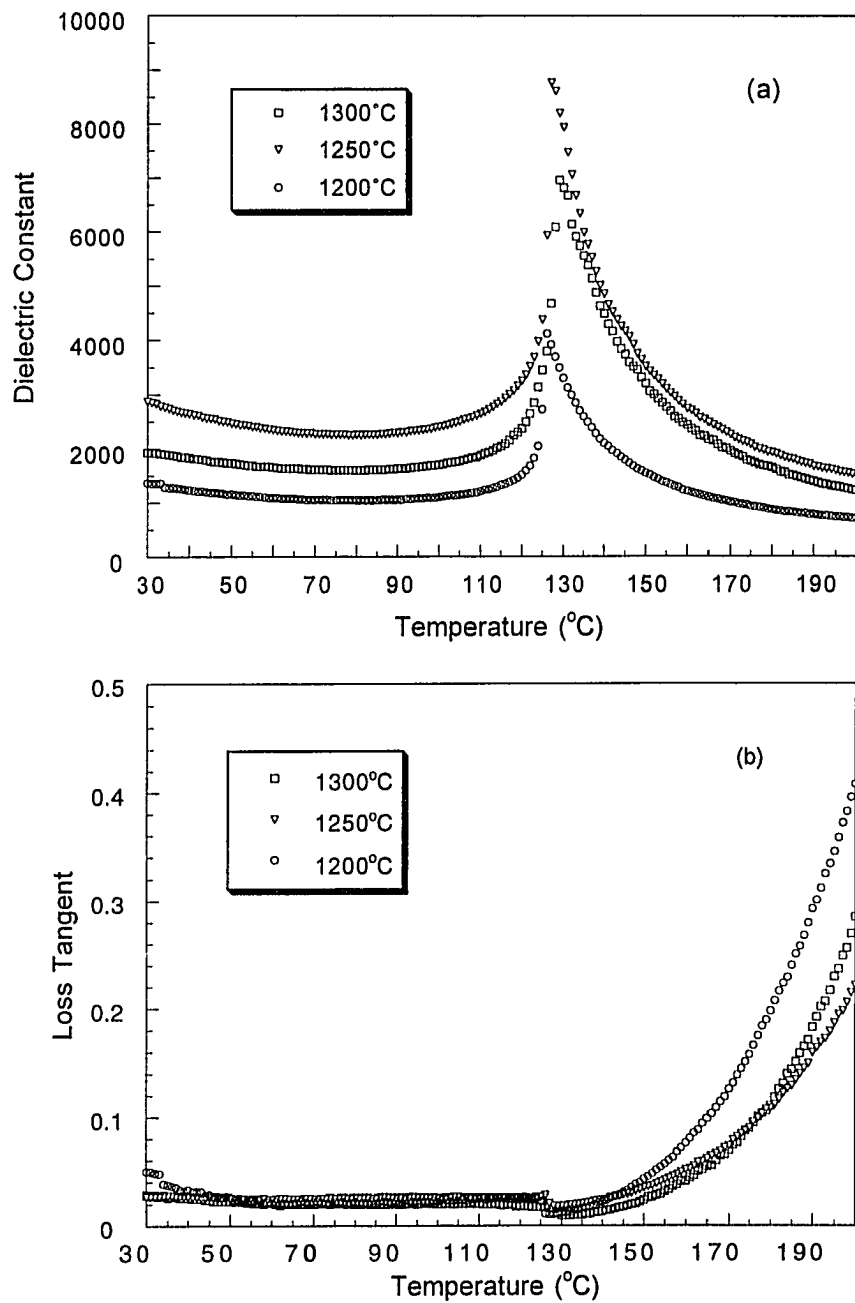


Figure 4.28. Dielectric properties: (a) dielectric constant and (b) loss tangent as a function of temperature for the BaTiO₃ (Cl⁻) sample sintered at various temperatures.

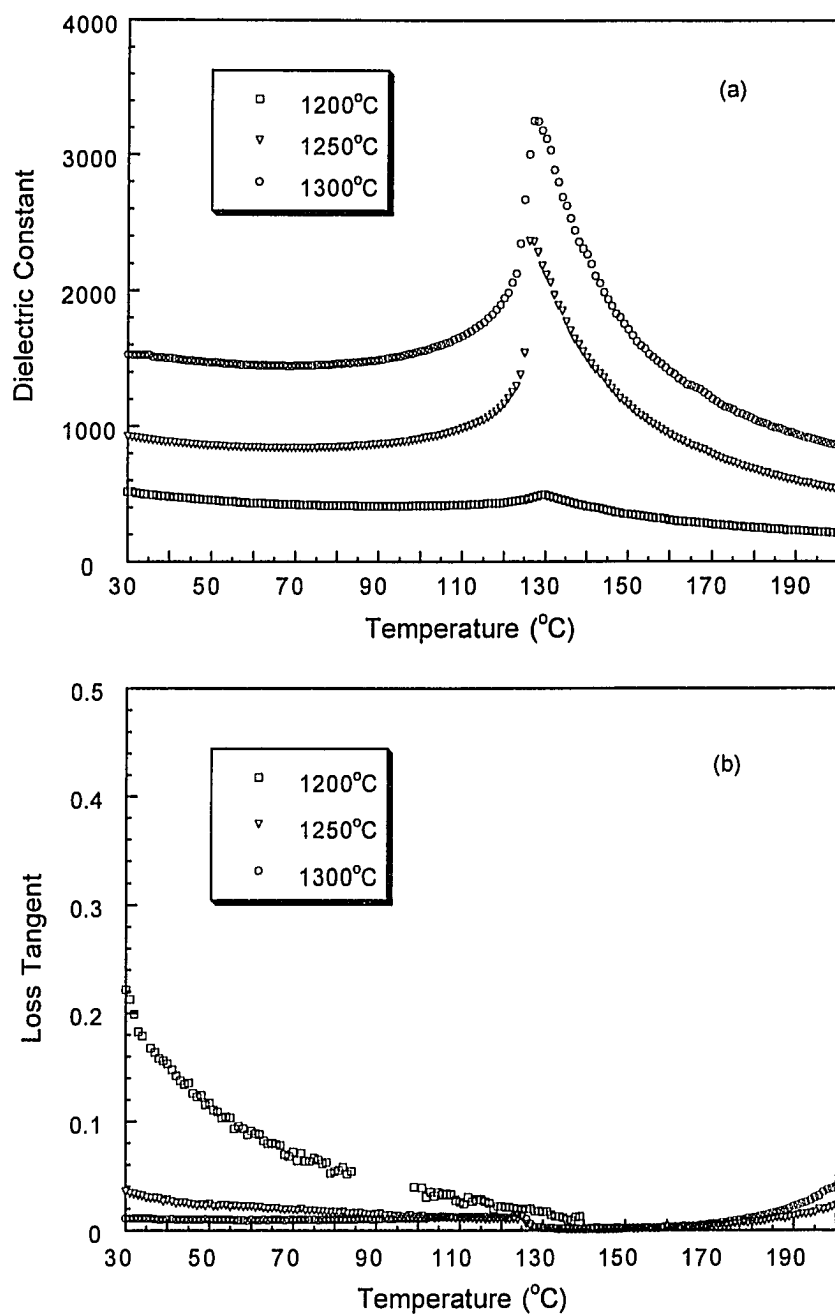


Figure 4.29. Dielectric properties: (a) dielectric constant and (b) loss tangent as a function of temperature for the BaTiO₃ (TAM) sample sintered at various temperatures.

On the other hand, the BaTiO₃ (TAM HPB) sample shows an increase in dielectric constant toward higher sintering temperatures (Figure 4.29). This may relate to the highly porous structure of the TAM samples sintered at temperatures lower than 1300°C, as evidenced by the density measurement (74% and 88% of the theoretical density for samples sintered at 1200 and 1250°C, respectively). The need for higher temperature sintering is due to the much coarser and more irregular-shaped particles in the powder, leading to the sintering occurring at higher temperatures (> 1300°C), as compared to the BaTiO₃ (Cl⁻) sample. Again, the much higher loss tangent for the sample sintered at 1200°C is due to its high porosity.

4.2.2. BaTiO₃ Ceramics from Hydrothermally Synthesized Powders with Various OH⁻ Concentrations

The sintering and the dielectric properties of the BaTiO₃ powders hydrothermally synthesized at 240°C with various OH⁻ concentrations (A, B and C) were studied together with the cubic powder synthesized at 95°C. The sinterability of the powders: cubic, B and C was first investigated using dilatometric measurements and the results are shown in Figure 4.30. It was noticed that powder A melted at 1340°C, and therefore the dilatometric measurement was not performed on this powder. For the temperature up to 1400°C, the cubic powder shows the highest shrinkage of about 24%, whereas it

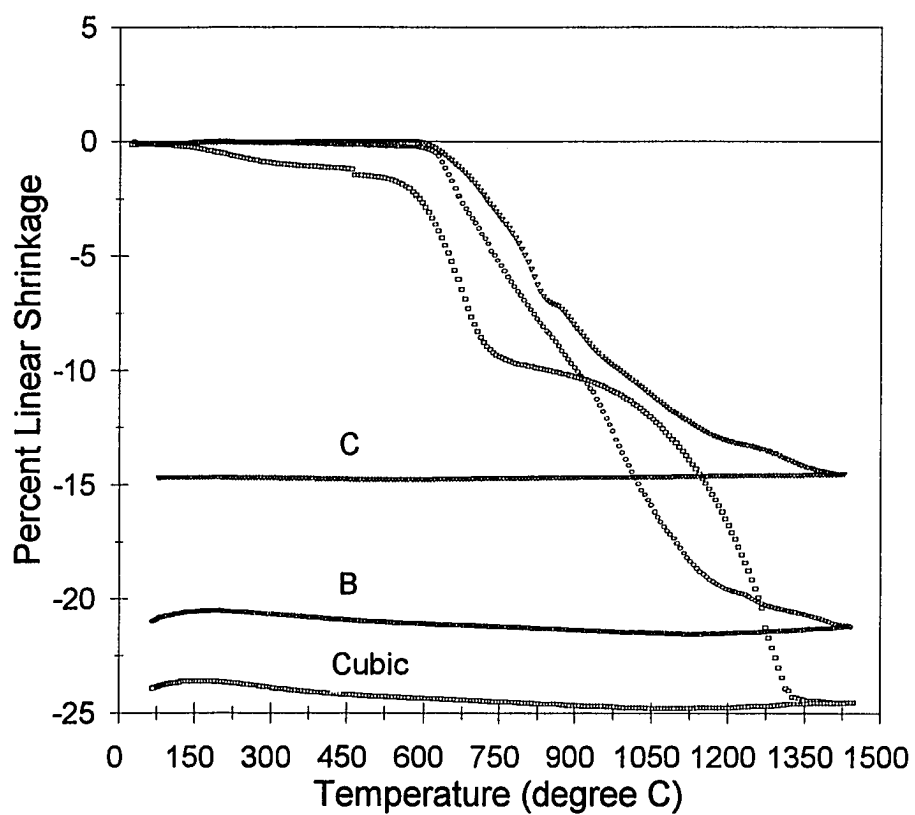
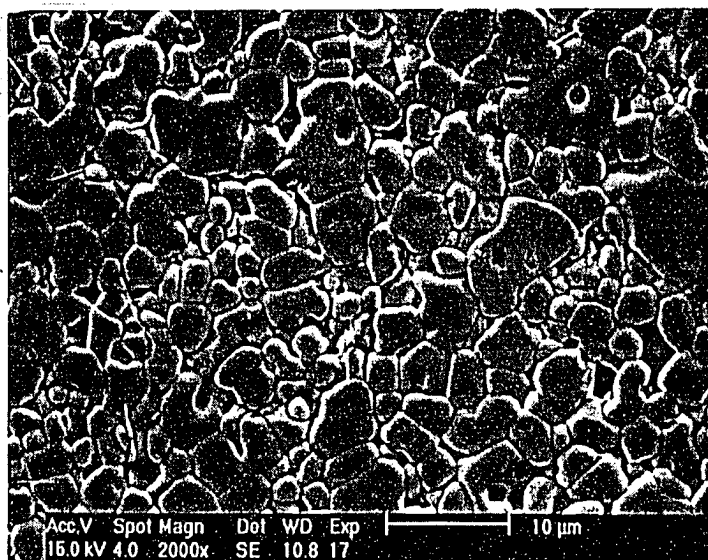


Figure 4.30. Dilatometric curves showing the linear percent shrinkage as a function of temperature for BaTiO_3 powders: cubic, B and C.

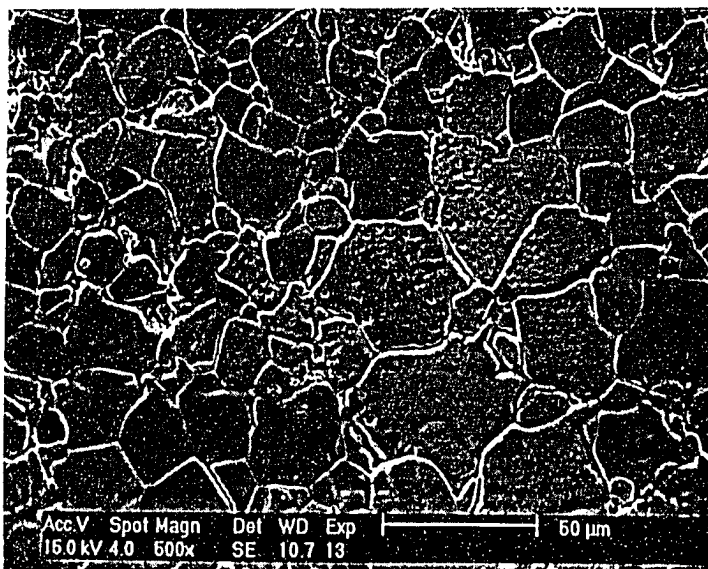
is about 20% and 15% for powders B and C, respectively. This may be attributed to the fact that the cubic powder has the lowest packing density (48%) compared with powders B and C (53% and 59%, respectively). The low green compact density of the cubic powder may result from the higher resistance of these rough, porous solid agglomerates to sliding and fracture [189]. The cubic powder obviously shows two stages of shrinkage, which may correspond to two different shrinkage mechanisms. This is typically observed for powders with fine particles [165, 351], and the reason has been suggested to be inhomogeneous densification of the agglomerates in the powders. The first shrinkage took place between 600~700°C; this is expected because of the ultrafine particles existing in the powder. There is a slowdown (shrinkage) between 700~1000°C, followed by a second shrinkage until the temperature is slightly above 1300°C. The second shrinkage is believed to be caused by the densification between relatively large agglomerates in the powder. It is also noticeable that the shrinkage rates of the powders B and C decrease as the temperature exceeds 1000°C (shown by decreasing slopes of the dilatometric curves), while the cubic powder shows a high shrinkage rate up to 1300°C. This indicates that powders B and C can reach relatively high density at lower temperatures as compared to the cubic powder.

I. Microstructure and dielectric properties of hydrothermal powders by conventional sintering

Hydrothermally synthesized powders, cubic, A, B and C, were sintered at temperatures ranging from 1200 ~ 1350°C for 2 hours at a heating rate of 5°C/min. Figures 4.31-4.33 show the SEM micrographs of the cubic powder sintered at 1250, 1300 and 1350°C, and B and C powders sintered at 1200, 1250 and 1300°C. Powder A, having significant excess of Ti (as indicated by ICP), melts at the sintering temperature of 1350°C; thus, its microstructure was not pursued in this study. Figures 4.34-4.37 show the dielectric constant and loss measurement as a function of temperature of selected sintered samples from the cubic, A, B and C powders. The results of sintering, density and dielectric property measurements are summarized in Table 4.6. The results indicate that the cubic powder gives a maximum dielectric constant of 2814 when sintered at 1250°C, corresponding to 93% of theoretical density and about 5 μm grain size. It is interesting to note that the density does not improve much at higher sintering temperatures (for the cubic powder). Instead, sintering at higher temperatures leads to rapid grain growth that lowers the dielectric constant. Powder A shows very low dielectric constant and high loss. It has been reported that BaTiO₃ powders with excess Ti form Ba₆Ti₁₇O₄₀ (second phase) during sintering, which is very detrimental to the dielectric properties of



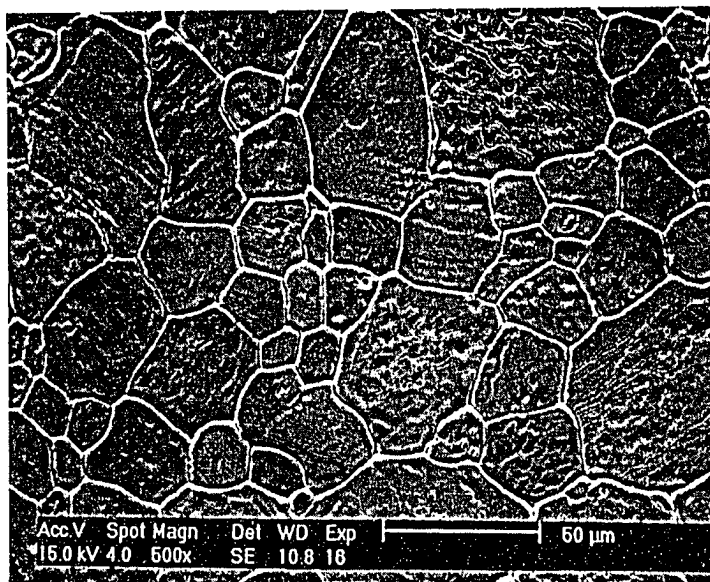
(a)



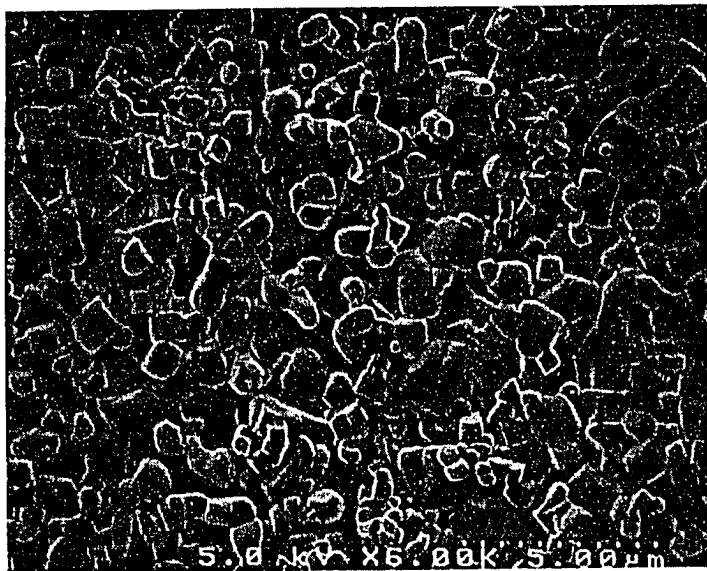
(b)

Figure 4.31. SEM micrographs of the cubic powder sintered at different temperatures: (a) 1250; (b) 1300 and (c) 1350°C.

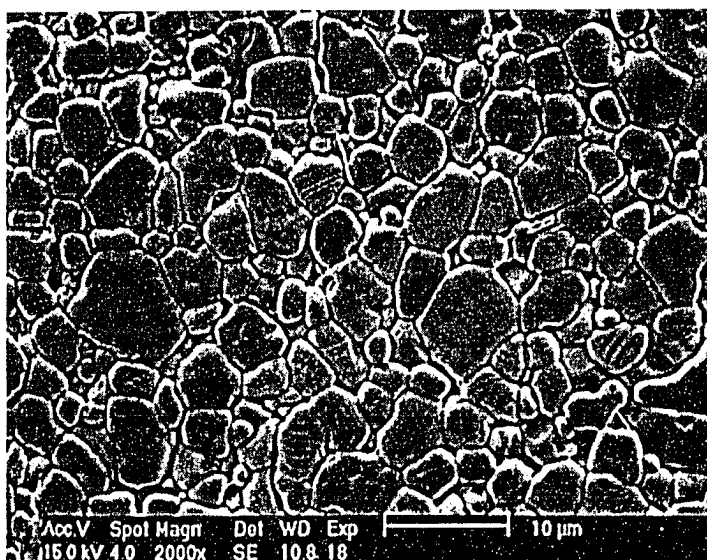
Figure 4.31. (continued),



(c)



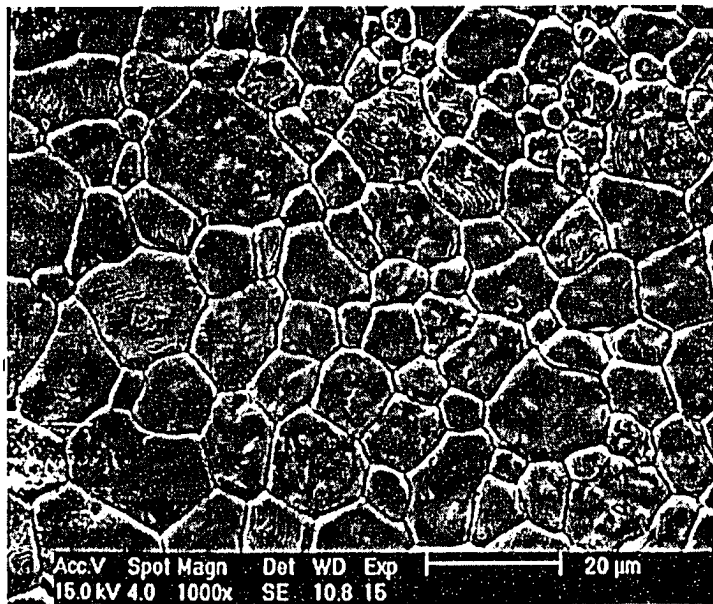
(a)



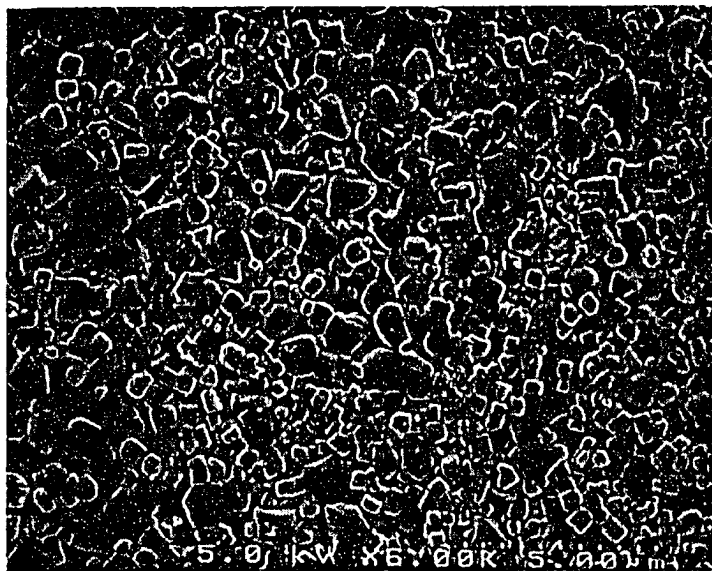
(b)

Figure 4.32. SEM micrographs of powder B sintered at different temperatures: (a) 1200; (b) 1250 and (c) 1300°C.

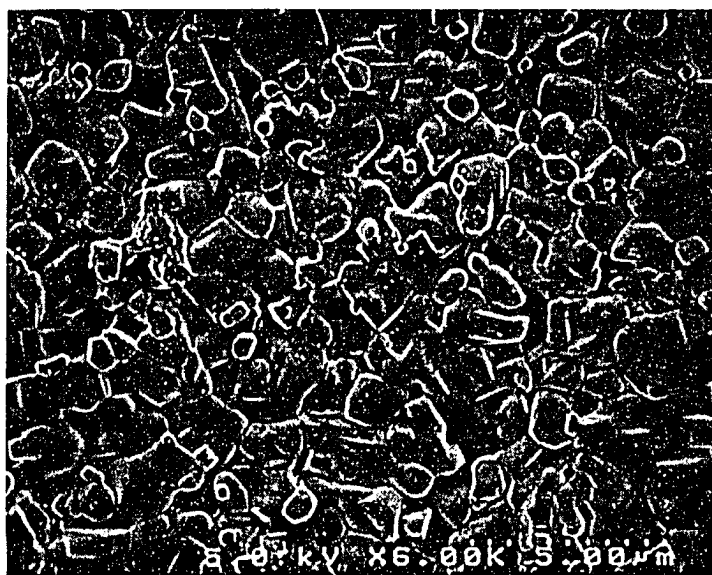
Figure 4.32. (continued),



(c)



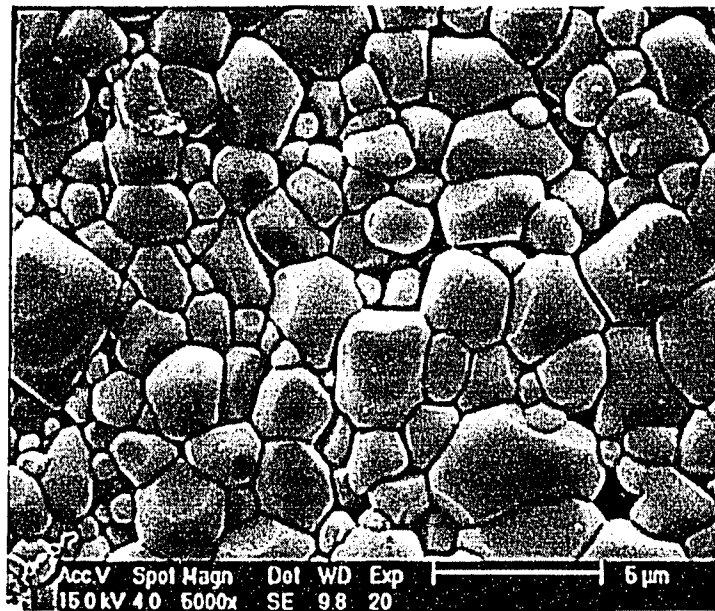
(a)



(b)

Figure 4.33. SEM micrographs of powder C sintered at different temperatures: (a) 1200; (b) 1250 and (c) 1300°C.

Figure 4.33. (continued),



(c)

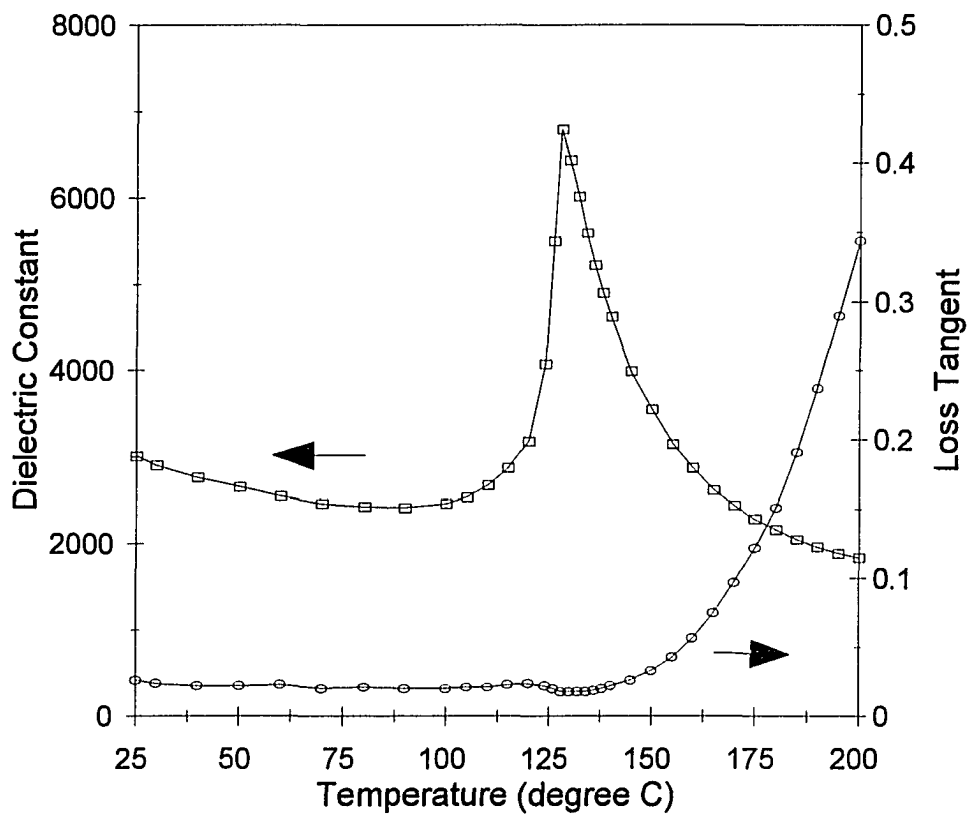
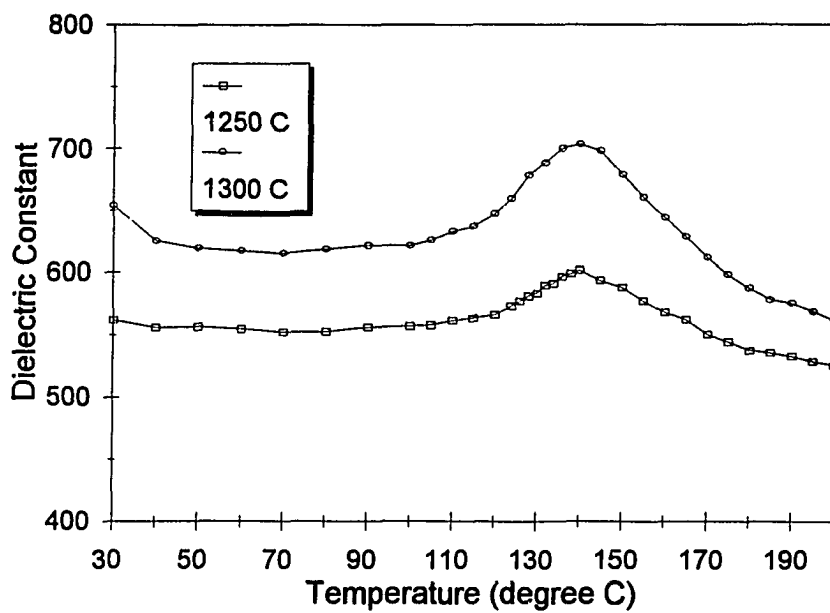
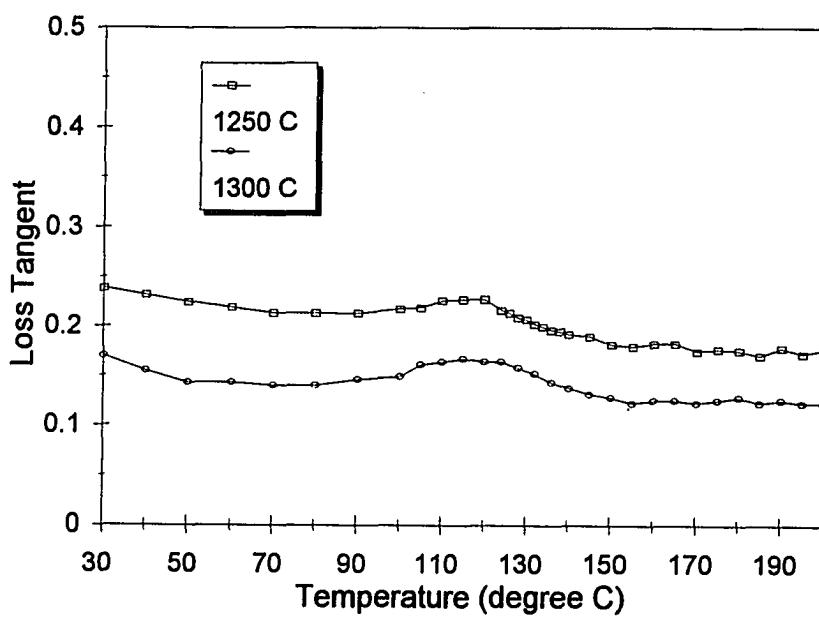


Figure 4.34. Dielectric constant and loss measurement as a function of temperature of the sample from the cubic powder sintered at 1250°C for 2 hours.

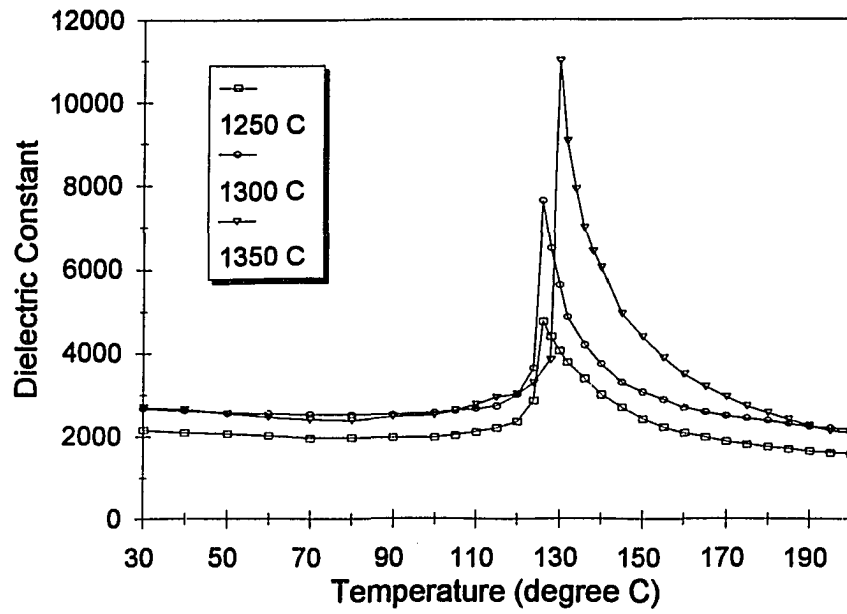


(a)

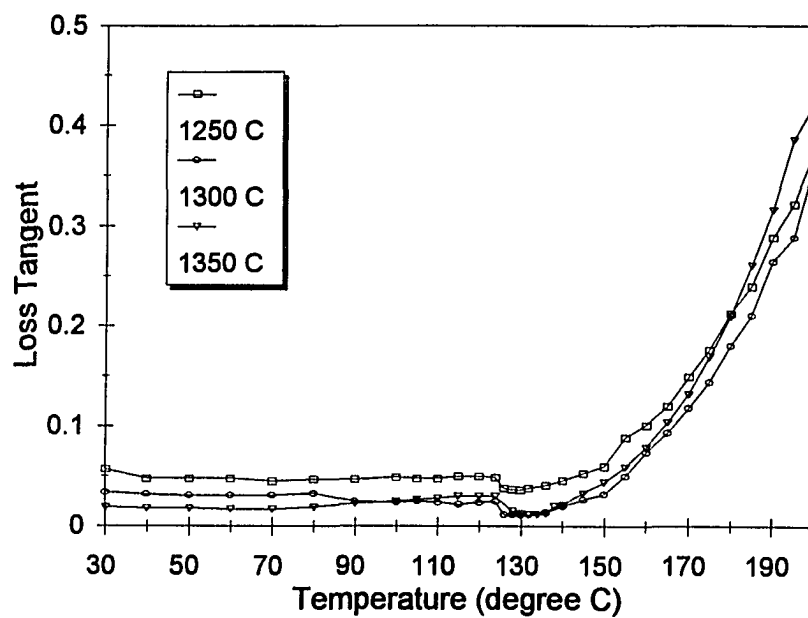


(b)

Figure 4.35. Dielectric constant and loss measurement as a function of temperature of selected sintered samples from powder A.

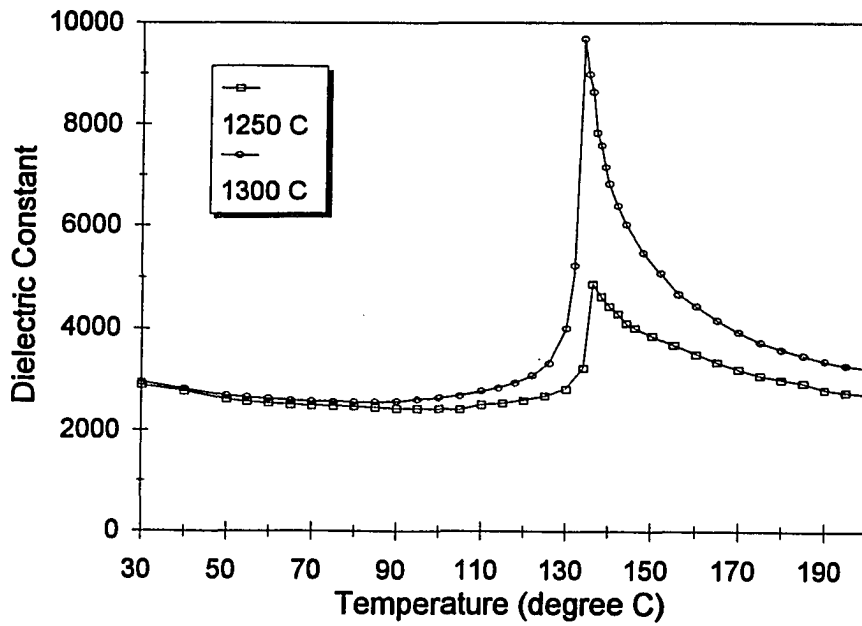


(a)

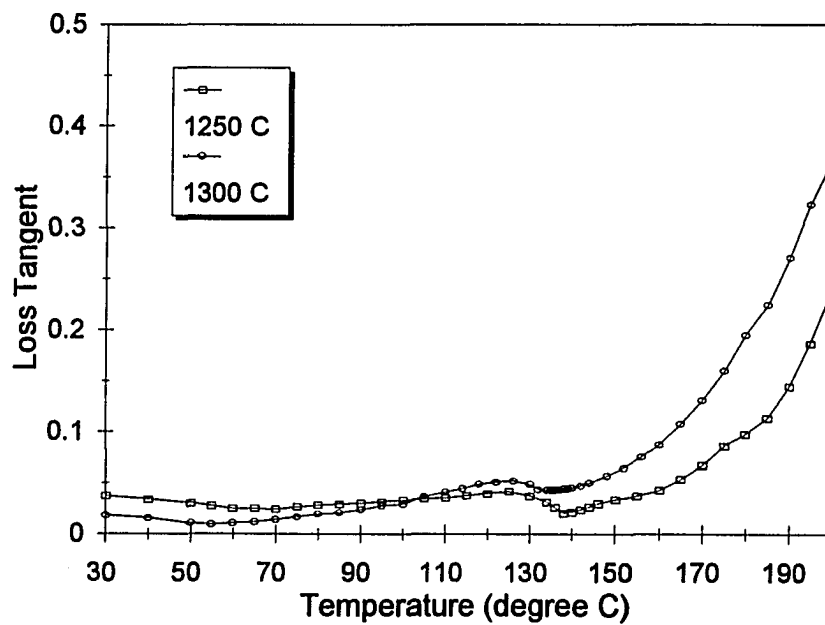


(b)

Figure 4.36. Dielectric constant and loss measurement as a function of temperature of selected sintered samples from powder B.



(a)



(b)

Figure 4.37. Dielectric constant and loss measurement as a function of temperature of selected sintered samples from powder C.

the samples [188, 352]. However, for powders B and C, a relatively high density can be reached at the sintering temperature of 1250°C, and approaches even higher values as the sintering temperature increases. More importantly, a limited grain growth was also noticed for powders B and C, and appears to become more significant as the tetragonality of the powders increases. A maximum dielectric constant of 3027 was observed for powder C sintered at 1300°C; the sintered sample achieves 97% of the theoretical density and has an average grain size of approximately 3 μm .

II. Fast-Sintering

Fast-sintering was performed on the hydrothermally synthesized cubic powder in an effort to enhance the densification during sintering. Figure 4.38 shows the SEM micrographs of the cubic powders sintered at 1250, 1300 and 1350°C for 5 minutes. Their dielectric properties are shown in Figure 4.39. The results are summarized in Table 4.7. It is remarkable that all samples show very limited grain growth and relatively high densities. The sample sintered at 1250°C gives a very high dielectric constant close to 3500 with almost an optimum grain size of 1 μm .

Table 4.6. Density and dielectric properties of the powders cubic, A, B and C sintered at various temperatures for 2 hours.

BaTiO ₃ Samples	Sintering temperature (°C)	<i>K</i> at 30°C	<i>tanδ</i> at 30°C	Density* (g/cm ³)	Grain size (μm)
cubic (95°C synthesis)	1200	1783	0.085	5.18 (86%)	---
	1250	2814	0.038	5.61 (93%)	~ 5
	1300	2663	0.039	5.63 (93%)	~ 20
	1350	2558	0.037	5.59 (94%)	~ 28
A (tetragonal)	1200	505	0.259	4.92 (82%)	---
	1250	561	0.238	5.07 (84%)	---
	1300	654	0.170	5.12 (85%)	---
	1350 [†]	---	---	---	---
B (tetragonal)	1200	1862	0.102	5.32 (88%)	---
	1250	2168	0.057	5.54 (92%)	~ 4
	1300	2676	0.025	5.69 (95%)	~ 10
	1350	2710	0.019	5.78 (96%)	---
C (tetragonal)	1200	2034	0.089	5.38 (89%)	---
	1250	2887	0.037	5.71 (95%)	~ 2
	1300	3027	0.021	5.82 (97%)	~ 3
	1350	2846	0.024	5.81 (97%)	---

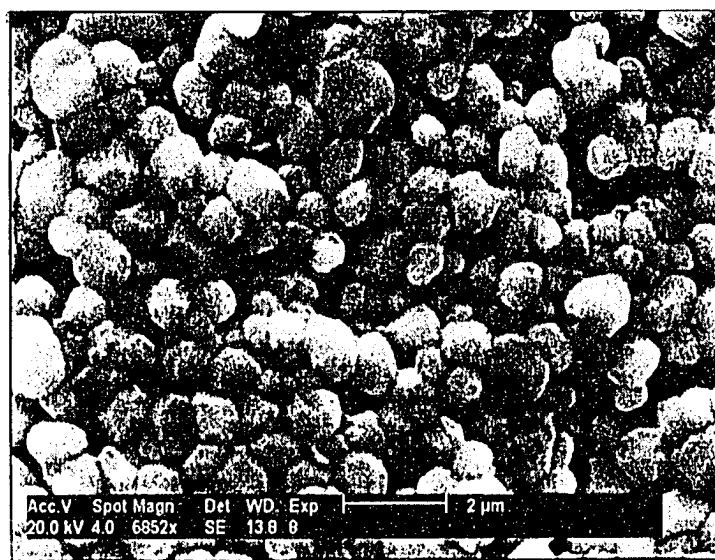
*: values in parentheses are the relative densities compared to the theoretical density; [†]: sample melted; ---: data not obtained.

Table 4.7. Density and dielectric properties of the cubic powders fast-sintered at various temperatures for 5 minutes.

Sintering temperature (°C)	K (30°C)	$\tan\delta$ (30°C)	Grain sizes (μm)	Density* (g/cm^3)
1250	3476	0.020	~ 1	5.53 (92%)
1300	3174	0.026	~ 2	5.65 (94%)
1350	2392	0.009	~ 4	5.71 (95%)

*: values in parentheses are the relative densities compared to the theoretical density.

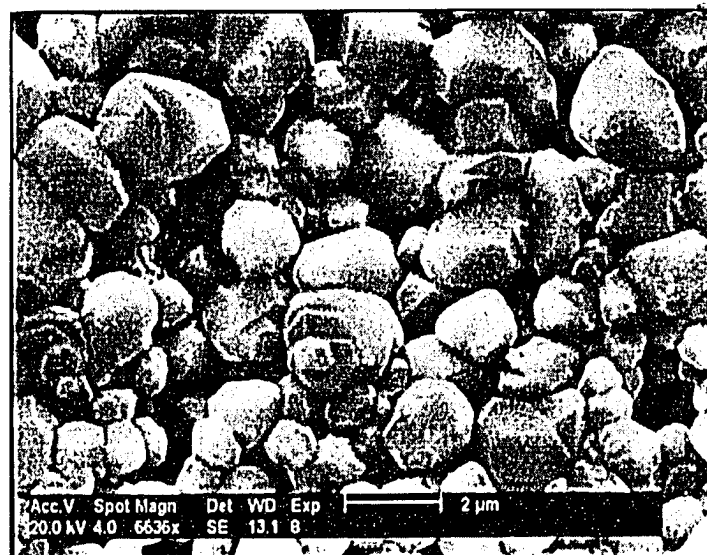
The cubic powder was also fast-sintered at 1250 and 1300°C for 15 minutes. The sintered samples have high densities of 5.76 (96%) and 5.89 g/cm^3 (98%), respectively. However, the grain sizes of the samples were estimated to be larger than 10 μm , leading to the decrease of the dielectric constant of the samples. The result of the dielectric property measurement as a function of temperature is shown in Figure 4.40.



(a)

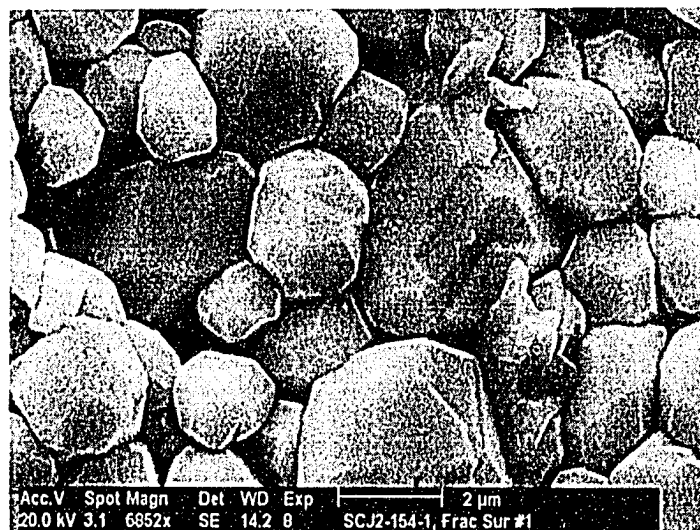
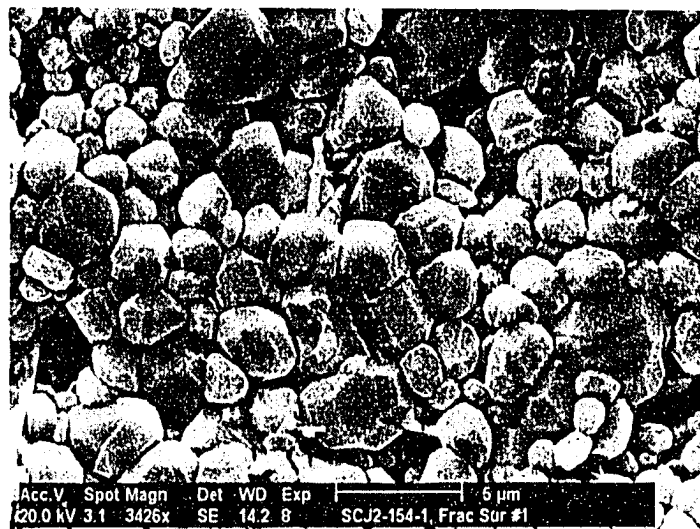
Figure 4.38. SEM micrographs of the hydrothermally synthesized BaTiO_3 cubic powder sintered at various temperatures for 5 minutes ($\sim 200^\circ\text{C}/\text{min}$): (a) 1250, (b) 1300 and (c) 1350°C. Each one is shown in two different scales.

Figure 4.38. (continued),

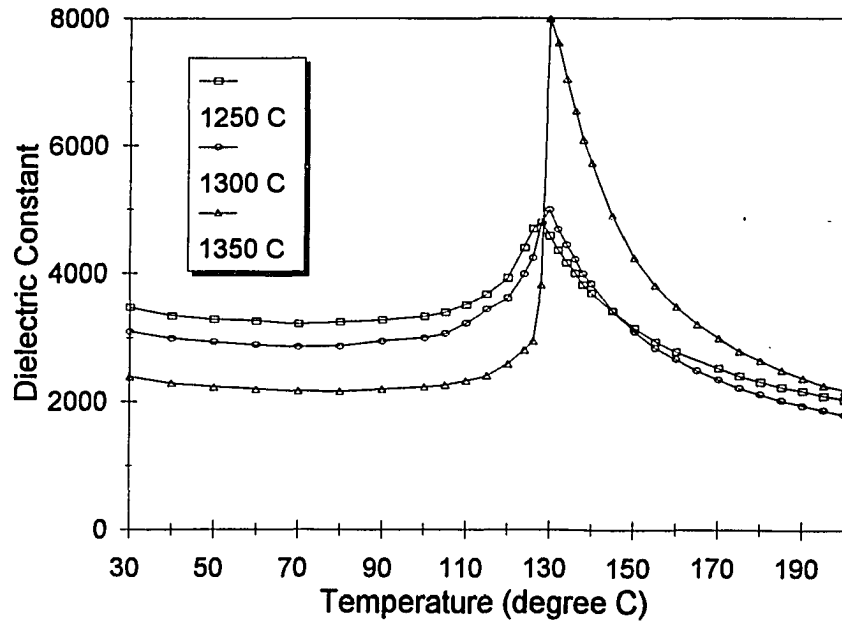


(b)

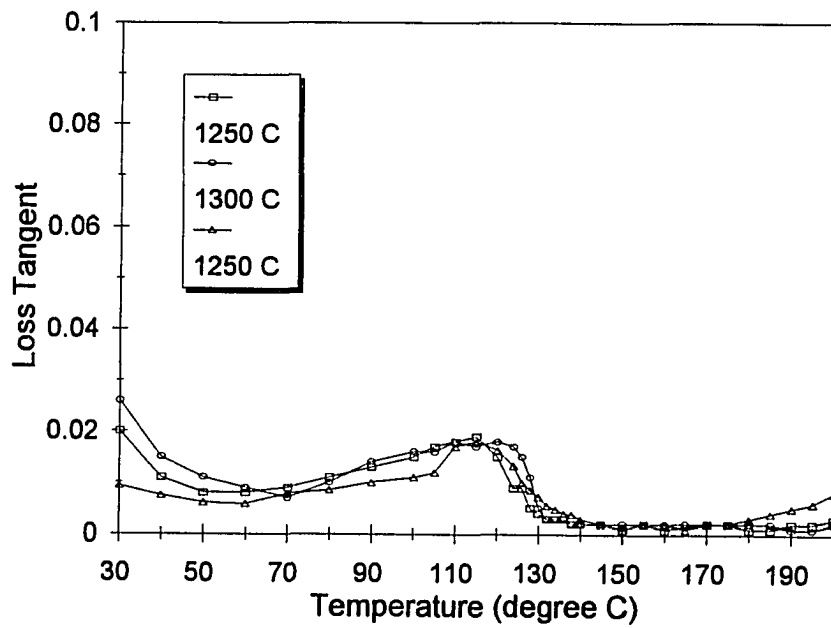
Figure 4.38. (continued),



(c)

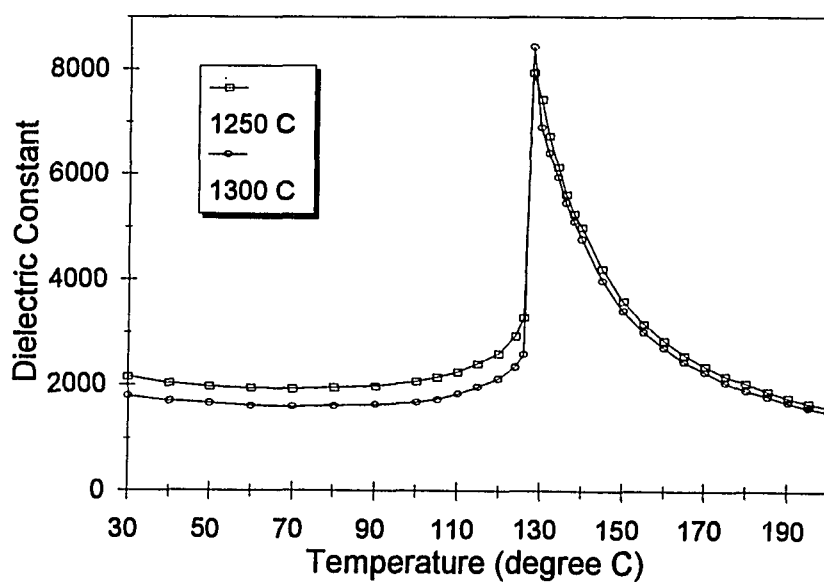


(a)

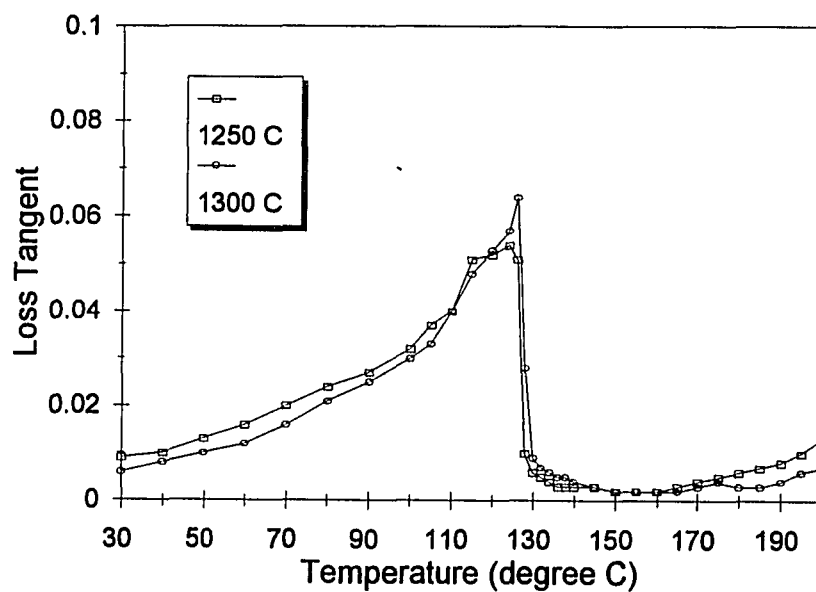


(b)

Figure 4.39. Dielectric properties: (a) dielectric constant and (b) loss tangent as a function of temperature for the hydrothermally synthesized cubic BaTiO_3 sample sintered at various temperatures for 5 minutes with a rate of about $200^\circ\text{C}/\text{min}$.



(a)



(b)

Figure 4.40. Dielectric properties: (a) dielectric constant and (b) loss tangent as a function of temperature for the hydrothermally synthesized cubic BaTiO_3 sample sintered at various temperatures for 15 minutes ($\approx 200^\circ\text{C}/\text{min}$).

4.2.3. Impedance Spectroscopy Analysis

In the electrical measurement of polycrystalline materials, the electrical data obtained are the response of the whole measurement assembly, including electrodes, lead-wires, and the sample. Moreover, in polycrystalline ceramics, both grains and grain boundaries contribute to the electrical properties. In order to extract the intrinsic properties of the materials, impedance spectroscopy analysis was used to separate the various contributions from these components according to their frequency dependence.

In this study, a BaTiO₃ ceramic pellet from the hydrothermally synthesized cubic powder sintered at 1250°C for 2 hours was used, since it has relatively high density and good dielectric properties. Plot of the capacitance vs. frequency is shown in Figure 4.41. An obvious dispersion of capacitance over the frequency range from 10 Hz to approximately 1 kHz was observed at elevated temperatures (> 200°C). The dispersion becomes more significant and shifts to higher frequencies as the temperature increases.

Figures 4.42-4.46 show the ac electrical data of the sample obtained at temperatures of 250, 300, 400, 450 and 500°C and plotted in the impedance plane, modulus plane, capacitance plane and admittance plane, respectively. Two plots corresponding to different temperature regimes are used for each plane in an effort to clearly delineate the relaxation behavior at various

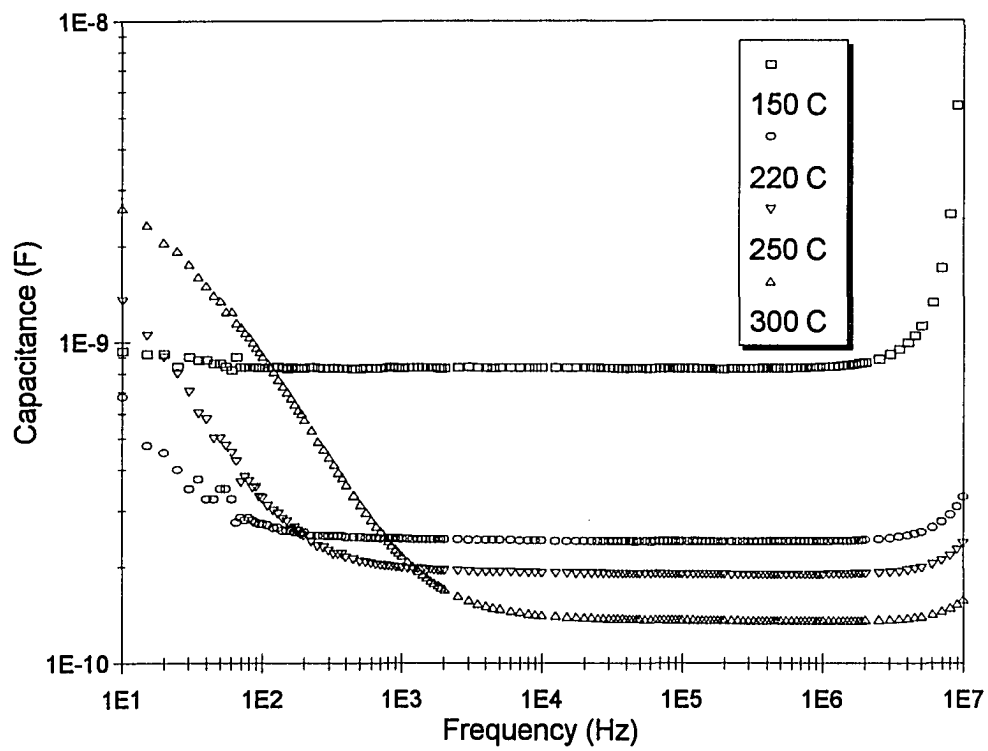


Figure 4.41. The capacitance versus frequency for the cubic sample sintered at 1250°C for 2 hours.

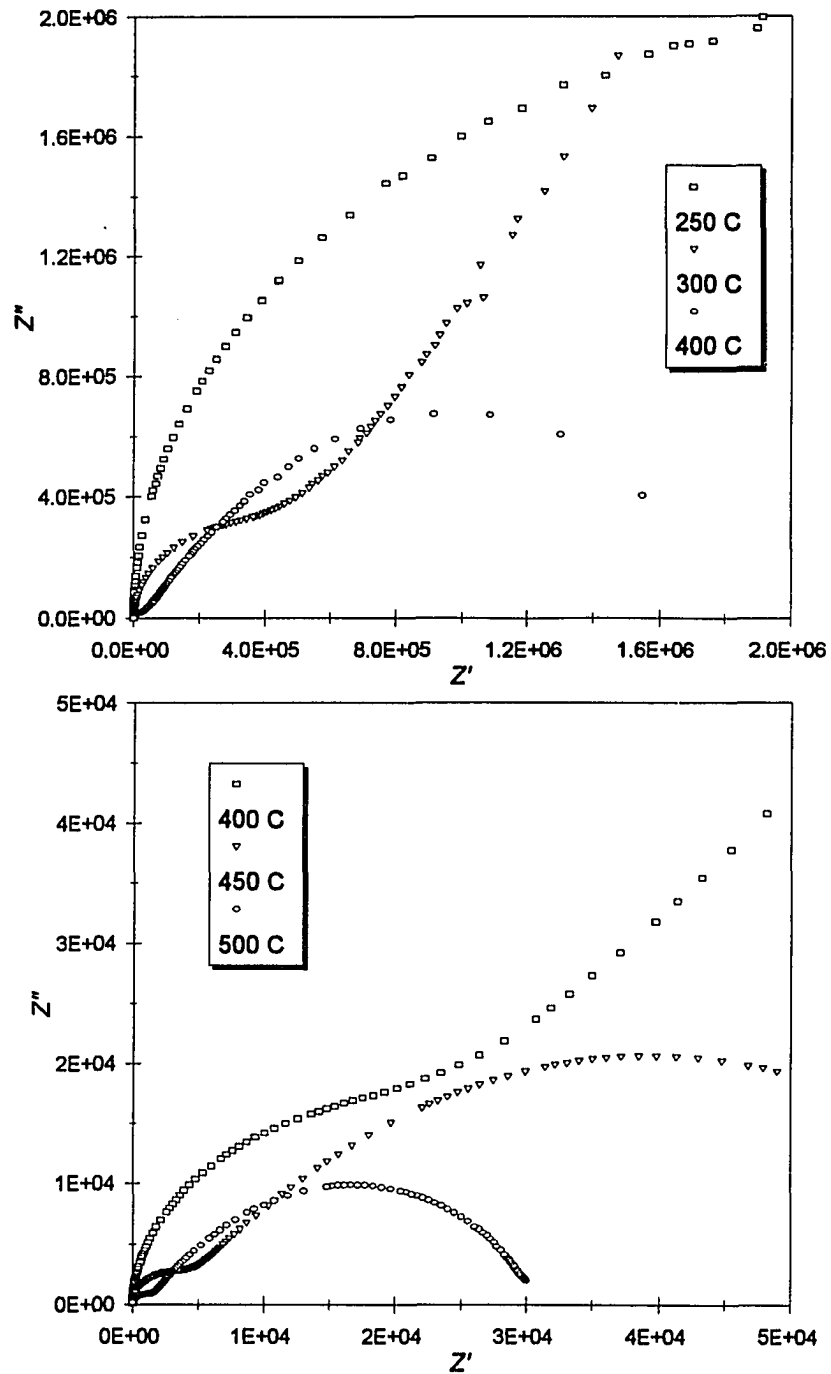


Figure 4.42. Impedance plots of the sintered ceramic sample measured at various temperatures. For the purpose of clarity, two separate plots are shown to illustrate the entire measuring temperature range.

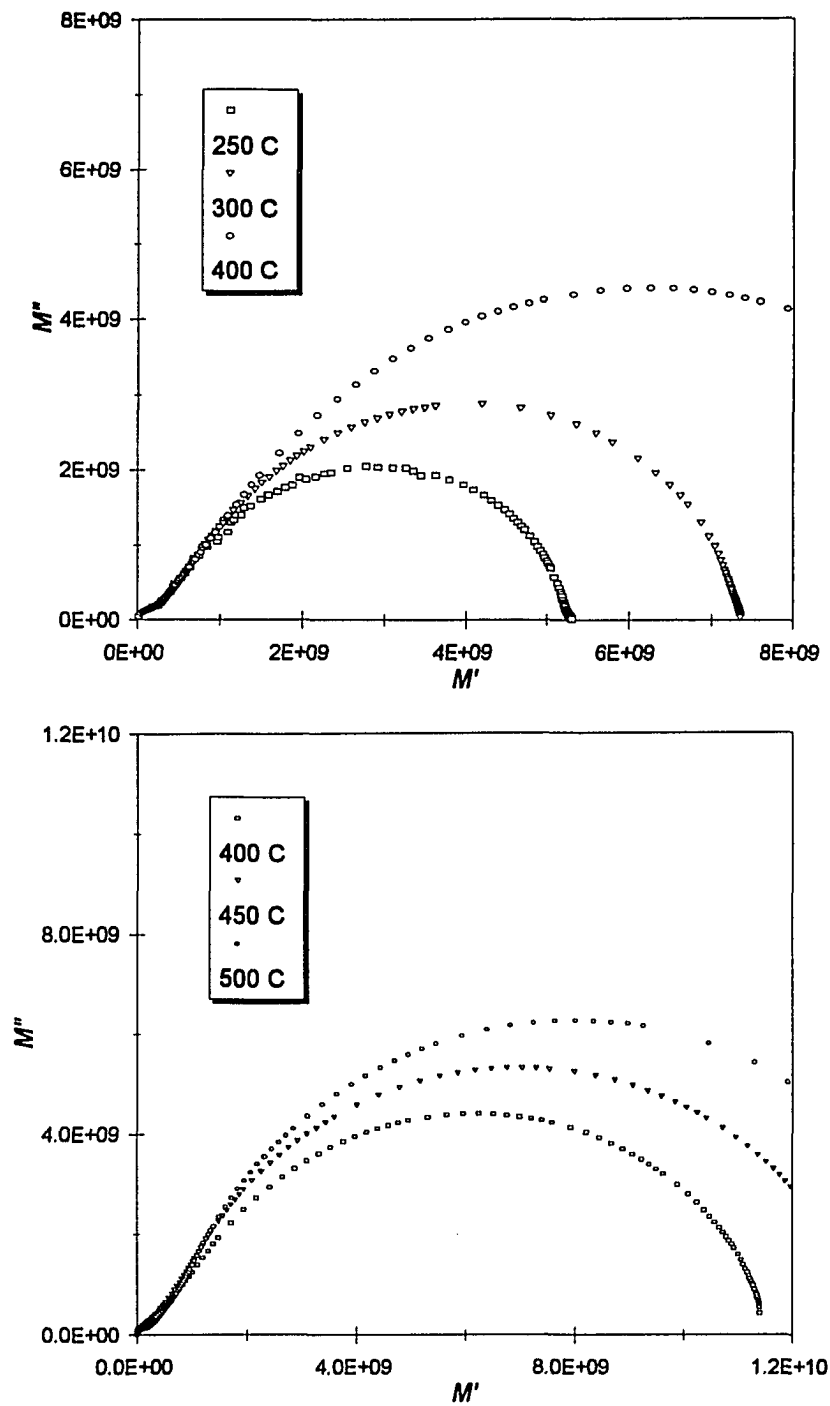


Figure 4.43. Modulus plots of the same sample as in Figure 4.42 at various temperatures.

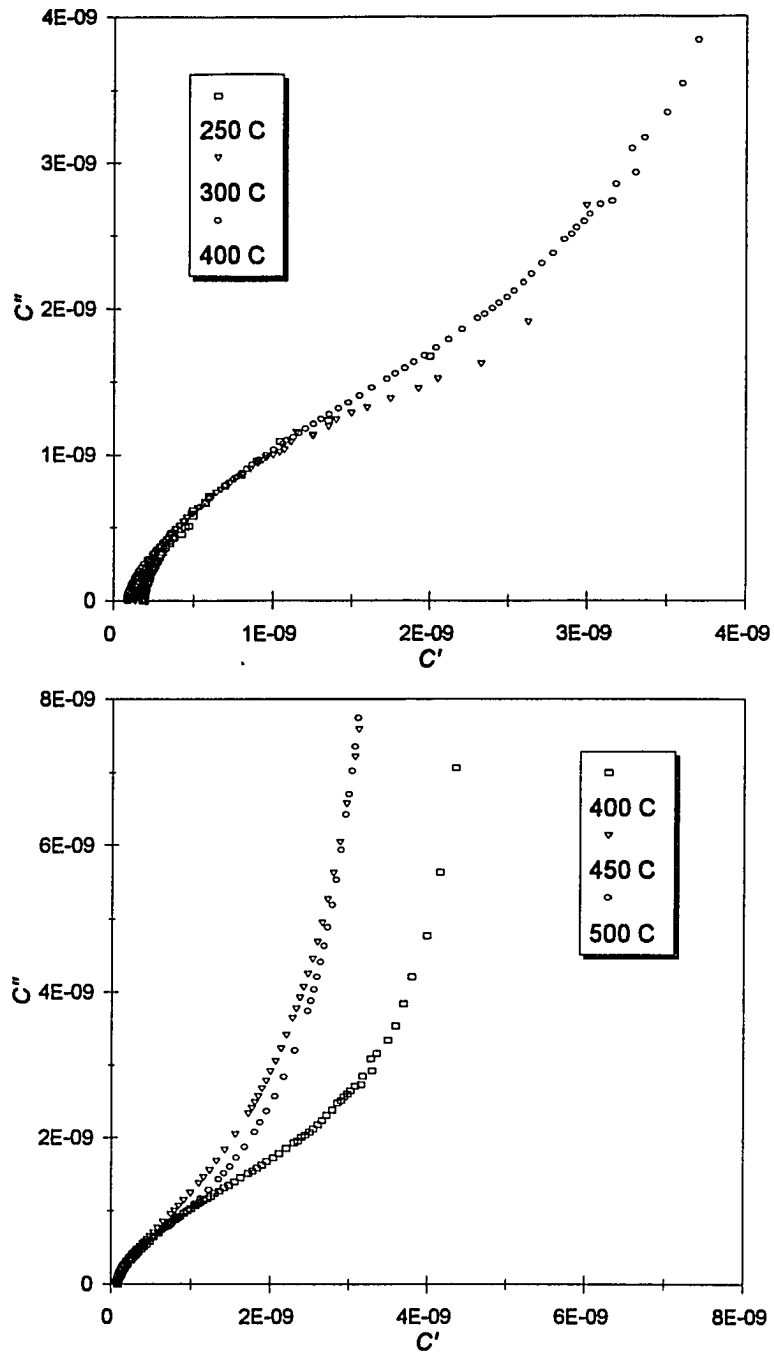


Figure 4.44. Capacitance plots of the same sample as in Figure 4.42 at various temperatures.

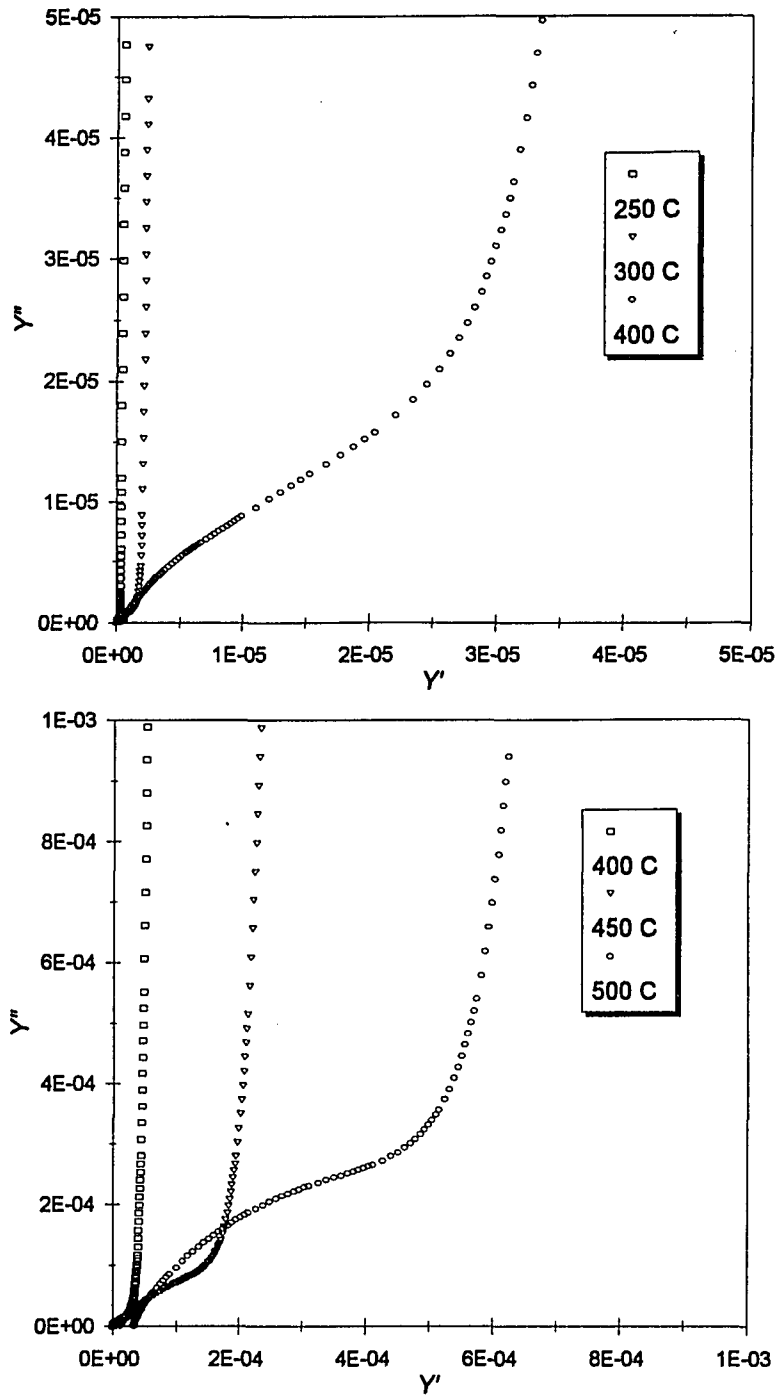


Figure 4.45. Admittance plots of the same sample as in Figure 4.42 at various temperatures.

temperatures. In the impedance plane (Figure 4.42), two semicircles were observed at temperatures above 250°C, with the low frequency semicircle (right side) emerging at 250°C and becoming more dominant at higher temperatures. When the same data are displayed in the modulus plane, M^* (Figure 4.43), a single semicircle corresponding to high frequency relaxation was prominent at all temperatures. However, there is small inflection of the spectrum in the low frequency range, corresponding to the low frequency relaxation observed in the Z^* -plane. When the electrical data are plotted in the capacitance plane (C^* -plane) (Figure 4.44), an incomplete semicircle in the high frequency region and a nearly vertical line in the low frequency region are observed. A similar behavior is evident in the admittance plane (Y^* -plane) (Figure 4.45); however, now the semicircle is in the low frequency region and the vertical line corresponds to the high frequency region.

The relaxation behavior of the sample at different temperatures was analyzed and the electrical parameter associated with the relaxations at various temperatures were extracted. To better illustrate the relaxation behavior and mechanisms associated with them, the electrical parameters obtained will be shown and discussed in Chapter V (Discussion).

4.3. Characterization of Hydrothermally Synthesized BaTiO₃ Thin Films

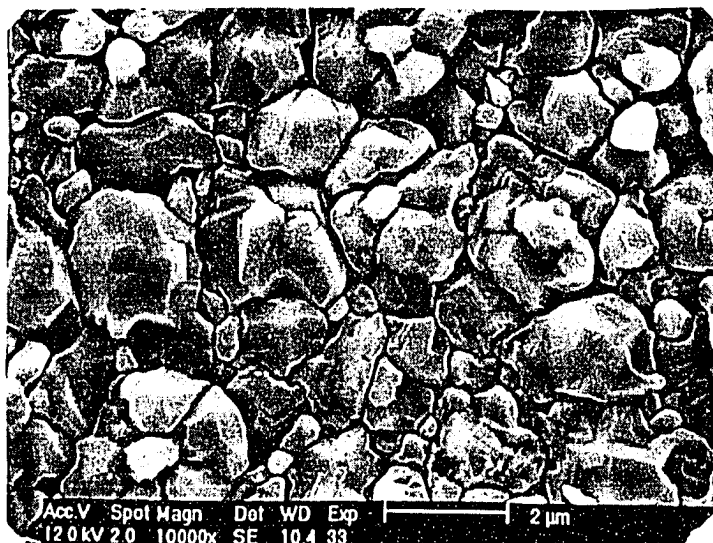
4.3.1. Microstructure

The morphology of the thin-film samples synthesized for 1 to 4 weeks are shown in Figure 4.46. The size and shape of the grains were found to be dependent on the synthesis time. For samples synthesized for 1 and 2 weeks, the grain shapes were very irregular and the average size increases from approximately 1.0 to 2.0 μm . It was also observed that for the sample synthesized for one week, there are some regions where the substrate is not completely covered with the BaTiO₃ film. As the time increases to 3 weeks, the grains are more regular in shape; however, the size distribution is more like bimodal with small grains sitting between the large grains. When the time increases further to 4 weeks, the grains remain regular in shape while the grains readjust the structure to achieve a more uniform distribution. Figure 4.47 shows the film surface at a low magnification, indicating that the films thus produced were reasonably smooth, dense and also free of cracks. It is interesting to note that the thickness of the film varies very little with the synthesis time; the film thickness remains about 0.5 μm for all the samples synthesized for 1 to 4 weeks. Figure 4.48 reveals the cross-sectional view of a representative film sample synthesized for 2 weeks.

The X-ray diffraction results are shown in Figure 4.49. No diffraction peaks corresponding to other phases are detected except those for BaTiO₃ and



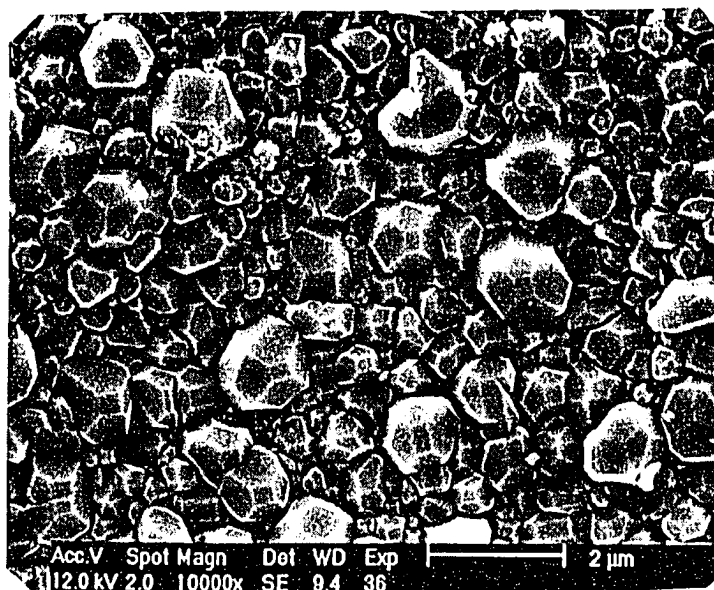
(a)



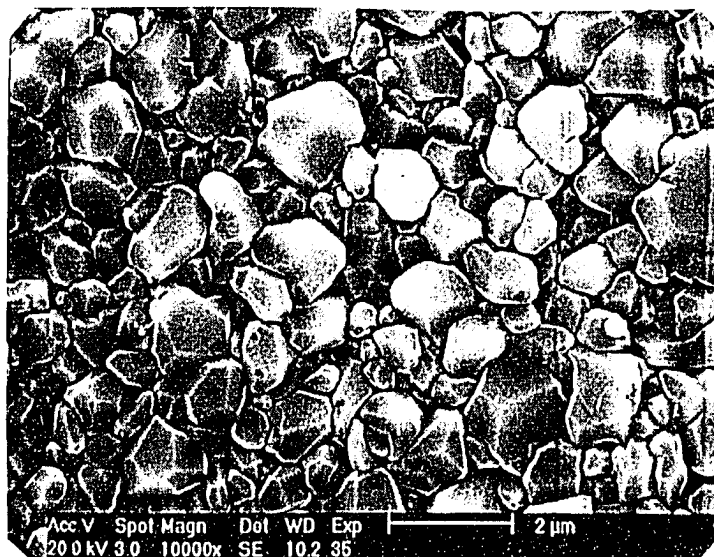
(b)

Figure 4.46. The SEM micrographs showing the morphology of the thin-film samples synthesized for various times: (a) 1; (b) 2; (c) 3 and (d) 4 weeks.

Figure 4.46. (continued),



(c)



(d)

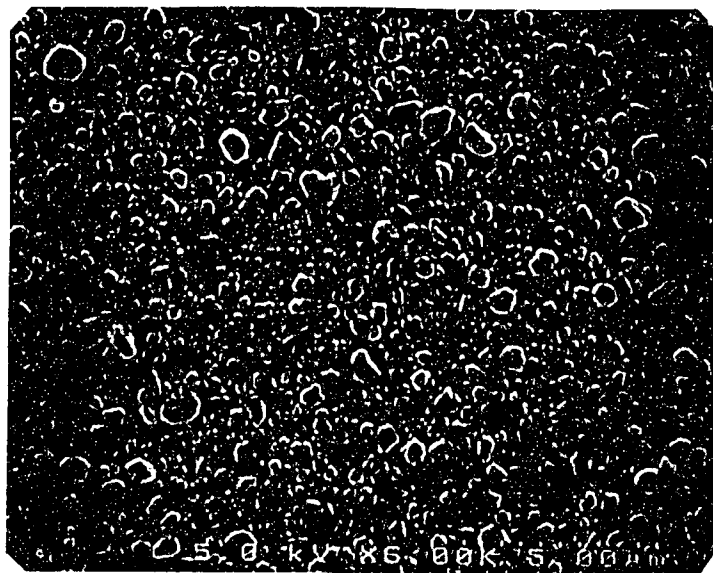


Figure 4.47. Low magnification SEM micrograph showing the smooth, dense film surface without observable cracks.

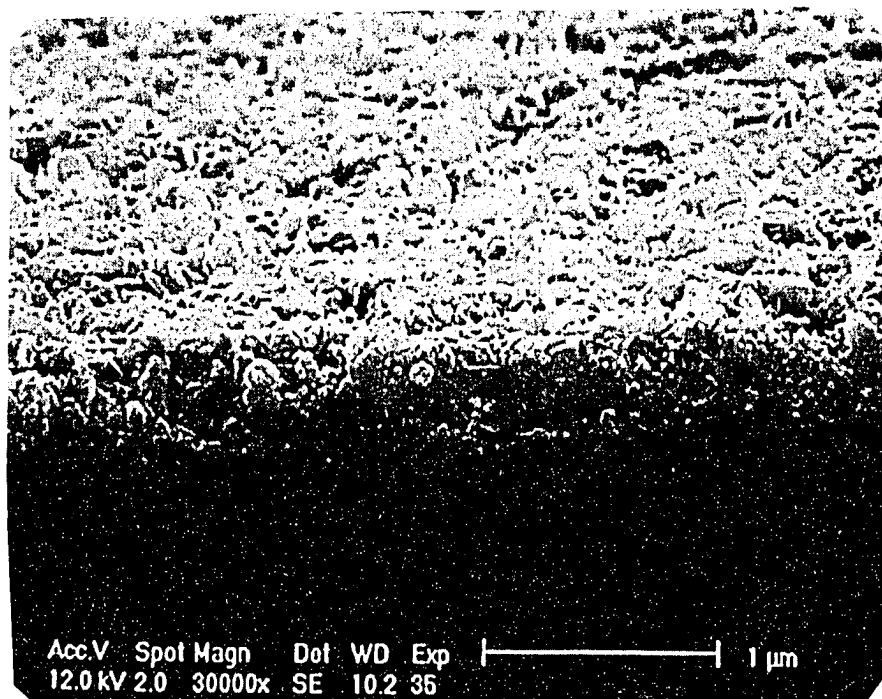


Figure 4.48. SEM micrograph of the cross-sectional view of the thin-film sample synthesized for 2 weeks.

Ti substrate. The intensity of the BaTiO₃ peaks increases with the synthesis time, suggesting improved crystallinity as it may correlate with the more regular grain shapes observed. The XRD scans between 44 and 46° of 2θ at different temperatures are shown in Figure 4.50. The evolution from the tetragonal to the cubic structure is observed for the sample synthesized for 2 weeks as temperature is raised above the Curie temperature (~130°C). Similar behavior is also observed for the samples synthesized for 3 and 4 weeks, suggesting the tetragonal nature of the thin films after 2 weeks synthesis.

4.3.2. Electrical Properties

I. Temperature dependence of dielectric constant (K) and loss tangent ($\tan\delta$)

The capacitance, C , and the loss tangent, $\tan\delta$, were measured as a function of temperature for all the films and their dielectric constant values, K , were calculated. The sample synthesized for one week exhibits a very high loss, high leakage current and low dc resistance. This may result from the short circuit formed during the measurement due to the incomplete film coverage over the substrate. Thus, further characterization on the sample was not pursued. Figure 4.51 shows the results of the measurement on the sample synthesized for 2 weeks at a frequency of 100 kHz from the room temperature to 200°C and subsequently cooled to room temperature. The data obtained during the heating

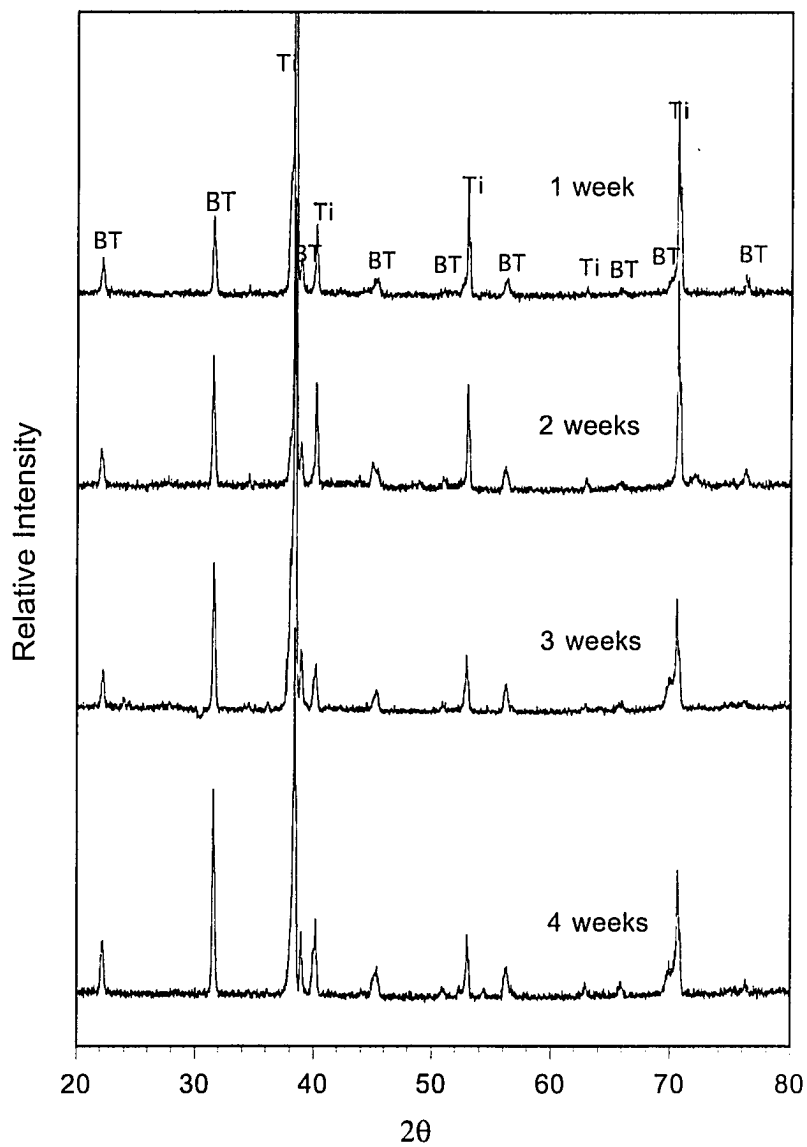


Figure 4.49. XRD patterns of the BaTiO₃ thin films synthesized for 1, 2, 3 and 4 weeks, respectively. BaTiO₃ and Ti phases are indicated as BT and Ti, respectively.

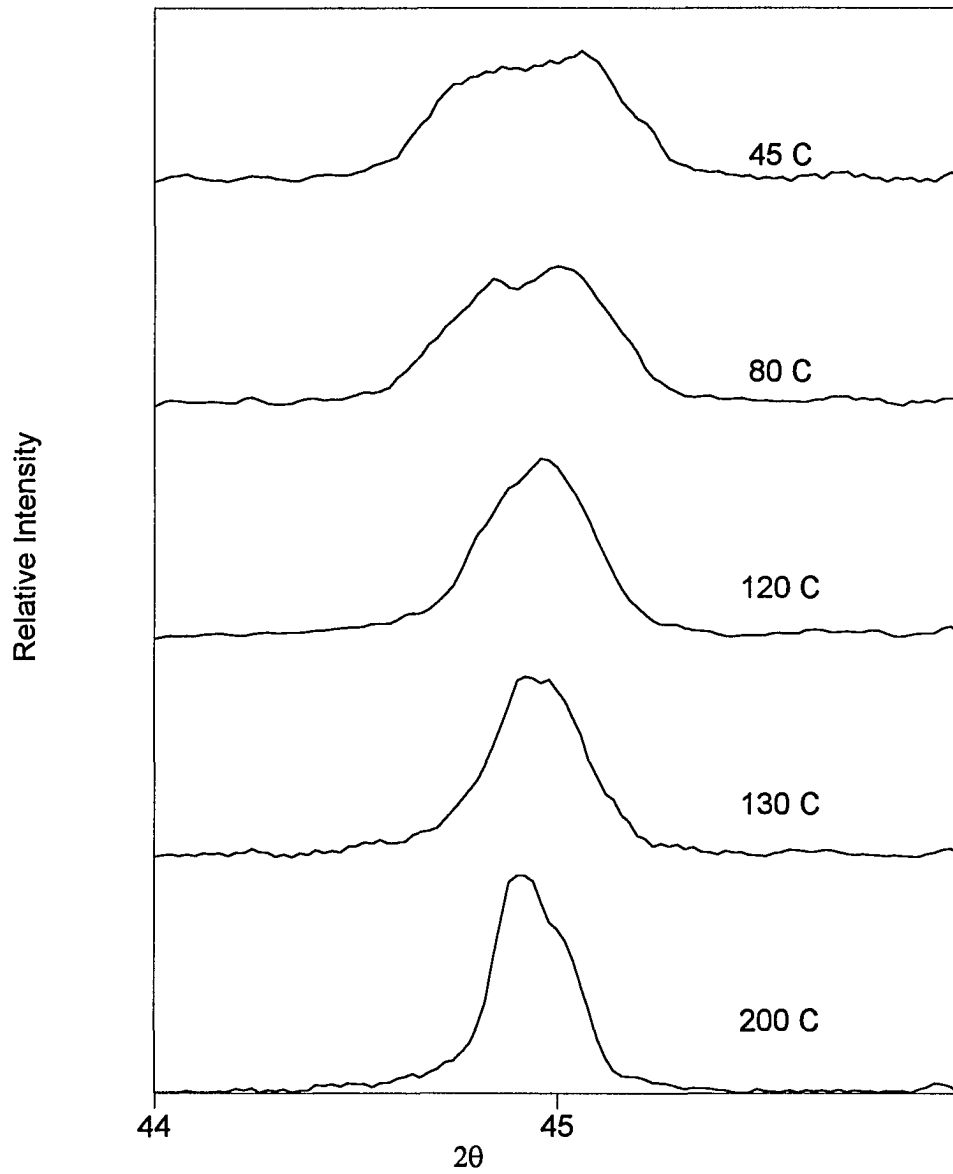


Figure 4.50. The XRD scans of 2θ between 44 and 46° at different temperatures for the BaTiO₃ film synthesized for 2 weeks.

cycle does not coincide with that obtained during the cooling cycle. This may be because of the humidity effect associated with surface-adsorbed hydroxyl groups on the sample [353-354]. Figure 4.52 shows the dielectric constant of the samples synthesized for 2, 3 and 4 weeks, measured at 100 kHz, and that of the sample (synthesized for 2 weeks) measured at 1 kHz. In all the runs, the paraelectric to ferroelectric transition, or the Curie transition, is not clearly observed from room temperature to 200°C, even though XRD suggests that the films are of the tetragonal symmetry.

II. Immittance spectroscopy analysis

In order to study the microstructural heterogeneity effects, such as defects and grain boundaries, the dielectric measurements were carried out as a function of frequency at several temperatures for samples synthesized for 2 weeks. Figure 4.53 shows the measured capacitance data of the sample as a function of frequency at 4 temperatures ranging from 150 to 300°C. In all cases, an obvious dispersion of capacitance over the frequency range from 10 Hz to approximately 1 kHz was observed at high temperatures (> 200°C). The dispersion becomes more significant as temperature increases. The behavior is similar to that observed for the sintered ceramic BaTiO₃. However, for the bulk BaTiO₃, the dispersion is more steep compared to that of the films and tends to

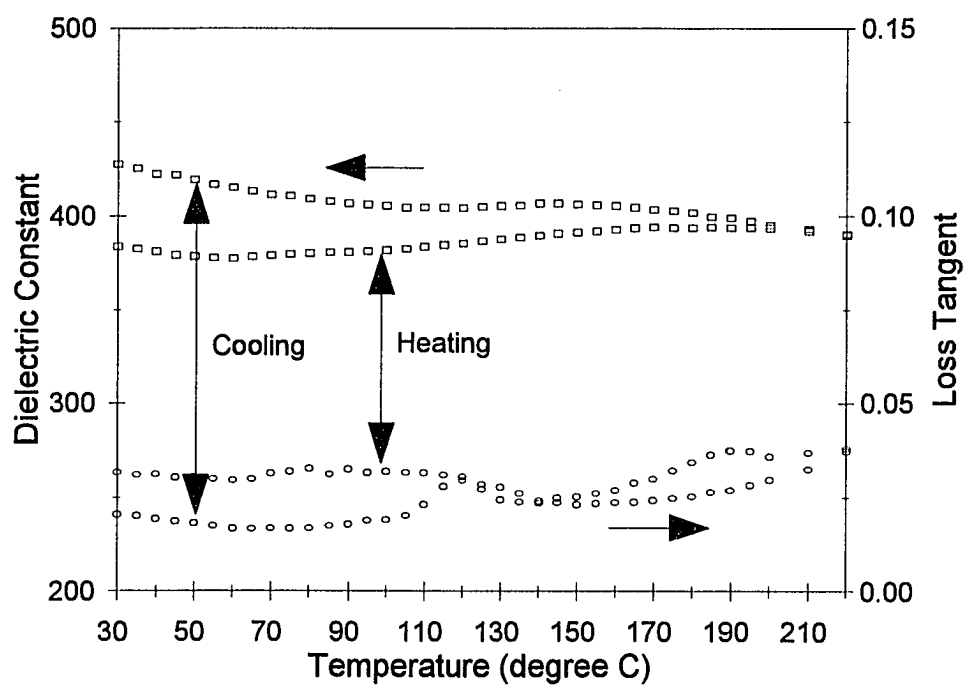


Figure 4.51. Dielectric properties of the film synthesized for 2 weeks at a frequency of 100 kHz from the room temperature to 200°C and subsequently cooled back to room temperature.

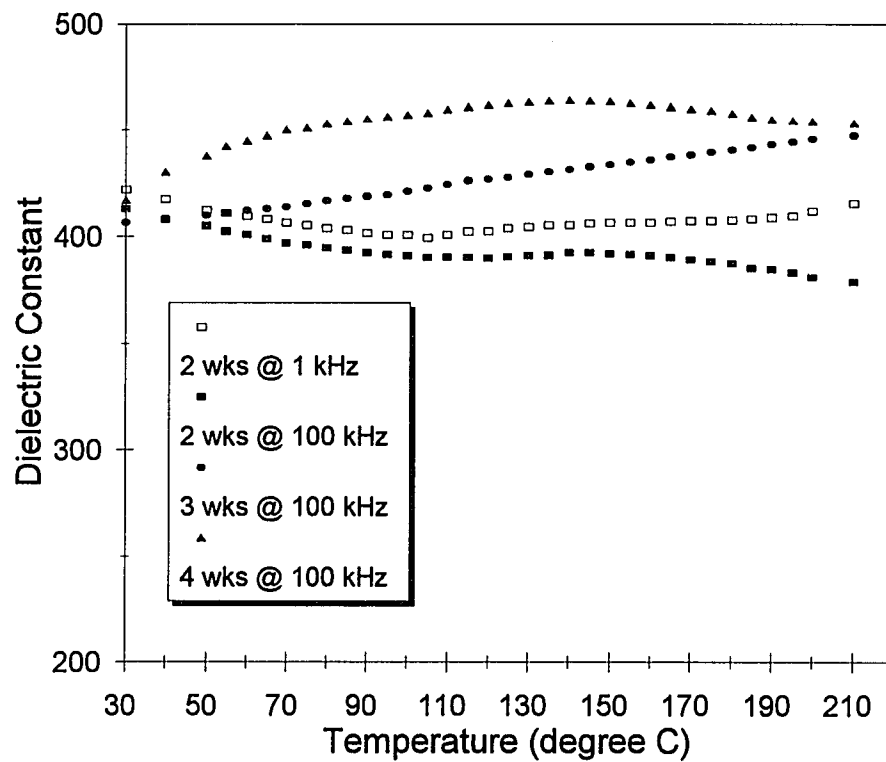


Figure 4.52. Dielectric measurement results of the films synthesized for 2, 3 and 4 weeks at a frequency of 100 kHz, together with that of 2 week's film at a frequency of 1 kHz.

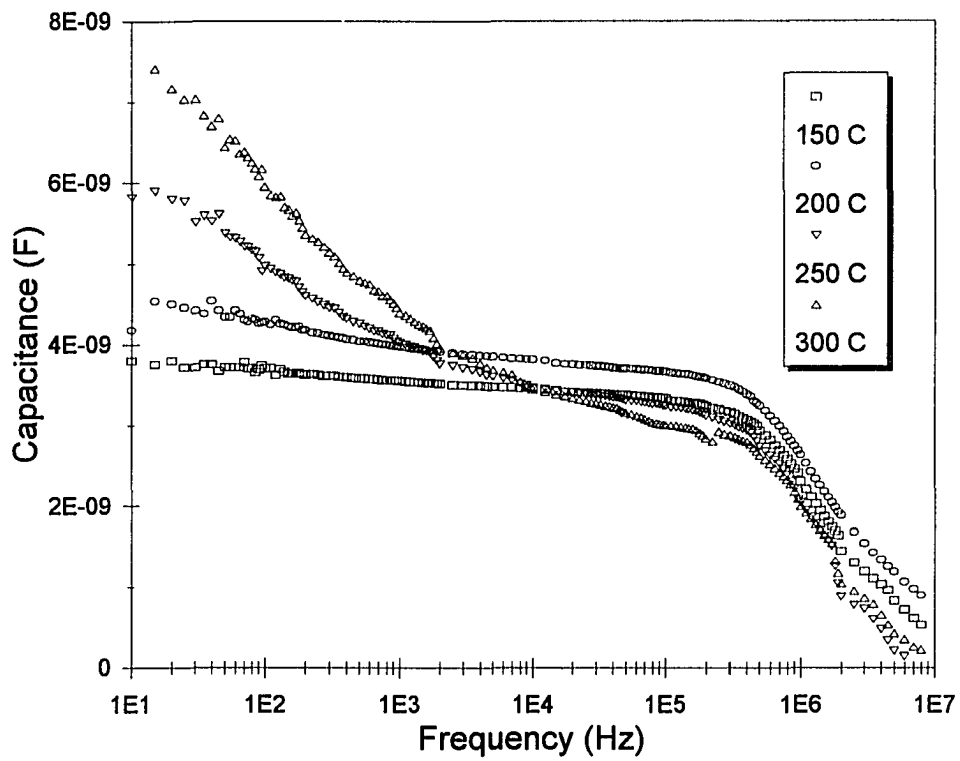


Figure 4.53. Measured capacitance data of the BaTiO₃ films synthesized for 2 weeks as a function of frequency at temperatures ranging from 150 to 300°C.

shift to higher frequencies as temperature increases.

In order to obtain more understanding of the film sample, immittance spectroscopy (IS) analysis was performed. Figures 4.54-4.57 show the *ac* electrical data plotted in the impedance (Z^*), modulus (M^*), complex capacitance (C^*) and admittance (Y^*) planes, respectively. More detailed analysis will be given in Chapter V (Discussion).

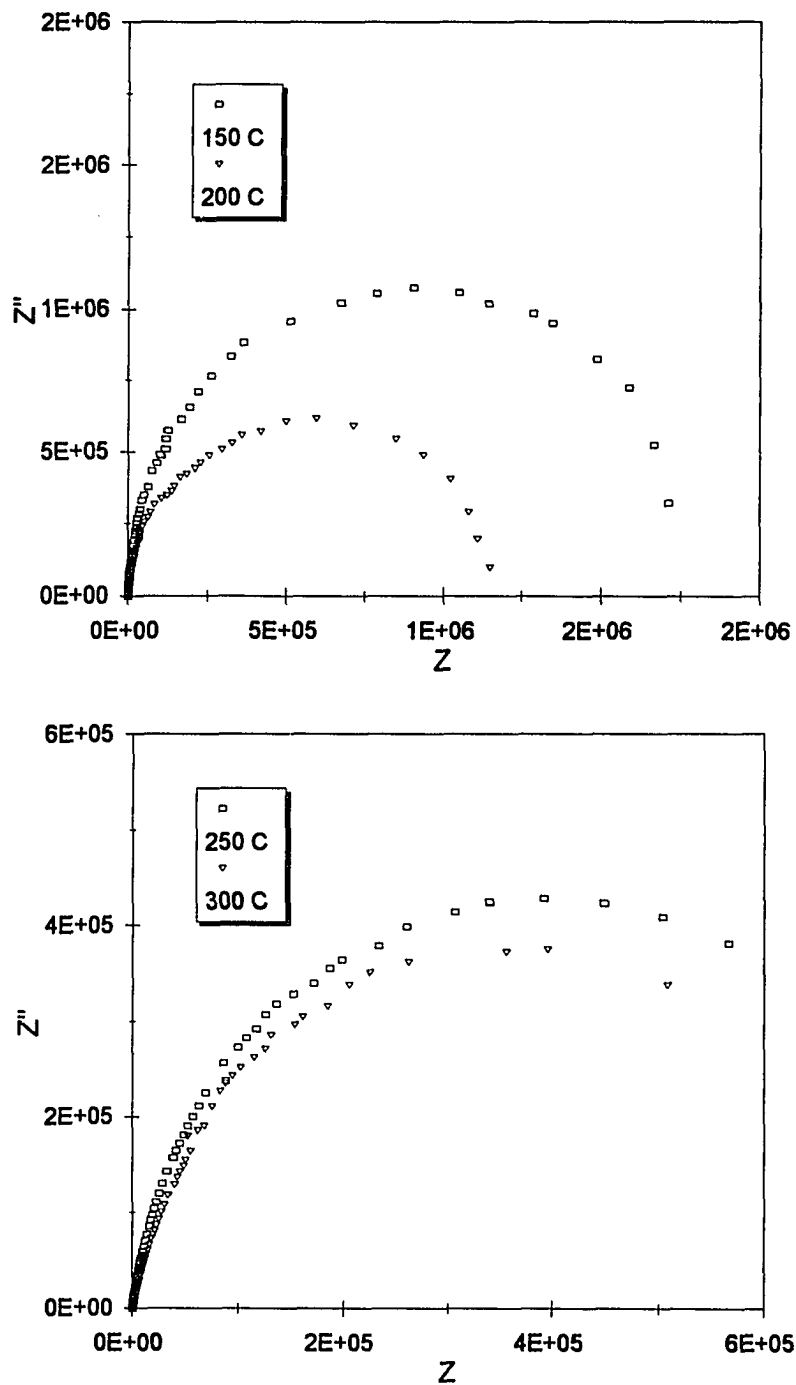


Figure 4.54. Impedance (Z^*) plots of the BaTiO_3 film synthesized for 2 weeks measured at various temperatures. For clarity, two separate plots were used to illustrate the entire measuring temperature range.

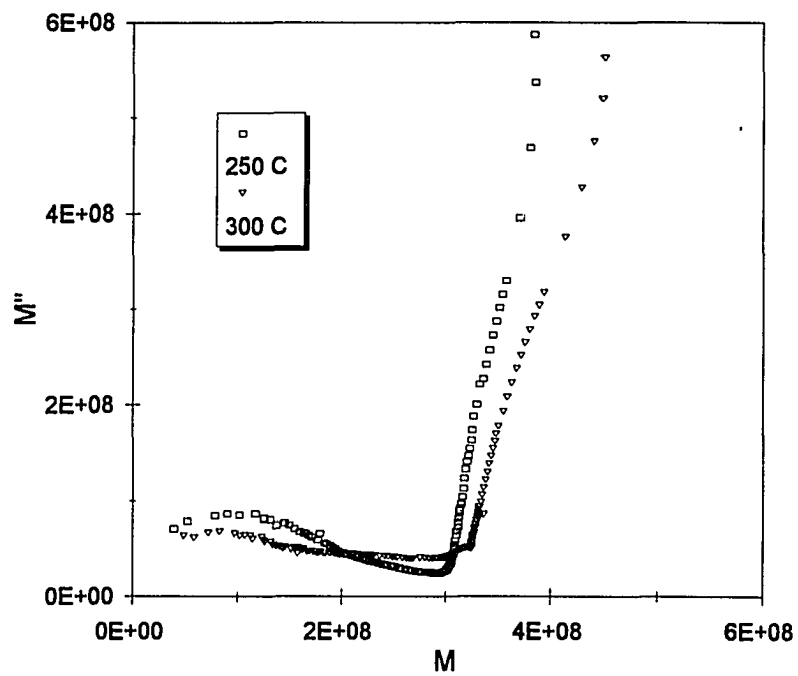
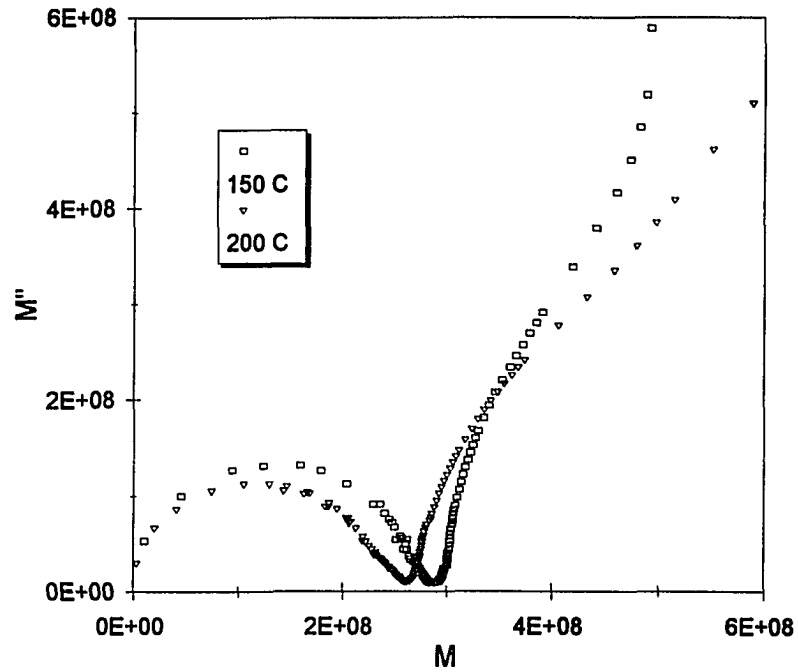


Figure 4.55. Modulus (M^*) plot of the same sample as in Figure 2.54 at various temperatures.

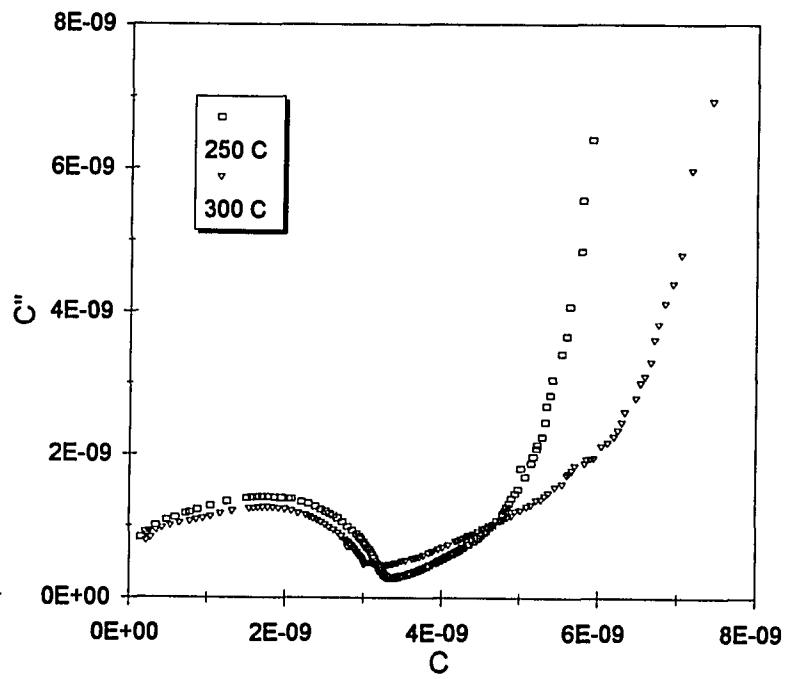
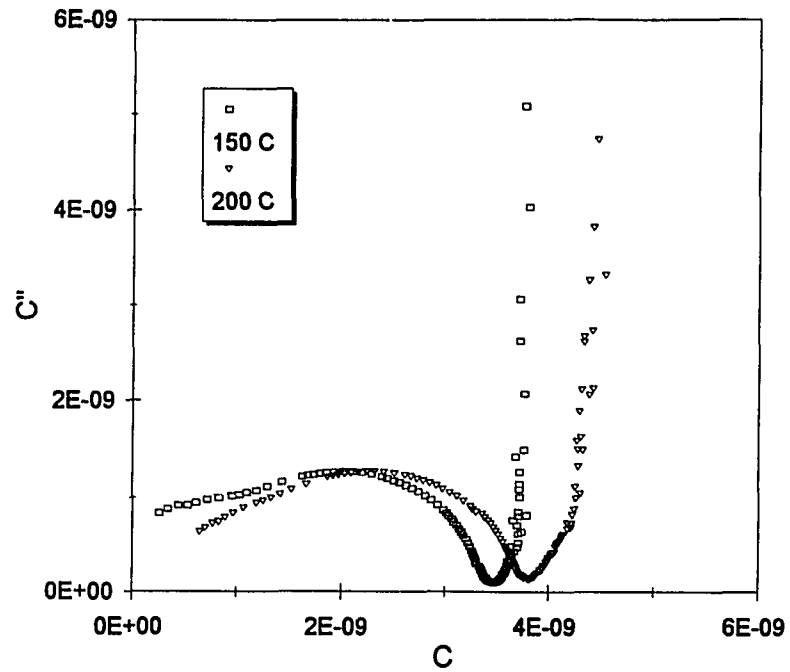


Figure 4.56. Complex capacitance (C^*) plot of the same sample as in Figure 2.54 at various temperatures.

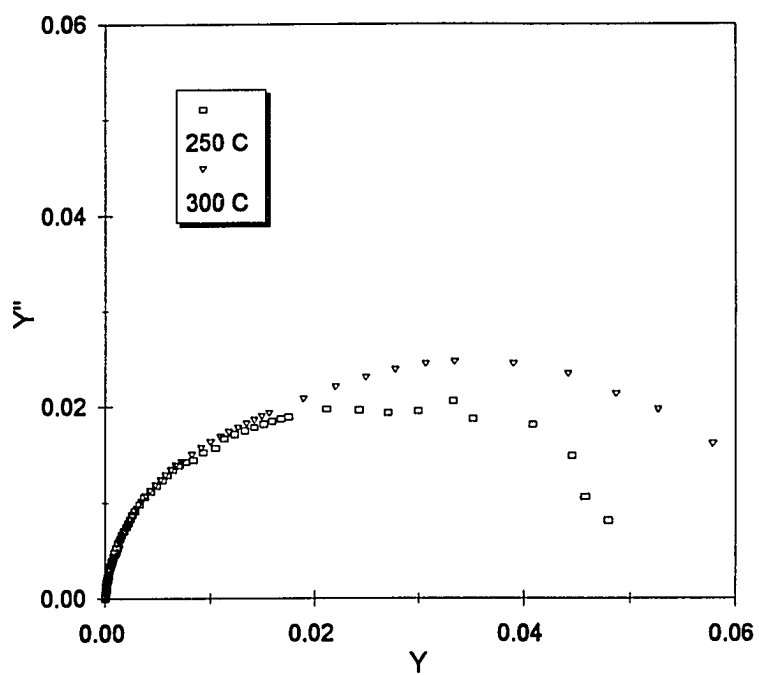
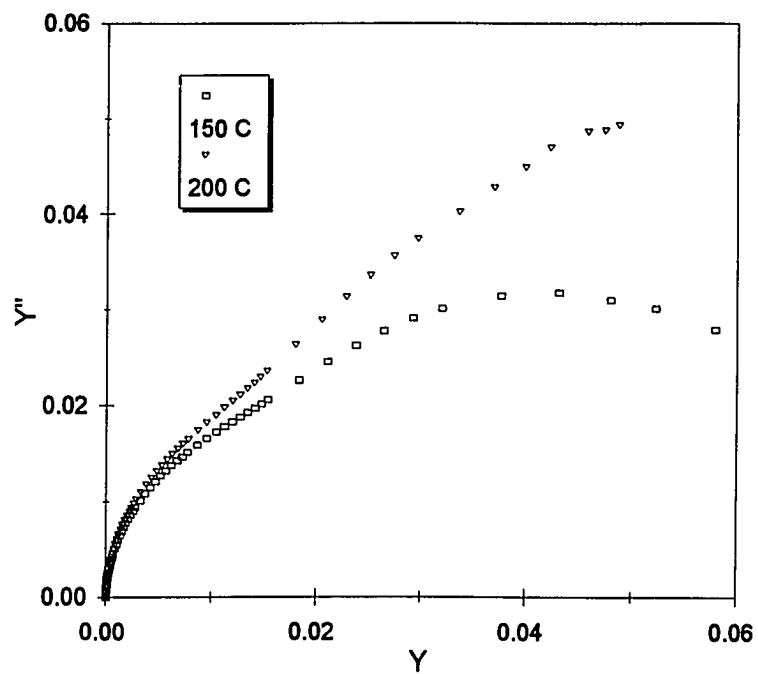


Figure 4.57. Admittance (Y^*) plot of the same sample as in Figure 2.54 at various temperatures.

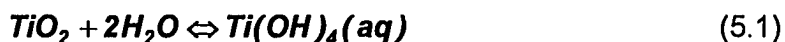
CHAPTER V

DISCUSSION

5.1. Hydrothermal Synthesis of BaTiO₃ Powders

5.1.1 Effect of Synthesis Conditions on Hydrothermal Synthesis of BaTiO₃ Powders

The hydrothermal formation of BaTiO₃ has been suggested to follow a dissolution/precipitation mechanism with the dissolution of the precursors in the solution and the formation of BaTiO₃ as precipitates. The chemical reactions for this process can be depicted as [93, 178, 328]:



It is evident from the reactions that high pH and high concentration of Ba ions are favored for the BaTiO₃ formation (forward reaction of Equation 5.2). Lower OH⁻ concentrations may result in the formation of a stable phase of TiO₂ instead of BaTiO₃. Therefore, it is crucial to maintain a high pH value (pH ≥ 13) during the hydrothermal synthesis reactions. In this study, pressure is fixed by adding the same amount of water in the digestion bomb. According to the stability

diagram calculated by Lencka *et al.* [172], both high pressure and pH are preferable for BaTiO₃ formation (Figure 2.21). Temperature may shift the boundaries between phase stability regions so that BaTiO₃ can be formed at slightly lower pH values (1~1.5 pH units). The reaction rate is also controlled by the temperature. Higher temperatures usually result in more rapid hydrothermal reactions, and thus BaTiO₃ crystals can be formed in a shorter time. The Ba/Ti ratio is also found to be important for hydrothermal synthesis. An excess amount of barium (Ba/Ti>1) promotes completion of the reactions during synthesis, while an excess amount of titanium (Ba/Ti<1) will cause formation of TiO₂.

Hydrothermal synthesis involves not only the chemical reactions to form the crystals (nuclei) of desired composition. It also provides a transport process essential for the crystals to grow. The driving force for the crystal growth is the reduction of the interfacial free energy or surface tension. From the thermodynamic point of view, smaller crystals possess higher chemical potentials and thus are more soluble compared to the larger crystals. As a result, smaller crystals tend to dissolve in the solution to form solute, which is subsequently transported (precipitated) onto the larger crystals. The growth of larger crystals at the expense of the smaller one is known as Ostwald ripening, which has been suggested to be the mechanism for particle growth in hydrothermal synthesis [93, 331]. The Ostwald ripening process is also

evidenced from the more homogeneous particle size observed in this study for the powders synthesized for a long time (e.g., 3 and 8 weeks) (Figure 4.6). The chemical reaction associated with this process is written as:



The transport rate of the solute is believed to be faster than the reaction rate in aqueous solution, and thus the rate-limiting step of the particle growth in hydrothermal synthesis is assumed to be the dissolution of the smaller particles.

Well known factors that play an important role in particle growth are the time and temperature of the synthesis. Higher temperatures and longer synthesis time ensure the completion of the ripening process, thus giving rise to larger particles. It has been found that an increase in particle size from 5 nm nuclei to the size of 200~300 nm occurs during a time period of 10 ~ 15 hours for the hydrothermal synthesis of BaTiO₃ with a Ba-Ti acetate gel precursor at 150°C [179]. Little increase in the particle size has been observed for longer processing times. Hydrothermal synthesis at 600°C has been reported to produce particles with sizes in the millimeter range [173], while only submicron particles can be produced at a temperature of 95°C [89, 174-175, 177]. In this study, BaTiO₃ powder synthesized at 95°C displays very fine particles of an agglomerate nature, and the morphology does not change upon longer synthesis times. On the other hand, powders synthesized at 240°C exhibit dispersed

particles of larger particle sizes which increase with time (Figure 4.8). The growth of particle sizes saturates slowly as the synthesis time further increases.

Not only temperature and synthesis time play important roles in the particle growth behavior in hydrothermal synthesis. The presence of different barium sources and OH^- concentrations are also found to affect the growth of BaTiO_3 particles. Since particle growth is governed by the dissolution of smaller particles in the solution, the influence of varying the synthesis conditions on the particle growth behavior can be related to the change in the dissolution behavior of the smaller particles. It is found that powders can be produced with increasing particle sizes by using various barium sources according to the following order: $\text{Ba}(\text{NO}_3)_2$, $\text{Ba}(\text{C}_2\text{H}_3\text{O}_2)_2$, BaCl_2 , BaBr_2 and BaI_2 . Correspondingly, it is found that the solubility of the barium sources in aqueous media exhibits the same trend, i.e., $\text{Ba}(\text{NO}_3)_2$ (34.2) < $\text{Ba}(\text{C}_2\text{H}_3\text{O}_2)_2$ (75) \approx BaCl_2 (60) < BaBr_2 (149) < BaI_2 (170). The numbers shown in parentheses are the solubility values in g/100 mL obtained in 100°C hot water [355]. This suggests that the more soluble barium salts may promote the dissolution of the smaller BaTiO_3 particles, which allows more a rapid particle growth process. The influence of the solubility on the dissolution process may be understood as follows: there is an overall equilibrium of the various species in the solution, including Ba^{2+} , Ti^{4+} and the anion of the barium salt (X^-). As the smaller BaTiO_3 particles dissolve and form Ba^{2+} and Ti^{4+} species, the equilibrium of the system

is destroyed. Two competing processes are present in the solution, where the dissolved Ba^{2+} species can either join with X^- species or recombine with Ti^{4+} species on the larger particles. The latter is believed to be favored if the barium salt has high solubility. In other words, barium ions will have less possibility to combine with X^- species.

It is surprising at first sight that $\text{Ba}(\text{OH})_2$ shows a high solubility in 100°C hot water (95 g/100mL), whereas very small particles are produced. This seems to contradict the solubility argument. However, one may consider the fact that the solubility of $\text{Ba}(\text{OH})_2$ is significantly limited by the high pH of the hydrothermal solution, and the resultant small particles are again expected. Indeed, for many hydrothermal processes applied in industry, a complex agent (or 'mineralizer' in hydrothermal terminology) is added to increase the solubility of otherwise sparingly soluble compounds to promote hydrothermal reactions [171].

Using $\text{Ba}(\text{OH})_2$ as both the barium and base sources, it has been shown that the pH of the solution influences both the formation [129] and kinetics of crystal growth of BaTiO_3 [356]. Herlt has reported that the rate of formation of BaTiO_3 becomes independent of $\text{Ba}(\text{OH})_2$ at concentrations greater than 1 M of the base [357]. Hydrothermal formation of BaTiO_3 is stable under high pH conditions [129, 173], whereas neutral conditions destabilize these crystals [129, 173, 178].

In the preliminary investigation, it was found that an OH^- concentration of 1 M produces the largest particles; however, it took a long time (8 weeks). It is expected that an optimum pH may exist for rapid particle growth. Moreover, according to Equation 5.2, the formation of BaTiO_3 is accompanied by a reduction of pH of the aqueous solution (by yielding H^+ ions), suggesting that maintaining a constant pH level during the synthesis period is very important for continuous particle growth. Usually this can be achieved by providing a buffer solution. However, the procedure is difficult to carry out at such high pH's (≥ 13). An alternative way was employed in this study by adding NaOH in the middle of the synthesis in an effort to maintain a sufficiently high pH level for continuous particle growth to take place.

Three sets of BaTiO_3 powders were synthesized with various OH^- concentrations: 0.3M, 0.5M and "buffered" 0.5M at 240°C , and the powders were labeled as powder A, B and C in this study. The sizes were found to be approximately 0.1, 0.3 and 0.5 μm (Figure 4.11). Particle growth is apparently promoted at higher OH^- concentrations. The significant increase in particle size of powder C demonstrates the importance of maintaining the high pH during the synthesis. It also proves that the use of the "buffered" solution is an effective way to promote particle growth.

5.1.2. Particle Size Effect on the Structure and Properties of BaTiO₃ Powders

I. Particle size and tetragonality

As mentioned above, in this study powders with various sizes were produced by controlling temperature, time, barium precursor and pH of the solution. A common and important characteristic of these powders is that they are not completely tetragonal. This is supported by the measurement of enthalpy change (ΔH) associated with the Curie transition using the DSC method. The ΔH value obtained for a well sintered BaTiO₃ ceramic sample (supposed to be completely tetragonal) is about 0.9 J/g, while those for the powders synthesized hydrothermally are smaller than this value (Table 4.1). The cubic powder synthesized at 95°C represents an extreme case where the complete disappearance of the Curie transition occurs with ΔH equal to zero. The tetragonality of these powders has been calculated by assuming the well sintered ceramic sample to be 100% tetragonal. It is found that the tetragonality of the powders increases with synthesis time (Figure 4.8). Also, by varying the barium sources and OH⁻ concentrations used in the synthesis, the tetragonality can also be changed.

When further examining the particle size and tetragonality data of the synthesized powders, there is a clear trend indicating an increase in the tetragonality with particle size. The powder of 37% tetragonality was obtained for a one week synthesis at 240°C with a particle size of about 0.23 μm , whereas

almost 100% tetragonality was achieved for the sample synthesized at 240°C for 8 weeks, with an average size of about 0.52 μm (Table 4.1). This size-tetragonality relationship is also followed for powders synthesized with various barium sources (Table 4.2), with the highest tetragonality corresponding to the largest particle size (in the case of BaI_2) and vice versa (in the case of Ba(OH)_2). In addition, the powders synthesized using various OH^- concentrations (powders A, B and C) also show an increase in tetragonality from less than 1% to almost 100%, with particle size increasing from 0.1 to 0.5 μm .

On the other hand, when the particle size is below a certain critical value, the powder may become cubic-like and display no ferroelectricity. This has been reported in the literature [6-9, 88-89]. In this study, the powder synthesized at 95°C shows very fine particles ($\sim 0.1 \mu\text{m}$) with cubic-like structure and exhibits no transition upon heating though the Curie temperature.

II. Defects and microstrains

Stabilization of the metastable cubic structure has been attributed to hydroxyl defects and microstrains associated with the lattice [9, 88-89]. The structural defects associated with the crystal lattice may lead to the distortion of the lattice and accompanying microstrains, which consequently stabilize the cubic structure.

The possible defect association with the BaTiO₃ lattice was examined for the powders A, B and C by using TGA and IR spectroscopy (Figures 4.18 and 4.22). Powder A has a relatively large amount of hydroxyl groups (8.2 mol%), which probably arises from the unreacted amorphous material (TiO₂) as suggested by TEM (Figure 4.14). However, for powders B and C, the concentration of OH⁻ groups is reduced significantly and becomes practically constant (1.4 and 0.8 mol%, respectively). The reason for the lower defect concentration in this study as compared with the others reported in the literature could be ascribed to the fact that the synthesis in this study was carried out at relatively higher temperature (240°C) and for longer time (one week). Since the ripening process corresponds to a general reduction of the free energy of the system, defect association with the lattice may cause the lattice distortion, which is not favored thermodynamically. As the process proceeds, the defects have a tendency to diffuse out of the interior of the particles, resulting in a low defect concentration of the powders.

The lattice strains were also measured for powders A, B and C and found to decrease slightly with an increase in particle size (Table 4.3). However, the values are overall very small ($<1.0 \times 10^{-3}$), possibly due to the relatively low defect concentrations of the powders. Therefore, in this study, the lattice strains and the defect concentration cannot be major factors to account for the stabilization of the cubic structure.

III. Crystal and molecular structure

TEM micrographs show that particles are well dispersed for powder B, whereas powder A has an agglomerate nature (Figure 4.14). High resolution TEM (HREM) reveals the lattice image of a particle from powder B, which is representative for all the particles (in powders B and C). The particle has a single crystal structure (from the diffraction pattern) and there is no indication of the presence of ferroelectric domains. Moreover, the existence of a surface layer around the particles, as reported in the literature [6], was not observed.

Raman spectroscopy provides further structural information at the molecular level. Although DSC data seem to imply a partial tetragonality of the powders, Raman data indicate that, at a molecular level, all powders are of a tetragonal symmetry. This is shown by the appearance of two Raman bands at 305 and 715 cm^{-1} (Figure 4.19), which is typical for the tetragonal BaTiO_3 structure and is caused by the distortion of the TiO_6 sublattice in a BaTiO_3 unit cell. As the tetragonal powder was heated up above the Curie temperature, these bands disappeared completely (Figure 4.20). The relatively low intensity of the bands for the powders synthesized at 95°C indicates the presence of the cubic phase in the powder (Figure 4.21).

IV. Size effect on ΔH of transition

It has been shown that ΔH associated with the Curie transition of the hydrothermally synthesized BaTiO₃ powders decreases with the particle size. However, the Raman data show the tetragonal symmetry of all the powders synthesized at 240°C. It has also been demonstrated in the previous section that arguments based on surface layers, defects and microstrains cannot be adopted for the ΔH decrease for the powders from C to A, since their contributions are relatively insignificant. A different interpretation has to be offered to explain what has been observed in this study.

Two sources of the size effects could be taken into account for this behavior. One is due to depolarization fields which may be present when surface charges caused by spontaneous polarization are not completely compensated. As mentioned in section 2.1.3, as particles get smaller, the domain configuration may not be favored due to the higher domain wall energy and single domain structure results. This has also been confirmed by the HREM study of powders B and C with no domain boundary region being observed. Therefore, as the particles become single domain, a strong depolarization field is set up in the particles. It has been calculated [56] for a ferroelectric thin film with partial charge compensation that the polarization, P , decreases as the film becomes thinner due to increasing depolarization field. Under a certain critical

dimension, the strong depolarization field may destroy the polar state, causing the polarization to drop to zero.

Another source of size effects is the change in the local polarization near the surface which is expected to occur over a distance comparable to the correlation length ξ of polarization fluctuations. Landau-Ginzburg's mean field theory [28-30] has been successfully applied to study this effect on the magnetic properties of ferromagnetic particles [70-74]. Recently, attempts have been made to apply this theory to ferroelectric thin films [75-77] and particles [78-79]. According to Landau's theory, the total free energy for a homogeneous ferroelectric of finite size can be expressed by the phenomenological equation using polarization (P) as an order parameter. The polarization at a certain position from the bulk toward the surface can be expressed in terms of two parameters: correlation length (ξ) and extrapolation length (δ). The correlation length ξ is considered as a measure of the average distance over which the fluctuations of polarization are correlated. Larger ξ means a longer distance for the dipoles to interact with each other. This length is responsible for the dominating temperature dependence of all physical quantities near the transition temperature ($\propto |T-T_c|^{-\nu}$, $\nu > 0$). For typical ferroelectrics, the value of ξ is estimated to be of the order of a few lattice spacings at temperatures far away from T_c , whereas at temperatures close to T_c , this effect is expected to become more significant (since ξ diverges there) [75-78]. The extrapolation length δ

describes the difference in coupling or ordering strength between the surface and the bulk. Figure 5.1 shows the variation of the local polarization $P(z)$ in the vicinity of a free plane surface ($z = 0$) as a function of z , a distance from the surface to interior (bulk) of a particle. The values of polarization at the surface and the bulk are denoted as P_s and P_∞ , respectively.

If the coupling strength of the bulk is larger than that of the surface, which is assumed to be the case in BaTiO_3 , the bulk will order before the surface does, or in other words, the surface will tend to be disordered in contrast to the bulk. Furthermore, the surface disordering will force the bulk to disorder to a certain degree within a range defined by the correlation length ξ . Therefore, as particles become smaller, relatively more bulk will be disordered. Eventually, the disordering will consume the entire bulk and the entire polar state will be destroyed. This behavior can be better illustrated by a schematic diagram as shown in Figure 5.2. Recently, Wang *et al.* [90] studied the dependence of the polarization on the particle size based on the mean-field theory and found that polarization decreases as the particles become smaller. Three assumptions were made in their calculations: each particle has a spherical shape, the polarizations are along the same direction and their magnitudes depend only on the radius of each spherical particle. Based on the above calculations, it was found that the polarization decreases as a function of the particle size and below

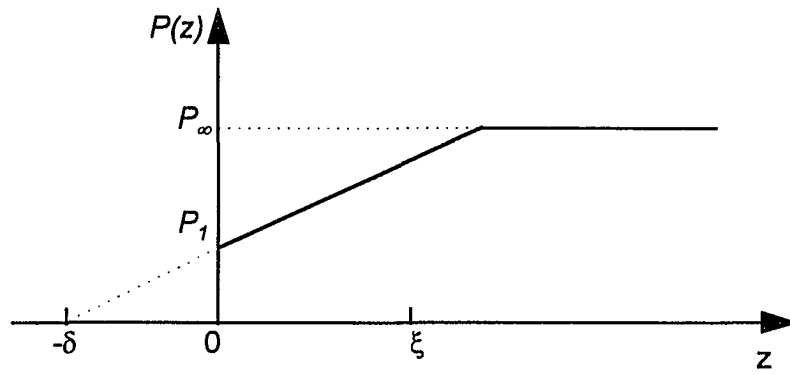


Figure 5.1. Variation of local polarization as a function of length from the surface to the interior of a ferroelectric particle [75].

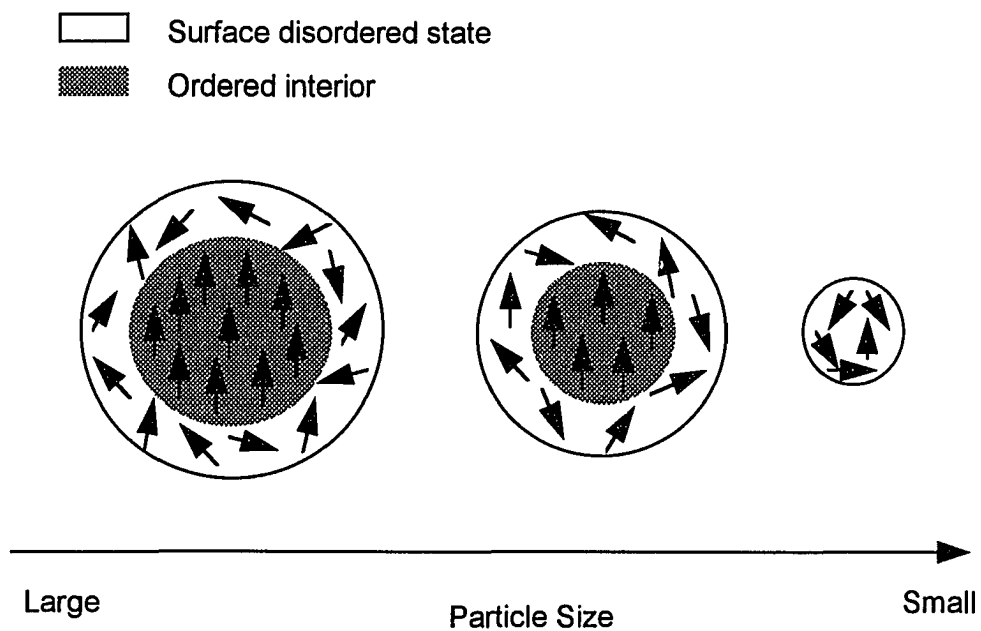


Figure 5.2. Schematic diagram to illustrate a particle from ordered to partially disordered and completely disordered as particle size decreases.

a critical particle size, 44 nm for BaTiO₃, the polarization drops to zero (shown in Figure 5.3) and ferroelectricity cannot be sustained. This state is called the superparaelectric state. Thus, in these ferroelectric materials, a size-driven transition from a polar to a non-polar state can occur.

It was shown in section 2.1.5 that ΔH of the Curie transition can be related to the polarization according to the following equation:

$$\Delta H = 2\pi P^2 T_c / C \quad (2.38)$$

where T_c is the transition temperature and C is the Curie-Weiss constant. It can be seen that ΔH decreases with decreasing polarization.

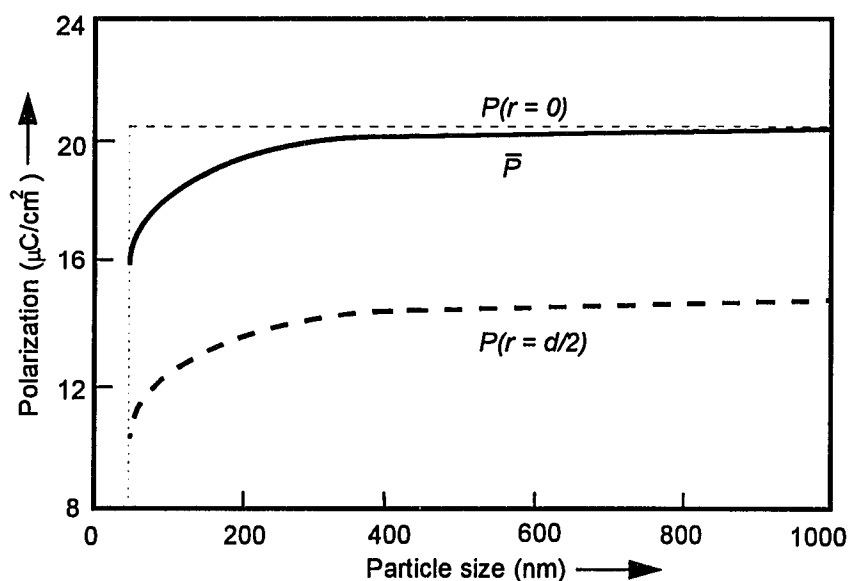


Figure 5.3. Size dependence of the polarization of a ferroelectric particle with first order transition; $P(r=0)$, $P(r=d/2)$ and \bar{P} are the polarizations at the center, at the surface and the average value, respectively [90].

In summary, the BaTiO₃ powders A, B and C examined in this study remain tetragonal down to a size of about 100 nm, with distorted TiO₆ octahedra in the lattice (as indicated by Raman spectroscopy). The decrease in ΔH could result from the decrease in polarization caused by the presence of the strong depolarization field, or the disordering of the bulk dipoles. The disordering becomes more severe as the particle size becomes smaller (Figure 5.2), resulting gradually in a transition from a polar to a non-polar state. This is coupled with an expected decrease in c/a ratio as observed from sample C to A. There is also a modest increase in strain as the particles become smaller in size, which could arise from the increased disordering of the dipoles. The more disordered dipoles result in an overall decrease in P , which causes the decrease in ΔH .

5.2. Sintering, Microstructure and Dielectric Properties of BaTiO₃

5.2.1 The Effect of Powder Characteristics and Sintering Conditions on Microstructure Development

It is generally believed that powders with fine and uniform particles can usually be sintered to a higher density at a lower temperature, as compared with powders with large and non-uniform particles. However, this rule was not exactly followed in this study. The cubic powder synthesized at 95°C has the smallest particle size, but only a low density (93%) was achieved upon sintering

at 1300°C (Table 4.6). Sintering at higher temperatures only results in exaggerated (abnormal) grain growth (Figure 4.31), with little improvement in the density. The behavior can be understood by considering the defective structure (hydroxyl defects) associated with the cubic powder, which cannot be modified during sintering until the temperature reaches very high values (>1100°C) [89]. This defective structure may hinder complete densification. Apparently, the agglomeration of the powder and inability to control the exaggerated grain growth are other possible accounting factors for the low final density observed in the cubic powder. The rapid abnormal grain growth may trap the pores inside the grains without eliminating them (as occurring in continuous grain growth), resulting in the low sintered density.

Exaggerated grain growth has long been observed in BaTiO₃ [352, 358-360]. In this study, the cubic and commercial (TAM HPB) powders showed a significant abnormal grain growth upon sintering, which are indicated by extremely large grains shown in the microstructure (Figure 4.31 and 4.25d). The exaggerated grain growth is more likely to occur when normal grain growth is inhibited by the presence of impurities or pores so that only a few grains with a curvature much larger than the average (exaggerated grains) are able to grow rapidly to very large sizes, whereas the smaller grains practically remain in their initial condition until they are consumed by the large grains [34]. Therefore, the exaggerated grain growth observed for the cubic and commercial powders may

be triggered by the defective structure of the powders which impedes the normal grain growth.

On the other hand, high sintered densities could be obtained for the tetragonal powders (Table 4.6). This may be attributed to the more ideal structure of the particles (with lower defect concentration), so the densification is not impeded by the rearrangement of the defective structure during sintering, which takes place in the cubic powder [184]. Limited grain growth was observed upon sintering the powders of high tetragonality. The resultant microstructure shows fine, uniform grains with the absence of the very large (exaggerated) grains (Figure 4.33). The powders of higher tetragonality represent more dispersed and homogeneous particles with a less defective structure, and therefore may allow more uniform grain growth and prevent the exaggerated grain growth from occurring. The relatively larger particle sizes of the tetragonal powders may be another factor that favors continuous grain growth [358].

Sintering temperature is always a controlling factor in the sintering process. Higher sintering temperatures usually result in higher sintered density, though it is not always true if an abnormal (exaggerated) grain growth takes place (Table 4.5). Since higher sintering temperature always promotes grain growth and results in larger grains, the choice of the sintering temperature should be carefully considered if both high density and fine grain size are required.

The effect of the sintering rate on the microstructure was also explored in this study. Extremely high sintering rate ($\sim 200^\circ\text{C}/\text{min}$), as compared with $5^\circ\text{C}/\text{min}$ for conventional sintering, was used during the sintering of the synthesized cubic powder from 1250 to 1350°C . All fast-sintered samples display uniform grains with much smaller sizes compared to those obtained in conventional low-rate sintering (Figure 4.38). Also, relatively high densities have been achieved in a very short time by employing the fast-sintering scheme. Table 4.7 shows that a 94% density was achieved for sintering at 1300°C for only 5 minutes. This is because of the enhanced densification process caused by a high lattice diffusion coefficient at high temperatures, in contrast to a relatively low surface diffusion coefficient responsible for the grain growth process (Figure 2.23). The dwell time is a non-negligible factor in fast-sintering process, since a relatively longer time results in much larger grain sizes upon the sintering ($>10\ \mu\text{m}$ when sintered at 1300°C for 15 minutes).

As mentioned above, efforts have been made to achieve a desired microstructure (fine grains and high density) of the sintered samples by controlling the sintering conditions in terms of temperature, time and heating rate. As will be shown in the next section, these efforts are necessary due to the significant influence of the microstructure on the dielectric properties of the BaTiO_3 samples.

5.2.2. The Influence of the Microstructure on Dielectric Properties

The results obtained for the sintered BaTiO₃ samples well illustrate the influence of grain size on the dielectric properties. Samples with smaller grain sizes usually show higher dielectric constant compared to those with larger grain sizes. This has been explained by an internal stress model developed by Buessem *et al.* [10] and later modified by Arlt *et al.* [45-49] incorporating the domain density contributions. The theory postulates that the high dielectric constant in the fine-grained ceramic BaTiO₃ is caused by high internal stresses present in the fine-grained BaTiO₃ as a result of the balance of free energies. The maximum dielectric constant has been expected to occur around 1 μm grain size, below which K decreases again due to the presence of pseudocubic phases.

Grain size distribution may also affect the dielectric constant. Very uniform size distribution eliminates the presence of unwanted very large grains, which is detrimental for achieving a very high dielectric constant. This is supported by the fact that the highest dielectric constants have been achieved in this study for the fast-sintered samples which display a uniform size distribution, though not very high densities (Table 4.7).

Density is another factor that affects the dielectric properties. The effect of porosity on the dielectric constant has been investigated by several authors [11-13]. Okazaki *et al.* concluded that porosity reduces the polarization per unit

volume but enhances the depolarization field. Therefore, a decrease in dielectric constant with increasing porosity was predicted. Banno and co-workers introduced a modified 'cubic' model assuming a two-phase composite system made of a bulk ceramic material and pores. Once again a decrease in dielectric constant with increasing porosity was predicted. Moreover, the internal stresses in the grains, which give rise to high dielectric constants, are also expected to be reduced by the presence of a porous structure. Therefore, high density is another important factor to achieve a high dielectric constant.

On the other hand, according to the data obtained in this study, loss tangent of the samples seems to be determined by sample density. High loss occurs for the samples sintered at low temperatures, which correspondingly have high porosity (Tables 4.5-4.6). Similar behavior has been reported by other authors [361-362]. However, the reason for this is not well understood. It may be because more space charges accumulate around the boundaries in the pore area, leading to higher dielectric loss.

5.3. Synthesis, Microstructure and Electrical Properties of BaTiO₃ Thin Films

5.3.1 Synthesis and Microstructure of BaTiO₃ Thin Film

BaTiO₃ thin films have been prepared after one week of synthesis under hydrothermal conditions. The films are well crystallized and no apparent second phases were observed (Figure 4.49). The grain size of the films is around 1 ~ 2

μm (Figure 4.46). The thickness of the films is found to be around $0.5 \mu\text{m}$ (Figure 4.48), with a slight decrease for the films synthesized for 3 and 4 weeks. The films synthesized for 2 weeks or longer are of a tetragonal symmetry as determined by XRD (Figure 4.50).

The mechanism of BaTiO_3 nuclei formation follows the one described in the powder synthesis. The amorphous titanium oxide on the surface of the substrate is first dissolved into the solution to form an aqueous $\text{Ti}(\text{OH})_4$ complex, which further reacts with barium ions in the solution to form BaTiO_3 (Equations 5.1-5.2). The high OH^- concentration again plays a vital role in the BaTiO_3 formation, since the films were not formed for pH lower than 13. The formation of BaTiO_3 nuclei may take place in the solution and newly formed nuclei are subsequently deposited (adsorbed) onto the substrate surface so as to reduce the overall surface energy of the system. However, it is more likely that the $\text{Ti}(\text{OH})_4$ complex first gets adsorbed onto the surface, followed by the nucleation reaction that takes place directly on the surface. After the nucleation, the BaTiO_3 crystals start to grow on the substrate (as the synthesis proceeds).

It was noted that second phase segregation along grain boundaries occurred if the Ti substrate was not well polished before synthesis. This is because unpolished substrate has many defect regions where the $\text{Ti}(\text{OH})_4$ complex can easily be absorbed. The accumulation of the titanium complex around the defect regions may cause the nucleation of $\text{Ba}_2\text{Ti}_9\text{O}_{20}$, which may

later segregate along the BaTiO₃ grain boundaries [324]. Such behavior was not observed in the polished samples.

It is believed that in the early stage of crystal growth, the grains grow freely along the substrate with a relatively rapid rate. However, once the BaTiO₃ film completely covers the substrate, the rate of growth is dramatically reduced. This is because further dissolution of the titanium ions into the solution (which is vital to the BaTiO₃ nuclei formation), requires the diffusion of the Ti ions through the film, which is a very slow process. Therefore, there is a critical time beyond which the thickness of the films remains almost constant.

Although the thickness ceases to increase, the ripening process can still take place. It was observed that the grains preferably grow laterally along the surface due to the limited nuclei in the solution. The grains re-adjust their structure through the dissolution/recrystallization process, resulting in a more regular shape of the grains (for the films with 3 and 4 weeks synthesis time).

BaTiO₃ films with greater thickness have been reported when electric current [81, 325-326, 328] or higher temperatures [81] were used. Applying the electric current can promote the oxidation of the Ti electrode, which ensures more Ti ions for the BaTiO₃ film formation [321]. Higher temperatures enhance the solubility of the titanium and also increase the supersaturation point. Therefore, more critical nuclei can be formed in the solution according to the classical nucleation theory, resulting in an increase in the film thickness.

5.3.2. Electrical Properties of BaTiO₃ Thin Films

The dielectric constant of the films was measured as a function of temperature (Figures 4.51-4.52), and it was found that there is no strong evidence of a dielectric constant anomaly near the Curie transition as observed in the ceramic BaTiO₃ samples. The diffuseness or disappearance of the Curie transition for BaTiO₃ thin films has been reported and a variety of mechanisms have been suggested to explain this abnormal behavior, such as a Schottky barrier layer [3, 307, 363], defects and microstructural heterogeneity [364], crystalline quality [364], internal and external stress effects [82, 280, 309], and the intrinsic size effect [367-369]. In this study, the films have relatively large grain size of around 1 to 2 μm . They are well-crystallized as evidenced by the sharp diffraction peaks with relatively higher intensities (Figure 4.49) and have a tetragonal symmetry as shown in Figure 4.50. In addition, since the synthesis was conducted at low temperatures for relatively long times, the structure is expected to be not very defective, which is yet to be confirmed by further experiments.

Therefore, several plausible explanations for the absence of the Curie transition can be proposed. One is based on the existence of the Schottky barrier at the film-electrode interface which may significantly modify the ferroelectric behavior of the thin films. The Schottky barrier results in a surface region consisting of space-charge carriers, and its dielectric properties are

invariant with temperature [3, 363]. The capacitance of the films may be expressed by the binomial series:

$$C = C_s \left\{ 1 - \frac{C_s}{C_b} + 2 \left(\frac{C_s}{C_b} \right)^2 + \dots \right\} \quad (5.4)$$

where C_s and C_b represent the capacitance of the surface layer and the bulk, respectively. It is assumed that $C_b > C_s$ for the ferroelectric thin films at room temperature. The temperature dependence of C is governed by C_s and the term in the parentheses. At the transition temperature, assuming the bulk to behave as a normal ferroelectric, C_b has a value many times higher than that at room temperature ($C_b \propto (T-T_0)^{-1}$) and therefore the term in the parentheses becomes unity. As a result, films with a surface layer of low dielectric constant do not show the usual dielectric anomaly near the Curie transition. It should be noted that this barrier layer effect cannot be very significant for the bulk ferroelectric materials. This is because the assumption of $C_b > C_s$ for the thin films is no longer valid for the bulk materials due to their much smaller C_b (resulting from much larger thickness of the bulk).

The second possible explanation comes from the stress consideration. The potentially large two-dimensional stresses involved in the thin film materials have been shown to alter the equilibrium domain structure, shift the Curie transition toward higher temperatures and cause the broadening of the transition [280, 364-366]. Desu [280] found an increase of the Curie temperature by 29°C

for an increase of compressive stress of ~ 350 MPa. However, in this study, there appears to be no transition in the temperature range from room temperature to 200°C . Further experiment is needed to characterize the stress behavior of the synthesized film samples.

As discussed earlier, the depolarization field may cause the instability of the ferroelectric phase for very fine BaTiO_3 particles. In a similar manner, a strong depolarization field has been suggested to be present in the ferroelectric thin films (which are slightly conducting) [8, 56, 364]. Batra *et al.* [56] performed a numerical analysis based on thermodynamic considerations and found that the associated depolarization field is size dependent and can change the magnitude of the polarization, the transition temperature and the coercive field. The strong depolarization field may destabilize the ferroelectric phase even for relatively thick films ($\sim 1 \mu\text{m}$).

5.4. Impedance Spectroscopy Analysis

5.4.1. Ceramic BaTiO_3 by Sintering the Hydrothermally Synthesized Cubic

Powder at 1250°C for 2 hours.

As shown in Figure 4.42, two semicircles appear within the measuring frequency range (5Hz-13MHz) above 250°C , corresponding to two different relaxation mechanisms. The relaxation time constants, $\tau_1 (= R_1C_1)$ and $\tau_2 (= R_2C_2)$ associated with the high and low frequency relaxations, respectively, are

obtained by fitting the semicircles using a least squares method. When the log of time constant (τ_1 and τ_2) is plotted as a function of $1/T$, an Arrhenius-type linear relation is obtained (Figure 5.4), indicating that the relaxations are thermally activated. The activation energies of the high and low frequency relaxations (E_{τ_1} and E_{τ_2}) are calculated from the slope and found to be 1.05 and 1.47 eV, respectively. The constituent components (R and C) of the time constants τ ($= RC$) for the two relaxations are also examined. The resistance values (R_1 and R_2) are obtained from the intercepts of the two semicircles and their temperature dependencies are shown in Figure 5.5. Once again, the resistances R_1 and R_2 exhibit Arrhenius-type temperature dependence and their activation energies (E_{R1} and E_{R2}) are calculated to be 0.88 and 1.43 eV, respectively. It was noticed that the activation energies of the low frequency relaxation obtained from the τ and R representations (E_{τ_2} and E_{R2}) are very close, while those for the high frequency relaxation (E_{τ_1} and E_{R1}) are distinguishable. The thermal behavior of τ , R and C can be expressed as:

$$\tau = RC = R^0 C^0 \exp[(E_R + E_C) / kT] = \tau^0 \exp(E_{\tau} / kT) \quad (5.5)$$

The equation shows that if the activation energy E_{τ} is equal to E_R , it will result in $E_C = 0$, suggesting that the capacitance, C , is temperature invariant. Therefore, from Equation (5.5), it can be deduced that C_2 is temperature invariant, whereas C_1 is temperature dependent.

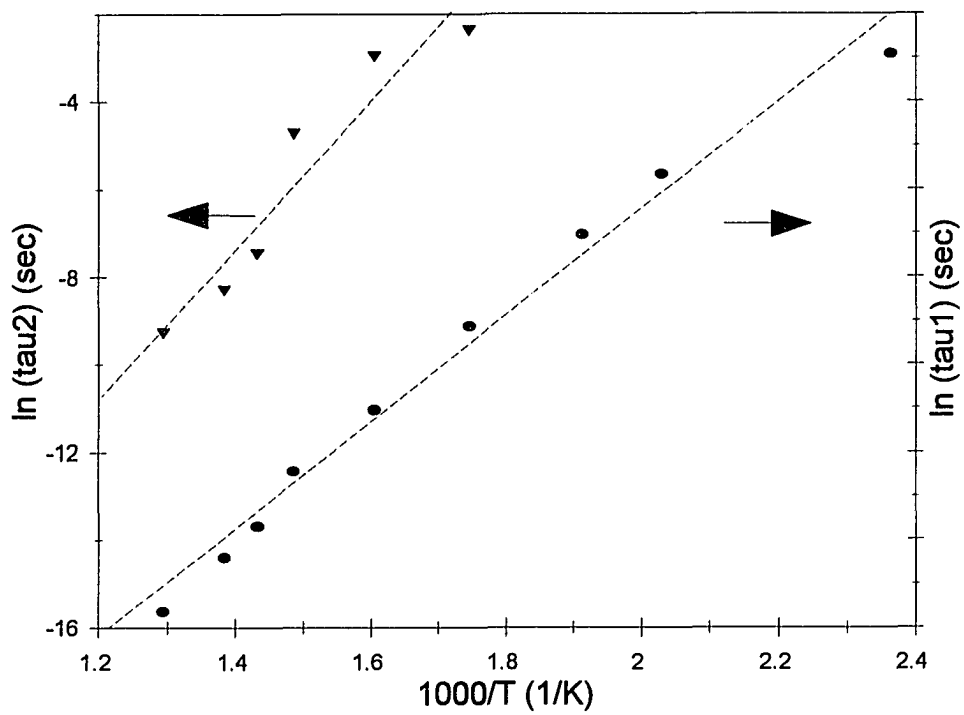


Figure 5.4. Temperature dependence of the relaxation times (τ_1 and τ_2) associated with the high- and low-frequency semicircles in the Z^* -plane.

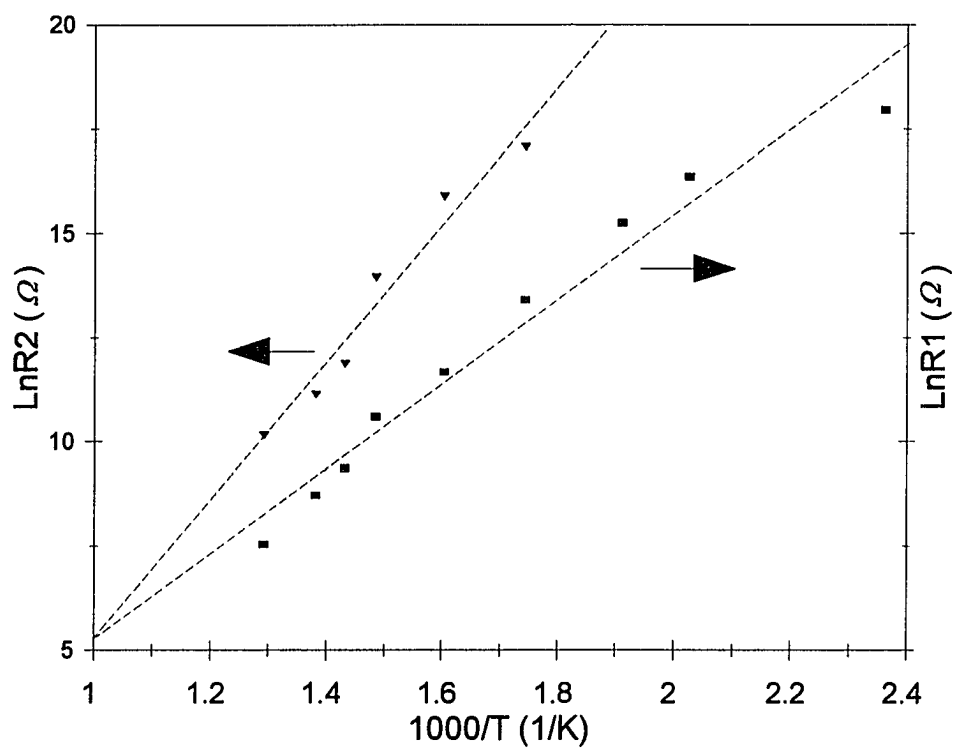


Figure 5.5. Temperature dependence of the resistances (R_1 and R_2) associated with the high- and low-frequency semicircles in the Z^* -plane.

In order to gain more insight into the mechanisms responsible for the high and low frequency relaxations, the capacitance values of the two relaxations (C_1 and C_2) were calculated according to the relation of $\tau = RC$, and their temperature dependence is shown in Figure 5.6. While C_1 exhibits a fairly good Curie-Weiss behavior, C_2 is temperature independent. Therefore, the high frequency relaxation may be attributed to the grain (bulk) contribution as its constituent capacitance displays a ferroelectric behavior. The low frequency relaxation, on the other hand, may be associated with grain boundaries due to the relatively large and temperature-independent C_2 values [237].

The temperature dependence of the depression angles associated with the two relaxations (θ_1 and θ_2) are shown in Figure 5.7. θ_1 at all the temperatures is less than 6° , suggesting a nearly Debye-type relaxation. The low frequency relaxation shows a larger depression angle of θ_2 around 10 to 20° . The large depression angle indicates a non-Debye type relaxation or a distribution of relaxation time caused by the defects or other heterogeneities in the conduction path, and this has been commonly observed in the grain boundary region [237]. Both θ_1 and θ_2 show a slight increase as a function of the temperature, indicating that the degree of heterogeneity increases with temperatures.

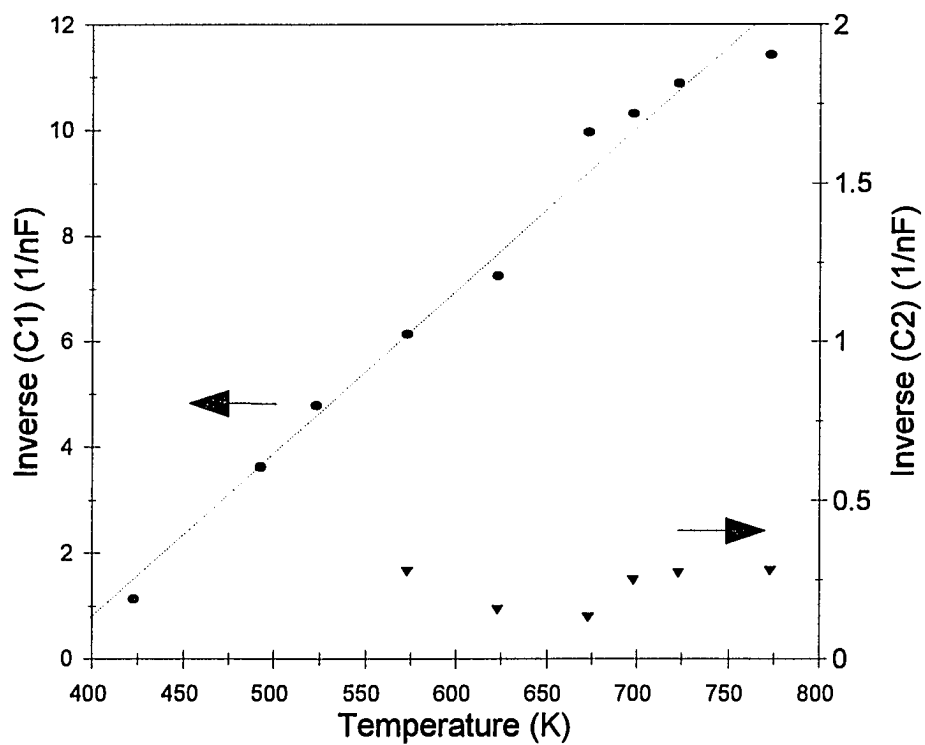


Figure 5.6. Temperature dependence of the capacitances (C_1 and C_2) associated with the high- and low- frequency relaxations in the Z^* -plane. The capacitances were calculated according to the relation of $\tau = RC$.

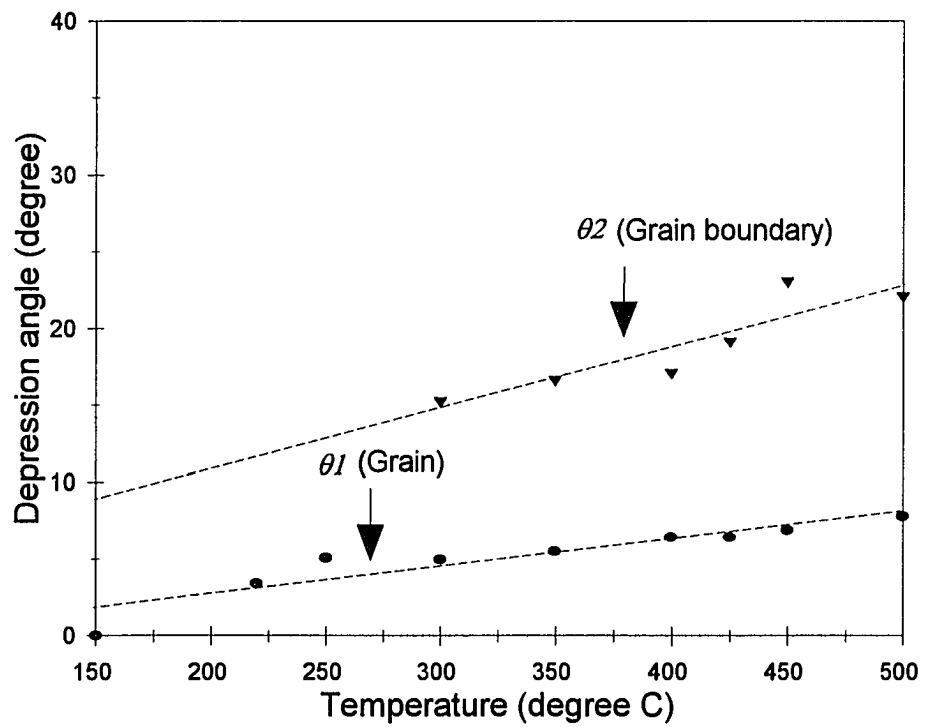


Figure 5.7. Temperature dependence of the depression angles (θ_1 and θ_2) associated with the grain and grain boundary relaxations in the Z^* -plane.

As shown in Figure 4.42, the high frequency relaxation associated with the grain contribution at 250°C covers the whole frequency range, whereas the low frequency relaxation (grain boundaries) is not observed. However, as temperature increases, the low frequency semicircle becomes visible and more nearly complete. The underlying reason for this can be given by examining the time constants for both relaxations (τ_1 and τ_2). As shown in Figure 5.4, both τ_1 and τ_2 decrease as temperature increases, implying an increase in peak frequencies of the semicircles ($\omega\tau = 1$ at the peak). As a result, more low frequency relaxation data are brought into the measuring range as the temperature increases, and thus the corresponding semicircle becomes more nearly complete at higher temperatures. Since all the impedance analysis instruments have frequency limitations, different relaxation mechanisms may not be revealed in a given frequency range for a specific instrument. However, by varying some experimental parameters, such as temperature (as in this case), it is possible to display the various relaxations in the given frequency range.

It is known that the band gap energy of BaTiO₃ is about 3.0 eV [370]. The activation energies for the two relaxations (E_{R1} and E_{R2}) are calculated to be 0.88 and 1.43 eV, which are smaller than half of the band gap value. This suggests that the conduction mechanism may not be intrinsic electronic conduction. Since the BaTiO₃ ceramic prepared here was of high purity, the extrinsic conduction

due to impurities could not be significant. The defect equilibrium can be described by Schottky type disorder:

$$0 = 3V_{O}^{\bullet\bullet} + V_{Ba}^{\prime\prime} + V_{Ti}^{\prime\prime\prime} \quad (5.6)$$

It has been experimentally verified that for undoped BaTiO₃ at the ambient ($p_{O_2} \sim 1$ atm), the electrical conductivity is dominated by a p -type conduction [370-371]. Smyth and coworkers [371] claim that the defect disorder is governed by simple charge neutrality based on an assumption that acceptors are the predominant impurities. However, Nowotny *et al.* found [370] that there is a large discrepancy between the reciprocal of the p_{O_2} exponent predicted by Smyth and that determined experimentally in the p -type regime. Thus, in this regime, the concentration of electron holes assumes substantial values which cannot be ignored. It can be related with the ion concentrations by

$$h^{\bullet} = 2[V_{Ba}^{\prime\prime}] + 4[V_{Ti}^{\prime\prime\prime}] \quad (5.7)$$

The p -type conductivity involves both concentration and mobility terms associated with electron holes, and both can be temperature dependent. This means that the activation energy obtained from the conductivity measurement may include both the formation and migration energy terms:

$$E_a = E_f + E_m \quad (5.8)$$

The migration energy of electron holes, assuming a hopping mechanism, has been given as 0.11 eV [370]. Therefore, the strong temperature dependence of

conductivity (activation energy of about 1.43 eV for the bulk) may come mainly from the formation energy of the electron holes, which is yet to be verified.

By performing a similar analysis in the modulus plane, M^* , the capacitance values associated with the two relaxations can be directly obtained from the intercepts on the x-axis. Their temperature dependence is shown in Figure 5.8. The capacitance from the grains again exhibits the Curie-Weiss behavior, similar to the one shown in Figure 5.6. The values are comparable to those obtained from the Z^* -plane. The values obtained from the M^* -plane, however, give a better fit for the linear dependence of the Curie-Weiss behavior associated with the grains (Figure 5.8), as compared to that shown in Figure 5.6. The line intersects the temperature axis at about 125°C, from which the Curie-Weiss temperature was determined to be $T_0 = 125^\circ\text{C}$. The capacitance values derived from the grain boundaries have the same invariant nature with temperature as shown in Figure 5.6, which results from the totally non-ferroelectric component associated with the grain boundaries.

One point worth mentioning is that in both the Z^* -plane and the M^* -plane at the elevated temperatures, one semicircle (e.g., low-frequency relaxation in the Z^* -plane) is dominant over the other (as the high-frequency relaxation in the Z^* -plane is hardly observable). This illustrates two important criteria in the IS analysis [233]:

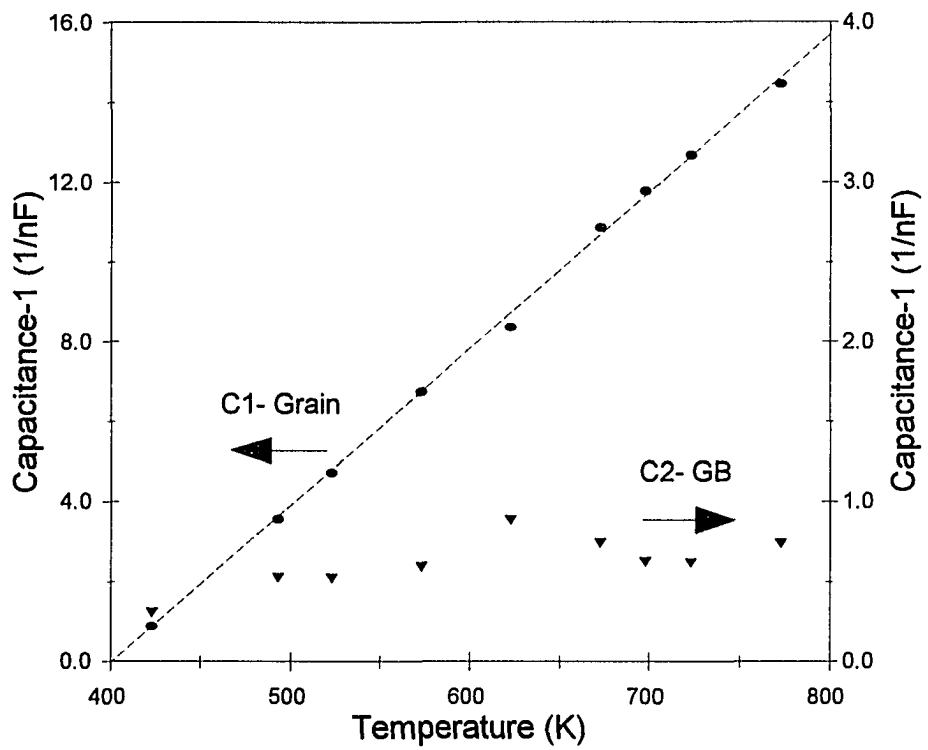


Figure 5.8. Temperature dependence of the capacitances (C_1 and C_2) associated with grain and grain boundary relaxations in the M^* -plane.

- two semicircles can be completely resolved and clearly represented in Z^* - and Y^* -planes if the resistance values of the two physical regions are very close to each other ($R_1 \approx R_2$) and the capacitance values are significantly different ($C_1 \neq C_2$).
- two semicircles can be completely resolved and clearly represented in M^* - and C^* -planes if the capacitance values of the two physical regions are very close to each other ($C_1 \approx C_2$) and the resistance values are significantly different ($R_1 \neq R_2$).

From the foregoing discussions, a plausible electric circuit configuration is constructed for the material system. The circuit can be represented by a voltage dividing model consisting of grain and grain boundary regions. The model is based on the electrical parameters extracted from the Z^* - and M^* -planes, and represented by a parallel R - C combination in series with another parallel R - C combination (Figure 5.9). The high frequency relaxation has been attributed to the bulk (grains) and the low frequency relaxation to the grain boundaries.

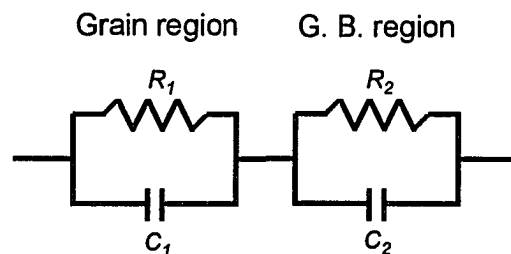


Figure 5.9. Equivalent circuit model corresponding to the two semicircular relaxations in the impedance plane. R_1 - C_1 and R_2 - C_2 combinations constitute the high- (grain) and low- frequency (grain boundary) relaxations, respectively.

The complex impedance of the circuit shown in Figure 5.9 can be expressed by the equation:

$$\begin{aligned} Z^*(\omega) &= (R_1^{-1} + j\omega C_1)^{-1} + (R_2^{-1} + j\omega C_2)^{-1} \\ &= Z' - jZ'' \end{aligned} \quad (5.9)$$

where:

$$\begin{aligned} Z' &= \frac{R_1}{1 + (\omega R_1 C_1)^2} + \frac{R_2}{1 + (\omega R_2 C_2)^2} \\ Z'' &= \frac{\omega R_1^2 C_1}{1 + (\omega R_1 C_1)^2} + \frac{\omega R_2^2 C_2}{1 + (\omega R_2 C_2)^2} \end{aligned}$$

ω is the angular frequency and $j = \sqrt{-1}$. The complex capacitance C^* can be related to Z^* by:

$$C^*(\omega) = \frac{1}{j\omega Z^*(\omega)} = C' - jC'' \quad (5.10)$$

Thus:

$$C' = \frac{\frac{(R_2 C_2)^2}{C_1} + \frac{(R_1 C_1)^2}{C_2} + \omega^2 \left(\frac{1}{C_1} + \frac{1}{C_2} \right)}{\left(\frac{1}{R_2 C_1 C_2} + \frac{1}{R_1 C_1 C_2} \right)^2 + \omega^2 \left(\frac{1}{C_1} + \frac{1}{C_2} \right)^2} \quad (5.11)$$

This equation can be further simplified by considering $R_1 \ll R_2$, which is the case in this study:

$$C' = \frac{C_2^{-1} + (\omega R_1 C_1)^2 (C_1^{-1} + C_2^{-1})}{C_2^{-2} + (\omega R_1 C_1)^2 (C_1^{-1} + C_2^{-1})^2} \quad (5.12)$$

According to the equation, the frequency dependence of real capacitance can be simulated by assigning the R and C values. The results are shown in Figure 5.10. They can be characterized by:

- a low frequency plateau (when $\omega \rightarrow 0$), where

$$\mathbf{C}' = \mathbf{C}_2 \quad (5.13)$$

- a dispersion centered at a frequency, f_m , which also corresponds to a maximum \mathbf{C}'' :

$$\begin{aligned} f_m &= [\omega \mathbf{C}_2 (\mathbf{C}_1^{-1} + \mathbf{C}_2^{-1}) R_1 \mathbf{C}_1]^{-1} \\ &= [2\pi R_1 (\mathbf{C}_1 + \mathbf{C}_2)]^{-1} \end{aligned} \quad (5.14)$$

- a high frequency plateau (when $\omega \rightarrow \infty$), where

$$\mathbf{C}' = (\mathbf{C}_1^{-1} + \mathbf{C}_2^{-1})^{-1} \quad (5.15)$$

The simulated capacitance spectra are very similar to those experimentally obtained at various temperatures (Figure 4.41). Although the low frequency plateau is not clearly displayed (due to the frequency limit of the instrument), the high frequency plateau, the shift of dispersion toward high frequencies and the increased magnitude of dispersion (Figure 4.41) sufficiently support the proposed equivalent circuit model.

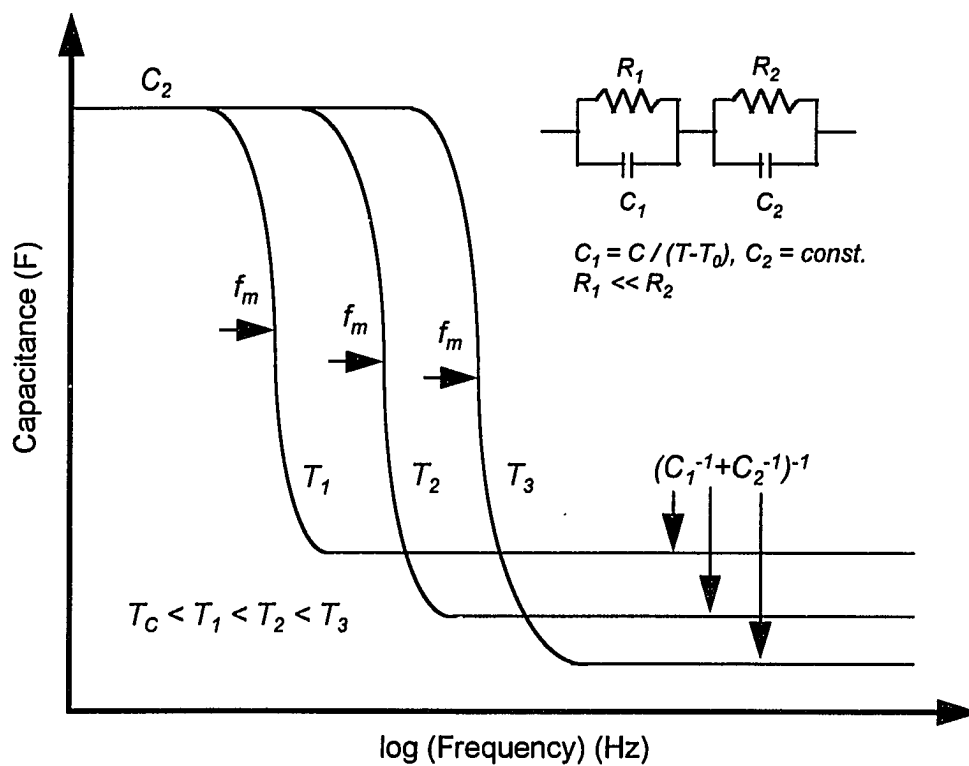


Figure 5.10. Schematic of the simulation results of frequency dependence of the capacitance for ferroelectric materials above T_c by assigning the R and C values.

5.4.2. Hydrothermally Synthesized BaTiO₃ Thin Films

IS analysis was also carried out on the BaTiO₃ thin film samples produced by hydrothermal synthesis for a time period of 2 weeks. There is only one semicircle observed in the impedance, Z^* plane (Figure 4.54), suggesting a complete dominance of one relaxation mechanism in the Z^* -plane. However, two relaxations can be resolved in the modulus, M^* plane (Figure 4.55). Based on the results of IS analysis on the bulk sample, the high frequency relaxation (right side) observed for the thin film sample is assigned to the grain contribution, while the low frequency relaxation corresponds to the grain boundary contribution. It is found that at low temperatures, the low frequency relaxation is more nearly ideal (smaller depression angles), which resembles a Debye-type relaxation. However, the relaxation departs from the ideal Debye-type behavior as temperature increases, as evidenced by a more depressed semicircle (Figure 4.55). This indicates an increase in the degree of heterogeneity at the grain boundaries, which are thermally activated at high temperatures (> 200°C). In the C^* -plane, it is found that at the high frequency end (left side), the capacitance values keep on decreasing toward the negative values, suggesting that an inductive component may set in at the high frequency limit. This inductive component may arise from the coupling of lead wires at high frequencies.

The analysis of the electrical data obtained from the immittance spectra is preliminary. Further analysis needs to be carried out to derive the capacitance and resistance values associated with grain and grain boundary contributions and their temperature dependence. It is also important to investigate the mechanism responsible for the thermally dependent phenomenon which occurs in the grain boundary region.

CHAPTER VI

SUMMARY AND CONCLUSIONS

Barium titanate powders were synthesized using the hydrothermal synthesis technique. The synthesis mechanism was examined in terms of various synthesis parameters such as temperature, time, pH and anion sources. The microstructure and properties of the powders were studied using different characterization techniques, including electron microscopy (SEM, TEM), thermal analysis (DSC, TG/DTA) methods, XRD and vibrational spectroscopy (IR and Raman) techniques. The mechanism responsible for the decrease in enthalpy change (ΔH) associated with the Curie transition and the appearance of the cubic-like structure of fine (submicron) size powders were examined.

The sintering behavior of these powders has also been investigated and compared with that of commercial powders. Correlations between the sintering conditions, microstructure and dielectric properties were established. The ac electrical data obtained from the sintered samples were analyzed using an immittance spectroscopy (IS) technique, and the electrical contributions from

different physical regions were differentiated based on their frequency responses.

Thin BaTiO₃ films were synthesized using hydrothermal synthesis, and their microstructure and electrical properties were examined. Their frequency dependent electric behavior was also investigated using the IS analysis.

Based on the results obtained, the following conclusions are made:

1. Well-crystallized tetragonal BaTiO₃ powders with high purity were synthesized at 240°C under hydrothermal conditions. The hydrothermal formation of BaTiO₃ is suggested to follow a dissolution/precipitation mechanism with the dissolution of the precursors in the solution and the formation of BaTiO₃ as precipitates. An Ostwald ripening process is responsible for the growth of the particles. The size of the particles could be controlled by adjusting the synthesis parameters, including temperature, time, pH, *etc.*
2. The enthalpy change (ΔH) associated with the Curie transition was determined and found to be proportional to the tetragonality of the powders. There appears to be a correlation between the particle size and ΔH (or tetragonality), with ΔH decreasing with the particle size. Although a near zero value of ΔH was obtained in smaller particles, Raman spectroscopy indicates a tetragonal symmetry of unit cells.

3. Hydroxyl defects and related lattice strains may not be the major factors responsible for the decrease of ΔH (or tetragonality) with particle size, as their magnitudes are relatively low. The decrease in ΔH (with particle size) is attributed to the depolarization field and/or the surface-disordered state (mean-field consideration). A strong depolarization field may be present in fine particles with a single-domain configuration, which results in the instability of the ferroelectric phase and a decrease in ΔH . The surface disordered state will cause more disordering of the dipoles in the particles as the particle size decreases, resulting in a decrease in ΔH and eventually a size-driven transition from the polar (ferroelectric) to non-polar (paraelectric) form.

4. Tetragonal powders showed better sinterability as compared to the cubic powder. This is because the tetragonal powders have a more ideal and homogeneous structure with fewer defects, which promotes low temperature sintering and prevents exaggerated grain growth. Sintering conditions (e.g., temperature, time and heating rate) have a strong influence on the microstructure development. Fast-sintering (with a heating rate around 200°C/min) has been shown to be an effective way to limit the grain growth and achieve relatively high density of the samples.

5. There is a correlation between the microstructure and the dielectric properties. As anticipated, samples with finer grain size (close to 1 μm) and higher density possess higher dielectric constant and lower loss.
6. Well-crystallized tetragonal BaTiO_3 thin films were directly produced using hydrothermal synthesis at 240°C . The film thickness was around 0.5 μm and remained constant as the synthesis further proceeded. The formation and growth mechanisms are suggested to follow those of the powders.
7. Thin-film BaTiO_3 had a dielectric constant around 400 ~ 500 with no indication of the Curie transition. This has been attributed to the influence of the Schottky barrier, stress and/or strong depolarization field.
8. Two semicircular relaxations were shown both in the impedance (Z^*) and modulus (M^*) planes for sintered samples, from which the capacitance (C_1 and C_2) and resistance (R_1 and R_2) values corresponding to the two relaxations were derived. The capacitance of the high frequency relaxation (C_1) exhibited a Curie-Weiss temperature dependence, and the relaxation is thereby associated with the grains. The capacitance of the low frequency relaxation (C_2) was relatively large and temperature invariant, and the relaxation might be associated with the grain boundary region. The equivalent circuit model of the sintered sample system is proposed to be a parallel R - C combination (grain) in series with another parallel R - C combination (grain boundary).

CHAPTER VII

SUGGESTIONS FOR FUTURE WORK

Barium titanate is often doped with other aliovalent cations to inhibit grain growth, or to obtain semiconducting properties. Although hydrothermal process has been used successfully to produce pure BaTiO₃ powders in this study, it would be important to know whether it can be adopted to introduce low level dopants into BaTiO₃ and to study their sintering behavior.

Barium titanate based positive temperature coefficient thermistors (PTCRs) have found numerous applications as temperature sensors, current limiters, current attenuation devices, *etc.* Although significant progress has been made in understanding the PTCR behavior, there are still discrepancies in the explanation of the temperature-resistivity behavior. Advances in wet-chemical synthesis of BaTiO₃-based powders with better characteristics in terms of chemical homogeneity, structural uniformity, and stoichiometry control will facilitate the study of the mechanism and properties of the PTCR thermistor.

In this study, hydrothermal synthesis of BaTiO₃ films has been investigated. The films showed low dielectric constant (300 ~ 400) and no

transition around the Curie temperature. It is necessary to understand the exact mechanism responsible for the disappearance of the Curie transition, which is not apparent based on the results of this study. Therefore, it is useful to further characterize the electrical behavior of the films, such as their hysteresis behavior, capacitance dependence on bias voltage (C-V measurement), and also the stress in the films.

The immittance spectroscopy (IS) analysis on the thin film samples in this study is preliminary. Further analysis is needed to extract relevant electrical parameters (e.g., capacitance and resistance) associated with microstructural features, such as grains and grain boundaries, substrate and electrode interface, and their temperature dependence.

REFERENCES

1. B. Wul and I. M. Goldman, *C. R. Acad. Sci. URSS.*, **46**, 139; **49**, 177 (1945).
2. B. Wul and I. M. Goldman, *C. R. Acad. Sci. URSS.*, **51**, 21 (1946).
3. M. E. Lines and A. M. Glass, *Principles and Applications of Ferroelectrics and Related Materials*, Clarendon Press, Oxford, 1977.
4. M. S. H. Chu and A. W. I. M. Rae, "Manufacturing Dielectric Powders," *Am. Ceram. Soc. Bull.*, **74** (6), 69 (1995).
5. J. M. Wilson, "Mineral Review," *ibid.*
6. M. Anliker, H. R. Brugger and W. Kanzig, "Das Verhalten von kolloidalen Seignetteelektrika III, Bariumtitanat BaTiO₃," *Helv. Phys. Acta.*, **27**, 99 (1954).
7. A. K. Goswami, "Dielectric Properties of Unsintered Barium Titanate," *J. Appl. Phys.*, **40**, 619 (1969).
8. D. R. Callaby, "Surface Layer of BaTiO₃," *J. App. Phys.*, **37**, 2295 (1966).
9. S. Naka, F. Nakakita, Y. Suwa and M. Inagaki, "Change from Metastable Cubic to Stable Tetragonal Form of Submicron Barium Titanate," *Bulletin Chem. Soc. Jap.*, **47**, 1168 (1974).
10. W. R. Buessem, L. E. Cross and A. K. Goswami, "Phenomenological Theory of High Permittivity in Fine-Grained Barium Titanate," *J. Am. Ceram. Soc.*, **49**, 33 (1966).
11. K. Okazaki and K. Nagata, "Effects of Grain Size and Porosity on Electric and Optical Properties of PLZT Ceramics," *J. Am. Ceram. Soc.*, **56**, 82 (1973).

12. K. Okazaki and H. Igarashi, "Importance of Microstructure in Electronic Ceramics," in *Ceramic Microstructure '76*, edited by R. M. Fulrath and J. A. Pask, Westview Press, Boulder, CO, p564, 1976.
13. H. Banno, "Effects of Shape and Volume Fraction of Closed Pores on Dielectric, Elastic, and Electromechanical Properties of Dielectric and Piezoelectric Ceramics-A Theoretical Approach," *Am. Ceram. Soc. Bull.*, **66**, 1332 (1987).
14. F. Jona and G. Shirane, *Ferroelectric Crystals*, Macmillan, New York, 1962.
15. E. Fatuzzo and W. J. Merz, *Ferroelectricity*, North-Holland, Amsterdam, 1967.
16. S. B. Lange, *Sourcebook of Pyroelectricity*, Gordon and Breach, London, 1974.
17. J. Valasek, "Piezoelectric and Allied Phenomena in Rochelle Salt," *Phys. Rev.*, **15**, 537 (1920).
18. J. Valasek, "Piezo-Electric and Allied Phenomena in Rochelle Salt," *Phys. Rev.*, **17**, 475 (1921).
19. B. T. Matthias, "New Ferroelectric Crystals," *Phys. Rev.*, **75**, 1771 (1949).
20. B. T. Matthias and J. P. Remeika, "Ferroelectricity in the Ilmenite Structure," *Phys. Rev.*, **76**, 1886 (1949).
21. G. Shirane, S. Hoshino and K. Suzuki, "X-ray Study of the Phase Transition in Lead Titanate," *Phys. Rev.*, **80**, 1105 (1950).
22. W. Cochran, *Phys. Rev. Lett.*, **3**, 412 (1959).
23. W. Cochran, "Crystal Stability and the Theory of Ferroelectricity," *Adv. in Phys.*, **9**, 387 (1960).
24. W. Cochran, "Crystal Stability and the Theory of Ferroelectricity Part II. Piezoelectric Crystals," *Adv. in Phys.*, **10**, 401 (1961).
25. W. Cochran, "Dynamical, Scattering and Dielectric Properties of Ferroelectric Crystals," *Adv. in Phys.*, **18**, 157 (1969).

26. P. W. Anderson, in *Fizika Dielektrikov*, edited by G. I. Skanavi, Akad. Nauk. SSSR, Moscow, 1960.
27. R. Binc and B. Zeks, *Soft Modes in Ferroelectrics and Antiferroelectrics*, North-Holland, Amsterdam, 1974.
28. L. D. Landau, "On the Theory of Phase Transitions," *Collected Papers of L. D. Landau*, edited by D. ter Haar, Gordon Breach, New York, 1965.
29. V. L. Ginzburg, *Zh. eksp. teor. Fiz.*, **15**, 739 (1945). **19**, 36 (1949).
30. V. L. Ginzburg and L. D. Landau, *JETP*, **20**, 1064 (1950).
31. A. F. Devonshire, "Theory of Barium Titanate, Part I," *Phil. Mag.*, **40**, 1040 (1949).
32. A. F. Devonshire, "Theory of Barium Titanate, Part II," *Phil. Mag.*, **42**, 1065 (1951).
33. A. F. Devonshire, "Theory of Ferroelectrics," *Adv. in Phys.*, **3**, 85 (1954).
34. W. D. Kingery, H. K. Bowen and D. R. Uhlmann, *Introduction to Ceramics*, 2nd Edition, John Wiley & Sons, New York, NY, 1976.
35. L. L. Hench and J. K. West, *Principles of Electronic Ceramics*, John Wiley & Sons, New York, NY, 1990.
36. A. J. Moulson and J. M. Herbert, *Electroceramics: Materials, Properties and Applications*, Chapman and Hall, London, 1990.
37. P. W. Forsbergh, Jr., "Domain Structures and Phase Transitions in Barium Titanate," *Phys. Rev.*, **76**, 1187 (1949).
38. W. J. Merz, "Domain Formation and Domain Wall Motions in Ferroelectric BaTiO₃ Single Crystals," *Phys. Rev.*, **95**, 690 (1954).
39. J. A. Hooton and W. J. Merz, "Etch Patterns and Ferroelectric Domains in BaTiO₃ Single Crystals," *Phys. Rev.*, **98**, 409 (1955).

40. M. Tanaka and G. Honjo, "Electron Optical Studies of Barium Titanate Single Crystal Films," *J. Phys. Soc. Jap.*, **19**, 954 (1964).
41. O. Eibl, P. Pongratz and P. Skalicky, "Crystallography of (111) twins in BaTiO₃," *Phil. Magn.*, **B57**, 521 (1988).
42. W. R. Cook, Jr., "Domain Twinning in Barium Titanate Ceramics," *J. Am. Ceram. Soc.*, **39**, 17 (1956).
43. Frank Kulcsar, "A Microstructure Study of Barium Titanate Ceramics," *J. Am. Ceram. Soc.*, **39**, 13 (1956).
44. R. C. de Vries and J. E. Burke, "Microstructure of Barium Titanate Ceramics," *J. Am. Ceram. Soc.*, **40**, 200 (1957).
45. G. Arlt and P. Sasko, "Domain Configuration and Equilibrium Size of Domains in BaTiO₃ Ceramics," *J. Appl. Phys.*, **51**, 4956 (1980).
46. G. Arlt, N. A. Pertsev and G. DeWith, "Dielectric Properties of Fine-Grained Ceramics," *J. Appl. Phys.*, **58**, 1619 (1985).
47. G. Arlt, "The Role of Domain Walls on the Dielectric, Elastic and Piezoelectric Properties of Ferroelectric Ceramics," *Ferroelectrics*, **76**, 451 (1987).
48. G. Arlt, "The Influence of Microstructure on the Properties of Ferroelectric Ceramics," *Ferroelectrics*, **104**, 217 (1990).
49. G. Arlt, "Twinning in Ferroelectric and Ferroelastic Ceramic: Stress Relief," *J. Mater. Sci.*, **25**, 2655 (1990).
50. G. Arlt and N. A. Pertsev, "Force Constant and Effective Mass of 90° Domain Walls in Ferroelectric Ceramics," *J. Appl. Phys.*, **70**, 2283 (1991).
51. S. B. Kim, T. J. Chung and D. Y. Kim, "Effect of External Compressive Stress on the Domain Configuration of Barium Titanate Ceramics," *J. Europ. Ceram. Soc.*, 147 (1993).
52. C. Kittel, "Theory of the Structure of Ferromagnetic Domains in Films and Small Particles," *Phys. Rev.*, **70**, 965 (1946).
53. J. Frenkel and J. Dorfman, *Nature*, **126**, 274 (1930).

54. L. Neel, *J. Phys. Radium.*, **5**, 241 (1944).
55. W. C. Elmore, *Phys. Rev.*, **54**, 1092 (1938); **60**, 593 (1941).
56. I. P. Batra, P. Wurfel and B. D. Silverman, "Phase Transition, Stability, and Depolarization Field in Ferroelectric Thin Films," *Phys. Rev.*, **8**, 3257 (1973).
57. H. I. Hsiang and F. S. Yen, "Dielectric Properties and Ferroelectric Domain of BaTiO₃ Powders," *Jpn. J. Appl. Phys.*, **32**, 5029 (1993).
58. A. A. Anan'eva, B. V. Strizkov and M. A. Ugryumova, "Some Anomalous Properties of Chemically Pure Barium Titanate," *Bull. Acad. Sci., USSR, Phys. Ser. (English Transl.)*, **24**, 1395 (1960).
59. K. Kinoshita and A. Yamaji, "Grain-Size Effects on Dielectric Properties in Barium Titanate Ceramics," *J. Appl. Phys.*, **47**, 371 (1976).
60. G. Shirane, F. Jona and R. Repinsky, *Proc. I. R. E.*, **42**, 1738 (1955).
61. L. Azaroff and J. J. Brophy, *Electronic Processes in Materials*, McGraw-Hill, New York, Chapter 12, 1963.
62. J. Harada, T. Pedersen and Z. Barnea, *Acta Crystallog.* **A26**, 336 (1970).
63. Y. Yamada, G. Shirane and A. Linz, *Phys. Rev.*, **177**, 848 (1969).
64. G. Shirane, J. D. Axe, J. Harada and A. Linz, *Phys. Rev.*, **B2**, 3651 (1970).
65. J. Harada, J. D. Axe and G. Shirane, *Phys. Rev.*, **B4**, 155 (1971).
66. J. R. Burfoot, *Ferroelectrics: An Introduction to the Physical Principles*, D. Van Nostrand Company Ltd., London, 1967.
67. G. Burns, *Solid State Physics*, Academic Press, Orlando, FL, 1985
68. Y. Xu, *Ferroelectric Materials and Their Applications*, North-Holland, Amsterdam, 1991.
69. W. J. Merz, *Phys. Rev.*, **91**, 513 (1953).

70. D. L. Mills, *Phys. Rev.* **B3**, 3887 (1971); **B8**, 4424 (1973).
71. K. Binder and P. C. Hohenberg, "Phase Transitions and Static Spin Correlations in Ising Model with Free Surfaces," *Phys. Rev.*, **6**, 3461 (1972).
72. K. Binder and P. C. Hohenberg, "Surface Effects on Magnetic Phase Transitions," *Phys. Rev.*, **B9**, 2194 (1974).
73. P. Kumar, "Magnetic Phase Transition at a surface: Mean-Field Theory," *Phys. Rev.*, **B10**, 2928 (1974).
74. T. Wolfram, R. E. Dewames, W. F. Hall and P. W. Palmberg, *Surf. Sci.*, **28**, 45 (1971).
75. R. Kretschmer and K. Binder, "Surface Effects on Phase Transitions in Ferroelectrics and Dipolar Magnets," *Phys. Rev.*, **B20**, 1065 (1979).
76. K. Binder, "Surface Effects on Phase Transitions in Ferroelectrics and Antiferroelectrics," *Ferroelectrics*, **35**, 99 (1981).
77. D. R. Tilley, B. Zeks, "Landau Theory of Phase Transitions in Thick Films," *Solid State Comm.*, **49**, 823 (1984).
78. M. G. Cottam, D. R. Tilley and B. Zeks, "Theory of Surface Modes in Ferroelectrics," *J. Phys. C: Solid State Phys.*, **17**, 1793 (1984).
79. V. A. Zhirnov, *Sov. Phys. JETP*, **35**, 822 (1959).
80. M. H. Frey and D. A. Payne, "Nanocrystalline Barium Titanate: Evidence for the Absence of Ferroelectricity in Sol-Gel Derived Thin-Layer Capacitors," *Appl. Phys. Lett.*, **63**, 2753 (1993).
81. K. Kajiyoshi, N. Ishizawa and M. Yoshimura, "Preparation of Tetragonal Barium Titanate Thin Film on Titanium Metal Substrate by Hydrothermal Method," *J. Am. Ceram. Soc.*, **74**, 369-74 (1991).
82. Y. Xu, C. H. Cheng and J. D. Mackenzie, "Electrical Characterization of Polycrystalline and Amorphous Thin Films of $\text{Pb}(\text{Zr}_x\text{Ti}_{1-x})\text{O}_3$ and BaTiO_3 Prepared by Sol-Gel Technique," *J. Non-Cryst. Solids*, **176**, 1 (1994).

83. K. Uchino, E. Sadanaga and T. Hirose, "Dependence of the Crystal Structure on Particle Size in Barium Titanate," *J. Am. Ceram. Soc.*, **72**, 1555 (1989).
84. T. Yamamoto, K. Urabe and H. Banno, "BaTiO₃ Particle-Size Dependence of Ferroelectricity in BaTiO₃/Polymer Composites," *Jap. J. Appl. Phys.*, **32**, 4272 (1993).
85. K. Saegusa, E. R. Wendell and H. K. Bowen, *J. Am. Ceram. Soc.*, **76**, 1505 (1993).
87. B. D. Begg, E. R. Vance, D. J. Cassidy, J. Nowotny, S. Blairs, "Particle Size Effect on the Room Temperature Structure of Barium Titanate," *Ceram. Trans.*, **41**, 169 (1994).
88. D. Hennings and S. Schreinemacher, "Characterization of Hydrothermal Barium Titanate," *J. Europ. Ceram. Soc.*, **9**, 41 (1992).
89. R. Vivekanandan and T. R. N. Kutty, "Characterization of Barium Titanate Fine Powders Formed from Hydrothermal Crystallization," *Powder Techn.*, **57**, 181 (1989).
90. Y. G. Wang, W. L. Zhong and P. L. Zhang, "Size Driven Phase Transition in Ferroelectric Particles," *Solid State Comm.*, **90**, 329 (1994).
91. S. Schlag and H. F. Eicke, "Size Driven Phase Transition in Nanocrystalline BaTiO₃," *Solid State Comm.*, **91**, 883 (1994).
92. G. Busca, V. Buscaglia, M. Leoni and P. Nanni, "Solid-State and Surface Spectroscopic Characterization of BaTiO₃ Fine Powders," *Chem. Mater.*, **6**, 955 (1994).
93. R. Asiaie, W. Zhu, P. K. Dutta and S. A. Akbar, "Characterization of Submicron Particles of Tetragonal BaTiO₃" *Submitted to Chem. Mater.*
94. B. Jaffe, W. R. Cook and H. Jaffe, *Piezoelectric Ceramics*, Academic Press, New York, 1971.
95. M. Cournil, M. Soustelle and G. Thomas, "Solid-Solid Reactions, I: Experimental Study of Barium Metatitanate Synthesis and Solid-Solid Reactions, II: Mechanism of Barium Metatitanate Synthesis," *Oxid. Metal*, **13**, 89 (1979).

96. A. Beauger, J. C. Mutin and J. C. Niepce, "Synthesis Reaction of Metatitanate BaTiO₃, Part 1 Effect of the Gaseous Atmosphere upon the Thermal Evolution of the System BaCO₃-TiO₂," *J. Mater. Sci.*, **18**, 3041 (1983).
97. A. Beauger, J. C. Mutin and J. C. Niepce, "Synthesis Reaction of Metatitanate BaTiO₃, Part 2 Study of Solid-Solid Reaction Interfaces," *J. Mater. Sci.*, **18**, 3543 (1983).
98. L. S. Millberg, "The Synthesis of Ceramic Powders," *J. Metals*, **Aug.**, 9 (1987).
99. P. P. Phule, S. H. Risbud, "Review Low-Temperature Synthesis and Processing of Electronic Materials in the BaO-TiO₂ System," *J. Mater. Sci.*, **25**, 1169 (1990).
100. A. Stein, S. W. Keller, T. E. Mallouk, "Turing Down the Heat: Design and Mechanism in Solid-State Synthesis," *Science*, **259**, 1558 (1993).
101. W. S. Claubaugh, E. M. Swiggard and R. Gilchrist, *J. Res. Natl. Bur. Std.*, **56**, 289 (1956).
102. P. K. Gallagher, F. Schrey and F. V. DiMarcello, "Preparation of Semiconducting Titanates by Chemical Methods," *J. Am. Ceram. Soc.*, **46**, 359 (1963).
103. J. M. Bind, T. Dupin, J. Schafer and M. Titeux, "Industrial Synthesis of Coprecipitated BaTiO₃ Powders," *J. Metals*, **8**, 60 (1987).
104. K. Kudaka, K. Iizumi and K. Sasaki, "Preparation of Stoichiometric Barium Titanyl Oxalate Tetrahydrate," *Am. Ceram. Soc. Bull.*, **72**, 1236 (1982).
105. T. T. Fang and H. B. Lin, "Factors Affecting the Preparation of Barium Titanyl Oxalate Tetrahydrate," *J. Am. Ceram. Soc.*, **72**, 1899 (1989).
106. F. U. Yen, C. T. Chang and Y. H. Chang, "Characterization of Barium Titanyl Oxalate Tetrahydrate," *J. Am. Ceram. Soc.*, **73**, 3422 (1990).

107. W. E. Rhine, R. B. Hallock, W. M. Davis and W. Wong-Ng, "Synthesis and Crystal Structure of Barium Titanyl Oxalate, $\text{BaTi}(\text{O})(\text{C}_2\text{O}_4)_2 \cdot 5\text{H}_2\text{O}$: A Molecular Precursor for BaTiO_3 ," *Chem. Mater.*, **4**, 1208 (1992).
108. W. E. Rhine, K. Saegusa, R. B. Hallock and M. J. Cima, "Control of Ceramic Powder Composition by Precipitation Techniques" in *Ceramic Powder Science III, Ceramic Transactions*, **12**, p107, Edited by G. L. Messing, S. Hirano and H. Hausner, American Ceramic Society, Columbus, 1990.
109. G. Pfaff, F. Schmidt, W. Ludwig and A. Feltz, *J. Thermal Anal.*, 771 (1988).
110. S. Bhattacharjee, M. K. Paria and H. S. Maiti, "Preparation of Amorphous and Crystalline Forms of Barium Titanyl Oxalate," *Ceram. Int.*, **16**, 211 (1990).
111. M. Pechini, *US patent*, **3330697**, July (1967).
112. B. J. Mulder, "Preparation of BaTiO_3 and Other Ceramic Powders By Coprecipitation of Citrates in an Alcohol," *Am. Ceram. Soc. Bull.*, **49**, 990 (1970).
113. D. Hennings and W. Mayr, *J. Solid State Chem.*, **26**, 329 (1978).
114. H. Salez, P. Odier and B. Cales, "Elaboration of Fine Micropowders From Organometallic Polymers Precursors," *J. Non. Cryst. Solids*, **82**, 314 (1986).
115. K. S. Mazdidasni, R. T. Dolloff and J. S. Smith II, "Preparation of High-Purity Submicron Barium Titanate Powders," *J. Am. Ceram. Soc.*, **52**, 523 (1969).
116. K. S. Mazdidasni and L. M. Brown, "Microstructure and Electrical Properties of Sc_2O_3 -Doped, Rare-Earth-Oxide-Doped, and Undoped BaTiO_3 ," *J. Am. Ceram. Soc.*, **54**, 539 (1971).
117. H. C. Graham, N. M. Tallan and K. S. Mazdidasni, "Electrical Properties of High-Purity Polycrystalline Barium Titanate," *J. Am. Ceram. Soc.*, **54**, 548 (1971).

118. K. S. Mazdiyasi and L. M. Brown, "Synthesis of Nb₂O₅-Doped BaTiO₃ with Improved Electrical Properties," *J. Am. Ceram. Soc.*, **55**, 633 (1972).
119. K. S. Mazdiyasi, "Fine Particle Perovskite Processing," *Am. Ceram. Soc. Bull.*, **63**, 591 (1984).
120. J. J. Ritter, R. S. Roth and J. E. Blendell, "Alkoxide Precursor Synthesis and Characterization of Phases in the Barium-Titanium Oxide System," *J. Am. Ceram. Soc.*, **69**, 155 (1986).
121. H. Okamura and H. K. Bowen, "Preparation of Alkoxides for the Synthesis of Ceramics," *Ceram. Int.*, **12**, 161 (1986).
122. H. C. Lu, L. E. Burkhart and G. L. Schrader, "Sol-Gel Process for the Preparation of Ba₂Ti₉O₂₀ and BaTi₅O₁₁," *J. Am. Ceram. Soc.*, **74**, 968 (1991).
123. C. J. Brinker and G. W. Scherer, "Sol Gel Glass: I. Gelation and Gel Structure," *J. Non-Cryst. Solids*, **70**, 301 (1985).
124. H. Schmidt, "Chemistry of Material Preparation by the Sol-Gel Process," *J. Non-Cryst. Solids*, **100**, 51 (1988).
125. S. N. B. Hodgson, J. Cawley, M. Clubley and E. A. Wilson, "Doping and Mixing of Ceramics Using Alkoxide precursors," *Novel Synthesis and Processing of Ceramics, British Ceram. Proc.*, **53**, ed. F. R. Sale, University Press, Cambridge, UK, p49 (1994).
126. A. Atkinson, J. Doorbar, D. L. Segal and P. J. White, "Sol-Gel Ceramic Stains," *Novel Synthesis and Processing of Ceramics, British Ceram. Proc.*, **53**, ed. F. R. Sale, University Press, Cambridge, UK, p49 (1994).
127. C. J. Brinker and G. W. Scherer, *Sol-Gel Science: the Physics and Chemistry of Sol-Gel Processing*, Academic Press, Boston, 1990.
128. H. Schmidt, "Sol-Gel Processing of Ceramics," *Ceramic Powder Sci. IV*, **22**, edited by S. I. Hirano, G. L. Messing and H. Hausner, The American Ceramic Society, Westerville, OH, p3, 1991.
129. S. S. Flaschen, "Aqueous Synthesis of Barium Titanate," *J. Am. Chem. Soc.*, **46**, 567 (1963).

130. K. Kiss, J. Magder, M. S. Vukasovich and R. J. Lockhart, "Ferroelectrics of Ultrafine Particle Size: I, Synthesis of Titanate Powders of Ultrafine Particle Size," *J. Am. Ceram. Soc.*, **49**, 291 (1966).
131. F. Chaput and J. P. Boilot, "Chemical Processing of (Ba, Sr)(Ti, Zr)O₃ Perovskite Ceramics," *J. Mater. Sci. Lett.*, **6**, 1110 (1987).
132. F. Chaput and J. P. Boilot, "Alkoxide-Hydroxide Route to Synthesize BaTiO₃-Based Powders," *J. Am. Ceram. Soc.*, **73**, 942 (1990).
133. M. I. Diaz-Guemes, T. G. Carreno and C. J. Serna, "Mechanism of Formation of MTiO₃ (M = Sr or Ba) by the Gel Method," *J. Mater. Sci.*, **24**, 1011 (1989).
134. C. Lemoine, B. Gilbert, B. Michaux, J. P. Pirard and A. J. Lecloux, "Synthesis of Barium titanate by the Sol-Gel Process," *J. Non-Cryst. Solids*, **175**, 1 (1994).
135. C. Sanchez, F. Babonneau, S. Doeuff and A. Leautic, in *Ultrastructure Processing of Advanced Ceramics*, ed. J. D. Mackenzie and D. R. Ulrich, p77, Wiley, New York (1988).
136. P. P. Phule and S. H. Risbud, "Sol-Gel Synthesis of Barium Titanate Powders Using Barium Acetate and Titanium (IV) Isopropoxide," *Adv. Ceram. Mater.*, **3**, 183 (1988).
137. P. P. Phule and S. H. Risbud, "Sol-Gel Synthesis and Characterization of BaTi₄O₉ and BaTiO₃ Powders," in *Better Ceramics Through Chemistry III*, edited by C. J. Brinker, D. E. Clark and D. R. Ulrich, Materials Research Society, p275 (1988).
138. G. Tomandl, H. Rosch and A. Stiegelschmitt, "Preparation of BaTiO₃ by Sol-Gel Processing," in *Better Ceramics Through Chemistry III*, edited by C. J. Brinker, D. E. Clark and D. R. Ulrich, Materials Research Society, p281 (1988).
139. A. Mosset, I. Gautier-Lundau, J. Galy, P. Strehlow and H. Schmidt, "Sol-Gel Processed BaTiO₃: Structural Evolution from the Gel to the Crystalline Powder," *J. Non-Cryst. Solids*, **100**, 339 (1988).

140. B. Samuneva, S. Jambazov, D. Lepkova and Y. Dimitriev, "Sol-Gel Synthesis of BaTiO₃ and Ba_{1-x}yCa_ySr_x(Zr_yTi_{1-y})O₃ Perovskite Powders," *Ceram. Int.*, **16**, 355 (1990).
141. T. Yoko, K. Kamiya and K. Tanaka, "Preparation of Multiple Oxide BaTiO₃ Fibres by the Sol-Gel Method," *J. Mater. Sci.*, **25**, 3922 (1990).
142. J. P. Grammatico and J. M. Proto Lopez, "Reaction Sequences in the Systems Ti(OⁱPr)₄ + Ba(CH₃COO)₂ and TiO₂ + Ba(CH₃COO)₂," *J. Mater. Sci.: Mater. in Electronics*, **3**, 82 (1992).
143. G. Pfaff, "Sol-Gel Synthesis of Barium Titanate Powders of Various Compositions," *J. Mater. Chem.*, **2**, 591 (1992).
144. M. Vallet-Regi, V. Ragel, J. Roman, J. L. Martinez, M. Labeau and J. M. Gonzalez-Calbet, "Texture Evolution of SnO₂ Synthesized by Pyrolysis of an Aerosol," *J. Mater. Res.*, **8**, 138 (1993).
145. T. M. Peters, H. Chein and D. A. Lundgren, *Aerosol Sci. Tech.*, **20**, 51 (1994).
146. A. I. Liapis, in *Handbook of Industrial Drying*, edited by A. S. Mujumdar, Marcel Dekker Inc., New York, 1987.
147. F. J. Schnettler, F. R. Monforte and W. W. Rhodes, *Sci. Ceramics*, **4**, 79 (1968).
148. A. Roosen and H. Hausner, in *Ceramic Powders*, ed. P. Vincenzini, Elsevier, Amsterdam, p773, 1983.
149. L. A. Xue, F. L. Riley and R. J. Brook, "Tert-butyl Alcohol – A Medium for Freeze-Drying: Application to Barium Titanate," *Trans. J. Brit. Ceram. Soc.*, **85**, 47 (1986).
150. N. J. Ali and S. J. Mline, "Synthesis and Properties of Barium Titanate Powder Derived from a Catechol Complex," *Trans. J. Brit. Ceram. Soc.*, **86**, 113 (1986).
151. I. Filkova and A. S. Mujumdar, in *Handbook of Industrial Drying*, edited by A. S. Mujumdar, Marcel Dekker Inc., New York, 1987.

152. F. V. Shaw, "Spray Drying: A Traditional Process for Advanced Applications," *Am. Ceram. Soc. Bull.*, **69**, 1484 (1990).
153. A. G. Merzhanov, in *Combustion and Plasma Synthesis of High-Temperature Materials*, edited by Z. A. Munir and J. B. Holt, VCH, New York, 1990.
154. H. C. Yi and J. J. Moore, "Review Self-Propagating High-Temperature (Combustion) Synthesis (SHS) of Powder-Compacted Materials," *J. Mater. Sci.*, **25**, 1159 (1990).
155. K. Kourtakis, M. Robbins, P. K. Gallagher and T. Tiefel, *J. Mater. Res.*, **4**, 1289 (1989).
156. K. Kourtakis, M. Robbins and P. K. Gallagher, "A Novel Synthetic Method for the Preparation of Oxide Superconductors: Anionic Oxidation-Reduction," *J. Solid State Chem.*, **82**, 290 (1989).
157. K. Kourtakis, M. Robbins and P. K. Gallagher, "Synthesis of $\text{Ba}_2\text{YCu}_3\text{O}_7$ Powder by Anionic Oxidation (NO_3^-)-Reduction (RCOO^- , where R is H, CH_3 , and CH_3CH_2)," *ibid.*, **83**, 230 (1989).
158. K. Kourtakis, M. Robbins and P. K. Gallagher, "Synthesis of $\text{Ba}_2\text{YCu}_3\text{O}_7$ by the SCD Method Using Amino Acid Salt Reducing Agents," *ibid.*, **84**, 88 (1990).
159. J. J. Kingsley and K. C. Patil, "A Novel Combustion Process for the Synthesis of Fine Particle α -Alumina and Related Oxide Materials," *Mater. Lett.*, **6**, 427 (1988).
160. J. J. Kingsley, K. Suresh and K. C. Patil, "Combustion Synthesis of Fine-Particle Metal Aluminates," *J. Mater. Sci.*, **25**, 1305 (1990).
161. K. Suresh, N. R. S. Kumar and K. C. Patil, "A Novel Combustion Synthesis of Spinel Ferrites, Orthoferrites and Garnets," *Adv. Mater.*, **3**, 148 (1991).
162. S. Sundar Manoharan, V. Prasad, S. V. Subramaniam and K. C. Patil, *Physica C*, **190**, 225 (1992).

163. M. M. Amala Sekar and K. C. Patil, "Combustion Synthesis and Properties of Fine-Particle Dielectric Oxide Materials," *J. Mater. Chem.*, **2**, 739 (1992).
164. Y. Zhang and G. C. Stangle, "Preparation of Fine Multicomponent Oxide Ceramic Powder by a Combustion Synthesis Process," *J. Mater. Res.*, **9**, 1997 (1994).
165. Z. Zhong and P. K. Gallagher, "Combustion Synthesis and Characterization of BaTiO₃," *J. Mater. Res.*, **10**, 945 (1995).
166. Z. Zhong and P. K. Gallagher, "Combustion Synthesis for BaTi₄O₉ and Pb_xBa_{1-x}Ti₄O₉," *Submitted to J. Mater. Res.*
167. G. W. Morey, "Hydrothermal Synthesis," *J. Am. Ceram. Soc.*, **36**, 279 (1953).
168. W. J. Dawson, J. C. Preston and S. L. Swartz, "Preprocessing Issues of Hydrothermal Synthesis of Fine Dielectric Powders," *Cer. Trans., Ceramic Powder Sci. IV*, **22**, edited by S. I. Hirano, G. L. Messing and H. Hausner, The American Ceramic Society, Westerville, OH, p27, 1991.
169. W. J. Dawson, "Hydrothermal Synthesis of Advanced Ceramic Powders," *Am. Ceram. Soc. Bull.*, **67**, 1673 (1988).
170. P. K. Dutta, R. Asiaie, S. A. Akbar and W. Zhu, "Hydrothermal Synthesis and Dielectric Properties of Tetragonal BaTiO₃," *Chem. Mater.*, **6**, 1542 (1994).
171. A. Rabenau, "The Role of Hydrothermal Synthesis in Materials Science," *J. Mater. Edu.*, **10**, 543 (1988).
172. M. M. Lencka and R. E. Riman, "Thermodynamic Modeling of Hydrothermal Synthesis of Ceramic Powders," *Chem. Mater.*, **5**, 61 (1993).
173. A. N. Christensen, "Hydrothermal Preparation of Barium Titanate by Transport Reactions," *Acta Chem. Scand.*, **24**, 2447 (1970).
174. R. Vivekanandan, s. Philip and T. R. N. Kutty, "Hydrothermal Preparation of Ba(Ti, Zr)O₃ Fine Powders," *Mat. Res. Bull.*, **22**, 88 (1986).

175. T. R. N. Kutty and R. Murugaraj, "Hydrothermal Precipitation and Characterization of Poly titanates in the System BaO-TiO₂," *J. Mater. Sci. Lett.*, **7**, 601 (1988).
176. R. Vivekanandan and T. R. N. Kutty, "Hydrothermal Synthesis of Ba(Ti, Sn)O₃ Fine Powders and Dielectric Properties of the Corresponding Ceramics," *Ceram. Intern.*, **14**, 207 (1988).
177. T. R. N. Kutty and P. Padmini, "Wet Chemical Formation of Nanoparticles of Binary Perovskites through Isothermal Gel to Crystallite Conversion," *Mater. Res. Bull.*, **27**, 945 (1992).
178. K. Osseo-Asare, F. J. Arriagada and J. H. Adair, *Cer. Tans., Ceramic Powder Sci. IV*, **20**, edited by G. L. Messing, E. R. Fuller, Jr., and H. Hausner, The American Ceramic Society, Westerville, OH, p47, 53, 1988.
179. D. Hennings, G. Rosenstein and H. Schreinemacher, "Hydrothermal Preparation of Barium Titanate from Barium-Titanium Acetate Gel Precursors," *J. Europ. Ceram. Soc.*, **8**, 107 (1991).
180. K. Fukai, K. Hidaka, M. Aoki and K. Abe, "Non-Ferroelectric Barium Titanate Ceramics," *Ceramic Dielectrics*, 344.
181. K. Abe and S. Matsumoto, "Hydrothermal Processing of Functional Ceramic Powders," *Ceramic Powder Sci. IV*, **22**, edited by S. I. Hirano, G. L. Messing and H. Hausner, The American Ceramic Society, Westerville, OH, p15, 1991.
182. K. Fukai, K. Hidaka, M. Aoki and K. Abe, "Preparation and Properties of Uniform Fine Perovskite Powders by Hydrothermal Synthesis," *Ceram. Inter.*, **16**, 285 (1990).
183. P. K. Dutta and J. R. Gregg, "Hydrothermal Synthesis of Tetragonal Barium Titanate," *Chem. Mater.*, **4**, 843 (1992).
184. P. Nanni, M. Leoni, V. Buscaglia and G. Aliprandi, "Low-Temperature Aqueous Preparation of Barium Metatitanate Powders," *J. Europ. Ceram. Soc.*, **14**, 85 (1994).
185. M. Alvazzi Delfrate, M. Leoni, P. Nanni, E. Melioli, B. E. Watts and F. Leccabue, "Electrical Characterization of BaTiO₃ Made by Hydrothermal Methods," *J. Mater. Sci.: Mater. in Electronics*, **5**, 153 (1994).

186. G. Pfaff, "BaTiO₃ Preparation by Reaction of TiO₂ with Ba(OH)₂," *J. Europ. Ceram. Soc.*, **8**, 35 (1991).
187. D. E. Rase and R. Roy, "Phase Equilibria in the System BaO-TiO₂," *J. Am. Ceram. Soc.*, **38**, 102 (1955).
188. K. W. Kirby and B. A. Wechsler, "Phase Relations in the Barium Titanate-Titanium Oxide System," *J. Am. Ceram. Soc.*, **74**, 1841 (1991).
189. D. W. Richerson, "Forming and Predensification, and Nontraditional Densification Processes," in *Engineered Materials Handbook, Vol. 4: Ceramic and Glasses*, edited by S. J. Schneider, ASM International, p187, 1991.
190. W. Coblenz, "Firing/Sintering: Densification," in *Engineered Materials Handbook, Vol. 4: Ceramic and Glasses*, edited by S. J. Schneider, ASM International, 1991.
191. P. Murray, D. T. Livey and J. Williams, "The Hot Pressing of Ceramics," in *Ceramics Fabrication Processes*, edited by W. D. Kingery, Technology Press M.I.T., Cambridge, Mass., p 147, 1958.
192. G. J. Oudemans, *Philips Tech. Rev.*, **29**, 45 (1968).
193. K. H. Hardtl, "A Simplified Method for the Isostatic Hot Pressing of Ceramics," *Philips Tech. Rev.*, **35**, 65 (1975).
194. C. Tomandl, A. Stiegelschnitt and K. Bermuth, "Hot-Isostatic Pressing of BaTiO₃," *Ber. DKG*, **64**, 389 (1987).
195. I. W. Jones and L. J. Miles, "Production of β-Al₂O₃ Electrolyte," *Proc. Brit. Ceram. Soc.*, **19**, 161 (1971).
196. S. R. Tan and G. J. May, *Sci. Ceram.*, **9**, 103 (1977).
197. M. P. Harmer, E. W. Roberts and R. J. Brook, "Rapid Sintering of Pure and Doped α-Al₂O₃," *Tans. J. Br. Ceram. Soc.*, **78**, 22 (1979).
198. M. P. Harmer, E. W. Roberts and R. J. Brook, in *Energy and Ceramics*, edited by P. Vincenzini, Elsevier Scientific, Amsterdam, p155, 1980.

199. A. Morrell and A. Hermosin, "Fast-Sintering of Soft Mn-Zn and Ni-Zn Ferrite Pot Cores," *Amer. Ceram. Soc. Bull.*, **59**, 626 (1980).
200. M. P. Harmer and R. J. Brook, "Fast Firing-Microstructural Benefits," *J. British Ceram. Soc.*, **80**, 147 (1981).
201. H. Mostaghaci and R. J. Brook, "Fast-Firing of Non Stoichiometric BaTiO₃," *J. British Ceram. Soc.*, **80**, 148 (1981).
202. H. Mostaghaci and R. J. Brook, "Production of Dense and Fine Grain Size BaTiO₃ by Fast Firing," *Trans. J. Br. Ceram. Soc.*, **82**, 167 (1983).
203. H. Mostaghaci and R. J. Brook, "Microstructure Development and Dielectric Properties of Fast-Fired BaTiO₃ Ceramics," *J. Mater. Sci.*, **21**, 3575 (1986).
204. J. M. Vieira, *PhD Thesis*, University of Leeds (1981).
205. J. G. Fagan and V. R. W. Amarakoon, "Reliability and Reproducibility of Ceramic Sensors: Part II, PTC Thermistors," *Am. Ceram. Soc. Bull.*, **72**, 69 (1993).
206. W. Heywang, "Barium Titanate as a Semiconductor with Blocking Layers," *Solid-State Electron.*, **3**, 51 (1961).
207. W. Heywang, "Resistivity Anomaly in Doped Barium Titanate," *J. Am. Ceram. Soc.*, **47**, 484 (1964).
208. W. Heywang and H. Brauer, "The Structure of the Potential Barriers in Semiconducting Barium titanate," *Solid-State Electron.*, **8**, 129 (1965).
209. W. Heywang, "Semiconducting Barium Titanate," *J. Mater. Sci.*, **6**, 1214 (1971).
210. G. H. Jonker, "Some Aspects of Semiconducting Barium Titanate," *Solid-State Electron.*, **7**, 895 (1964).
211. G. H. Jonker, "Halogen Treatment of Barium titanate Semiconductors," *Mater. Res. Bull.*, **2**, 401 (1967).
212. G. H. Jonker and E. E. Havinga, "The Influence of Foreign Ions on the Crystal Lattice of Barium Titanate," *Mater. Res. Bull.*, **2**, 401 (1967).

213. J. Daniels, K. H. Hardtl, D. Hennings and R. Wernicke, "Defect Chemistry and Electrical Conductivity of Doped Barium Titanate Ceramics, Part I-V," *Philips Res. Rep.*, **31**, 487 (1976).
214. D. C. Sinclair and A. R. West, "Impedance and Modulus Spectroscopy of Semiconducting BaTiO₃ Showing Positive Temperature Coefficient of Resistance," *J. Appl. Phys.*, **66**, 3850 (1989).
215. D. C. Sinclair and A. R. West, "Effect of Atmosphere on the PTCR Properties of BaTiO₃ Ceramics," *J. Mater. Sci.*, **29**, 6061 (1994).
216. D. C. Sinclair and A. R. West, "Use of Succinic Acid to Test the Stability of PTCR Barium Titanate Ceramics under Reducing Conditions," *J. Am. Ceram. Soc.*, **78**, 241 (1995).
217. C. H. Lai and T. Y. Tseng, "Analysis of the AC Electrical Response for (Ba,Pb)TiO₃ Positive Temperature Coefficient Ceramics," *IEEE Trans. Comp. Pack. Manuf. Technol.*, **17**, 309 (1994).
218. B. Huybrechts, K. Ishizaki and M. Takata, "Review: The Positive Temperature Coefficient of Resistivity in Barium Titanate," *J. Mater. Sci.*, **30**, 2463 (1995).
219. A. B. Alles and V. L. Burdick, "Grain Boundary Oxidation in PTCR Barium Titanate Thermistors," *J. Am. Ceram. Soc.*, **76**, 401 (1993).
220. Y. M. Chiang and T. Takagi, "Grain-Boundary Chemistry of Barium Titanate and Strontium Titanate: I-II," *J. Am. Ceram. Soc.*, **73**, 3278 (1990).
221. S. B. Desu and D. A. Payne, "Interfacial Segregation in Perovskites: I-IV," *J. Am. Ceram. Soc.*, **73**, 3391 (1990).
222. Y. M. Chiang and T. Takagi, "Comment on 'Interfacial Segregation in Perovskites: I-IV,'" *J. Am. Ceram. Soc.*, **75**, 2017 (1992).
223. S. B. Desu and D. A. Payne, "Reply to 'Comment on 'Interfacial Segregation in Perovskites: I-IV,'" *J. Am. Ceram. Soc.*, **75**, 2020 (1992).
224. P. Blanchart, J. F. Baumard and P. Abelard, "Effects of Yttrium Doping on the Grain and Grain-Boundary Resistivities of BaTiO₃ for Positive

- Temperature Coefficient Thermistors," *J. Am. Ceram. Soc.*, **75**, 1068 (1992).
225. C. Gillot and J. P. Michenaud, "PTC Effect in Doped BaTiO₃ Ceramics: Evidence for a Bulk Contribution," *J. Phys. D: Appl. Phys.*, **27**, 2180 (1994).
225. J. R. Macdonald, *Impedance Spectroscopy: Emphasizing Solid Materials and Systems*, John Wiley & Sons, New York, 1987.
226. J. E. Bauerle, "Study of Solid Electrolyte Polarization by a Complex Admittance Method," *J. Phys. Chem. Solids*, **30**, 2657 (1969).
227. I. M. Hodge, M. D. Ingram and A. R. West, "Impedance and Modulus Spectroscopy of Polycrystalline Solid Electrolytes," *J. Electroanal. Chem.*, **53**, 429 (1975).
228. A. Hooper, "A Study of the Electrical Properties of Single Crystal and Polycrystalline β -Alumina Using Complex Plane Analysis," *J. Phys. D: Appl. Phys.*, **10**, 1487 (1977).
229. S. S. Liou and W. L. Worrell, "Electrical Properties of Novel Mixed-Conducting Oxides," *Appl. Phys. A*, **49**, 25 (1989).
230. N. Matsui, "Equivalent Circuit Analysis of Mixed-Conductor/Electrode System by Impedance Spectroscopy," *Solid State Ionics*, **57**, 121 (1992).
231. K. Eguchi, T. Setoguchi, T. Inoue and H. Arai, "Electrical Properties of Ceria-Based Oxides and Their Applications to Solid Oxide Fuel Cells," *Solid State Ionics*, **52**, 165 (1992).
232. I. C. Vinke, B. A. Boukamp, K. J. DeVries and A. J. Burggraaf, "Mixed Conductivity in Terbia-Stabilized Bismuth Oxide," *Solid State Ionics*, **57**, 91 (1992).
233. M. A. Alim, *The Influence of Grain Boundaries in Metal Oxide Varistors on Their AC Electrical Behavior*, Ph.D Dissertation, Marquette University, Milwaukee, WI, 1986.
234. A. M. Azad, L. B. Younkman, S. A. Akbar and M. A. Alim, "Characterization of TiO₂-Based Sensor Materials Using Impedance Spectroscopy," *J. Am. Ceram. Soc.*, **77**, 481 (1994).

235. A. M. Azad, S. A. Akbar, L. B. Younkman and M. A. Alim, "High Temperature Admittance Response of Anatase-Based Gas Sensors," *J. Am. Ceram. Soc.*, **77** (1994).
236. V. D. Patton, C. C. Wang, S. A. Akbar and M. A. Alim, "The ac Electrical Behavior of Polycrystalline Ytria," *J. Appl. Phys.*, **78**, 1757 (1995).
237. C. C. Wang, W. H. Chen, S. A. Akbar and M. A. Alim, "High-Temperature ac Electrical Behavior of Polycrystalline Calcium Zirconate," submitted to *J. Appl. Phys.* (1995).
238. M. A. Seitz, "Study of Heterogeneous Composite Materials via Lumped Parameter/Complex Plane Analysis," *Inter. J. Hybr. Microelec. (I.S.H.M.)*, **3**, 1 (1980).
239. M. A. Alim, S. Khanam and M. A. Seitz, "Immittance Spectroscopy of Smart Components and Novel Devices," *Active and Passive Elec. Comp.*, **16**, 153 (1994).
240. S. H. Chu and M. A. Seitz, "The ac Electric Behavior of Polycrystalline ZrO_2 -CaO," *J. Sol. St. Chem.*, **23**, 297 (1978).
241. R. H. Cole and K. S. Cole, "Dispersion and Absorption in Dielectrics: I. Alternating Current Characteristics," *J. Chem. Phys.*, **9**, 341 (1941).
242. R. H. Cole and K. S. Cole, "Dispersion and Absorption in Dielectrics: II. Direct Current Characteristics," *J. Chem. Phys.*, **10**, 98 (1942).
243. M. A. Alim, *The Influence of Grain Boundaries in Metal Oxide Varistors on Their ac Electric Behavior*, Ph.D Dissertation, Marquette University, Milwaukee, WI, 1986.
244. A. K. Jonscher, "Review Article: The 'Univeral' Dielectric Response," *Nature*, **267**, 673 (1977).
245. K. L. Ngai, A. K. Jonscher and C. T. White, "On the Origin of the Universal Dielectric Response in Condensed Matter," *Nature*, **288**, 185 (1979).
246. A. K. Jonscher, "The Universal Dielectric Response: A Review of Data and Their New Interpretation," *Phys. Thin Films*, **11**, 205 (1980).

247. L. M. Sheppard, "Advances in Processing of Ferroelectric Thin Films," *Ceram. Bull.*, **71**, 85 (1992).
248. T. L. Rose, E. M. Kelliher, A. N. Scoville and S. E. Stone, "Characterization of *Rf*-Sputtered BaTiO₃ Thin Films Using a Liquid Electrolyte for the Top Contact," *J. Appl. Phys.*, **55**, 3706 (1984).
249. S. K. Dey and J. J. Lee, "Cubic Paraelectric (Nonferroelectric) Perovskite PLT Thin Films with High Permittivity for ULSI DRAM's and Decoupling Capacitors," *IEEE Trans. Electron Devices* **ED-39**, 1607 (1992).
250. D. L. Polla, C. Ye, P. Schiller, T. Tamagawa, W. P. Robbins, D. Glumac and C. C. Hsueh, *Mater. Res. Soc. Symp. Proc.*, **243**, 55 (1992).
251. S. Y. Wu, J. Takei and M. H. Francombe, *Ferroelectrics*, **10**, 209 (1976).
252. M. Okuyama, Y. Hamakawa, *Ferroelectrics*, **63**, 243 (1985).
253. A. D. Fisher and J. N. Lee, *SPIE Proc.*, **634**, 352 (1986).
254. M. Kitabatake, K. Wasa, " ", *Jpn. J. Appl. Phys.*, **24**, Suppl. 22, 33 (1985).
255. D. Bondurant and F. Gnadinger, "Ferroelectrics for Nonvolatile RAMs," *IEEE Spectrum*, **26**, 30 (1989).
256. L. H. Parker and A. F. Tasch, "Ferroelectric Materials for 64 Mb and 256 Mb DRAMs," *IEEE Circuits Device Mag.*, **6**, 17 (1990).
257. P. Li, T. M. Lu and H. Bakhru, "High Charge Storage in Amorphous BaTiO₃ Thin Films," *Appl. Phys. Lett.*, **58**, 2639 (1991).
258. G. H. Haertling, "Ferroelectric Thin Films for Electronic Application," *J. Vac. Sci. Technol.*, **A9**, 414 (1991).
259. A. Patel, N. M. Shorrocks and R. W. Whatmore, *Mater. Res. Soc. Symp. Proc.*, **243**, 67 (1992).
260. K. Sreenivas, M. Sayer, D. J. Baar and M. Nishioka, "Surface Acoustic Wave Propagation on Lead Zirconate Titanate Thin Films," *Appl. Phys. Lett.*, **52**, 709 (1988).

261. C. K. Jen, C. Neron, G. Yi, M. Sayer, M. Castonguay and J. D. N. Cheeke, "Acoustic Lenses Employing PZT Thin Film Transducers," *Mater. Sci. Eng.*, **A122**, 21 (1989).
262. Y. C. Yeh and T. Y. Tseng, "Humidity-Sensitive Electrical Properties of Ba_{0.5}Sr_{0.5}TiO₃ Porous Ceramics," *J. Mater. Sci. Lett.* **7**, 766 (1988).
263. Z. Zhigang and Z. Gang, *Ferroelectrics*, **101**, 43 (1990).
264. T. Ishihara, K. Kometani, Y. Mizuhara and Y. Takita, "Mixed Oxide Capacitor of CuO-BaTiO₃ as a New Type CO₂ Gas Sensor," *J. Am. Ceram. Soc.*, **75**, 613 (1992).
265. N. H. Beltran, V. M. Fuenzalida, C. R. Grahmann and A. Cabrera, in European Ceramic Society Second Conference, September 1991, Augsburg, Germany, abstract G36.
266. L. I. Maissel and R. Glang, Eds., *Handbook of Thin Film Technology*, McGraw-Hill, New York, 1970.
267. T. D. Bonifield, *Deposition technologies for Films and Coatings: Developments and Applications*, R. F. Bunshah, Ed. Noyles, Park Ridge, NJ, 1982, pp. 365-384.
268. C. Feldman, "Formation of Thin Films of BaTiO₃ by Evaporation," *Rev. Sci. Instrum.*, **26**, 463 (1955).
269. Y. Y. Tomashpolski, *Ferroelectrics*, **7**, 253 (1974).
270. K. Iijima, T. Terashima, K. Yamamoto, K. Hirata and Y. Bando, "Preparation of Ferroelectric BaTiO₃ Thin Films by Activated Reactive Evaporation," *Appl. Phys. Lett.*, **56**, 527 (1990)
271. Y. Yano, K. Iijima, Y. Daitoh and Y. Bando, "Epitaxial Growth and Dielectric Properties of BaTiO₃ Films on Pt Electrodes by Reactive Evaporation," *J. Appl. Phys.*, **76**, 7833 (1994).
272. J. A. Thornton, "High Rate Sputtering Techniques," *Thin Solid Films*, **80**, 1 (1981).

273. J. D. Jorgenson, M. A. Beno, D. G. Hinks, L. Soderholm, K. J. Volin, R. L. Hitterman, J. D. Grace, I. K. Schuller, C. U. Segre, K. Zhang and M. S. Kleefisch, "Oxygen Ordering and the Orthorhombic-to-Tetragonal Phase Transition in $\text{YBa}_2\text{Cu}_3\text{O}_{7-x}$," *Phys. Rev.*, **B36**, 3608 (1987).
274. K. Sreenivas and M. Sayer, "Characterization of $\text{Pb}(\text{Zr}, \text{Ti})\text{O}_3$ Thin Films Deposited from Multi-element Metal Targets," *J. Appl. Phys.*, **64**, 1484 (1989).
275. H. Schafer, H. Schmitt, K. H. Ehses and G. Kleer, "Sputtering of BaTiO_3 Thin Ferroelectric Films," *Ferroelectrics*, **22**, 775 (1978).
276. K. Sreenivas, M. Sayer and P. Garrett, "Properties of D. C. Magnetron-Sputtered Lead Zirconate Titanate Thin Films," *Thin Solid Films*, **172**, 251 (1989).
277. H. Kawano, K. Morii and Y. Nakayama, "Microstructural and Dielectric Properties of BaTiO_3 Thin Films Prepared by Atom Beam Sputtering," *Mater. Lett.*, **12**, 252 (1991).
278. Q. X. Jia, Z. Q. Shi and W. A. Anderson, " BaTiO_3 Thin Film Capacitors Deposited by *rf* Magnetron Sputtering," *Thin Solid Film*, **209**, 230 (1992).
279. H. Kawano, K. Morii and Y. Nakayama, "Effects of Crystallization on Structural and Dielectric Properties of Thin Amorphous Films of $(1-x)\text{BaTiO}_{3-x}\text{SrTiO}_3$ ($x=0-0.5, 1.0$)," *J. Appl. Phys.*, **73**, 5141 (1993).
280. S. B. Desu, "Stress Induced Modifications in Ferroelectric Films," *Phys. Stat. Sol.*, **A 141**, 119 (1994)
281. Q. X. Jia, L. H. Chang and W. A. Anderson, "Low Leakage Current BaTiO_3 Thin Film Capacitors Using a Multilayer Construction," *Thin Solid Film*, **259**, 264 (1995).
282. D. Dijkkamp, T. Venkatesan, X. D. Wu, S. A. Shaheen, N. Jisrawi, Y. H. Min-Lee, M. L. McLean and M. Croft, "Preparation of Y-Ba-Cu Oxide Superconductor Thin Films Using Pulsed Laser Evaporation from High T_c Bulk Material," *Appl. Phys. Lett.*, **51**, 619 (1987).
283. D. Dijkkamp et al., *Novel Superconductivity, Proceedings of the International Workshop on Novel Mechanisms of Superconductivity*, Plenum, New York, 1987, p 725-731.

284. A. E. M. De Veirman, J. Timmers, F. J. G. Hakkens, J. F. M. Cillessen and R. M. Wolf, "TEM and XRD Characterization of Epitaxially Grown PbTiO_3 Prepared by Pulsed Laser Deposition," *Philips. J. Res.*, **47**, 185 (1993).
285. C. Bjormander, K. Sreenivas, M. Duan, A. M. Grishin and K. V. Rao, "Thickness Dependence of the Coercive Electric Field of Laser Ablated Niobium-Doped Lead-Zirconium-Titanate Films," *Appl. Phys. Lett.*, **66**, 2493 (1995).
286. R. W. Vest and J. Xu, " PbTiO_3 Films from Metalloorganic Precursors," *IEEE Trans. Ultrason. Ferroelectr. Freq. Control*, **35**, 711 (1988).
287. R. W. Vest and J. Xu, "Preparation and Properties of PLZT Films from Metallo-organic Precursors," *Ferroelectrics*, **93**, 21 (1989).
288. S. G. Yoon and H. G. Kim, "Characterization and Electrical Properties of Chemical Vapor Deposited Ferroelectric Lead Titanate Films on Titanium," *IEEE Trans. Ultrason. Ferroelectr. Freq. Control*, **37**, 333 (1990).
289. J. R. Hanrahan, E. Sanchez and J. J. Santiago, "Synthesis of Ferroelectric Thin Films via Metalloorganic Decomposition," *Thin Solid Films*, **202**, 235 (1991).
290. Y. Sakashita, T. Ono and H. Segawa, "Preparation and Electrical Properties of MOCVD-Deposited PZT Thin Films," *J. Appl. Phys.*, **69**, 8352 (1991).
291. H. Nakazawa, H. Yamane and T. Hirai, "Metalorganic Chemical Vapor Deposition of BaTiO_3 Films on MgO (100)," *Jap. J. Appl. Phys.*, **30**, 2200 (1991).
292. G. Braunstein, G. R. Paz-Pujalt and M. G. Mason, "The Processes of Formation and Epitaxial Alignment of SrTiO_3 Thin Films Prepared by Metallo-organic Decomposition," *J. Appl. Phys.*, **73**, 961 (1993).
293. Y. Sakashita and H. Segawa, "Dependence of Electrical Properties on Film Thickness in $\text{Pb}(\text{Zr}_x\text{Ti}_{1-x})\text{O}_3$ Thin Films Produced by Metalorganic Chemical Vapor Deposition," *J. Appl. Phys.*, **73**, 7857 (1993).

294. V. P. Dravid, H. Zhang, L. A. Wills and B. W. Wessels, "On the Microstructure, Chemistry, and Dielectric Function of BaTiO₃ MOCVD Thin Films," *J. Mater. Res.*, **9**, 426 (1994).
295. S. R. Gilbert, B. W. Wessels, D. A. Neumayer, T. J. Marks, J. L. Schindler and C. R. Kannewurf, "Preparation of Ba_{1-x}Sr_xTiO₃ Thin Films by Metalorganic Chemical Vapor Deposition and Their Properties," *Mater. Res. Soc. Symp. Proc.*, **335**, 41 (1994).
296. D. L Kaiser, M. D. Vaudin, G. Gillen, C. S. Hwang, L. H. Robins and L. D. Rotter, "Growth of BaTiO₃ Thin Films MOCVD," *Mater. Res. Soc. Symp. Proc.*, **335**, 47 (1994).
297. D. L Kaiser, M. D. Vaudin, G. Gillen, C. S. Hwang, L. H. Robins and L. D. Rotter, "Growth and Characterization of Barium Titanate Thin Films Prepared by Metalorganic Chemical Vapor Deposition," *J. Cryst. Growth*, **137**, 136 (1994).
298. E. Ching-Prado, R. S. Katiyar and J. J. Santiago-Aviles, "Micro-Raman Study of BaTiO₃ Thin Films Prepared by the Metalorganic Decomposition Technique," *J. Raman Spectrosc.*, **25**, 215 (1994).
299. S. K. Dey, K. D. Budd, D. A. Payne, "Thin-Film Ferroelectrics of PZT by Sol-Gel Processing," *IEEE Trans. Ultrason., Ferroelectr. Freq. Control*, **35**, 80 (1988).
300. G. Yi, Z. Wu, M. Sayer, "Preparation of Pb(Zr, Ti)O₃ Thin Film by Sol Gel Processing: Electrical, Optical, and Electro-Optic Properties," *J. Appl. Phys.*, **64**, 2717 (1989).
301. N. D. S. Mohallem and M. A. Aegerter, *Mater. Res. Soc. Symp. Proc.*, **121**, 515 (1988).
302. K. Y. Chen, L. L. Lee and D. S. Tsai, "Barium and Strontium Titanate Films from Hydroxide-Alkoxide," *J. Mater. Sci. Lett.*, **10**, 1000 (1991).
303. M. N. Kamalasanan, S. Chandra, P. C. Joshi and A. Mansingh, "Structural and Optical Properties of Sol-Gel-Processed BaTiO₃ Ferroelectric Thin Films," *Appl. Phys. Lett.*, **59**, 3547 (1991).

304. T. Hayashi, N. Ohji, K. Hirohara, T. Fukunaga and H. Maiwa, "Preparation and Properties of Ferroelectric BaTiO₃ Thin Films by Sol-Gel Process," *Jpn. J. Appl. Phys.*, **32**, 4092 (1993).
305. J. F. Champion, D. A. Payne, H. K. Chae and Z. K. Wu, "Chemical Processing of Barium Titanate Powders and Thin Layer Dielectrics," *Ceramic Powder Sci. IV*, **22**, edited by S. I. Hirano, G. L. Messing and H. Hausner, The American Ceramic Society, Westerville, OH, p15, 1991.
306. T. Tani, Z. Xu, P. Moses and D. Payne, "Temperature-Dependent Property Measurement on Multi-Electroded Thin-Layer Dielectrics," *Rev. Sci. Instrum.*, **65**, 2107 (1994).
307. M. N. Kamalasanan, N. D. Kumar and S. Chandra, "Dielectric and Ferroelectric Properties of BaTiO₃ Thin Films Grown by the Sol-Gel Process," *J. Appl. Phys.*, **74**, 5679 (1993).
308. M. N. Kamalasanan, N. D. Kumar and S. Chandra, "Structural and Microstructural Evolution of Barium Titanate Thin Films Deposited by the Sol-Gel Process," *J. Appl. Phys.*, **76**, 4603 (1994).
309. T. Hayashi, N. Ohji and H. Maiwa, "Film Thickness Dependence of Dielectric Properties of BaTiO₃ Thin Films Prepared by Sol-Gel Method," *Jpn. J. Appl. Phys.*, **33**, 5277 (1994).
310. A. Seifert, F. F. Lange and J. S. Speck, "Epitaxial Growth of PbTiO₃ Thin Films on (001) SrTiO₃ from Solution Precursors," *J. Mater. Res.*, **10**, 680 (1995).
311. T. Tani, J. F. Li, D. Viehland and D. A. Payne, "Antiferroelectric-Ferroelectric Switching and Induced Strains for Sol-Gel Derived Lead Zirconate Thin Layer," *J. Appl. Phys.*, **75**, 3017 (1994).
312. R. W. Schwartz, D. Dimos, S. J. Lockwood and V. M. Torres, "Electrical Properties of Sol-Gel PZT Thin Films for Decoupling Capacitor Applications," *Ferroelectric Films III, Mater. Res. Soc. Sym. Proc.*, **310**, edited by B. A. Tuttle, E. R. Myers, S. B. Desu and P. K. Larsen, p59 (1993).
313. S. Merklein, D. Sporn and A. Schonecker, "Crystallization Behavior and Electrical Properties of Wet-Chemically Deposited Lead Zirconate Titanate Thin Films," *Ferroelectric Films III, Mater. Res. Soc. Sym. Proc.*,

- 310**, edited by B. A. Tuttle, E. R. Myers, S. B. Desu and P. K. Larsen, p263 (1993).
314. I. M. Reaney, K. Brooks, R. Klissurska, C. Pawlaczyk and N. Setter, "Use of Transmission Electron Microscopy for the Characterization of Rapid Thermally Annealed, Solution-Gel, Lead Zirconate Titanate Films," *J. Am. Ceram. Soc.*, **77**, 1209 (1994).
315. K. Higuchi, K. Miyazawa and T. Sakuma, "Microstructure Characterization of Sol-Gel Derived PZT Films," *J. Mater. Sci.*, **29**, 436 (1994).
316. S. J. Lockwood, R. W. Schwartz, B. A. Tuttle and E. V. Thomas, "Solution Chemistry Optimization of Sol-Gel Processed PZT Thin Films," *Ferroelectric Films III, Mater. Res. Soc. Sym. Proc.*, **310**, Ed. by B. A. Tuttle, E. R. Myers, S. B. Desu and P. K. Larsen, p275 (1993).
317. T. Kawano, T. Sei and T. Tsuchiya, "Preparation of Ferroelectric (Pb,La)(Zr,Ti)₃ Thin Films by Sol-Gel Process and Dielectric Properties," *Jpn. J. Appl. Phys.*, **30**, 2178 (1991).
318. T. Tani and D. A. Payne, "Lead Oxide Coatings on Sol-Gel-Derived Lead Lanthanum Zirconium Titanate Thin Layers for Enhanced Crystallization into the Perovskite Structure," *J. Am. Ceram. Soc.*, **77**, 1242 (1994).
319. M. Yoshimura, S. E. Yoo, M. Hayashi and N. Ishizawa, *Jpn. J. Appl. Phys.*, **28**, L 2007 (1989).
320. N. Ishizawa, H. Banno, M. Hayashi, S. E. Yoo and M. Yoshimura, "Preparation of BaTiO₃ and SrTiO₃ Polycrystalline Thin Films on Flexible Polymer Film Substrate by Hydrothermal Method," *Jpn. J. Appl. Phys.*, **29**, 2467 (1990).
321. K. Kajiyoshi, K. Tomono, Y. Hamaji and T. kasanami, "Contribution of Electrolysis Current to Growth of SrTiO₃ Thin Film by the Hydrothermal-Electrochemical Method," *J. Mater. Res.*, **9**, 2109 (1994).
322. M. E. Pilleux and V. M. Fuenzalida, "Hydrothermal BaTiO₃ Films on Silicon: Morphological and Chemical Characterization," *J. Appl. Phys.*, **74**, 4664 (1993).

323. C. R. Cho, E. Shi, M. S. Jang, S. Y. Jeong and S. C. Kim, "Structural and Electrical Properties of BaTiO₃ Thin Films on Si(100) Substrate by Hydrothermal Synthesis," *Jpn. J. Appl. Phys.*, **33**, 4984 (1994).
324. E. Shi, C. R. Cho, M. S. Jang, S. Y. Jeong and H. J. Kim, "The Formation Mechanism of Barium Titanate Thin Film Under Hydrothermal Conditions," *J. Mater. Res.*, **9**, 2914 (1994).
325. M. Hayashi, N. Ishizawa, S. E. Yoo and M. Yoshimura, "Preparation of Barium Titanate Thin Film on Titanium-Deposited Glass Substrate by Hydrothermal-Electrochemical Method," *J. Ceram. Soc. Jpn.*, **98**, 93 (1990).
326. S. E. Yoo, M. Hayashi, N. Ishizawa and M. Yoshimura, "Preparation of Strontium Titanate Thin Film on Titanium Metal Substrate by Hydrothermal-Electrochemical Method," *J. Am. Ceram. Soc.*, **73**, 2561 (1990).
327. K. Shimomura, T. Tsurumi, Y. Ohba and M. Daimon, "Preparation of Lead Zirconate Titanate Thin Film by Hydrothermal Method," *Jpn. J. Appl. Phys.*, **30**, 2174 (1991).
328. R. Bacsa, P. Ravindranathan and J. P. Dougherty, "Electrochemical, Hydrothermal, and Electrochemical-hydrothermal Synthesis of Barium Titanate Thin Film on Titanium Substrate," *J. Mater. Res.*, **7**, 423 (1992).
329. R. Bacsa, J. P. Dougherty and L. J. Piliore, "Low-temperature Synthesis of BaTiO₃ Thin Film on Silicon Substrate by Hydrothermal Reaction," *Appl. Phys. Lett.*, **63**, 1053 (1993).
330. P. Bendale, S. Venigalla, J. R. Ambrose, E. D. Verink, Jr. and J. H. Adair, "Preparation of Barium Titanate Films at 55°C by an Electrochemical Method," *J. Am. Ceram. Soc.*, **76**, 2619 (1993).
331. R. Asiaie, *Spectroscopic, Thermal and Dielectric Properties of Hydrothermally Prepared BaTiO₃*, Ph.D Dissertation, The Ohio State University, Columbus, Ohio, 1995.
332. G. K. Williamson and W. H. Hall, "X-ray Line Broadening from Filled Aluminium and Wolfram," *Acta Metall.*, **1**, 22 (1953).

333. G. Ziegler, "Structure and Morphological Investigations of Ceramic Powders and Compacts," *Powder Met. Int.*, **10**, 70 (1978)
334. B. E. Warren and J. Bischof, *J. Am. Ceram. Soc.*, **21**, 49 (1938).
335. Klug, H. P.; Alexander, L. E., *X-Ray Diffraction Procedure for Polycrystalline and Amorphous Materials*, Carnegie-Mellon University Press, New York, 1973.
336. B. D. Cullity, *Elements of X-ray Diffraction*, 2nd Ed., Addison-Wesley, 1978.
337. K. L. Williams, *Introduction to X-ray Spectrometry*, Allen & Unwin, London, 1987.
338. J. C. Farinas and M. Barba, "Chemical Analysis by Inductively Coupled Plasma Atomic Emission Spectrometry of Semiconducting Ceramics of Barium Titanate Doped with Various Metal Oxides," *Mikrochim. Acta [Wien]*, **3**, 299 (1989).
339. Landolt-Bornstein, *Numerical Data and Functional Relationships in Science and Technology*, Part III, Vol. 3, p 51, 1989.
340. H. Blattner, W. Kanzig and W. Merz, *Helv. Phys. Acta* **1949**, *22*, 35.
341. C. H. Perry and D. B. Hall, *Phys. Rev. Lett.*, **15**, 700 (1965).
342. L. Rimai, J. L. Parsons, J. T. Hickmott and T. Nakamura, *Phys. Rev.*, **168**, 623 (1968).
343. M. Didomenico, S. H. Wemple, S. P. S. Porto and R. P. Bauman, *Phys. Rev.*, **174**, 522 (1968).
344. A. Chaves, R. S. Katiyar and S. P. S. Porto, *Phys. Rev.*, **B10**, 3522 (1974).
345. J. Javadpour, and N. G. Eror, *J. Am. Ceram. Soc.*, **71**, 206 (1988).
346. R. Ruppin, *Phys. Stat. Sol. B*, **64**, 701 (1974).
347. R. Ruppin, *J. Phys. C: Solid State Phys.*, **8**, 1969 (1975).

348. J. T. Last, *Phys. Rev.*, **105**, 1740 (1957).
349. M. I. Diaz Guemes, T. Gonzalez Carreno and C. J. Serna, *Spectrochim. Acta*, **45A**, 589 (1989).
350. G. Busca, G. Ramis, J. M. G. Amores, V. S. Escribano, P. Piaggio, *J. Chem. Soc., Faraday Trans.*, **90**, 3181 (1994).
351. T. J. Carbone and J. S. Reed, "Microstructure Development in Barium Titanate: Effects of Physical and Chemical Inhomogeneities," *Am. Ceram. Soc. Bull.*, **58** [5], 512 (1979).
352. D. Kolar, "Chemical Reaction Controlled Microstructures and Properties of Ferroelectric Ceramics," in *Chemistry of Electronic Ceramic Materials*, edited by P. K. Davies and R. S. Roth, Technomic, Lancaster, PA, 1990.
353. A. J. Mountvala, *J. Am. Ceram. Soc.*, **54**, 544 (1971).
354. M. N. Kamalasanan, N. D. Kumar and S. Chandra, "Dielectric and Ferroelectric Properties of BaTiO₃ Thin Films Grown by the Sol-Gel Process," *J. Appl. Phys.*, **74**, 5679 (1993).
355. *Handbook of Chemistry and Physics*, 71st Edition, edited by D. R. Lide, CRC Press, 1991.
356. L. I. Shvets, N. A. Ovramenko and F. D. Ovcharenko, *Dokl. Akad. Nauk. SSSR*, **248**, 889 (1979).
357. W. Hertl, *J. Am. Ceram. Soc.*, **71**, 879 (1988).
358. J. E. Burke, "Grain Growth in Ceramics," in *Kinetics of High Temperature Process*, edited by W. D. Kingery, Wiley, New York, 1959.
359. Y. Matsuo, H. Sasaki, "Exaggerated Grain Growth in Liquid Phase Sintering of BaTiO₃," *J. Am. Ceram. Soc.*, **54**, 471 (1971).
360. D. Hennings, "Recrystallization of Barium Titanate Ceramics," *Sci. Ceram.*, **12**, 405 (1984).
361. J. F. Fernandez, P. Duran and C. Moure, "Dielectric and Microstructural Properties of Sintered BaTiO₃ Ceramics Prepared from Different TiO₂ Raw Materials," *J. Mater. Sci.*, **26**, 3257 (1991).

362. T. T. Fang, H. L. Hsieh and F. S. Shiau, "Effects of Pore Morphology and Grain Size on the Dielectric Properties and Tetragonal-Cubic Phase Transition of High-Purity Barium Titanate," *J. Am. Ceram. Soc.*, **76**, 1205 (1993).
363. J. R. Slack and J. C. Burfoot, "Electrical Properties of Flash Evaporated Ferroelectric BaTiO₃ Thin Films," *J. Phys. C: Solid State Phys.*, **4**, 898 (1971).
364. R. E. Newnham, K. R. Udayakumar and S. Trolier-McKinstry, "Size Effects in Ferroelectric Thin Films," in *Chemical Processing of Advanced Materials*, edited by L. L. Hench and J. K. West, John-Wiley & Sons, 1992.
365. V. V. Mukhortov, Y. S. Nikitin, I. N. Zakharchenko, M. G. Radchenko, Y. I. Golovko and V. P. Dudkevich, *Sov. Phys. J. Tech. Phys.*, **33**, 867 (1988).
366. Z. Syrowiak, Y. S. Nikitin, E. V. Sviridov, V. M. Mukhortov and V. P. Dudkevich, *Izv. Akad. Nauk SSR, Ser fiz.*, **55**, 500 (1991).
367. A. A. Gitel'son, A. M. Lerer, V. S. Mikhalevskii, V. M. Mukhortov and S. V. Orlov, "Physical Properties of (Ba, Sr)TiO₃ Ferroelectric Thin Films in Weak Electric Fields," *Sov. Phys. Solid. State*, **19**, 1121 (1977).
368. S. V. Biryukov, V. M. Mukhortov, A. M. Margolin, Y. I. Golovko, I. N. Zakharchenko, V. P. Dudkevich and E. G. Fesenko, "Phase Transitions in Polycrystalline and Heteroepitaxial Ferroelectric Films," *Ferroelectrics*, **56**, 115 (1984).
369. D. Hennings, M. Klee and R. Waser, "Advanced Dielectrics: Bulk Ceramics and Thin Films," *Advan. Mater.*, **3**, 334 (1991).
370. J. Nowotny, "Defect Structure, Electrical Properties and Transport in Barium Titanate," *Ceram. Inter.*, **20**, 213 (1994).
371. N. H. Chan, R. K. Sharma and D. M. Smyth, "Nonstoichiometry in Undoped BaTiO₃," *J. Am. Ceram. Soc.*, **64**, 556 (1981).